FRITZ-HABER-INSTITUT
MAX-PLANCK-GESELLSCHAFT

Chemical electron microscopy of perimeter structures in bimetallic nanocatalyst systems

M. Sc. Liseth Johana Duarte Correa

Berlin 2024

Chemical electron microscopy of perimeter structures in bimetallic nanocatalyst systems

vorgelegt von
M. Sc.
Liseth Johana Duarte Correa
ORCID: 0000-0002-7944-7029

an der Fakultät II - Mathematik und Naturwissenschaften
der Technischen Universität Berlin
zur Erlangung des akademischen Grades
Doktorin der Naturwissenschaften
– Dr. rer. nat. –
genehmigte Dissertation

Promotionsausschuss:
Vorsitzender: Prof. Dr. Maria Andrea Mroginski
Gutachter: PD Dr. Thomas Lunkenbein
Gutachter: Prof. Dr. Arne Thomas
Gutachter: Prof. Dr. Thomas W. Hansen
Gutachter: Prof. Dr. Malte Behrens
Tag der wissenschaftlichen Aussprache: 08. Dezember 2023

Berlin 2024

Die vorliegende Arbeit wurde im Zeitraum von Mai 2019 bis August 2023 im Arbeitskreis von Prof. Dr. Robert Schlögl am Fritz-Haber-Institut der Max-Planck-Gesellschaft durchgeführt.

Abstract

Currently, scientists seek energy conversion options that are both environmentally and economically sustainable. A promising option is the use of transition-metal containing layered double hydroxides (LDH) as catalyst precursors. In addition, employing a combination of two metals in a bimetallic system can improve the catalyst's properties compared to monometallic materials. The nickel and copper bimetallic systems are interesting combinations for catalyst applications. However, there are still open research questions due to contradictory results. Some previous research has reported a miscibility gap for thin films of Ni-Cu; a point where the two elements do not form an alloy or solid solution that is often omitted within investigations of supported nanoalloys. In addition, more research is needed to understand the structure-function relationship of Ni-Cu bimetallic catalysts derived from LDH precursors. The aim of this thesis was to study the Ni-Cu bimetallic catalysts using materials derived LDH precursor. Through chemical electron microscopy as a primary characterization technique, combined with complementary techniques (thermogravimetric analysis, temperature-programmed reduction, X-ray diffraction, X-ray photoelectron spectroscopy, near edge X-ray adsorption fine structure, among others), we unraveled the properties of the materials after synthesis, activation, and catalytic testing. The catalytic evaluation entailed two paragon examples of current importance: carbon dioxide hydrogenation and ammonia decomposition reactions. In addition, owing to the significance of transmission electron microscopy (TEM) analysis in this thesis and the potential damage during electron-matter interaction, a systematic analysis of beam damage in the TEM was conducted for the first time for this LDH system. The analysis describes the structural changes resulting from electron beam irradiation on LDH and derived materials.

First, four materials with different Ni:Cu metal compositions were chosen and synthesized from an LDH precursor, using carbonates as interlayer anions and Al as support: two with a monometallic (NiAl and CuAl), and two with a bimetallic (NiCu(4:1)Al and NiCu(1:1)Al) composition. The results showed that all LDH samples presented platelet-like morphology. The calcination process transformed the metal hydroxides into mixed metal oxides (MMO), where the Al_2O_3 remained amorphous. The study of the activation process highlighted three main aspects. (1) Mild calcination at 290 °C, in contrast to 600 °C as a harsh calcination method, helped to lower the reduction temperature of Ni-containing samples, probably by avoiding the formation of a Ni-spinel structure. (2) The presence of low amounts of copper (Ni/Cu ratio = 4), usually atomically dispersed, promoted the reducibility of nickel by reducing the temperature of the reduction peak by 100 °C. (3) Upon reduction at 450 °C, the samples containing Ni exhibited uniformly dispersed nanoparticles with a particle size of 3.7 nm. The bimetallic samples showed an enrichment of Cu at their surfaces. Further investigation with in situ XRD using NiCu(4:1)Al sample suggested that above 600 °C the Cu from the surface was incorporated into the Ni lattice forming an alloy.

Catalytic evaluation on the selected reactions showed the different roles of nickel and copper species. During CO_2 hydrogenation at atmospheric pressure and various temperatures (from 500 to 600 °C), Ni promoted methanation, whereas adding Cu suppressed such methane formation by improving CO selectivity (RWGS activity). On ammonia decomposition at ambient pressure, the Ni particles - potential active centers - were blocked by adding Cu. This significantly decreased hydrogen production. Characterization of the spent catalysts showed that Ni may provide stability to the catalysts, especially noticeable during CO_2 hydrogenation. When Cu was added in a 1:1 ratio, remarkable segregation occurred after both reactions. Here, Cu particles with sizes above 100 nm were visible.

Furthermore, we performed detailed experiments on one bimetallic sample using operando TEM. A striking CO and H_2O production for CO_2 hydrogenation was observed at 800 mbar and 600 °C. The results presented here have sparked further research questions, with operando TEM being identified as a promising method for gaining a more comprehensive understanding of atomic-level changes in a working catalyst.

In conclusion, the findings reported in this dissertation contributed to the fundamental understanding of Ni-Cu bimetallic systems, particularly derived from LDH precursors. We emphasized their bimetallic functionalities in key reactions for a possible H_2-based economy, such as CO_2 hydrogenation and ammonia decomposition reactions.

Zusammenfassung

Aktuell suchen Wissenschaftler nach Energieumwandlungsoptionen, die sowohl umwelt- als auch wirtschaftlich nachhaltig sind. Eine vielversprechende Option ist die Verwendung von Übergangsmetallen, die geschichtete Doppelhydroxide (layered double hydroxides, LDH) als Katalysatorvorläufer enthalten. Zusätzlich kann die Anwendung einer Kombination von zwei Metallen in einem bimetallischen System die Eigenschaften des Katalysator im Vergleich zu momometallischen Systemen verbessern. Die Nickel- und Kupferbimetallsysteme sind interessante Kombinationen für Katalysatoranwendungen. Aufgrund widersprüchlicher Ergebnisse gibt es jedoch noch offene Forschungsfragen. In einigen früheren Forschungsarbeiten wurde eine Mischungslücke für dünne Ni-Cu-Filme festgestellt, d. h. ein Punkt, an dem die beiden Elemente keine Legierung oder feste Lösung bilden, was bei Untersuchungen von geträgerten Nanolegierungen oft übersehen wird. Darüber hinaus sind weitere Forschungsarbeiten erforderlich, um die Struktur-Funktions-Beziehung von bimetallischen Ni-Cu-Katalysatoren, welche aus LDH-Vorläufern gewonnen werden zu verstehen. Ziel dieser Arbeit war es, die bimetallischen Ni-Cu-Katalysatoren, die unter Verwendung von LDH-Vorläufermaterialien hergestellt wurden, zu untersuchen. Mittels chemischer Elektronenmikroskopie als primäre Charakterisierungstechnik, kombiniert mit ergänzenden Techniken (thermogravimetrische Analyse, temperaturprogrammierte Reduktion, Röntgenbeugung, Röntgen-Photoelektronenspektroskopie, Röntgen-Nahkanten-Absorptions-Spektroskopie, u.a.), haben wir die Eigenschaften der Materialien nach der Synthese, Aktivierung und katalytischen Tests untersucht. Die katalytischen Tests umfassten zwei Musterbeispiele von aktueller Bedeutung: Kohlendioxid-Hydrierung und Ammoniak-Zersetzungsreaktionen. Aufgrund der Bedeutung der Transmissionselektronenmikroskopie (TEM) in dieser Arbeit und der möglichen Schädigung bei der Elektronen-Materie-Wechselwirkung wurde zudem erstmals eine systematische Analyse der Effekte durch Strahlschäden durchgeführt. Die Analyse beschreibt die strukturellen Veränderungen, die sich daraus an LDH und abgeleiteten Materialien ergeben.

Zunächst wurden vier Materialien mit unterschiedlichen Ni:Cu-Metallzusammensetzungen ausgewählt und aus einer LDH-Vorstufe synthetisiert, wobei Carbonate als Zwischenschichtanionen und Al als Trägermaterial verwendet wurden: zwei Systeme mit monometallischer (NiAl und CuAl) und zwei mit bimetallischer Zusammensetzung (NiCu(4:1)Al und NiCu(1:1)Al) wurden hergestellt. Die Ergebnisse zeigten, dass alle LDH-Proben eine plättchenartige Morphologie aufwiesen. Durch den Kalzinierung-

sprozess wurden die Metallhydroxide in Mischmetalloxide (MMO) umgewandelt, wobei das Al_2O_3 amorph blieb. Bei der Untersuchung des Aktivierungsprozesses wurden drei Hauptaspekte festgestellt. (1) Die milde Kalzinierung bei 290 °C, im Gegensatz zur harten Kalzinierungsmethode bei 600 °C, trug dazu bei, die Reduktionstemperatur in den Ni-haltigen Proben zu senken. Es ist davon auszugehen, dass durch die Temperaturreiduzierung der Kalzinierungsmethode die Bildung einer Ni-Spinell-Struktur vermieden wurde. (2) Das Vorhandensein geringer Mengen an Kupfer (Ni/Cu-Verhältnis = 4), das in der Regel atomar dispergiert ist, förderte die Reduzierbarkeit von Nickel, indem es die Temperatur des Reduktionspeaks um 100 °C senkte. (3) Nach der Reduktion bei 450 °C wiesen die Ni enthaltenden Proben gleichmäßig verteilte 3.7 nm große Nanopartikel auf, und die bimetallischen Proben zeigten eine Anreicherung von Cu an ihren Oberflächen. Weitere Untersuchungen mit in situ XRD unter Verwendung einer NiCu(4:1)Al-Probe deuteten darauf hin, dass oberhalb von 600 °C das Cu von der Oberfläche in das Ni-Gitter eingebaut wurde und eine Legierung bildet.

Die katalytische Testung der ausgewählten Reaktionen zeigte die unterschiedlichen Rollen der Nickel- und Kupferspezies. Bei der CO_2-Hydrierung unter Atmosphärendruck mit verschiedenen Temperaturen (von 500 bis 600 °C) förderte Ni die Methanbildung, während die Zugabe von Cu diese Methanbildung durch Verbesserung der CO-Selektivität (RWGS-Aktivität) unterdrückte. Bei der Zersetzung von Ammoniak bei Umgebungsdruck wurden die Ni-Teilchen – potenziell aktive Zentren – durch den Zusatz von Cu blockiert. Dies verringerte die Wasserstoffproduktion erheblich. Die Charakterisierung der verbrauchten Katalysatoren zeigte, dass Ni den Katalysatoren Stabilität verleihen kann, was besonders bei der CO_2-Hydrierung auffällt. Wurde Cu im Verhältnis 1:1 zugesetzt, kam es nach biden Reaktionen zu einer bemerkenswerten Entmischung. Hier waren nun Cu-Partikel mit einer Größe von über 100 nm sichtbar.

Darüber hinaus führten wir detaillierte Experimente an einer Bimetallprobe unter Operando-TEM-Bedingungen durch. Bei 800 mbar und 600 °C wurde eine außergewöhnliche CO- und H_2O-Produktion für die CO_2-Hydrierung beobachtet. Die hier vorgestellten Ergebnisse haben weitere Forschungsfragen aufgeworfen, wobei sich operando-TEM als vielversprechende Methode erwiesen hat, um ein umfassenderes Verständnis der Veränderungen auf atomarer Ebene in einem funktionierenden Katalysator zu erlangen.

Zusammenfassend lässt sich sagen, dass die in dieser Dissertation berichteten Ergebnisse zum grundlegenden Verständnis von Ni-Cu-Bimetall-Systemen, insbesondere aus LDH-Vorläufern, beigetragen haben. Wir haben ihre bimetallischen Funktionen in Schlüsselreaktionen für eine mögliche H_2-basierte Wirtschaft hervorgehoben, wie z. B. CO_2-Hydrierung und Ammoniak-Zersetzungsreaktionen.

Contents

List of Tables

List of Figures

List of abbreviation

- 2D: 2-dimensional
- 3D: 3-dimensional
- AFD: Annular dark field
- BE: Binding energy
- BET: Brunauer-Emmett-Teller
- BF: Bright field
- BJH: Barrett-Joyner-Halenda
- DRIFTS: Diffuse reflectance infrared Fourier transform spectroscopy
- DRM: Dry reforming of methane
- EDX: Energy-dispersive X-ray spectroscopy
- EELS: Electron energy-loss spectroscopy
- ELNES: Energy loss near edge structure
- ESEM: Environmental scanning electron microscopy
- FBR: Fixed-bed reactor
- FWHM: Full-width half-maximum
- HAADF: High angle annular dark field
- HRTEM: High resolution transmission electron microscopy
- HV-RT: High vacuum, room temperature
- ICP: Inductively coupled plasma
- LDH: Layered double hydroxides
- MEMS: Microelectromechanical system
- MMO: Mixed metal oxides
- MSI: Metal-support interaction
- NEXAFS: Near edge X-ray adsorption fine structure
- OTEM: Operando transmission electron microscopy
- QMS: Quadrupole mass spectrometer
- RWGS: Reverse water gas shift reaction
- STEM: Scanning transmission electron microscopy
- TCD: Thermal conductivity detector

- TEM: Transmission electron microscopy
- TGA: Thermogravimetric analysis
- TOS: Time of stream
- TPD: Temperature-programmed desorption
- TPR: Temperature-programmed reduction
- WGS: Water gas shift reaction
- WHSV: Weight hourly space velocity
- XPS: X-ray photoelectron spectroscopy
- XRD: X-ray diffraction
- ZLP: Zero-loss peak

Motivation

Heterogeneous catalysts are used in numerous industrial processes, where nanoparticles play an important role in the achievement of chemical transformations. Improvement of these nanocatalytic systems is usually performed by empirical optimization. To contribute to a better rational catalyst design, a deep understanding of the nanoscale and its relationship with the catalytic performance is crucial. Chemical electron microscopy [1] offers the possibility to unravel several properties of the material at the atomic scale, which, when combined with other characterization tools, can provide a big picture of the material.

Among the most widely used catalysts, bimetallic supported materials are becoming very important because of their increased catalyst activity, selectivity, and stability compared to their supported monometallic catalysts. For instance, the combination of nickel and copper has been of interest for several decades, especially for hydrogenation of carbon dioxide [2]. However, investigations of the NiCu system have shown contradictory results, such as the formation of a NiCu alloy [3] or two segregated phases [4]. These differences are related to the different synthesis precursors and the specific thermal pretreatment used. Thus, a systematic and complete analysis of NiCu bimetallic systems is required for providing a knowledge base that allows a rational design. To perform systematic studies, we narrowed down synthesis preparation to the use of layered double hydroxides (LDH) precursor. With the LDH approach, it is possible to produce well-defined, uniform distribution, and controlled-sized nanoparticles.

Therefore, the aim of the present work was to acquire a fundamental understanding of the NiCu system derived from LDH precursors, from their synthesis and activation to their catalytic application. The properties of the catalysts were then correlated with their performance in the relevant chemical energy conversion reactions: hydrogenation of CO_2 and decomposition of ammonia. Carbon dioxide reduction is crucial in view of the mitigation of global climate change, and ammonia decomposition is a promising molecule for transporting and storing hydrogen.

This PhD investigation was carried out within the scope of Unifying Systems in Catalysis (UniSysCat) in collaboration with other groups in the Department of Inorganic Chemistry (AC), BasCat - UniCat BASF Joint Lab, and the Heterogeneous Reactions Department of the Max-Planck-Institut für Chemische Energiekonversion (MPI-CEC).

The thesis is composed of six chapters. Chapter 1 presents an introduction to chemical electron microscopy, the heterogeneous catalysis of nickel-copper bimetallic systems, and the LDH materials as catalyst precursors. A brief review of the literature on the two relevant reactions -ammonia decomposition and CO_2 hydrogenation- is also presented. In Chapter 2, the instrumentation and experimental details are described.

The results chapters are divided into four parts. The physicochemical properties of the series of *M*-Al LDH materials, where *M* represents four different Ni:Cu combinations (1:0, 4:1, 1:1 and 0:1), are described in Chapter 3. The interaction between Ni and Cu to form Ni-Cu bimetallic particles is presented and analyzed. Using several characterization techniques, the activation procedure to obtain small and well-dispersed metal nanoparticles is also discussed. The activation conditions concluded from these studies are then applied to catalytic testing (Chapter 4) on reverse water gas shift (RWGS) and ammonia decomposition reactions. The results from the RWGS reaction highlight the main features of the structure-function relationship for Ni-Cu bimetallic systems and the key of stability.

The most interesting sample from previous results, NiCu(4:1)Al, was chosen for in situ and operando characterization, described in Chapter 5. The structural and morphological changes during activation are illustrated, and a clear correlation between X-ray diffraction and TEM characterization is presented. Furthermore, the changes in the material during operando TEM experiments for the RWGS reaction are illustrated. The results indicate that catalytic analysis is essential not only in ex situ characterization but also in operating conditions, i.e., recording the conversion while monitoring structure and morphology.

Given the high relevance of chemical electron microscopy characterization and LDH as a promising catalyst precursor, Chapter 6 is dedicated to studying the influence of electron beam irradiation during TEM characterization. Finally, a summary of the main findings is presented in Chapter 7.

1 Introduction and overview

A fundamental understanding of catalytic systems can contribute to a better catalyst design. Both theoreticians and experimentalists have joined efforts to understand the active sites of catalytic systems: from studies of clean surfaces to the real catalysts. One of the most indispensable and complete characterization techniques in wide areas of applications (material science and inorganic materials), is transmission electron microscopy. More specifically, "chemical electron microscopy" has been described as a "nano-laboratory to characterize morphological, crystallographic, compositional, and electronic properties of catalysts" [5].

This chapter covers the fundamentals of transmission electron microscopy (TEM), important for future chapters. Afterward, the most relevant investigations of Ni-Cu bimetallic systems obtained, including clean surfaces and supported porous materials, are outlined.

TEM is relevant for understanding the properties of bimetallic catalytic systems and their dynamic changes during or after catalysis. It can decipher the mixing patterns of bimetallic materials: alloyed state, segregated, or as Janus particles. In this PhD thesis, the chemical (transmission) electron microscopy technique was the primary one used, and it was complemented with other characterization techniques to gain a fundamental understanding of the NiCu bimetallic system.

1.1 Transmission electron microscopy

Transmission electron microscopy is a powerful tool for characterizing materials that unravel several properties of the specimen at the atomic scale with a single machine. Since Knoll and Ruska's first operational description of *Elektronenmikroskop* in 1932 [6], this technique has been widely used in various fields, both in physical and life sciences. In particular, chemical electron microscopy is of utmost importance for studying materials such as nanocatalyst systems. Using a TEM, the imaging resolution can reach several angstroms, and structural atomic scale information can be revealed. In addition, TEM can also provide information about the chemical composition because of the strong electron-specimen interaction. Today, (HR)TEM is a standard characterization method in scientific research, academic education, and industry.

A representation of a transmission electron microscope is shown in Figure 1 [7]. The system can be divided into three main parts: (1) the illumination system (electron source and condenser lens), (2) the objective lens and specimen stage, and (3) the intermediate and projector lens. The powder sample or specimen is usually prepared by dipping the TEM grid into powder or dropping the suspension of powder suspended in a suitable solvent (e.g. water or ethanol) into the TEM grid. The prepared sample on the TEM grid must be thin enough so that the electrons can be transmitted, but also stable enough to withstand the electron beam without considerable change in its properties. The electron beam-sample interaction is necessary to obtain all the relevant information, as will be described in the following paragraphs; however, it may also cause temporary or permanent changes in the material. Therefore, special attention should be paid to the sample damage during the TEM studies.

1.1.1 HRTEM and electron diffraction

TEM or HRTEM images can be formed by illuminating a larger area of the specimen in an *imaging* mode. For that, the objective aperture, positioned in the back focal plane of the objective lens, can be inserted to control the scattered electrons that contribute to the image formation. The intermediate lens is set to focus on the image plane, which is further magnified by the projector lens and appears in the detectors. Structural and morphological information (i.e. size, shape, location, and distribution) of the nanoparticles can be obtained. The imaging mode can be switched to *diffraction* mode and electron diffraction can be performed in the same machine. When switching from image mode to diffraction mode, the intermediate lens is adjusted to focus on the diffraction pattern in the back focal plane of the specimen. The diffraction pattern is magnified by the projector lens and recorded with specialized cameras. Using a selected area electron diffraction (SAED) aperture enables the selection of a specific area for diffraction. This can be used to determine the structure type, symmetry, and crystalline information of the catalysts from nanoscale areas. [7] The local crystal structure observed by electron diffraction can be complemented or contrasted with the bulk crystallographic information obtained by X-ray diffraction (XRD).

1.1.2 Scanning TEM and chemical analysis

Moreover, scanning TEM (STEM) of the sample by using a convergent beam is also possible and a STEM image is formed pixel by pixel. While scanning over the sample area, the electrons transmitted through the sample are collected by different detectors (see Figure 1b). The bright-field detector (BF) collects signals with very small scattering angles with semiangle $\theta < 10$ mrad, the annular dark field (ADF) with semiangle θ between 10 and 50 mrad, and the high angle ADF (HAADF) detector collects signals with semiangle θ > 50 mrad. Images collected with the HAADF detector show atomic contrast (Z-contrast). Due to Rutherford scattering, the collected signal intensities are dependent on the atomic number Z but also on the thickness of the sample. Therefore, chemical compositional information can be revealed because a material with a higher Z shows a higher intensity.

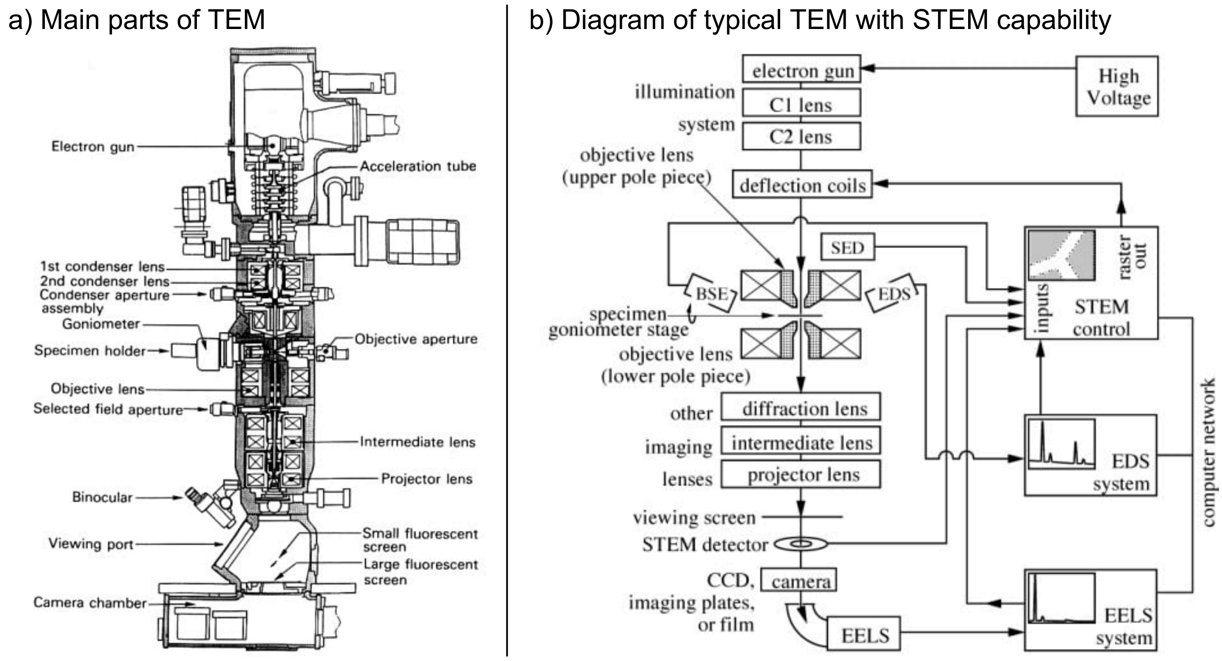

a) Main parts of TEM

b) Diagram of typical TEM with STEM capability

Figure 1: a) Main parts of the transmission electron microscope; b) Block diagram of typical TEM with STEM capability.

Reproduced from [7].

The high-energy electrons interact with the sample in an elastic (without energy exchange) or inelastic (with energy exchange) manner. Inelastic scattering arises from the interaction with the core atoms of the specimen. It provides a variety of signals that can serve as unique identifiers for chemical analysis during electron microscopy. Energy-dispersive X-ray spectroscopy (EDX) uses only the generated X-ray signals; meanwhile, electron energy-loss spectroscopy (EELS) uses the energy-loss signals of the transmitted electrons. Elemental identification and elemental mapping are used to uncover the composition and arrangement of catalysts. This turns the electron microscopy technique into a far more powerful tool, chemical or analytical electron microscopy, for revealing the chemistry of the specimen.

1.1.2.1 Energy-dispersive X-ray spectroscopy (EDX)

The characteristic X-ray energy is defined by the difference between the two shell energies of the electrons that participate in the ionization process (the first electron ejected and the second electron, from a higher-energy shell that filled the hole left by the first one). The specific spectral lines are named according to the shell from which the electron was ejected in combination with the shell of the electron that fills the hole. A K_α X-ray is emitted when filling a K-shell hole with an L-shell electron; a K_β X-ray, when it is filled with an M-shell electron; an L_α, X-ray or L_β X-ray when an L-shell hole is filled with an M-shell or N-shell electron, respectively. In EDX, the signals are usually collected above the specimen, and the spectrum consists of element-specific characteristic peaks with well-defined energies.

The detection depends on whether the atom emits an X-ray or not, and the area from which the radiation can be collected (0.9 steradian for Thermo Scientific Talos F200X microscope). For light elements, X-ray emission is limited as described by the fluorescence yield, and therefore the identification is more difficult than in EELS [8].

1.1.2.2 Electron energy-loss spectroscopy (EELS)

EELS signals are formed with transmitted electrons that interact with the core electrons of the specimen and lose a certain amount of energy. This energy is transferred to the X-rays or into other forms. The energy losses of the transmitted electrons are detected and collected below the specimen. EEL spectrum has three regions. The zero-loss peak (ZLP) represents the electrons that have not lost energy. The low-loss region contains electrons that have interacted with weakly bound electrons in the sample. And in the high-loss region are the electrons that have interacted with tightly bound core electrons of the atoms in the sample. Chemical information is contained in both the low-loss and high-loss regions. Identification of light elements is more accessible than using EDX.

The high-loss (core-loss) region comprises ionization edges, which are characteristic of the atom involved. Ionization is the primary event in which a core-shell electron is ejected into empty states. As in EDX, the core-shell involved in the ionization process defines its nomenclature. For example, a K shell electron (1s electrons) gives rise to a K edge; the L shell electrons can cause L_1 edge (from 2s electrons), or $L_{2,3}$ edges (from 2p electrons). The core-loss region consists of near-edge or fine structure (energy-loss near-edge structure, ELNES), and extended fine structure [9]. The ELNES spectrum's shape is used to identify the bonding properties and oxidation states (density of states) of the elements.

For optimal EELS measurements, the sample should be thin enough. The thickness can be estimated from the ZLP signal, in terms of the inelastic mean free path (t/λ). The recommended thickness values are between $0.0 \leq t/\lambda \leq 1.5$ to assess a good ELNES [10].

1.1.3 In situ and operando TEM (OTEM)

The set of methods mentioned above has been widely utilized to determine the characteristics of the catalyst in atomic detail. Properties such as particle size, composition, crystallinity, and the presence of defects can be revealed. Additionally, studying the changes in catalyst particles is crucial in heterogeneous catalysis to understand how the catalyst surface works under relevant industrial conditions. For that reason, several research groups have used in situ and operando techniques, both in microscopy (HRTEM and STEM) and spectroscopy.

One of the first in situ TEM studies from 2001 [11] concluded that conventional TEM is not optimal for heterogeneous catalysis investigation because the nanoparticles behave differently under a given chemical potential. They are dynamic and complex. In situ and operando electron microscopy approaches allow the study of changes at the nanoscale under certain applied potentials (i.e. gas composition, temperature). There are two types of in situ TEM setup [12], which are represented in Figure 2. One is the environmental TEM, an open cell system where gas is introduced directly into the TEM column, which has to be differentially pumped for allowing a proper detection [13]. The other is the use of gas-cell holders or closed-cell approach, in which the sample is prepared between the two electron transparent windows of a microelectromechanical system (MEMS) device [14], [15]. In both cases, the electron beam may affect the catalysts and the reaction, and the resolution may be lower due to sample-gas or electron-matter interactions [13]. Furthermore, the mechanical strength of the window restricts the use of MEMS-based cells to pressures of up to 1 bar. The advances in methodologies and instruments enable the comprehension of catalytic systems on an atomic level by integrating various disciplines [5].

Operando measurements require simultaneous characterization (electron microscopy, in this case) with direct evidence of conversion or activity-selectivity measurements [16]. Product detection might be restricted mainly by the amount of material deposited on the chip. Overcoming this requires the introduction of more material that interacts with the gas (for example, in a newly designed pellet reactor [17]), or the use of a highly sensitive mass spectrometer (MS). By using MEMS-based TEM sample holders with a gas analyzer, the dynamic refaceting of nanoparticles was observed for the first time during CO oxidation [18]. The developments of aberration-corrected microscopes have enabled characterization at higher spatial resolutions [19]. During the last decade, several more studies have used OTEM, as shown in Figure 3. The number of publications per year in the last 10 years with 'operando transmission electron microscopy has grown significantly [20].

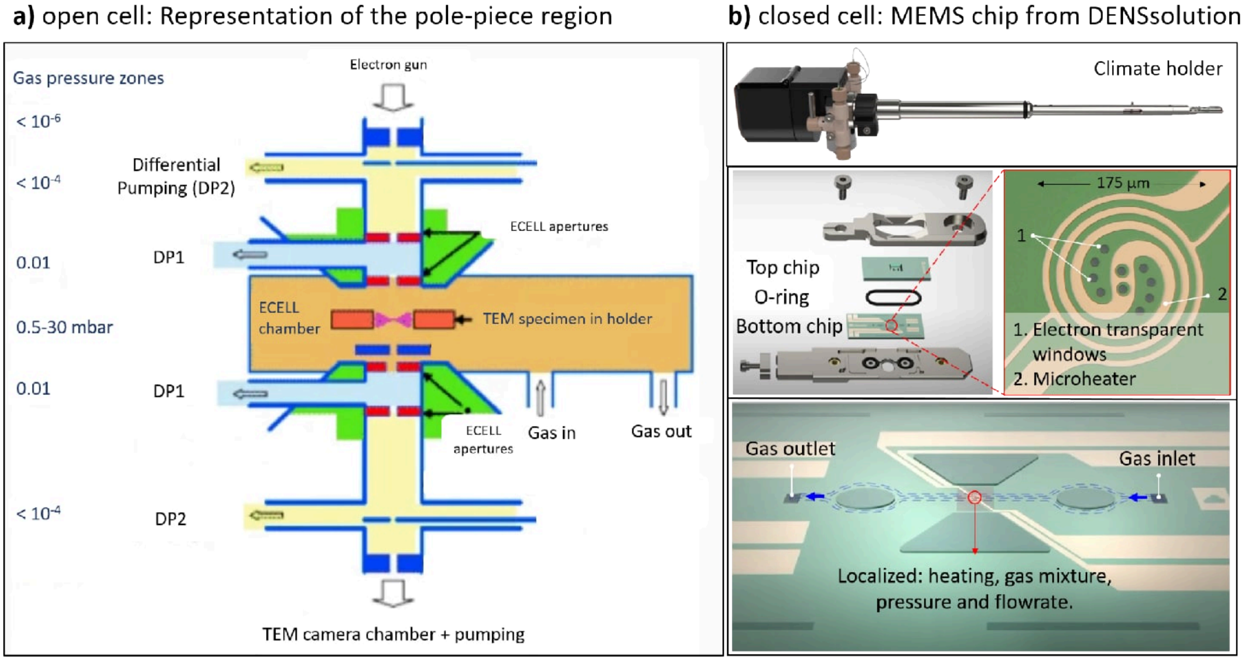

Figure 2: Representation of in situ TEM operation: a) open cell, a schematic of the pole-piece region within an ETEM for controlled gas exposure with differential pumping; b) close cell or MEMS chip-based.

Adapted from [21] and [22].

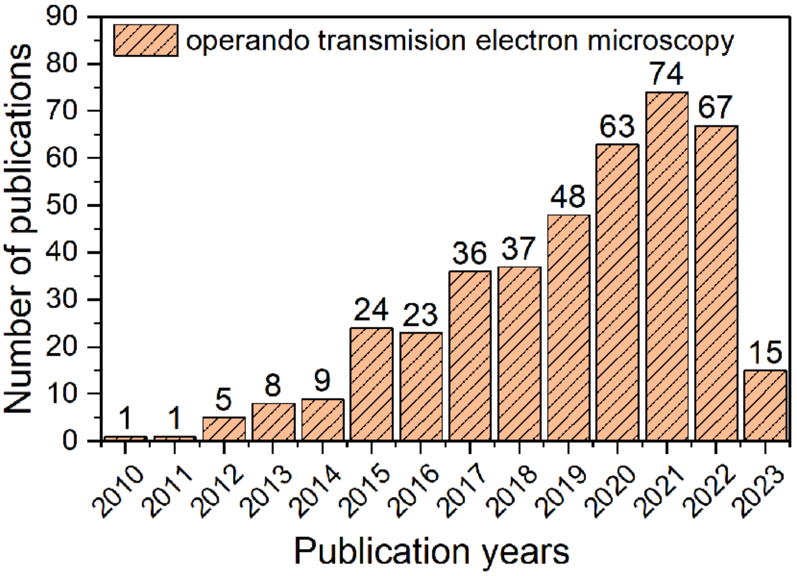

Figure 3: Number of publications by year during the last decade with *"operando transmission electron microscopy"* for all research topics.

Retrieved April 25, 2023, from Web of Science [20].

Recent reviews show that spatially resolved OTEM investigations have great potential, but there are still challenges to overcome [23]–[26]. The interpretation of the results can be complicated by (most likely) differences in kinetics between nanoreactors and laboratory-scaled reactors (fix bed reactor, plug-flow reactor, continuous stirred tank reactor, etc.). Discrepancies arise from differences in geometry, size, inlet flow, residence time regime, and most significantly, mass and heat transport. Another challenge is overinterpretation because the electron beam may induce changes. Therefore, careful and systematic experiments are needed. In general, it is recommended to use low electron doses to minimize beam-induced artifacts. Finally, there is still a material gap, which is the (usual) absence of supported material during OTEM experiments.

In recent years, contributions from our group have contributed to the fundamental understanding of catalytic systems. For example, Plodinec *et al.*, showed time-resolved changes of Pt foil and nanoparticles with different resolutions (from 1 Å to several mm) by combining environmental scanning electron microscopy (ESEM) and OTEM. These changes evolved to increase stable surface facets during CO oxidation [27], [28]. Oscillatory phase transition (redox behavior) was observed on nickel foil [29] and copper foil and nanoparticles [30], [31] during the dry reforming of methane (DRM) and the hydrogen oxidation reaction, respectively. The oxide-metal phase transition controlled the production of syngas [29]. The copper phase transition was dominated by the gas composition, and the activity emerged near a phase boundary [30]. Complementary OTEM investigations of nickel nanoparticles showed that the deactivation during DRM is due to Ni carbide formation [32].

These investigations clearly contribute to the fundamental understanding of catalytic systems. However, in a real industrial process, the complexity is increased by the presence of support, which is in fact part of the catalysts. The support in a catalyst plays an important role in increasing the dispersion of the metal sites and the textural properties (porosity and surface area), which define the contact area of the material interacting with the educts and products. Moreover, supports might act in synergy with the metal sites during catalytic reactions. The dynamic of the support has been investigated by in situ TEM of Pd and Pt supported on TiO_2. The results revealed the metal-support interaction by a titania overlayer formation at atmospheric pressure and high temperatures in different H_2 - O_2 atmospheres [33], [34]. Recently, our group studied the reversibility and thickness of an overlayer on $CuZnAlO_x$ during reverse water gas shift reaction. Overlayer properties vary depending on the gas composition and temperature [35].

1.2 Bimetallic catalytic systems

Catalysis is at the center of most chemical processes. The “simplest” model systems for describing catalysts are the single-crystal surfaces. Their study has improved the fundamental understanding of heterogeneous catalysis by the description of the adsorption of atoms and molecules over several clean surfaces [36], [37]. With the combination of two or more elements, in a material, like the bimetallic systems, specific properties can be tuned. These properties often show better performance than their monometallic counterparts [38], [39].

Specifically, Ni-Cu bimetallic surfaces have garnered considerable attention in heterogeneous catalysis. Their study offers a platform for exploring synergistic effects that can enhance catalytic performance. Both metals have face-centered-cubic structures with slightly different lattice parameters (3.51 and 3.61 Å, for Ni and Cu, respectively). Ni-Cu-based catalysts are usually prepared by impregnation or precipitation. The metal precursors are supported on an oxidic matrix to increase the surface area and dispersion. A crucial aspect of studying Ni-Cu systems lies in the reduction treatment. During this process, Cu and Ni precursors (usually oxides) are consecutively reduced to metals in two events. Despite the two separate reduction events, they can form a solid solution in cupro-nickel binary alloys [3], [40]. Nevertheless, there is conflicting data indicating that Cu is segregated and does not form a binary alloy [41], [42] due to the miscibility gap noted in the phase diagram [43]. The (Cu) segregation changes the perimeter structures available for catalysis and therefore, may influence the catalytic performance. Furthermore, the properties of the final material depend highly on the particular synthesis method and thermal treatment.

Given the discrepancies described and the relevance of bimetallic systems, further investigations of Ni-Cu systems are needed. Particularly in fundamental studies on the properties of bimetallic systems compared to monometallic ones. This understanding can pave the way for designing and exploring other bimetallic systems with unique properties and potential applications in catalysis.

1.3 Layered double hydroxides materials

Heterogeneous catalysts are usually composed of a high surface area material (support) where the metallic nanoparticles are anchored. The preparation method highly influences the final properties and catalytic performance of the material. In general, it is important to produce well-defined materials with uniform distribution, controlled size, and good stability. Layered double hydroxides (LDH) can serve as a starting point to produce well-dispersed nanoparticles after the activation process, i.e., calcination and reduction. In the last decades, these kinds of materials have gained interest as catalyst precursors. [44], [45].

LDH or ”doppelschichtstrukturen” was first named in 1942 [46] without an accurate description of its structure. Its real structure was described in the 60's by Allman [47] and Tylor [48]. As shown in Figure 4, the LDH structure is based on the Brucite-like layer and is naturally occurring in the hydrotalcite mineral (Mg-Al-hydroxycarbonate). The brucite layer is composed of $Mg(OH)_2$ octahedra which are neutrally charged. In the hydrotalcite-like compounds (or LDH), some Mg^{2+} cations are replaced by Al^{3+} or similar trivalent cations, producing a positively charged layer. The charged layer is compensated with negatively charged species such as NO_3^-, Br^-, Cl^-, F^-, OH^-, SO_4^{2-}, and CO_3^{2-} anions, among others, located in the interlayer domain. LDH structures are also known as "hydrotalcite-like compounds" due to past characterizations using hydrotalcite mineral [45]. One of the advantages of using LDH precursors as catalysts is the versatility of using different metals and modifying the M^{2+}/M^{3+} molar ratio. The content of M^{3+} should be in the range of 0.2 to 0.33 to obtain the pure hydrotalcite phase [45]. LDH materials can be great candidates for catalysts because of their phase pure precursors, high specific surface area, presence of surface basic and acidic centers, metal dispersion, and the possibility of using more than one divalent metal. Also, the memory effect allows the LDH to keep its morphology after thermal treatment and restructuring onto LDH if the appropriate conditions are met [49].

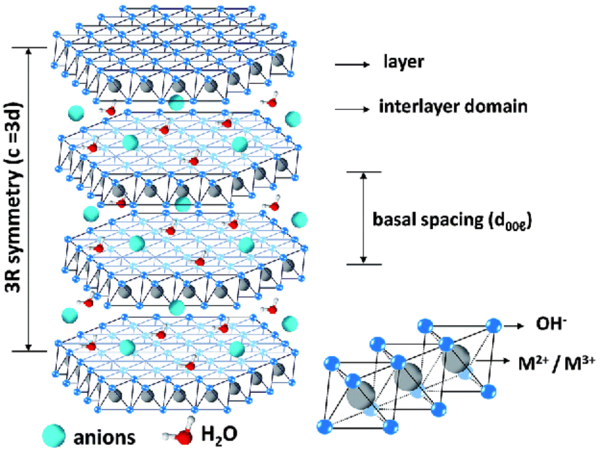

Figure 4: Scheme of the layered double hydroxide structure.

Reproduced from [50].

Due to this variety of properties, LDH materials were used in oxygen/hydrogen evolution reactions and water splitting [51]–[53]. After thermal treatment, the calcined LDH (so-called mixed metal oxides, MMO), can be applied as an adsorbent in water remediation due to its memory effect [54], [55]. Topotactical transformation of LDH materials can produce metallic nanoparticles (reducible species) supported on non-reducible oxides, which have been used in H_2 production or in hydrogenation reactions, among others [56], [57]. However, the properties of the activated material are intimately related to the composition and the pretreatment conditions. Ni reducibility decreases when the calcination temperature increases due to stronger interaction of Ni with Al or Mg at higher temperatures, forming periclase-type $Mg(Ni,Al)O_x$ or Ni-spinel structures [58], [59]. The process becomes more complex when using two divalent metals, like the combination Ni-Cu. More research is necessary to comprehend the impact of the calcination temperature on its reducibility.

LDH materials have been the focus of very few in situ TEM investigations. Using in situ TEM, C. Hobbs studied MgAl and NiFe-LDH, observing their behavior under different thermal and biomedical conditions [60]. Thermal heating studies showed that NiFe LDH evolved to a heterogeneous structure of NiO particles embedded in the $NiFe_2O_4$ matrix; while the MgAl LDH transformed to a porous matrix without spherical particles [61]. The influence of electron irradiation of NiFe LDH on its structural changes was also investigated: the beam induces oxidation of the hydroxide layers [62].

For catalysis applications, the ex situ characterization of the pristine material (as prepared), the activated one (reduced), and the spent catalysts (after reaction) are important. However, as the active state of the catalyst is reached under reaction conditions (i.e. in the presence of the educts and products at certain temperature and pressure), the analysis under operando is of paramount importance.

1.4 Relevant reactions for chemical energy conversion

1.4.1 Hydrogenation of carbon dioxide

The increasing worldwide production of carbon dioxide (CO_2) is attributed to be the main human source of the greenhouse effect [63]. Therefore, it is necessary to seek environmental remediation processes that use CO_2. For example, one of the most promising catalytic processes for converting CO_2 is by hydrogenation via the reverse water gas shift (RWGS) reaction to produce CO (Equation 1). CO is an important part of the syngas, which can be used as feedstock for the synthesis of important products (methanol, fertilizers, among others), or for the production of long-chain hydrocarbons via Fischer-Tropsch synthesis [64], [65]. As the RWGS reaction is endothermic ($\Delta H^0 = 41$ kJ·mol^{-1}), the catalytic production of CO is favored at higher temperatures. At low temperatures, the exothermic Sabatier methanation (Equation 2) is favored, especially over nickel-based catalysts, reducing the CO selectivity.

$$CO_2 + H_2 \leftrightarrow CO + H_2O \quad \Delta H^0 = 41\, kJ \cdot mol^{-1} \quad (1)$$

$$CO_2 + 4H_2 \leftrightarrow CH_4 + 2H_2O \quad \Delta H^0 = -164\, kJ \cdot mol^{-1} \quad (2)$$

The catalytic reaction for RWGS occurs over a metal surface and has been studied for several decades. The proposed reaction pathways are redox (direct CO-O dissociation) and associative or hydrogen mediated (CO-O dissociation is assisted by H_2) mechanisms [66]–[68]. Both mechanisms can coexist under reaction conditions and may vary widely depending on factors like catalyst precursors, preparation method, and activation treatment. Among the different materials tested for the RWGS reaction, noble metal-based catalysts (Pt and Rh) have exhibited promising reaction conversions and CO selectivities [69], [70], but their applicability is limited due to the high cost and low availability of the raw material. Thus, researchers have focused on developing low-cost transition-metal catalysts for the RWGS reaction. Cu-based catalysts, which are also used for methanol synthesis [71] are a promising option for the RWGS showing a CO_2 conversion of ~ 60% [72], [73]. However, they are limited by their thermal stability, i.e., the catalysts easily sinter at high temperatures.

The use of bimetallic catalyst systems has shown better results compared to their monometallic counterparts. Recently, mechanistic studies have shown that the combination of Cu and Ni can be promising for the RWGS reaction [74]. The Ni species in the catalytic system act as an active site of CO_2 methanation, producing synthetic natural gas [75]. The bimetallic combination Ni and Cu has been tested for the RWGS reaction after preparation by impregnation, confirming that the formation of the NiCu alloy is a good strategy to improve the selectivity to CO [76]. Another study showed that a Cu-Ni alloy supported on activated carbon with a Cu:Ni ratio of 2:1 is more active in the direct water-gas shift (WGS) reaction, compared to their monometallic counterpart and also superior to Cu:Ni supported on activated carbon. However, this combination was unstable over several cycles of operation [77]. In addition, the preparation method plays a major role in the catalytic performance, and the two-dimensional materials or nanocomposites, as a starting point, are a better approach that leads to highly dispersed metal species.

There is a lack of studies on the use of LDH-derived catalysts for RWGS, especially in-depth contributions about the understanding of the structural and surface dynamics are missing [66]. To the best of our knowledge, Ni-Cu bimetallic catalysts derived from LDH have not been studied on the RWGS reaction before. Recently, Summa *et al.* studied the effect of Cu on Ni-Mg-Al hydrotalcite-based materials for CO_2 methanation, concluding that the addition of Cu increased the number of basic sites and the catalytic performance toward methane formation [78]. Furthermore, Marocco *et al.* evaluated Ni-Al catalysts from LDH-precursors also for CO_2 methanation under different operating conditions [79]. The catalysts exhibited remarkable stability under reaction conditions (constant CH_4 yield at 350 °C during 140 h). However, the reasons for the good stability were not discussed.

1.4.2 Ammonia decomposition

Since the first industrial plant was established in 1913, ammonia (NH_3) synthesis has been a very important reaction mainly produced using iron-based catalysts at temperatures between 400 and 600 °C, and pressures of 100-400 bar [80], [81]. The first studies on ammonia decomposition were mainly conducted to obtain a basic understanding of the synthesis process rather than to develop a catalyst for the deactivation reaction. Therefore, a lot of knowledge has been gathered [82]. Facing the energy crisis and climate change, this knowledge may enable the use of ammonia as a carbon-free hydrogen carrier [83], [84]. The produced H_2 can be used in a fuel cell or directly in a combustion device. The advantage of using ammonia for hydrogen storage is the existing technology for ammonia synthesis and transport [84]. Several reviews summarize the wide branch of opportunities that ammonia has as an energy carrier for the future, the main catalysts employed, and the effects of the promoters and support [85]–[88].

$$2NH_3 \leftrightarrow N_2 + 3H_2 \quad \Delta H^0 = 92.44\, kJ \cdot mol^{-1} \quad (3)$$

NH_3 decomposition is performed at low or atmospheric pressures. It is an endothermic process (Equation 3) that is favored at higher temperatures. Catalysts for ammonia synthesis are iron-based materials operating at high pressures. Under decomposition conditions, the iron-based material can form stable bulk iron nitrides that block the active sites, making it unsuitable for the ammonia decomposition process. The ideal catalyst for the decomposition of NH_3 must then have very different nitrogen binding energies, compared to the synthesis catalysts [89]. The most active catalyst for NH_3 decomposition is ruthenium-based material; the nickel-based catalyst is the second best, with the benefit of being a low-cost transition metal [90]. Ni-based catalysts is already used in small-scale commercial ammonia decomposition reactors operated at 850 °C and atmospheric pressure [91].

The rate-determining step for ammonia synthesis is the activation or dissociative adsorption of the nitrogen molecule [92]. For ammonia decomposition, the mechanism is more complex. The adsorption of NH_3 initiates on (probably) a metal site (*) to form NH_3*; here, the asterisk (*) denotes adsorbed on a surface site. Then sequential dehydrogenation of NH_3* by the cleavage of the N-H bonds produces H* species that are combined to form and release H_2. Lastly, the recombination of two N* species forms N_2, which is finally desorbed from the surface. Another rate-determining step could be the recombinative desorption of dinitrogen from the surface or the cleavage of the N-H bond. This depends on the external reaction conditions, such as partial pressures, temperatures, and especially catalyst formulation [93]. For example, for nickel surfaces operated at high temperatures, the rate is controlled by the adsorption of NH_3; however, at low temperatures, nitrogen desorption is the dominating one [94]. Furthermore, Ganley *et al.*, also concluded that nitrogen desorption is the rate-determining step for Ni, Ru, Co, Fe, and Cr catalysts; whereas this was not the case for Rh, Ir, Pt, Pd, and Cu [95].

Ammonia decomposition is a structure-sensitive reaction and the optimal particle size of nickel supported on alumina is between 1.8 and 2.9 nm [96]. Computational studies show that the desorption of atomic nitrogen depends on the metallic nickel facet: the desorption of N_2 from Ni(111) is more favorable compared to other facets [97]. Furthermore, strongly adsorbed N atoms would block some of the step sites of the Ni(211) facet. The strong adsorption of N on Ni sites might generate the formation of nickel nitrides. Copper, on the other hand, is not as active as nickel, ruthenium, and cobalt, and does not form nitrides [98]. There is no direct evidence that the nitride phase improves the activity.

The nature of the catalyst precursor plays an important role in the characteristics of the final catalysts. Ni-based LDH materials have been used as a catalyst precursor for the ammonia decomposition reaction, showing that the catalyst prepared from nitrates (NO_3^-) has higher activity compared to the ones prepared from chlorides (Cl^-) [99]. Moreover, in the LDH-derived catalysts, the metal-support interacts via a spillover effect of surface hydrogen species. This interaction improves the performance of the ammonia decomposition [100], [101] and could also be related to an increase in the basicity of the support and the amount of Ni^0 sites exposed [102]. Similarly, in the liquid phase, the dehydrogenation of ammonia-borane was enhanced by Ru nanoparticles embedded in the CaAlOx support owing to the specific LDH preparation technique [103].

Despite the progress of ammonia decomposition and CO_2 hydrogenation studies using materials derived from LDH, there is still an opportunity to expand fundamental knowledge. The purpose of this study was to understand the effect of Cu on the catalytic performance of the Ni catalyst prepared by LDH precursor. The detailed kinetic mechanism is not considered in the scope of this work.

In this thesis, the synthesis of four LDH materials is briefly described. $M_{0.7}Al_{0.3}$ that vary in the molar content of the divalent metal (M) and Al is kept constant. The Ni:Cu molar ratio was set to 1:0, 4:1, 1:1 and 0:1 to form $Ni_{0.7}Al_{0.3}$, $Ni_{0.56}Cu_{0.14}Al_{0.3}$, $Ni_{0.35}Cu_{0.35}Al_{0.3}$, $Cu_{0.7}Al_{0.3}$, correspondingly. Carbonate (CO_3^{2-}) anions were used in the interlayer domain. The properties of these materials were studied by combining different analytical techniques. Bulk and micro structure were investigated using XRD and TEM, respectively. The morphology and 3D structure of the layered material were examined using TEM-tilt series. In addition, thermogravimetric studies comparing all materials were performed. The inspection of the temperature-programmed reduction (TPR) profile using two different calcination temperatures defines the optimal calcination pretreatment. The characterization of the reduced samples is thoroughly described, highlighting the metal-support interaction, which is directly related to the catalytic performance.

2 Experimental and characterization methods

2.1 LDH synthesis

NiCuAl-LDH synthesis was performed in a co-precipitation approach with constant pH in an automated laboratory reactor (Mettler Toledo LabMax). The coprecipitation method of LDH synthesis is schematically shown in Figure 5. Synthesis was carried out as follows: 300 mL 0.5 M Na_2CO_3 solution was added to LabMax under 300 rpm stirring. The pH was manually adjusted to 9 with a concentrated HNO_3 solution. To start precipitation, the 1 M mixed metal nitrate solution of $Ni(NO_3)_2$, $Cu(NO_3)_2$ and $Al(NO_3)_3$, and a 3 M NaOH solution (to control the pH) were added dropwise simultaneously to the Na_2CO_3 solution in the reactor. The dropwise addition was performed under stirring at a controlled speed: 600 g of metal solution was dosed dropwise in 30 min. During the addition, the suspension was kept at a temperature of 30 °C. The suspension was then filtered (12A) and washed several times with deionized water until a conductivity of the liquid phase below 0.5 $mS\cdot cm^{-1}$ was reached. Drying was carried out at 50 °C for 2 days in a drying cabinet, and a bluish-green precursor was obtained. Then an ion exchange was carried out in order to replace the remaining nitrates from the precursor for carbonate ions. A suspension of 2.5 g of the dry sample in 15 mL of Milli-Q H_2O and 250 mg of Na_2CO_3 was stirred at 300 rpm for 2 h at 30 °C. The washing and drying procedures were then repeated. LDH with different molar ratio ($Ni_{0.7}Al_{0.3}$, $Ni_{0.56}Cu_{0.14}Al_{0.3}$, $Ni_{0.35}Cu_{0.35}Al_{0.3}$, and $Cu_{0.7}Al_{0.3}$) were prepared as described above, including the ion exchange. For simplicity, the samples will be named NiAl, NiCu(4:1)Al, NiCu(1:1)Al and CuAl, respectively. A thermal treatment will be indicated by appending the name with "_ox290_red450" when it is calcined, for example, at 290 °C and reduced at 450 °C.

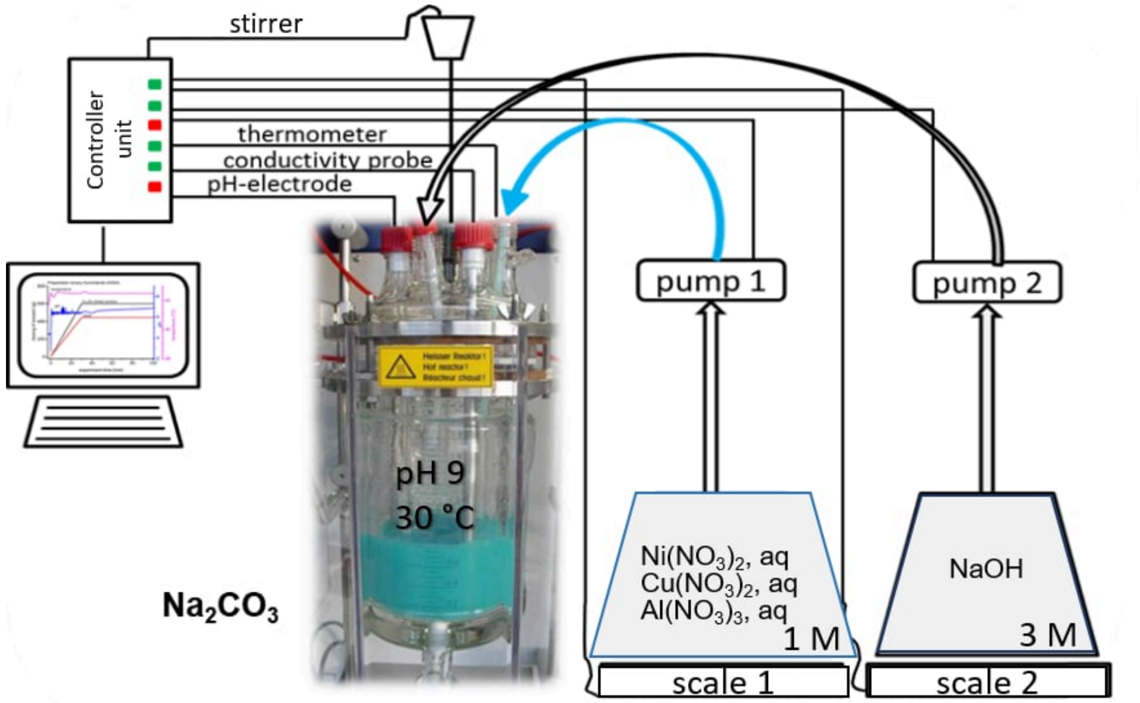

Figure 5: Schematic representation of the LDH synthesis in a Mettler Toledo LabMax setup.

Adapted from [104].

2.2 Powder X-ray diffraction

2.2.1 Ex situ X-ray diffraction

Ex situ powder X-ray diffraction (XRD) measurements were performed in Bragg-Brentano geometry on a Bruker AXS D8 Advance II theta/theta diffractometer, using Ni filtered Cu $K_{\alpha 1+2}$ radiation and a position sensitive energy dispersive LynxEye silicon strip detector. The sample powder was filled into the cavity of a low background Si single crystal sample holder, the surface of the powder bed being level with the sample holder edge (front loading). In the case of air sensitive samples, an airtight version of the sample holder equipped with an X-ray transparent dome was loaded in a glove box under argon atmosphere. XRD Rietveld based powder pattern fitting was performed using the TOPAS software (version 5, ©1999-2014 Bruker AXS).

2.2.2 Quasi in situ X-ray diffraction (calcination)

Quasi in situ XRD data was collected on a STOE Theta/theta X-ray diffractometer (Bragg-Brentano geometry, Cu $K_{\alpha1+2}$ radiation, secondary graphite monochromator, scintillation counter) equipped with an Anton Paar XRK 900 in situ reactor chamber. For the in situ calcination, the gas feed was controlled by Bronkhorst mass flow controllers, using 20 $mL_n{\cdot}min^{-1}$ O_2 and 80 $mL_n{\cdot}min^{-1}$ He as inert balance gas. All diffractograms were taken at 25 °C between temperature treatments. The sample was heated using a ramp of 6 $°C{\cdot}min^{-1}$ to 185 °C and held for 5 h, afterwards it was rapidly cooled down for the XRD acquisition. Subsequently, the sample was quickly heated (20 $°C{\cdot}min^{-1}$) to the previous temperature (185 °C) to continue heating at 6 $°C{\cdot}min^{-1}$ to 250 °C, held for 24 h and 600 °C, for 30 min.

2.2.3 Quasi in situ X-ray diffraction (reduction)

In situ reduction XRD experiments were carried out in a STOE STADI P transmission diffractometer with Debye-Sherrer geometry, equipped with a STOE INSITU HT2 capillary reaction chamber. The MYTHEN 1k energy dispersive position sensitive detector collected the intensity of the diffracted Mo $K\alpha1$ radiation obtained by using a primary Ge (111) monochromator. 17 mg of NiCu(4:1)Al calcined sample (S35648), with a sieve fraction between 200 and 300 µm, was placed between SiO_2 wool in a quartz glass capillary with an inner diameter of 1.6 mm and mounted on the HT2 reaction chamber. A total flow of 20 $mL_n{\cdot}min^{-1}$ of 5% H_2 was established in He, and two sets of diffraction scans were acquired: a 10 min scan at high temperatures and an approximately 2.5 h scan at 50 °C to exclude thermal expansion. Figure 6 shows the temperature profile used during the experiment. The heating ramp was 2 $°C{\cdot}min^{-1}$ and 50 $°C{\cdot}min^{-1}$ for cooling and reheating to the previous temperature, respectively. The formation of H_2O was evidenced in the MS during the experiment, as product of the reduction process.

For detailed analysis, Rietveld-based powder pattern fitting was performed using TOPAS software (version 5 ©1999-2014 Bruker AXS). A constant fit model was maintained throughout the series to avoid the introduction of artificial changes and to better differentiate the variations. Thus, both oxide and metal phases were included in all fits, even if one or the other had only a negligible contribution. Since Cu and Ni are very similar in their scattering power and indistinguishable in a solid solution, the two phases used in the fits were rock salt type NiO for the oxide component and fcc Ni representing the Ni-Cu bimetallic alloy. A minor potential contribution of nanocrystalline CuO in the starting material was ignored for the sake of fit stability.

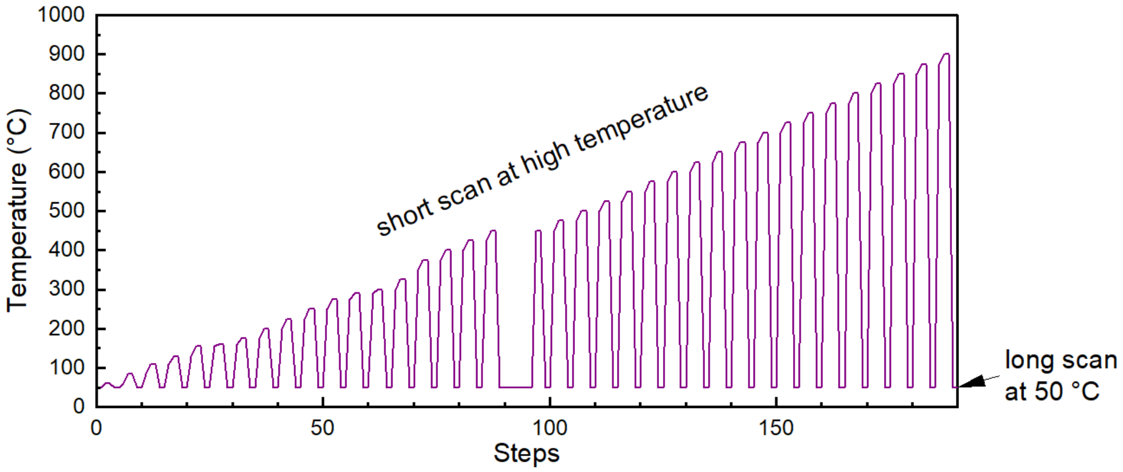

Figure 6: Temperature profile during in situ XRD reduction experiment.

The fitting of both series of diffractograms (acquired at HT and at 50 °C) considered peak broadening because of size, but the strain contribution was neglected because the HT diffractograms contain only two reflections. The background was modeled with a combination of a zero-order polynomial with a reciprocal function because it produced the most reasonable background shape. Furthermore, a couple of broad peaks were added to the model for a better fit. They are present from the beginning and might be related to amorphous alumina, or the background caused by the capillary.

2.3 Nitrogen sorption isotherms

Specific surface areas of the LDH precursors and calcined LDH materials were estimated by N_2 physisorption (Quantachrome Autosorb-1) and evaluated using Brunauer-Emmett-Teller (BET) theory for surface area and Barrett-Joyner-Halenda (BJH) method for pore size distribution. Approximately 100 mg of each sample was used for the experiment. Prior to the acquisition of the adsorption-desorption isotherms, the LDH samples were outgassed for 2 h at 100 °C; and the mixed metal oxides (i.e. LDH after calcination) at 250 °C.

2.4 Elemental analysis

Metal content analysis of Al, Ni, and Cu was performed using inductively coupled plasma mass spectroscopy (ICP-MS-2030). Approximately 20 mg of each sample was dissolved in nitric acid by microwave digestion at 200 °C for 1 h prior to analysis. Both experiments were performed in the Department of Molecular Catalysis at the Max Planck Institute for Chemical Energy Conversion.

2.5 Thermogravimetric analysis

Thermogravimetric analysis was performed in a Netzsch TG 209 F1 Libra thermobalance with top loading and coupled with a Pfeiffer OmniStar TM Quadrupole mass spectrometer for the gas-phase analysis. Approximately 15 mg of the sample was used and heated to 1000 °C at 2 $°C·min^{-1}$ under synthetic air (21% O_2 in Ar) using a total gas flow of 70 $mL·min^{-1}$.

2.6 Transmission electron microscopy

Transmission electron microscopy (TEM) and scanning TEM (STEM) studies were carried out using two microscopes: a Thermo Scientific Talos F200X and an aberration-corrected Jeol JEM-ARM200F, both operating at 200 kV acceleration voltage. The LDH and LDH-derived samples for TEM/STEM investigations were dry-prepared using lacey carbon coated Au-grids if not stated otherwise. Both LDHs and MMO samples were analyzed using a double-tilt and single tilt sample holder for Talos and Jeol microscopes, respectively. The activated or reduced samples were transferred from the glovebox to the microscopes to minimize contact with air, using Gatan vacuum transfer holders VTST4006 and single tilt 648, for Jeol and Talos microscopes, respectively.

2.6.1 TEM tilt series

Different views of two selected samples (one calcined and one reduced) were collected by TEM images at different tilt angles on a Talos F200X microscope. The microscope was operated at 200 kV acceleration voltage, a condenser aperture (C2) of 150 μm diameter was used, the electron flux density was less than 20 $e^{-}·nm^{-2}·s^{-1}$. The sample was suspended in ethanol, sonicated for 5 minutes, and drop casted onto a QUANTIFOIL® Holey Carbon film on an Au 200 mesh TEM grid. When the solvent was dried, the grid was placed, with its diagonal parallel to the axis of the holder, on an advanced tomography holder Model 2020, Fischione (FP 90997/19). This allows for imaging at high tilt angles.

For the acquisition, the FEI Tomography software, Version 4.0 (PN 1062977D) was used. The collected TEM images were combined in the ImageJ software. The complete 3D reconstruction was not part of the thesis, but the video and series of images are presented to reveal the 3D morphology of the LDH and derived materials.

2.6.2 STEM-EDX

STEM experiments using high-angle annular dark field (HAADF) and bright field (BF) detectors, as well as energy dispersive X-ray spectroscopy (EDX) were carried out using a Thermo Scientific Talos F200X electron microscope. A condenser aperture (C2) of 70 µm diameter was used and a screen-current of ca. 0.5 nA was set. EDX elemental analysis was performed using the SuperX EDX system consisting of four silicon drift detectors (SDD) that cover 0.9 sr. The elemental mappings were exported showing net intensities and using a pre-filtering Gaussian blur with � 1.0 or 1.5. The relative local compositions were estimated by quantification of the integrated spectra using an empirical background subtraction model, absorption correction assuming 50 nm sample thickness and the Brown-Powell ionization cross-section model.

2.6.3 HR(S)TEM and SAED

High-resolution aberration-corrected (S)TEM was performed using a Jeol JEM-ARM200F electron microscope equipped with two aberration correctors (for probe-forming and image forming lenses) operated at 200 kV acceleration voltage and 10 µA emission current, using a 30 µm condenser lens aperture (resulting in a convergence semiangle of 22.8 mrad). For selected area electron diffraction (SAED) experiments, a 20 µm SA aperture was used. The particle size distribution from the activated samples was obtained from STEM-HAADF images by analyzing at least 150 particles per sample using ImageJ.

2.6.4 STEM-EELS

For electron energy-loss spectrometry (EELS) a Gatan GIF Quantum energy filter was used in the Jeol JEM-ARM200F microscope. The dispersion was set to 0.1 eV per channel and an energy resolution of 0.7 eV was determined by measuring the full width at half maximum (FWHM) of the zero-loss peak. For DualEELS the low-loss region was recorded using an energy shift of 0 eV while for the high-loss region, an energy shift of 800 eV was used. This allowed us to simultaneously record the zero-loss peak and the Ni and Cu $L_{2,3}$-edges, respectively. For the Al $L_{2,3}$ edges and O K-edges, the energy shift was set to 70 eV and 500 eV, respectively. The spectrometer entrance aperture of 5 mm and a camera length of 3 cm were used (resulting in a collection semiangle of 35.1 mrad). Electron doses were set to ca. 1.08x10^8 electrons s^{-1} in order to minimize the changes of the structure induced by the electron beam during the TEM experiments. EELS data evaluation was performed using digital micrograph GMS3, Gatan, Inc. The zero-loss peak was used for energy calibration in the high-loss region and to estimate the thickness using the inelastic mean free path (t/λ). [9]. The spectra were deconvolved to exclude plural scattering effects due to sample thickness.

2.7 Calcination and temperature-programmed reduction

2.7.1 Calcination

The first step in the activation procedure of the LDHs is a calcination process. Approximately 80 mg of powder of each as-synthesized LDH material was introduced into a U-tube capillary quartz reactor (internal diameter 8 mm), placed in an oven, and exposed to a continuous gas flow during heating. The instrument was equipped with a mass spectrometer (MS - Pfeiffer OmniStar® quadrupole) and a thermal conductivity detector for gas product analysis. For the calcination, a gas mixture of 21% O_2 in He with a total flow rate of 100 mL·min^{-1} was used. The heating rate was set to 2 °C·min^{-1} until a temperature of 290 °C was reached with 3 h dwelling time, or a temperature of 600 °C was reached with 10 min dwelling time. The product of the calcination process is called mixed metal oxides (MMO).

2.7.2 Reduction

The second step of the activation is a reduction treatment under H_2 atmosphere. Using the same setup, after cooling down and purging with Ar, the gas mixture was switched to 5% H_2 in Ar with the same total flow (100 mL·min^{-1}) to perform the reduction, i.e., temperature-programmed reduction (TPR) at 300, 450, 600 or 900 °C, with a heating ramp of 2 °C·min^{-1}. After the setup was cooled down naturally, in each case the activated material was transferred under an inert atmosphere to the glove box to perform subsequent analytical investigations. The degree of reduction was calculated according to the following equation:

$$Red(\%) = \frac{H_2^{Exp}}{H_2^{Th}} * 100$$

where, H_2^{Exp} is the experimental H_2 consumption, and H_2^{Th} is the theoretical amount of H_2 required for reducing all the Cu^{2+} and/or Ni^{2+} species.

2.8 Microcalorimetry

The catalysts' surface was studied by conducting microcalorimetry experiments using a SETARAM MS70 Calvet calorimeter. The calcined samples were reduced ex situ at 450 °C (2 $°C·min^{-1}$) in 5% H_2 in Ar for 3 h and transported under air-free conditions to the calorimeter. CO was adsorbed at 30 °C for 5 h and subsequent evacuation up to 10^{-8} mbar at 30 °C. After the equilibrium was reached, another adsorption cycle was performed under identical conditions. The adsorption-desorption procedure was repeated three times. Pressure, adsorption temperature, and heat signals were recorded during all dosing steps. Metal surface areas (M = Ni and/or Cu) were determined by assuming an adsorption stoichiometry of CO_{ads}: M_{surf} = 1:1.

2.9 DRIFTS of CO adsorption

Diffuse reflectance infrared Fourier transform (DRIFT) spectroscopy experiment was carried out using a Cary 680 Series FTIR Spectrometer from Agilent Technologies equipped with a MCT detector at a spectral resolution of 2 cm^{-1} and accumulation of 1024 scans. An in situ cell (Harrick Praying MantisTM diffuse reflectance attachment DRP-P72 was used. The samples (NiAl_ox290, NiCu(4:1)Al_ox290, and CuAl_ox290) were reduced for 3 h in the reaction chamber using 50 $mL·min^{-1}$ of 5% H_2 in Ar with a heating rate of 2 $°C·min^{-1}$ up to 450 °C. Then, the cell was evacuated, kept under vacuum for 30 min, and the sample cooled down to room temperature. The pressure in the DRIFTS cell reached 10^{-6} mbar and spectra were recorded at 30 °C while dosing CO at increasing equilibrium pressures ranging from 0.1 to 9 mbar. Spectra before CO dosing were used as background and subtracted from the following spectra.

2.10 CO_2 - TPD

The basicity of the reduced materials was measured by CO_2 -TPD using a setup (iKube reactor) designed at the AC department and built by Premex® reactor GmbH. It is composed of a double reactor configuration that measures the sample and the reference (standard CuO) simultaneously. The set-up is equipped with thermal conductivity detectors located at the inlet and outlet of each reactor to monitor the desorbing gas. 10 mg of each calcined sample was placed in between quartz wool, in the isothermal zone of a quartz tube of 2 mm inner diameter. Before the TPD experiment, the sample was reduced in situ using 5% H_2 in Ar, with a heating rate of 2 $°C·min^{-1}$ to 450 °C, and kept for 3 h. The sample was then cooled to 50 °C in He and exposed to pure CO_2 flow for 1 h to saturate the surface. Later, the CO_2 was changed for pure He and flowed for 15 min to remove weakly bound CO_2 molecules. The desorption profile was carried out at the temperature range of 50 to 600 °C with a heating rate of 10 °C·min^{-1}. The obtained profile reflects the relative amount of basic sites, and the desorption temperature indicates its strength (weak, medium, and strong).

2.11 NEXAFS - XPS

Near-edge X-ray absorption fine structure (NEXAFS) spectroscopy and X-ray photoelectron spectroscopy (XPS) measurements were performed at the UE56-2 PGM-2 beamline at BESSY II synchrotron facility. The experiments were carried out in a stainless steel NAP-XPS chamber described elsewhere [105]. About 20 mg of each sample were pressed to form 6 mm diameter pellets. Air-sensitive samples were pressed inside an argon-containing glovebox and mounted on a sapphire sample holder between a stainless steel backplate and a stainless steel cap. The resolution of the photon energy was set to 700 meV for the Cu $L_{2,3}$ edge (≈ 930 eV) and Ni $L_{2.3}$ edge (≈ 850 eV), and 250 meV at the O K-edge (≈ 520 eV). Each NEXAFS spectrum was obtained in total electron yield mode, measuring the current passing through a nozzle about 0.5 mm from the surface of the sample. Furthermore, all NEXAFS spectra were normalized to the incident photon flux.

NEXAFS and XPS spectra were acquired on the calcined LDH samples with different compositions (NiAl, NiCu(4:1)Al, NiCu(1:1)Al and CuAl) after the ex situ reduction at 450 °C or 600 °C using 5% H_2 in Ar at 1 bar in a TPR set up (for more details of the reduction, see section 2.7.2). The transport of the sample to the vacuum chamber in the synchrotron facility was carried out without air contact. Despite all the measures taken during transport to prevent oxidation of the reduced samples, some typical features of metal oxides were observed. Therefore, a re-reduction was performed in situ inside the analysis chamber at 250 °C, in 0.5 to 1 mbar of H_2 and heated at a rate of 15 °C·min^{-1}. The XPS core levels of Ni 2p and Cu 2p of the reduced samples were acquired using a resolution of 0.1 eV. The XPS calibration was done using the Fermi level and adjusted individually for each core level. During the experiment, the photon energy was adjusted to make the kinetic energy of the outcoming photoelectron equal to 150 eV to have the same probing depth for both nickel and copper. The estimation of the inelastic mean free path (IMFP, λ), was 5 Å, and the probing depth was between 1 and 3 λ; which corresponds to 10 Å. The relative quantification was performed using OriginPro, Version 2022b, by integration of the signals and considering the cross-section, different photon fluxes at different photon energies, and asymmetry factors.

2.12 Catalytic experiments

2.12.1 Hydrogenation of carbon dioxide

Catalytic experiments were carried out in BasCat - UniCat BASF JointLab facilities. The setup, operated at atmospheric pressure and temperature of 600 °C, was designed by Integrated Lab Solutions (ILS, Berlin, Germany) and equipped with a quartz tube as a fixed bed reactor with an inner diameter of 6 mm. The LDH precursors were initially calcined ex situ at 290 °C in synthetic air, pressed and sieved to 100-200 µm fraction. The amount of MMO materials was fixed to 15 mg for all runs and diluted in 85 mg of SiO_2. In an activation step, all catalysts were first reduced in situ for 60 min at 450 °C in 100 mL·min^{-1} of 10% H_2 in He with a heating rate of 10 °C·min^{-1}. After the reduction step, the reactor was purged with 100 mL·min^{-1} of He flow for 15 min. The reactor temperature was increased to 500 °C with a heating rate of 10 °C·min^{-1}. Subsequently, the He flow was replaced with a reactant mixture (40 mL·min^{-1} CO_2: 40 mL·min^{-1} H_2:20 mL·min^{-1} He). The reaction temperature was modified in a heating up – cooling down cycle at temperature steps of 500 – 550 – 600 °C. The resulting catalyst weight hourly space velocity (WHSV) was 400,000 mL·g^{-1}·h^{-1}. Educts and products were analyzed online by gas chromatography equipped with a TCD detector. Carbon dioxide conversion (X_{CO_2}), carbon monoxide selectivity (S_{CO}), and methane selectivity (S_{CH_4}) were defined as:

$$
\begin{aligned}
X_{(CO_2)} &= \frac{[CO_2]^{in}-[CO_2]^{out}}{[CO_2]^{in}} * 100\\
S_{(CO)} &= \frac{[CO]^{out}}{[CO_2]^{in}-[CO_2]^{out}} * 100\\
S_{(CH_4)} &= \frac{[CH_4]^{out}}{[CO_2]^{in}-[CO_2]^{out}} * 100
\end{aligned}
$$

2.12.2 Ammonia decomposition

Catalytic experiments for ammonia decomposition were performed in a homebuilt reactor (Haber setup) located in the Inorganic Chemistry Department facilities. The reaction was performed in a quartz tube used as a fixed bed reactor, operating at atmospheric pressure and temperature steps between 400-600 °C. All samples were previously calcined at 290 °C for 3 h, pressed and sieved to 200-300 µm fraction. For each experiment, approximately 50 mg of the calcined sample was dispersed in 100 mg of SiC (355- 400 µm). In situ activation was carried out at 450 °C for 1 h using 50 mL·min^{-1} of 20% H_2 in Ar. Subsequently, the catalyst was cooled to 400 °C, and 100% NH_3 flow was supplied to the catalyst bed with a total flow rate of 30 mL·min^{-1} and a WHSV of 36000 mL·g^{-1}·h^{-1}. The catalyst temperature was increased stepwise from 400 °C to 450, 500, 550, and 600 °C, and later cooled back to 400 °C. Steady-state conversions were measured at each temperature step for 1 h. The NH_3 conversion was recorded using an ammonia detector (Binos 1.2 IR spectrometer, Rosemount). NH_3 was diluted with N_2 to 10% before reaching the detector. Considering the volume expansion of the NH_3 decomposition, the conversion (X_{NH_3}) was calculated based on the following equation:

$$X_{NH_3} = \frac{[NH_3]^{in} - [NH_3]^{detector} * (\frac{10+X_{NH_3}}{10})}{[NH_3]^{in}} * 100$$

2.13 Operando TEM

Operando Transmission electron microscope experiments were carried out in a homebuilt operando TEM setup, equipped with a gas feeding and gas analysis (Figure 7a). The specifications of the setup have been reported elsewhere [106]. The setup is compatible with a commercial MEMS-based gas cell TEM holder: DENSsolutions climate holder. Outgoing gases were analyzed using the HIDEN HAL/3F Quadrupole mass spectrometer (QMS). Imaging during the experiments was performed using a Cs-corrected FEI TITAN 20-300 operated at 300 kV and equipped with a TVIPS XF416 camera. Different positions were analyzed during the experiments to exclude the influence of the electron beam on the observed changes (morphology and structure).

2.13.1 Sample preparation

Two samples were prepared for operando experiments: one LDH as-prepared, the NiCu(4:1)Al LDH (internal number: S34504); and the MMO or calcined sample at 290 °C, NiCu(4:1)Al_ox290 (internal number: S36645). For sample preparation, the upper and lower parts of the MEMS chip were plasma cleaned for 2 min using a mixture of oxygen and argon plasma. Approximately 5 mg of powder was dispersed in 1 mL of Milli- Q water and sonicated for 5 min. Subsequently, an aliquot of 0.5 µL was dropped onto the bottom chip (Figure 7b-1). Following a 15-minute air-drying period, the chip was assembled with the O-ring and top chip. Finally, the top chip (silicon nitride window) was aligned with the bottom chip (Figure 7b-3.), and the leak test was performed. Based on the dispersion of 5 mg·mL^{-1}, and the volume used 0.5 µL, it is probable that only 2.5 µg (or less) of the sample was deposited on the chip.

After the first preparation, the particles had weak adhesion to the silicon nitride window and flew away easily upon interaction with the beam. Therefore, the second experiment needed more sample preparation steps as there were not enough areas with particles for TEM analysis during the first experiment. The calcined sample (NiCu(4:1)Al_ox290), underwent sieving to obtain a fraction < 80 µm before dispersion. Additionally, the bottom chip was carbon-coated with a thickness of a few nanometers (< 2 nm) after plasma cleaning.

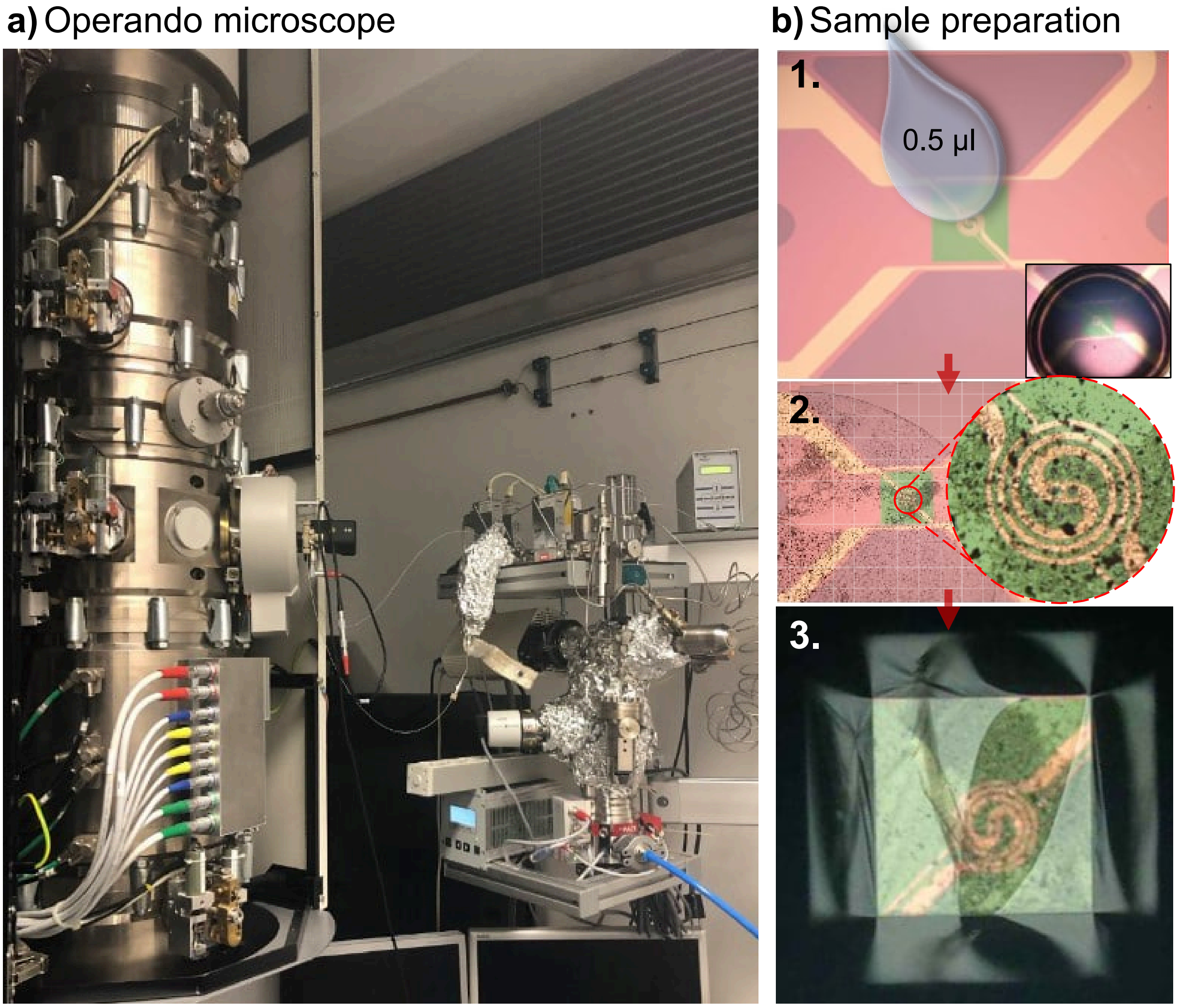

Figure 7: a) Photograph of the operando TEM setup. b) Preparation of the MEMS chip: 1. An aliquot of the catalyst suspended in water is deposited onto the bottom chip. 2. Micrograph of the MEMS chip after sample preparation. 3. View of the chip after aligning the top window.

Photograph (a) adapted from [106].

2.13.2 Conditions during operando experiments

The DENS Climate holder – after checking for leaks - was introduced into the Titan microscope. The gas lines were evacuated for at least 30 min every time before setting any gas feed. The total gas flow was controlled by a high-precision flowmeter (Bronkhorst), using between 15 and 25 µL·min^{-1}. In almost all cases, gases could settle overnight.

2.13.2.1 LDH sample (Experiment #1)

The LDH sample was calcined in situ using 20% O_2 in He flow (24 µL·min^{-1} and 1.2 bar as inlet pressure) and heated to 350 °C. Subsequently, it was reduced using 10% H_2 in He and similar flow and inlet pressure. To determine whether the conversion was detectable under the operando conditions, the reaction was performed over a weekend without TEM or characterization. The reaction mixture CO_2:H_2:He was set to a ratio of 1:1:0.5 and the total flow through the cell to 17 µL·min^{-1}, and an inlet pressure of 0.80 bar. The temperature was increased at 2 °C·min^{-1} to 600 °C and was held every 50 °C (from 400) for a minimum of 2 h.

2.13.2.2 Calcined sample (Experiment #2)

The calcined sample may have reconstructed to LDH during OTEM preparation due to the memory effect and contact with water (Milli-Q). Therefore, the first step was calcination using 20% O_2 in He (22 µL·min^{-1} and 1.1 bar as inlet pressure) at 290 °C for 3 h. Subsequently, a mixture of 10% H_2 in He was used for the reduction process (21 µL·min^{-1} and 1.0 bar), which was performed at temperatures up to 450 °C. Then, as in experiment #1, the reaction mixture CO_2:H_2:He was used with a ratio of 1:1:0.5 and 20 µL·min^{-1} with a pressure of 0.84 bar. The temperature was increased using a rate of 2 °C·min^{-1} to a maximum of 600 °C.

2.13.3 Electron dose

The effects of the beam can be completely negligible when the appropriate low dose is used. This value must be below the damage threshold. Figure 8 shows two series of images acquired using different electron beam doses: 1100 and 606 e^{-}·Å^{-2}·s^{-1}. For the series of images A, the morphology changes when illuminated by the beam: some nanoparticles were formed and are visible in the image acquired at 100 °C. However, when analyzing the series of images B, these changes are not visible, and the material kept the same morphology after heating to 120 °C. Therefore, the electron dose was kept below 606 $e^{-}\cdot Å^{-2}\cdot s^{-1}$. At this value, damages due to electron beam-matter interactions are assumed to be negligible [12]. For the high resolution imaging of the sample, when heated to 350 °C and higher, the electron dose was always chosen below 1100 $e^{-}\cdot Å^{2}s^{-1}$.

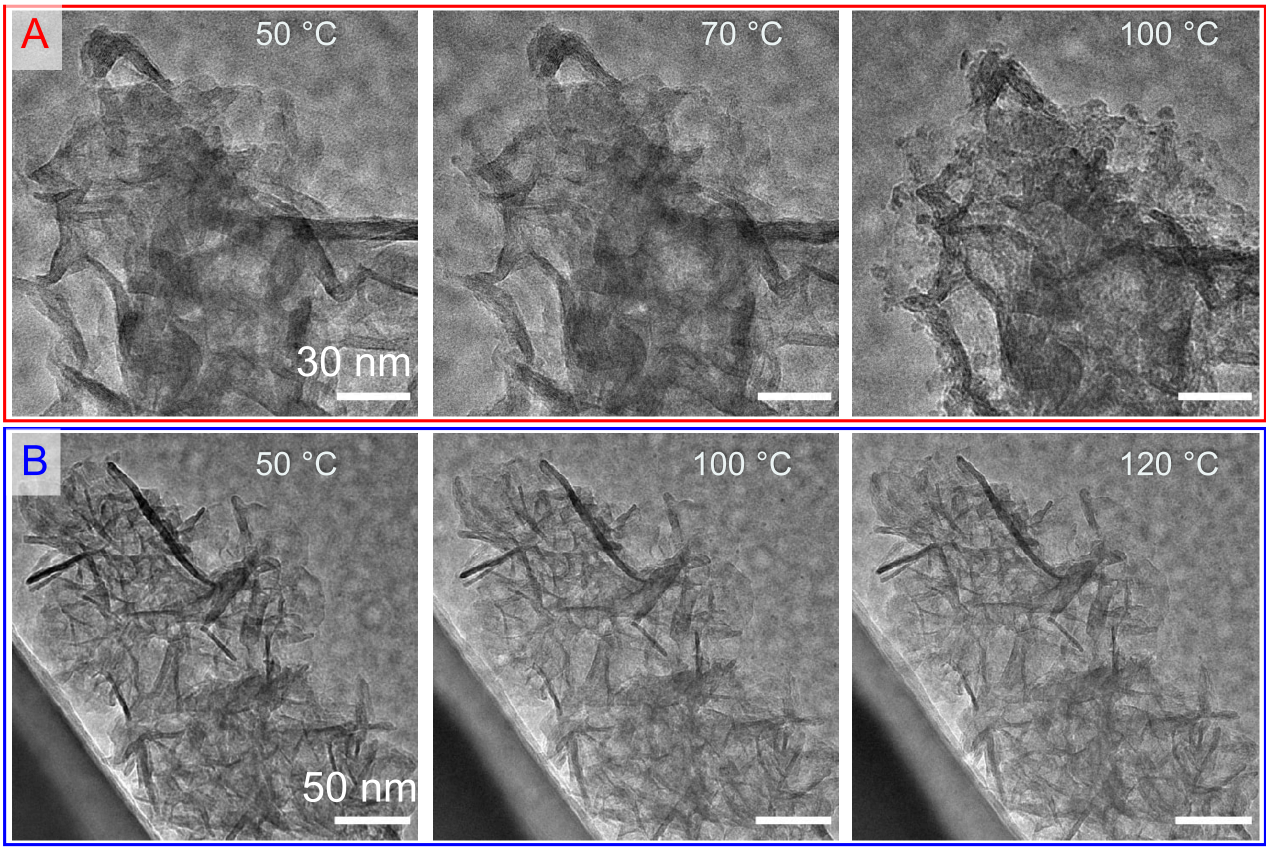

Figure 8: TEM micrographs acquired at different temperatures during calcination. a) using electron dose of 1100 $e^{-}\cdot Å^{-2}\cdot s^{-1}$, and b) using 606 $e^{-}\cdot Å^{-2}\cdot s^{-1}$.

2.14 Fixed-bed reactor experiment

To estimate the apparent activation energy for the RWGS reaction an experiment in a fixed-bed tubular steel reactor (Chinchen reactor) were performed. 15 mg of NiCu(4:1)Al_ox290 sample (sieve fraction 200 - 300 µm), was mixed with 50 mg of SiC. The material was placed inside the reactor of 4 mm diameter and the experiment was carried out at atmospheric pressure. The precatalyst was reduced in situ under 350 $mL\cdot min^{-1}$ of 5% H_2 in Ar, heated at 2 $°C\cdot min^{-1}$ to 450 °C and held for 3 h at the latter temperature. A reaction mixture of CO_2:H_2:Ar was set in the 1:1:0.5 ratio. The reaction temperature was set to 350, 400, 450, and 550 °C using a heating rate of 10 $°C\cdot min^{-1}$ and kept at each temperature for 1 h to obtain a steady state. The quantification of products was performed by online gas chromatography equipped with TCD and FID.

3 Preparation of highly dispersed metallic nanoparticles from NiCuAl-layered double hydroxides

This chapter describes the properties of NiCuAl-LDH and the activation procedure in order to obtain highly dispersed metallic nanoparticles. The thermal decomposition and the effect of calcination temperature on the reducibility are presented. The reduction profiles of the bimetallic sample suggested two separate events: (1) reduction of Cu, which promotes the (2) reduction of Ni. However, the characterization of the reduced material showed transient core-shell properties of the Ni-Cu system that eventually can form an alloy. The metal-support interaction is also studied.

3.1 As-prepared LDH properties

LDH materials with the general formula $[M^{2+}{}_{0.7}Al^{3+}{}_{0.3}(OH)_2]^{0.3+}$ $(CO_3)^{2-}{}_{0.15}\cdot mH_2O]^{x-}$ (M^{2+} = Ni^{2+} and/or Cu^{2+}) were synthesized by co-precipitation at constant pH 9, as described in the experimental details. The amount of divalent metals M^{2+} was varied using different Ni:Cu ratios of 1:0, 4:1, 1:1, and 0:1. Samples are denoted as bimetallic when using both Ni and Cu as divalent ions. The labels and relative molar content of the LDH samples measured on a macro- and local-scale are summarized in Table 1. The relative metal content obtained by ICP-MS was close to the target values.

Table 1: List of LDH samples with their relative metal content estimated from the bulk (ICP-MS) and local (STEM-EDX) scale.

Sample label	**Sample description**	**Relative metal content (ICP-MS) [mol%]**			**Relative metal content (STEM-EDX) [mol%]**		
		Ni	**Cu**	**Al**	**Ni**	**Cu**	**Al**
NiAl	$Ni_{0.7}Al_{0.3}$	0.75	-	0.25	0.65	-	0.35
NiCu(4:1)Al	$Ni_{0.56}Cu_{0.14}Al_{0.3}$	0.57	0.15	0.28	0.5	0.15	0.35
NiCu(1:1)Al	$Ni_{0.35}Cu_{0.35}Al_{0.3}$	0.37	0.35	0.28	0.28	0.36	0.36
CuAl	$Cu_{0.7}Al_{0.3}$	-	0.71	0.29	-	0.65	0.35

The X-ray diffractograms of the LDH material are shown in Figure 9. All Ni-containing samples exhibit defined reflections of the hydrotalcite-like phase ($Ni_{2.4}Cu_{3.04}Al_{2.56}(OH)_{16}(CO_3)_{1.28}\cdot 9.84\cdot H_2O$, PDF 2-00-052-1628). The defining feature of the hydrotalcite is the intense lines at low 2θ angles, which indicate the basal spacing (00*l*). The main reflection (003) at $2\theta = 11.6°$ corresponds to the direction of the stacking fault of the brucite-like layers. The CuAl sample shows a higher long-range order or crystallinity observed by the sharper reflections in the XRD pattern, compared to the other synthesized LDH materials. Most of the reflections fit to those of $Cu(OH)_2$ (PDF 2-01-072-0140) and similar X-ray diffractograms have been reported for CuAl LDH materials by Trujillano *et al.* [107].

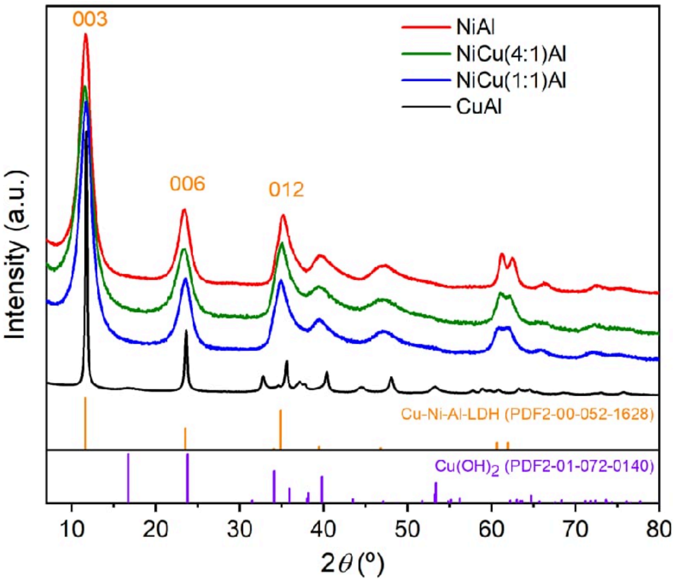

Figure 9: X-ray diffractograms of the as-synthesized LDH samples: NiAl, NiCu(4:1)Al, NiCu(1:1)Al, and CuAl.

A detailed XRD analysis on the NiCu(4:1) sample may indicate a mixture of two phases (SI Figure 61), either separately as two discrete phases, or intermixed. The first one corresponds to the usual rhombohedral hydrotalcite-3R structure (ABCABC stacking) and the second one to the hexagonal 2H structure (ABAB stacking). Assuming the single 3R phase for the LDH structure, from the XRD pattern a refined value for the unit-cell parameter *c* of 22.763 Å can be deduced, which agrees with the value reported in the literature for similar structures (22.703 Å) [108]. TEM images of the four synthesized LDH samples are shown in Figure 10. Estimation of the c parameter of the NiCu(4:1)Al sample from TEM results leads to a similar value of 22.2(7) Å compared to the estimated value by XRD. However, a slightly lower value might be expected because of the shrinking of the layers in the vacuum environment of the microscope as a result of the removal of water molecules from the interlayer gallery. The estimated value from XRD is an averaged representation of the bulk over the *whole* sample; whereas the one observed in TEM, is a detailed local analysis from one part of the sample. The value estimated from XRD represents the overall bulk of the sample, while the observed in TEM is a detailed local analysis of a particular part of the sample.

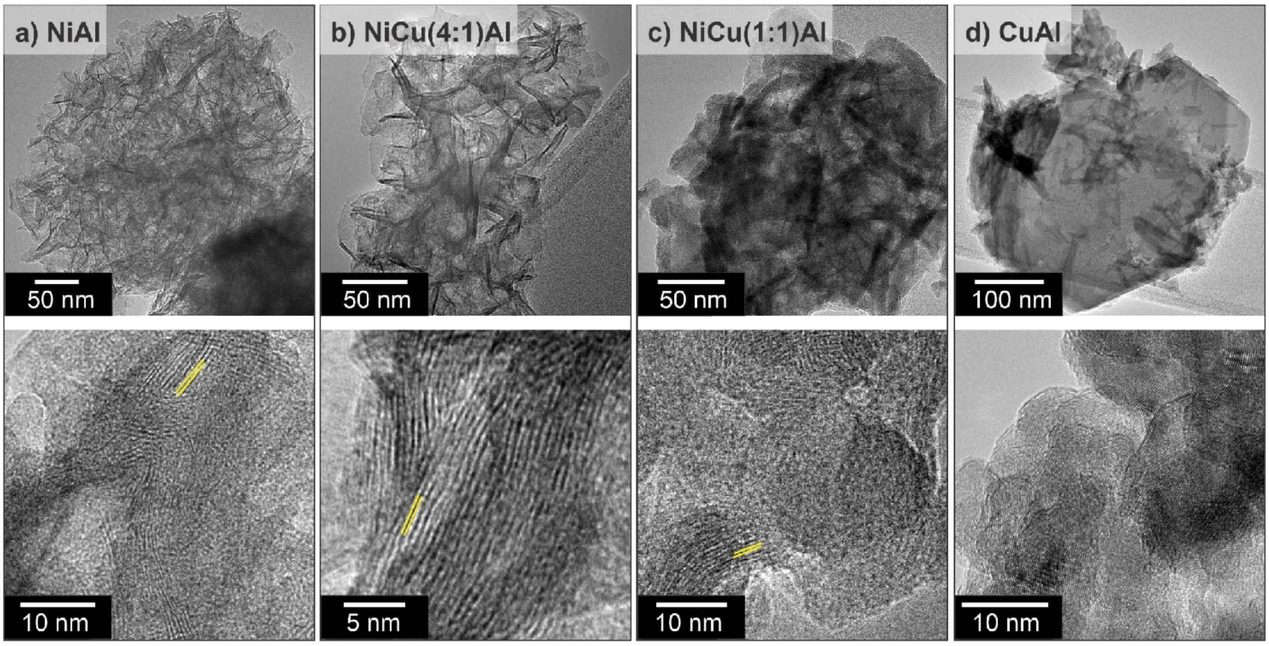

Figure 10: Transmission electron micrographs of pristine LDH samples synthesized with different metal loading: a) NiAl, b) NiCu(4:1)Al, c) NiCu(1:1)Al, and d) CuAl. The yellow lines represent the d-spacing between the layers, clearly visible for the Ni-containing samples.

The morphology of the as-prepared NiAl and NiCu(4:1)Al LDH samples show a flower-type structure with nanoplatelet structures oriented in different directions as shown in Figure 10. We confirmed that the flat appearance is not a projection artifact by tilting experiments performed on NiCu(4:1)Al_290 (SI Figure 62). For the sample NiCu(1:1)Al this structure is losing the flowering-like properties until it becomes just platelets with different dimensions and directions, as is observed for the CuAl sample. The morphological difference of the CuAl sample compared with the Ni-containing samples may be explained by the structural (geometric) distortion of the Cu ions, the Jahn-Teller effect, typically observed among octahedral complexes, where the axial bond can be shorter or longer than the equatorial bonds [109]. Interestingly, the CuAl sample was the LDH sample with the highest long-range order observed on their XRD patterns.

STEM-EDX mappings were recorded to verify the elemental distribution of the synthesized LDH samples; the results are shown in Figure 11. Furthermore, integrated EDX spectra were extracted from an area of 25 nm x 25 nm, which is marked in the images. The data corroborates the homogeneous distribution of the elements after the synthesis. Obtained from the same area, the local elemental composition shows values similar to the targeted ones (see Table 1). The bimetallic materials exhibit an elemental ratio of Ni/Cu = 0.7 and

3.3, respectively, which differ slightly from the theoretical values of Ni/Cu = 1 and 4, respectively. In contrast to very local STEM-EDX measurements, ICP-MS as a method to investigate the bulk composition leads to values of 1.0 and 3.9 for the corresponding molar ratios (see Table 1). The slight differences may be due to the scale of the measurement: one local and one bulk averaged. This difference might represent a slight redistribution of the elements at the local scale.

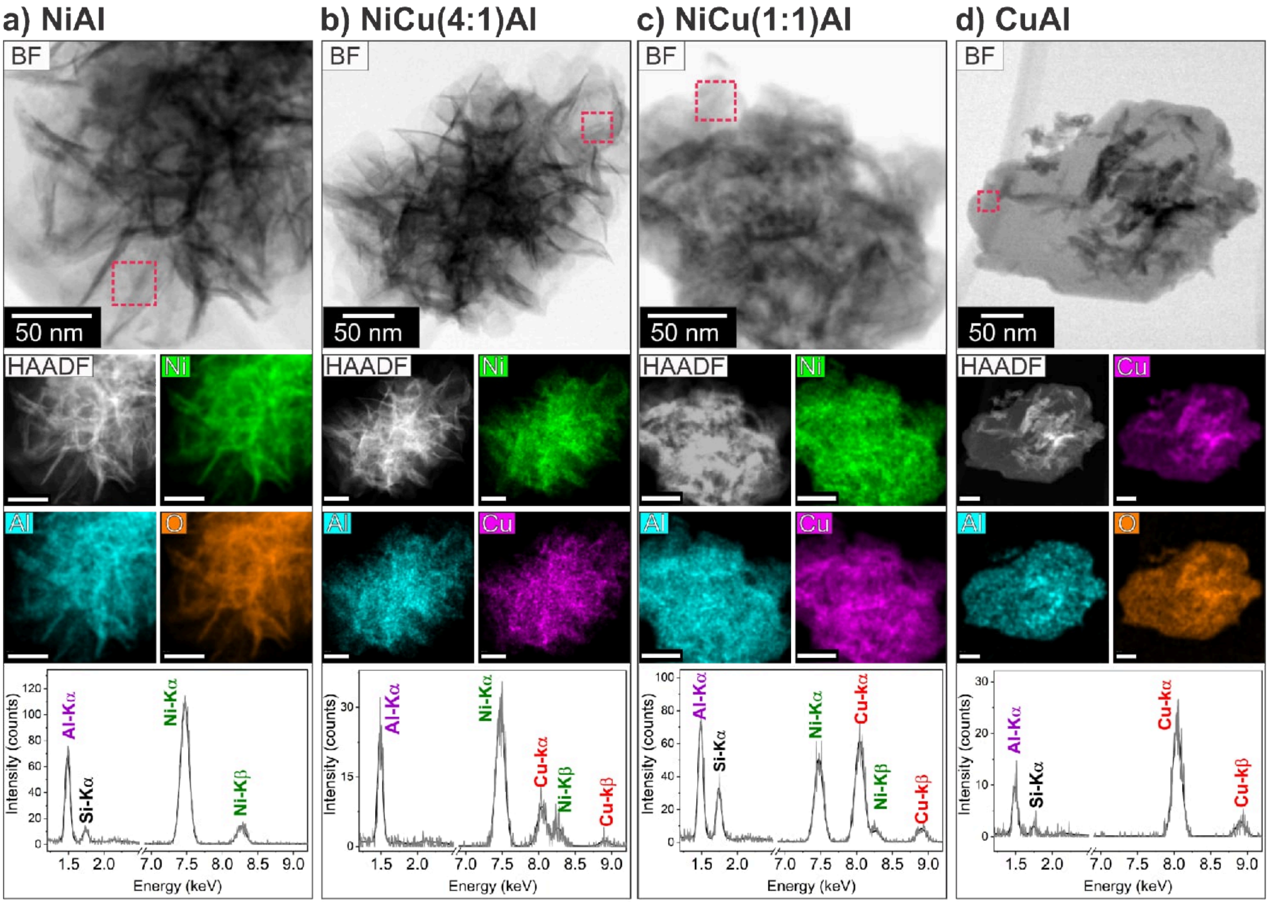

Figure 11: STEM-EDX images and elemental mappings of pristine LDH samples synthesized with different metal loadings: a) NiAl, b) NiCu(4:1)Al, c) NiCu(1:1)Al, and d) CuAl. The spectra at the bottom are the integrated spectra extracted from the corresponding marked area (25 nm x 25 nm).

The textural properties, N_2 adsorption-desorption isotherms, and pore size distributions of the LDH and calcined samples are shown in Figure 12. For all samples, the isotherms (Figure 12a and b) are type IV, characteristic of mesoporous materials, with hysteresis -due to capillary condensation in mesopore structures- type H3, according to the IUPAC classification [110]. The hysteresis does not exhibit any limiting adsorption at high p/p_0. This behavior can be caused by the presence of nonrigid aggregates (i.e., an assembly of particles that are loosely coherent) of platelet-like structures giving rise to slit-shaped pores [110], [111]. These pores are actually the spaces between the platelets where multilayer adsorption and pore filling can occur.

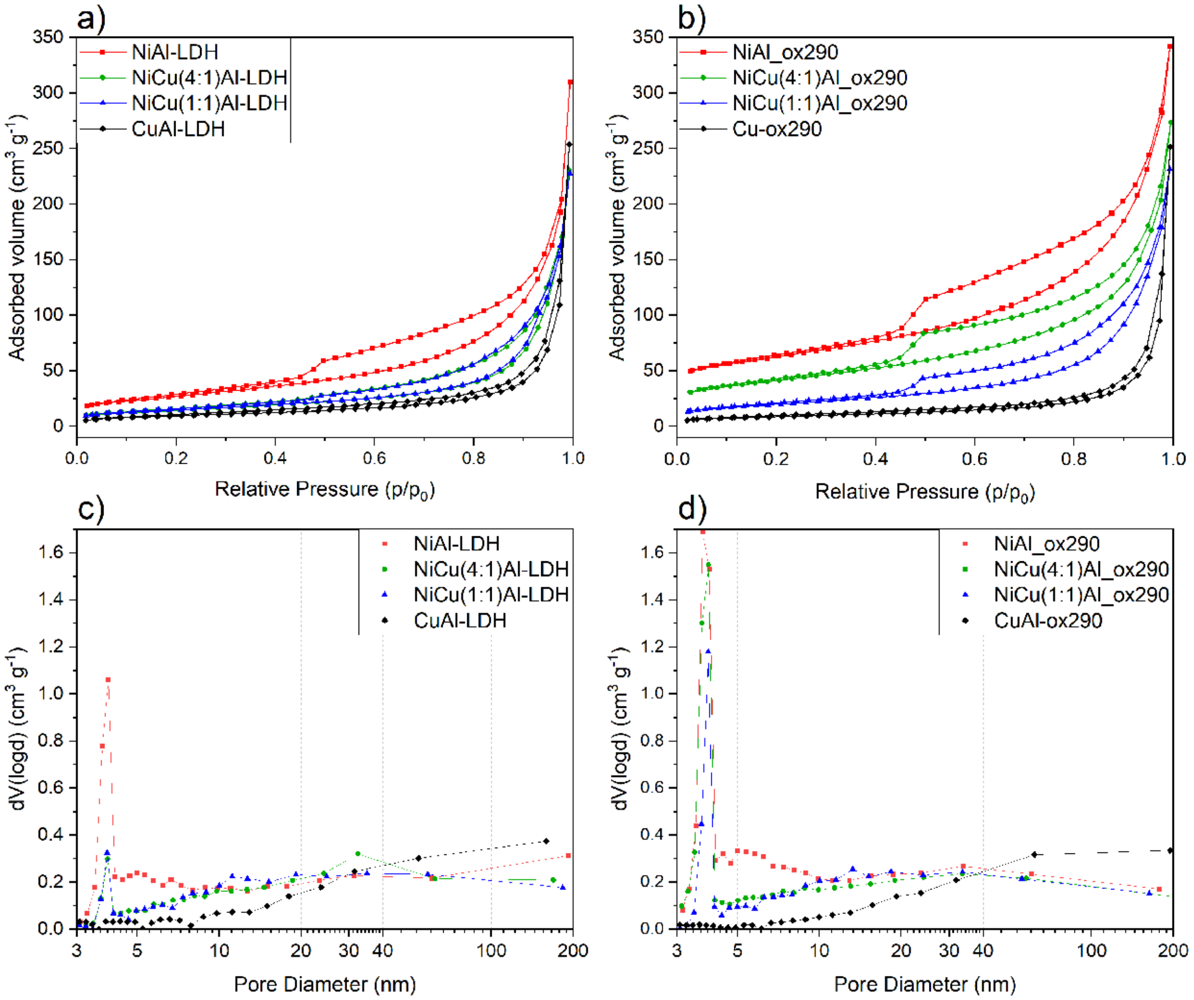

Figure 12: Nitrogen adsorption-desorption isotherms of a) LDH samples and b) LDH calcined at 290 °C; and pore size distributions of c) LDH samples and d) LDH calcined at 290 °C.

Within LDH materials, the NiAl-LDH presents a wider hysteresis loop than the CuAl-LDH, which may be an indication of different porous thicknesses or interlayer space where the water is randomly located. Both bimetallic samples (NiCu(4:1)Al and NiCu(1:1)Al LDH) show a very similar hysteresis loop. This may indicate that the content of Cu present in the system does not affect the capillary condensation. Due to the nature of the nonrigid pores, the assessment of pore size distribution is not completely reliable [112]. However, an estimation using the BJH model gives a range of mesopores from 3 to 5 nm in all samples but CuAl.

The isotherms of the calcined samples showed distinct N_2 adsorbed volumes at low relative pressures (p/p_0 ~ 0.22), as seen in Figure 12b (plots shown without offset). This N_2 volume decreases as the Ni content decreases, with NiAl_ox290 having the highest (50 $cm^3 \cdot g^{-1}$), followed by NiCu(4:1)Al_ox290 (31.0 $cm^3 \cdot g^{-1}$), NiCu(1:1)Al_ox290 (13.2 $cm^3 \cdot g^{-1}$), and CuAl_ox290 (5.6 $cm^3 \cdot g^{-1}$). The porous volume in the calcined samples

(Figure 12d) is visibly higher than in the as-prepared LDHs (Figure 12c), except for the CuAl sample. Using the BET equation, the specific surface areas were determined and decreased as Ni content decreased, from 98.4 $m^2 \cdot g^{-1}$ for NiAl-LDH to 34 $m^2 \cdot g^{-1}$ for CuAl-LDH (Table 2). The surface area depends on the calcination temperature, as has been published [45], [113]. In agreement with the gain of pore volume after calcination, the specific surface area of the materials also increased by over 110% for NiCu(4:1)Al and NiAl samples; 33% for the NiCu(1:1)Al sample; and it did not increase for the CuAl sample.

Table 2: Textural properties of the LDH precursors and the mixed metal oxides (i.e., LDH calcined at 290 °C).

Sample (LDH)	**Molar ratio Ni:Cu:Al**	**BET-SA ($m^2 \cdot g^{-1}$)**	**Sample (MMO)**	**BET-SA ($m^2 \cdot g^{-1}$)**	**Relative increase of SA (%)**
NiAl	7:0:3	98.42	**NiAl_ox290**	212.08	115
NiCu(4-1)Al	5.6:1.4:3	52.36	**NiCu(4-1)Al_ox290**	143.83	175
NiCu(1-1)Al	3.5:3.5:3	53.52	**NiCu(1-1)Al_ox290**	70.96	33
CuAl	0:7:3	34.21	**CuAl_ox290**	30.97	(-9)

Note: The specific surface area was estimated by the BET method.

3.2 Thermal decomposition of LDH

Figure 13 displays the thermogravimetric curves of the as-synthesized LDH samples that were obtained under synthetic air (21% O_2 in Ar). The figure includes the corresponding mass spectrometry signals of the m/z ratios of 18 (H_2O, blue curves) and 44 (CO_2, red curves).

The water signal indicates two major steps during thermal decomposition: dehydration (i.e. removal of interlayer water), and dehydroxylation. The removal of interlayer water occurs at low temperatures, where the release of the physically adsorbed water may also take place. With the NiAl sample, the interlayer water is removed from 50 °C to 220 °C. When adding Cu to the LDH, NiCu(4:1)Al's upper limit of this range shifts to lower temperatures, i.e., below 195°C, and 165°C for NiCu(1:1)Al. Ab initio studies of LDH dehydration with CO_3^- as a counterion, revealed that water molecules are important for the stability of the layered structure by enhancing the hydrogen bond between the layers and the intercalated species. The stronger the interaction is, the higher the temperature of dehydration (Costa et al., 2011). The product of the layers' dehydroxylation ($2OH^- \rightarrow O^{2-} + H_2O$), water, is seen at elevated temperatures and differs in each sample. For the Ni-containing samples, this occurs at higher temperatures (360 °C > T > 200 °C); while for the CuAl sample, the dehydroxylation and water release occur at T < 210 °C.

The CO_2 signal represents the decomposition of carbonates, resulting in the formation of metal oxides, also called mixed metal oxides (MMO), or the release of physisorbed CO_2. Carbonate decomposition occurs at 310 °C for the NiAl and NiCu(4:1)Al samples, but at a higher temperature of 625 °C for the CuAl sample. The NiCu(1:1)Al sample shows two peaks for carbonates decomposition at 280 °C and 570 °C, which might be intimately related to Ni-carbonates and Cu-carbonates, respectively. Previous studies have shown that Cu-based materials prepared from hydroxycarbonates can form high-temperature carbonates (peak at around 600 °C) after calcination [114]. The absence of the second (high temperature) peak for the NiCu(4:1)Al sample may be related to the intimate interaction of Cu with Ni or the atomic dispersion of Cu into the Ni oxide system. Similar results have been published by several authors [50], [115].

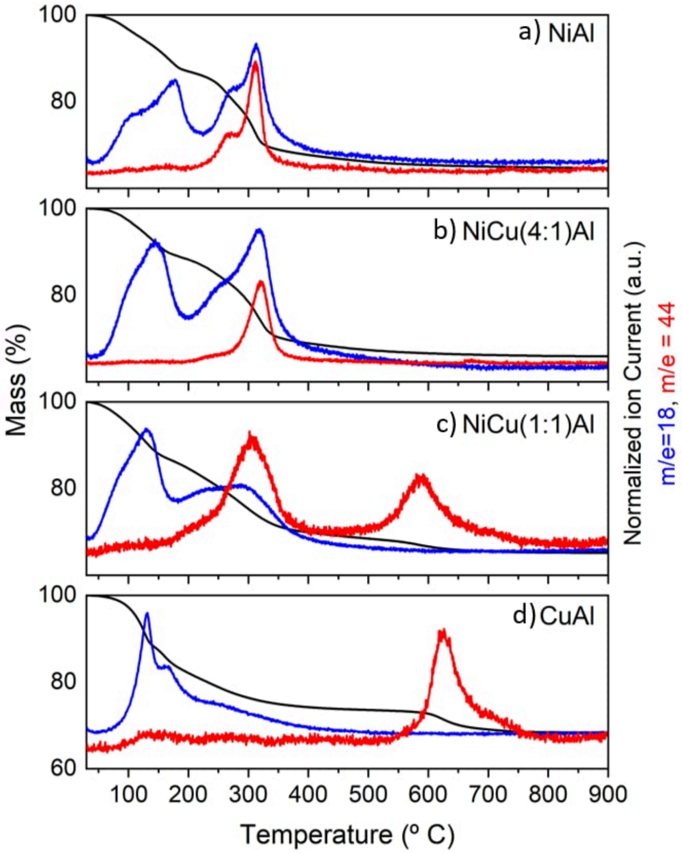

Figure 13: Thermogravimetric analysis of LDH samples: a) NiAl, b) NiCu(4:1)Al, c) NiCu(1:1)Al, and d) CuAl. Black trace mass, blue trace water, red trace CO_2.

The presence of residual carbonates (also called high temperature carbonates) after calcination might be beneficial for performing catalysis, because they could suppress sintering during reactions [116], [117]. A temperature of 290 °C was chosen for the calcination pretreatment, details will be explained in the next section 3.3. X-ray diffractograms of four calcined samples are shown in Figure 14. For all corresponding samples, the main reflections show their respective Ni and Cu oxides. Moreover, the amorphous background may indicate the alumina support and probably uncalcined precursor. The broad peaks in the pattern may represent a combination of small crystallite sizes and microstrains present on the material. No segregation was found in the local composition of calcined materials through STEM-EDX analysis (See STEM-EDX images of NiCu(4:1)Al_ox290 sample in SI Figure 63).

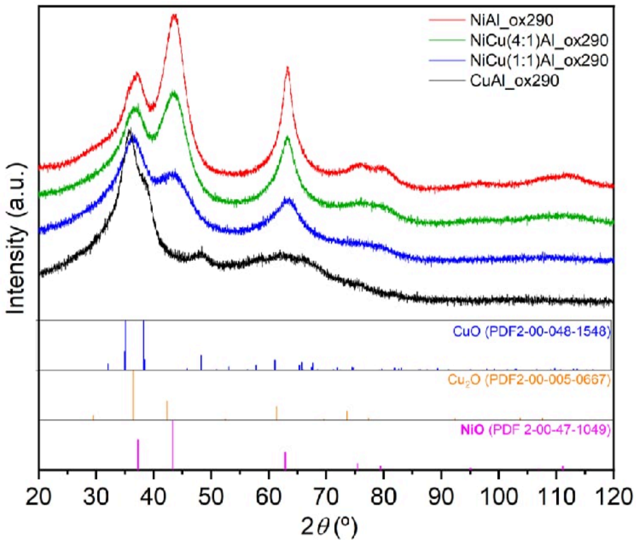

Figure 14: X-ray diffractograms of metal oxides: NiAl_ox290, NiCu(4:1)Al_ox290, NiCu(1:1)Al_ox290 and CuAl_ox290.

3.3 Effect of calcination temperature on reducibility

The properties of the activated sample depend on the history of its treatment. Thus, the influence of the calcination temperature on the reduction profile was studied for all LDH samples. Figure 15 shows the temperature-programmed reduction (TPR) profile of NiAl, NiCu(4:1)Al, NiCu(1:1)Al and CuAl LDH samples previously calcined at 290 °C (red curves) and 600 °C (black curves). In addition, the corresponding MS signals of H_2O (m/z=18) and CO_2 (m/z=44) are shown. The Cu^{2+} species are reduced at lower temperatures, ca. 150 °C, while the reduction of Ni^{2+} species is above 200 °C. As it is observed, the Ni^{2+} reduction peak shifts ~ 100 °C to higher temperatures, when the calcination was at 600 °C, compared to 290 °C. This shift may be due to the sintering of NiO particles during calcination at 600 °C. Furthermore, X-ray diffractograms of NiCu(4:1)Al calcined at 600 °C (SI

Figure 64) showed sharper peaks due to the increased long-range order [118]. The platelet-like morphology persists even after calcination, as observed in the TEM images (SI Figure 64b and c). For the NiAl sample calcined at 290 °C, a small peak of the H_2 consumption (TCD signal) is observed at temperatures below 100 °C. Despite the absence of a distinct signal in MS, this peak may be associated with the reduction of atomically dispersed Ni^{2+} species. The H_2O signal is not present because it condenses on the reactor tube and cannot reach the spectrometer at this temperature. The peak was not seen in the sample calcined at 600 °C, showing that calcination temperature affects the sorption properties.

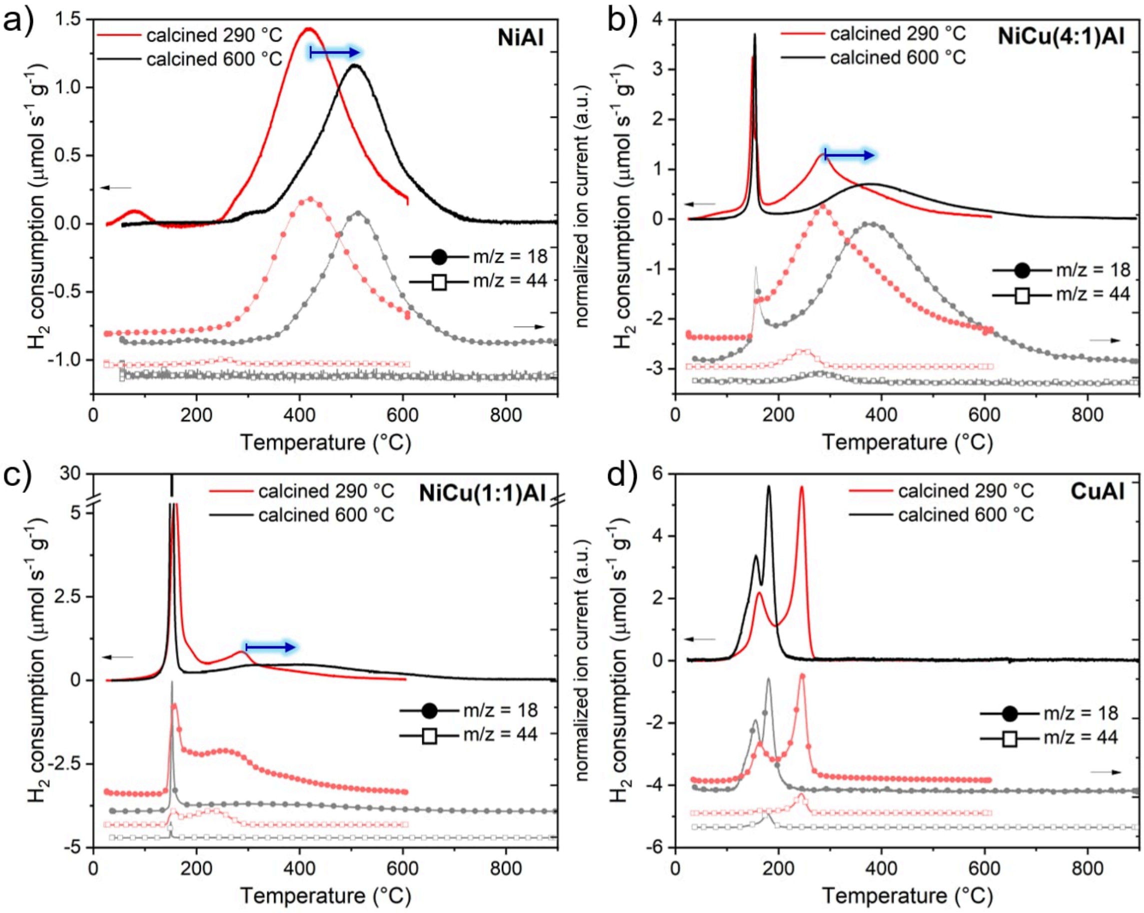

Figure 15: TPR profile of LDH-derived materials previously calcined at 290 °C and 600 °C of a) NiAl, b) NiCu(4:1)Al, c) NiCu(1:1)Al, and d) CuAl samples. H_2 consumption and mass signals of H_2O (m/z=18), filled symbols; and CO_2 (m/z=44), open symbols.

The percentage of reduction is presented in Table 3.

Table 3: H_2 consumption of Cu and Ni oxide species during the reduction of LDH-derived materials: NiAl, NiCu(4:1)Al, NiCu(1:1)Al, and CuAl samples previously calcined at 290 °C. Numbers in brackets indicate the degree of reduction.

Sample		**H_2 consumption (μmol·g^{-1})**			
		Measured			**Theoretical H_2 required**
		ox290_red450	**ox290_red600**	**ox600_red900**	
NiAl	Ni:	4966 (75%)	5836 (88%)	6188 (94%)	6598
NiCu(4:1)Al	Cu:	1287 (97%)	1328 (100%)	1293 (97%)	1333
	Ni:	4184 (78%)	4777 (90%)	5396 (100%)	5333
NiCu(1:1)Al	Cu:	3263 (100%)	3241 (100%)	3032 (93%)	3252
	Ni:	2578 (80%)	2912 (90%)	3274 (100%)	3252
CuAl	Cu:	5858 (87%)	5885 (87%)	6695 (100%)	6738

The reduction profiles of CuAl samples are affected by the calcination temperature in a more complex manner. Cu^{2+} species may get stepwise reduced to Cu^{1+} and to Cu^0, demonstrated by the two reduction events [119], [120]. Another explanation can be that these two events may result from the reduction of dispersed and bulk CuO species [121]. This two-event reduction of Cu^{2+} is not visible for the bimetallic samples, probably because of the absence of bulk CuO species. Considering the mass signal m/z 44 (CO_2) in Figure 15d, it is confirmed that the second peak in m/z 18 corresponds to the reduction of Cu^{2+} that interacts stronger with carbonates. In that region, a simultaneous presence of water and CO_2 signals was observed. Furthermore, Cu-based LDH materials can form high-temperature carbonates [122], which are not removed after calcination at 290 °C but are partially removed above 600 °C (see Figure 13). Interestingly, these Cu-carbonate species may be reduced at lower temperatures when calcination at 600 °C was used.

On the other hand, the mass signal m/z 44 (CO_2) was negligible for the NiAl sample. With increasing Cu content, (sample NiCu(4:1)Al), the CO_2 signal became visible. It appears at lower temperatures for the sample calcined at 290 °C. With the sample NiCu(1:1)Al, the CO_2 signal follows the shape of the consumed H_2, indicating the correlation of Cu and Ni species with carbonates. The Ni^{2+} reduction peak appears much broader than the sharp Cu reduction peak.

The bimetallic NiCu(4:1)Al sample, calcined at both temperatures, displays a sharp Cu^{2+} reduction peak, as demonstrated by Figure 15b. This effect occurs because of Cu species that are atomically dispersed and reduced at the same temperature. It was similar for sample NiCu(1:1)Al calcined at 600 °C, but when 290 °C was used, a broader Cu^{2+} reduction event was observed. It could represent a stepwise reduction of Cu^{2+} species or energetically different CuO sites that require a wide range of temperatures for reduction.

The results demonstrated that when the calcination treatment was mild, the reduction process required a mild temperature. Additionally, the use of high temperatures during the pretreatment could result in the formation of Ni spinel species. These species are highly thermostable and required also high temperatures of reduction [123]. Therefore, a temperature of 290 °C was the most suitable for calcination, producing gentle reduction conditions and avoiding spinel formation.

3.4 Effect of reduction temperature

The sample NiCu(4:1)Al_ox290 (LDH calcined at 290 °C) was used to study the effect of reduction temperature on activated material properties. The material was reduced at three different reduction temperatures: 300, 450 and 900 °C. The X-ray diffractograms of the reduced samples are shown in Figure 16a. The sample NiCu(4:1)Al_ox290_red300 still contains Ni oxide species. The sample NiCu(4:1)Al_ox290_red450 does not have any oxide contribution according to XRD and shows reduced species. The sample NiCu(4:1)Al_ox290_red900 shows sharp reflections related to metallic species, i.e. long-range order species. To support this, we investigated the Ni $L_{2,3}$-edge EEL spectra of the same three samples mentioned above, which are shown in Figure 16b.

It should be noted that the EEL spectra were acquired on a local scale on a single nanoparticle, while the XRD data gives bulk or integral information. The identification of species is done by comparing specific features of the spectra (for example the L_2-edge – L_3-edge energy splitting and L_3/L_2 intensity ratio) with reference spectra (SI Figure 66) reported in the literature [124]. Table 4 shows the characteristic features of Ni^0 and Ni^{2+}, as well as those of the reduced samples. As observed in the Table 4, the samples NiCu(4:1)Al_ox290_red300 and NiCu(4:1)Al_ox290_red450 show contributions of both metallic and oxidic species of Ni. However, for the sample NiCu(4:1)Al_ox290_red450 the features are apparently closer to metallic Ni. The sample NiCu(4:1)Al_ox290_red900 shows mainly contributions of metallic Ni. During EELS acquisition, the Cu L-edge signal could not be observed, which is due to the atomically dispersed Cu species and low Cu content. However, Cu was confirmed from STEM-EDX elemental analysis of the sample NiCu(4:1)Al_ox290_red450 (Figure 17).

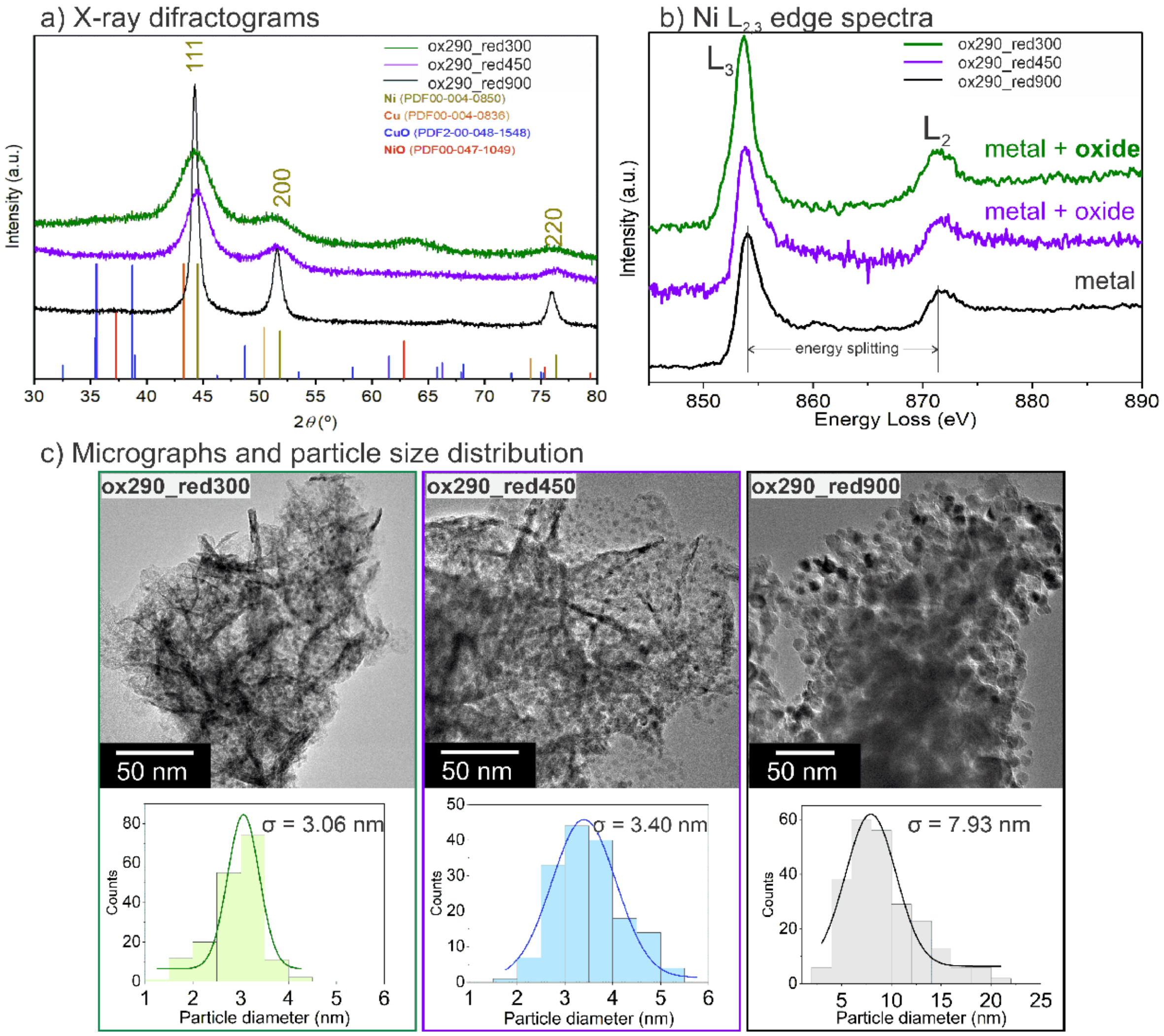

Figure 16: Characterization of NiCu(4:1)Al calcined at 290 °C and reduced at 300 °C, 450 °C and 900 °C: a) X-ray diffractograms, b) electron energy loss spectra, and c) TEM micrographs with particle size distribution (PSD); σ represents the distribution width.

Table 4: Characteristic features of Ni $L_{2,3}$-spectra: energy splitting and intensity ratio, of samples after reduction at different temperatures.

Sample	L_2 - L_3 energy splitting	L_3/L_2 intensity ratio	Characteristics
Ni^0	17.7	1.6	metal
Ni^{2+}	17.3	3.0	oxide
NiCu(4:1)Al_ox290_red300	17.4	2.5	metal + oxide
NiCu(4:1)Al_ox290_red450	17.6	2.2	metal + oxide
NiCu(4:1)Al_ox290_red900	17.7	1.9	metal

Note: Features for Ni^0 and Ni^{2+} were retrieved from [124], [125].

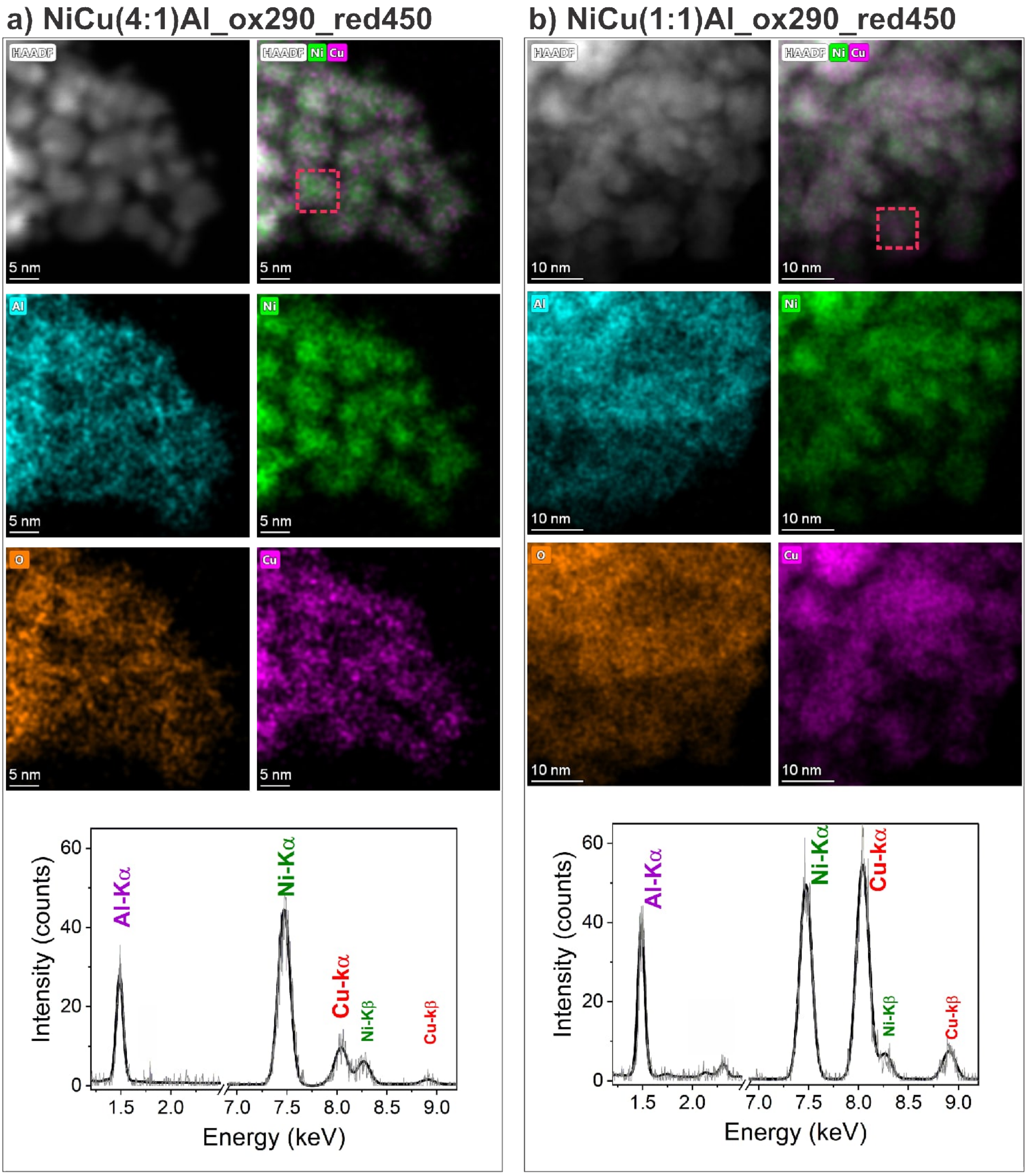

Figure 17: STEM-EDX mapping of a) NiCu(4:1)Al_ox290_red450 and b) NiCu(1:1Al)_ox290_red450. The integrated spectrum from the marked area (7 nm x 7 nm) shows the coexistence of both metals Ni and Cu within the same nanoparticle (C-coated Au TEM grid).

The particle sizes of the metallic species play a vital role in catalysis [126]. Figure 16c shows TEM images and the particle sizes distribution (PSD) of the samples NiCu(4:1)Al_ox290_red300, NiCu(4:1)Al_ox290_red450 and NiCu(4:1)Al_ox290_red900. The TEM images clearly show platelet structures decorated with small nanoparticles when the material was reduced at 300 °C and 450 °C. At a higher reduction temperature of 900 °C, the metallic nanoparticles were sintered to the large particles and with a wider PSD. The PSD reveals that for NiCu(4:1)_ox290_red300, the nanoparticles were on average 3 nm in size or below. The sample NiCu(4:1)_ox290_red450 has an average particle size of 3.5 nm, and the sample reduced at 900 °C exhibits an average particle size of 13 nm.

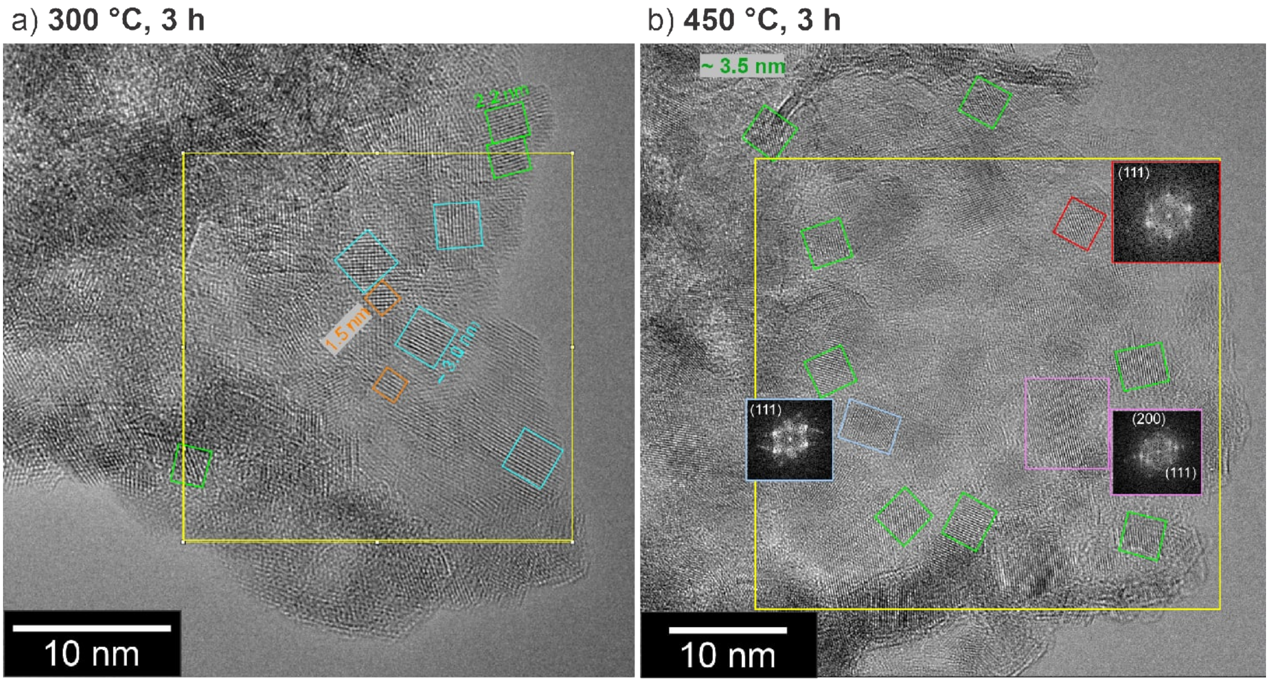
a) **300 °C, 3 h**
b) **450 °C, 3 h**

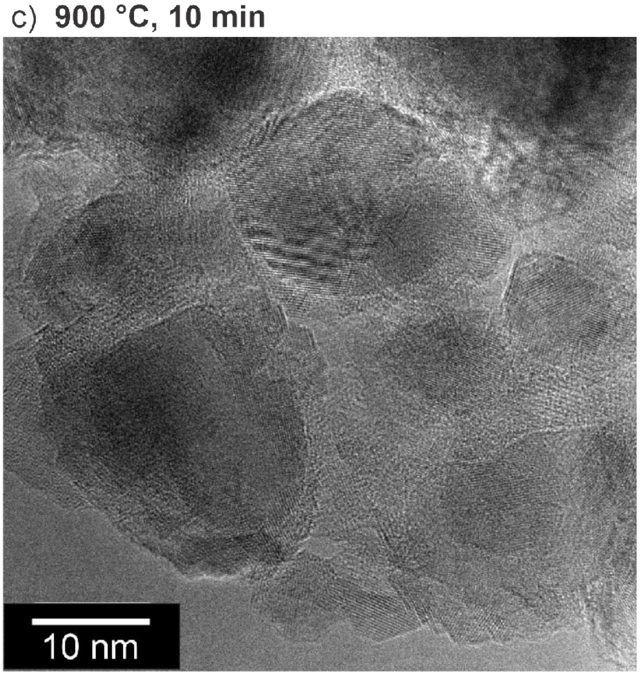
c) **900 °C, 10 min**

Figure 18: HRTEM of NiCu(4:1)Al_ox290C reduced at 300, 450 and 900 °C. The squares of different colors represent nanoparticles of different sizes.

Metal nanoparticle formation from mixed oxides can occur through nucleation and growth [127]. This may happen via several phenomena: atom-to-atom or cluster-to-cluster formation. The high dispersion of the metal precursor promotes the formation of small and well-dispersed nanoparticles on the alumina sheets. Interestingly, HRTEM images of the material reduced at 300 °C show small nanoparticles in a similar orientation, and direction [111], with respect to the sheet (Figure 18). This represents the preferential growth orientation for nanoparticle formation which might depend on the catalyst precursor [128]. Using 450 °C as reduction temperature, the nanoparticles are still uniformly distributed along the sheet but probably reorient within the sheet while growing. After reduction at 900 °C, sintering became evident and the particles tend to agglomerate.

From the activation study, we chose the conditions for activation of the material prior to catalytic evaluation: calcination at 290 °C and reduction at 450 °C, both processes with a dwell time of 3 h. Using these conditions, the morphology of the activated materials consists of metallic Cu and/or Ni nanoparticles supported on alumina with 2D sheet structures (TEM tilt series of NiCu(4:1)Al_ox290_red450 is shown in SI Figure 65).

3.5 Ni-Cu interaction: effect on the reducibility

Nickel and copper composition affect the reducibility, as it is visible in the reduction profile. Figure 19 shows the TPR profiles of the samples NiAl_ox290, NiCu(4:1)Al_ox290, NiCu(1:1)Al_ox290, and CuAl_ox290. The figure is complemented by their X-ray diffractograms after reduction. Comparing the Ni reduction peak of the samples NiAl_ox290 and NiCu(4:1)Al_ox290, a shift of ca. 110 °C to lower temperatures is observed when Cu is present. Further addition of Cu (sample NiCu(1:1)Al_ox290) did not influence the Ni reduction temperature. The reducibility of Ni is enhanced due to electron donation from Cu to Ni [129], and the H_2 spillover effect [130], [131]. The degree of reduction was calculated by comparing the amount of H_2 consumed during the TPR experiment with the theoretical value (Table 3). After reduction at 450 °C, the samples NiAl_ox290, NiCu(4:1)Al_ox290, NiCu(1:1)Al_ox290 showed 75%, 78%, and 80% of Ni^{2+} reduction, respectively. Although there is just a small difference (3 and 2%), it may indicate that the incorporation of Cu gradually promotes the reducibility of Ni. On the other hand, the Cu^{2+} was fully reduced in the samples NiCu(4:1)Al_ox290 and NiCu(1:1)Al_ox290, but it was just 87% for CuAl_ox290 sample. This lower amount of reduced Cu may be related to a portion of Cu species that are not available for reduction because they are probably forming high-temperature carbonates [121].

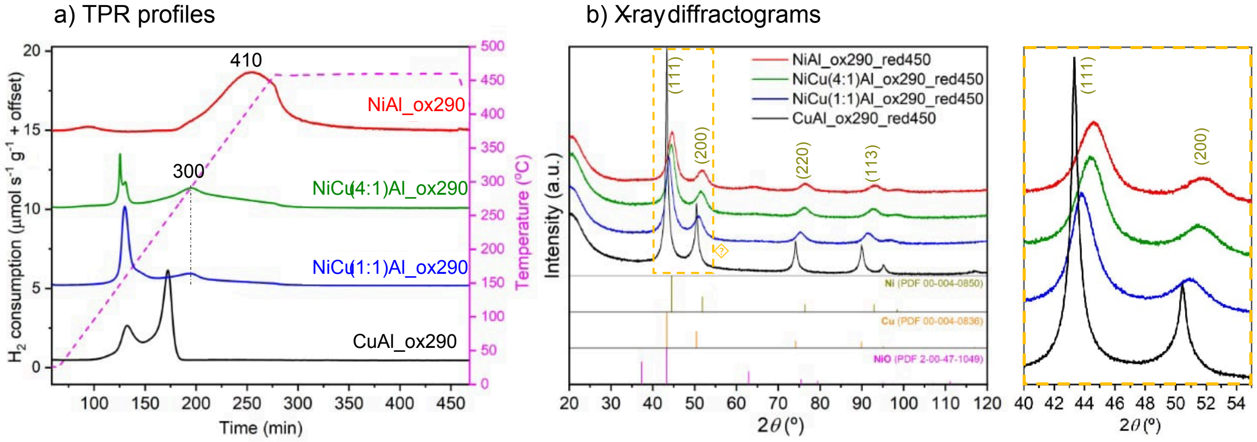

Figure 19: a) TPR profiles and (b) X-ray diffractograms of NiAl_ox290, NiCu(4:1)Al_ox290, NiCu(1:1)Al_ox290, and CuAl_ox290. (Catalyst mass: 80 mg, flow: 100 mL·min^{-1} of 5% H_2 in Ar, heating rate 2 °C·min^{-1})

The four samples were collected and transferred under an inert atmosphere for characterization by XRD and analytical TEM. The X-ray diffractograms are shown in Figure 19b. The amorphous contribution at approximately 2θ = 20° is due to the sample holder during the measurement. The NiAl_ox290_red450 sample shows the presence of both metallic Ni and NiO species. Metallic Cu was observed in XRD for the CuAl_ox290_red450 sample. The bimetallic samples (NiCu(4:1)Al_ox290_red450 and NiCu(1:1)Al_ox290_red450) exhibited mainly metallic species with a slightly (almost unnoticed) NiO at 2θ values of ca. 38° and 62°. The minor presence of oxides in the reduced samples could be due to the 20% which was not reduced during the process (Table 3). Diffraction peaks between Ni and Cu in the bimetallic samples confirm successful alloy formation [129], [132]. For a more quantitative analysis, the lattice parameters were obtained using Rietveld-based whole powder pattern fitting and it is shown in Figure 20 (SI Table 5). The observed lattice parameter for NiCu(1:1)Al_ox290_red450 matches the expected value for Vegard-type behavior. However, the sample NiCu(4:1)Al_ox290_red450 shows a deviation that may be related to an incomplete or inhomogeneous $Ni_{(1-x)}Cu_x$ alloy formation. The electron microscopy results support the statement of alloy formation by the elemental analysis of a single nanoparticle (STEM-EDX maps, indicated in Figure 17) and by high-resolution TEM images in Figure 21. The HRTEM images reveal d-spacings of the lattice distances oriented in the [111] direction that slightly increased from 0.204 nm for NiAl_ox290_red450 to 0.209 nm for NiCu(1:1)Al_ox290_red450. The increase is explained by the incorporation of Cu into the Ni-Cu alloy phase [133].

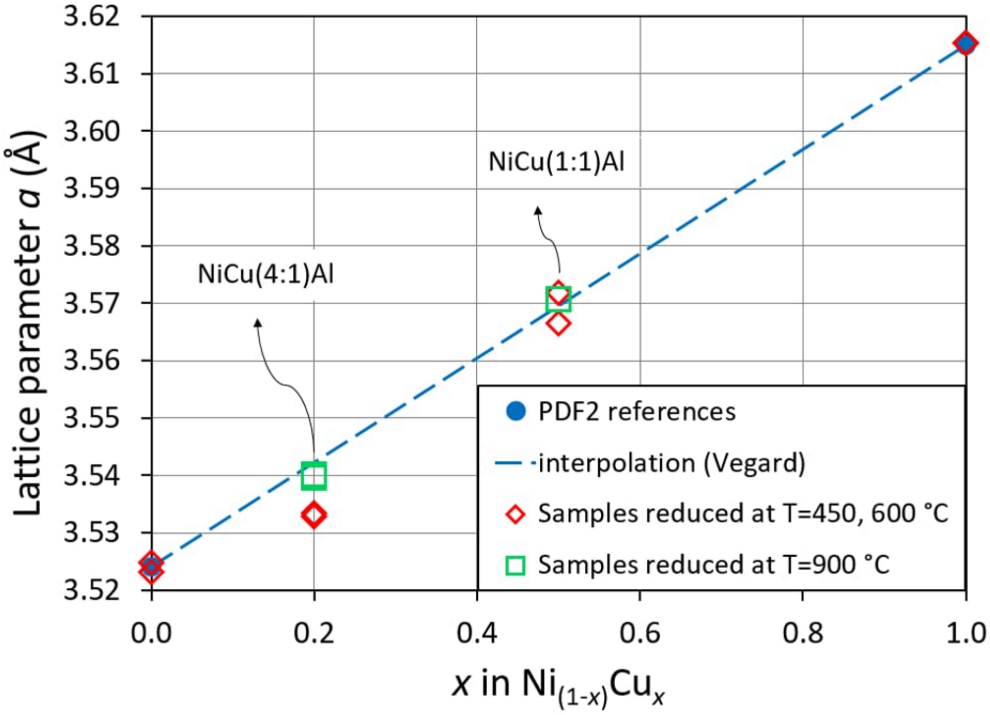

Figure 20: Lattice parameter as a function of the alloy composition for samples reduced at 450 and 600 °C (red rhombus) and 900 °C (green squares). (Catalyst mass: 80 mg, flow: 100 mL·min^{-1} of 5% H_2 in Ar, heating rate 2 °C·min^{-1})

To enhance the XRD analysis, reduced samples at different temperatures were incorporated into the study, and the lattice parameter is also included in Figure 20. A closer look reveals in fact incomplete or inhomogeneous $Ni_{(1-x)}Cu_x$ alloy formation when the samples were reduced at 450 and 600 °C. The samples reduced at 900 °C fit better to the Vegard-type behavior. The deficit of Cu in the solid solution could be explained by the possible segregation of Cu to the surface [41], [42]. The phase diagram of the Ni-Cu binary system includes a miscibility gap region over a wide range of compositions (20 < wt% Ni < 100) in the solid state below a certain critical temperature (T_c) [43]. It means that for films, there is no solid solution below T_c but segregation of its constituents. Several researchers have reported (experimentally and theoretically) a T_c between 300 to 700 °C [134]–[137], mainly for thin films or bulk crystals. However, for bimetallic nanoparticles, the phase transformation is much more complex and size-dependent [138]. For real catalytic systems, the interaction with the support introduces even more complexity.

Figure 22 displays STEM-HAADF images and particle size distributions of NiAl_ox290_red450, NiCu(4:1)Al_ox290_red450, NiCu(1:1)Al_ox290_red450 and CuAl_ox290_red450. The Ni-containing samples had a unimodal distribution of particle sizes at approximately 3.5 nm. Cu_ox290_red450 sample showed bigger particles (up to 22 nm), probably because of weak Cu - Al_2O_3 interaction.

a) NiAl_ox290_red450

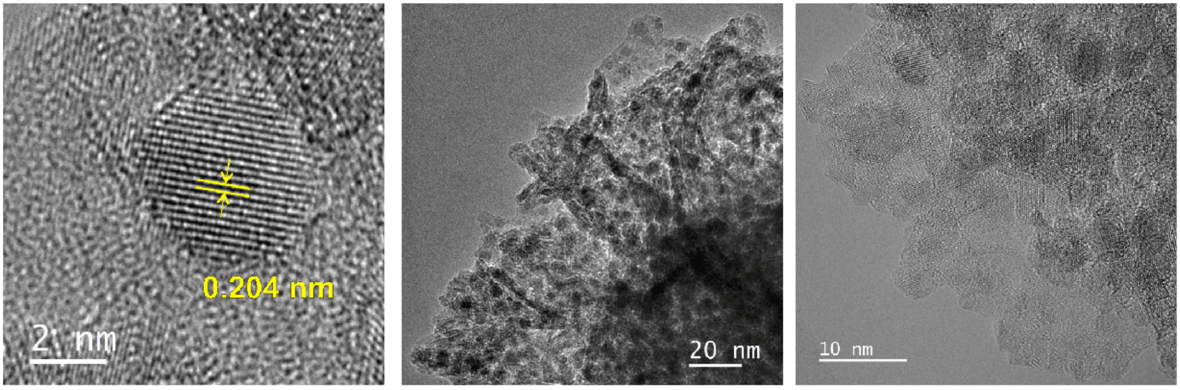

b) NiCu(4:1)Al_ox290_red450

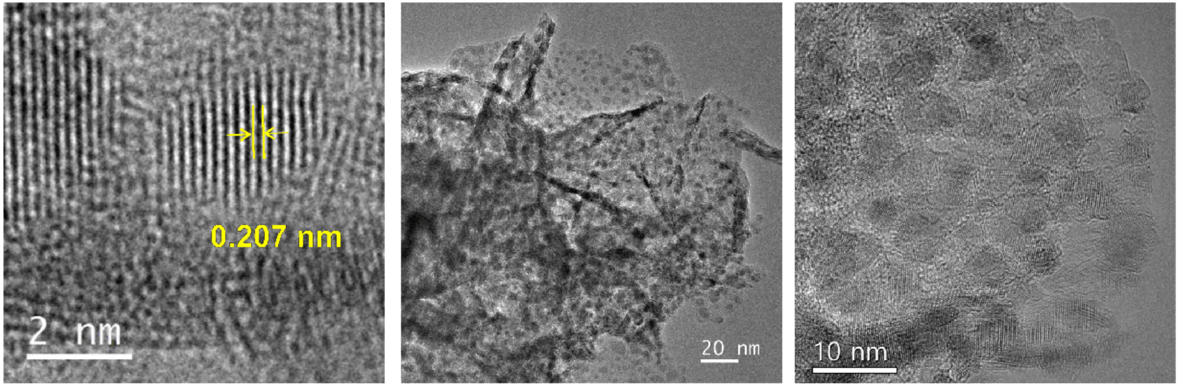

c) NiCu(1:1)Al_ox290_red450

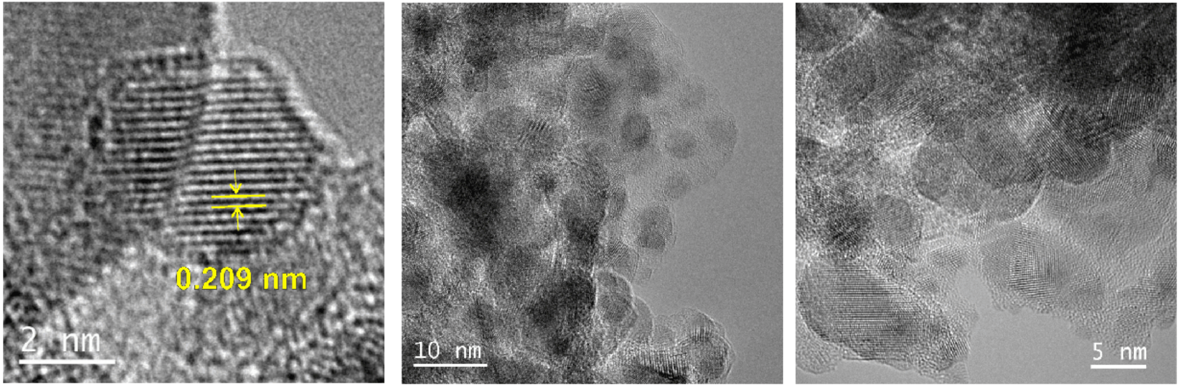

d) CuAl_ox290_red450

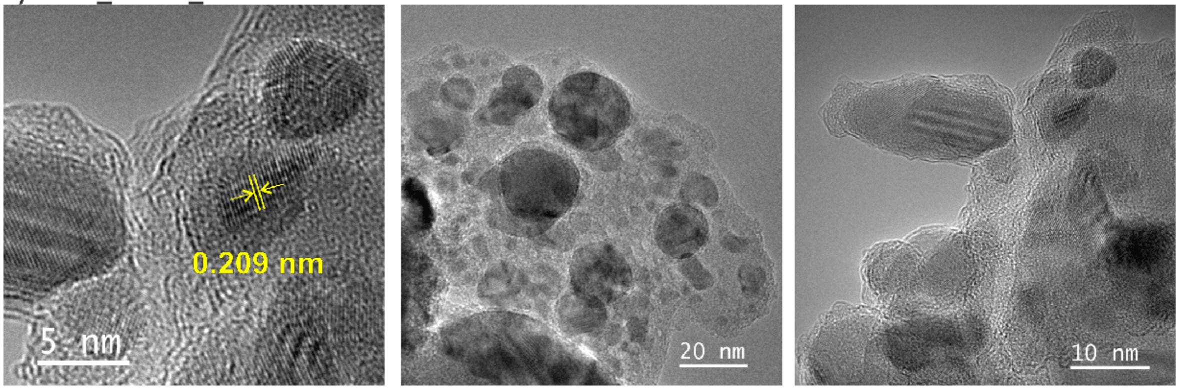

Figure 21: HRTEM images of a) NiAl_ox290_red450, b) NiCu(4:1)Al_ox290_red450, c) NiCu(1:1)Al_ox290_red450, and d) CuAl_ox290_red450 samples. Inset numbers (yellow) represent the observed lattice planes d-spacings.

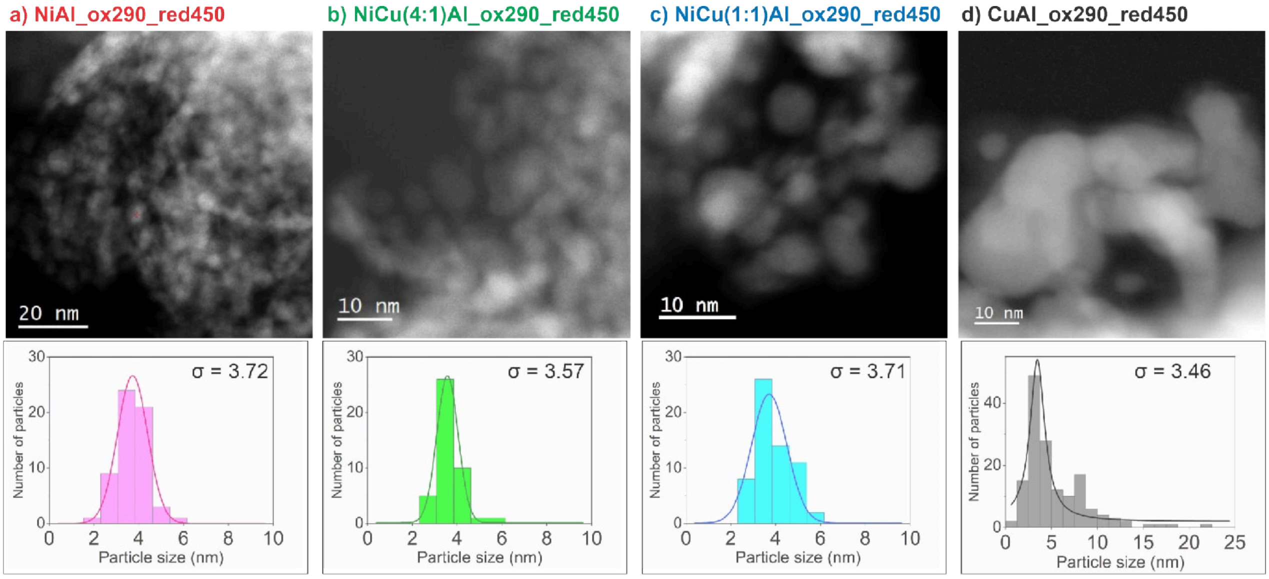

Figure 22: STEM-HAADF images and particle size distributions (inset) of the NiAl_ox290_red450, NiCu(4:1)Al_ox290_red450, NiCu(1:1)Al_ox290_red450 and CuAl_ox290_red450 samples.

3.6 NEXAFS - XPS

Near-edge X-ray absorption fine structure (NEXAFS) spectroscopy was used to investigate the oxidation state of nickel and copper of the reduced materials at 450 and 600 °C. The Cu L_3-edge and Ni $L_{3,2}$-edge of four samples with varying compositions (NiAl, NiCu(4:1)Al, NiCu(1:1)Al and CuAl) are presented in Figure 23a and b. The spectra were acquired operating in the Total Electron Yield (TEY), which probes roughly 20 nm depth. The samples were reduced ex situ at 1 bar and at different temperatures (450 and 600 °C) using 5% H_2 in Ar, as described in the experimental section 2.7.2. The samples were transported in an argon atmosphere to the vacuum chamber for XPS-NEXAFS characterization to prevent exposure to air. Although transported in air-free conditions, nearly all samples exhibited features of oxidic species under high vacuum and room temperature (HV RT). In the Cu L_3-edge, the pre-peak at around 931 eV is characteristic of CuO [139] (see curve CuO-reference and dotted curves *a*, *c*, *e* and *f* in Figure 23a). On the Ni L-edge (Figure 23b), the oxidic species are represented by the characteristic feature around 855.5 eV (NiO or $Ni(OH)_2$) [140]. Therefore, in situ re-reduction was performed under mild conditions for all samples; 0.5 mbar of H_2 at 250 °C was used to reverse the oxidation that probably occurred during the transport. After in situ re-reduction, the oxidic features (Ni and Cu-oxide) were less intense in all samples, except for the samples previously reduced at 450 °C (solid curves *g*, *h* and *i* in Figure 23b). However, the Ni L-edge peak at 853.5 eV lies in between the reference spectra of Ni and NiO, which suggests the presence of both the metallic and oxide species. The incomplete reduction aligns with the estimated degree of reduction through hydrogen consumption (see Table 3).

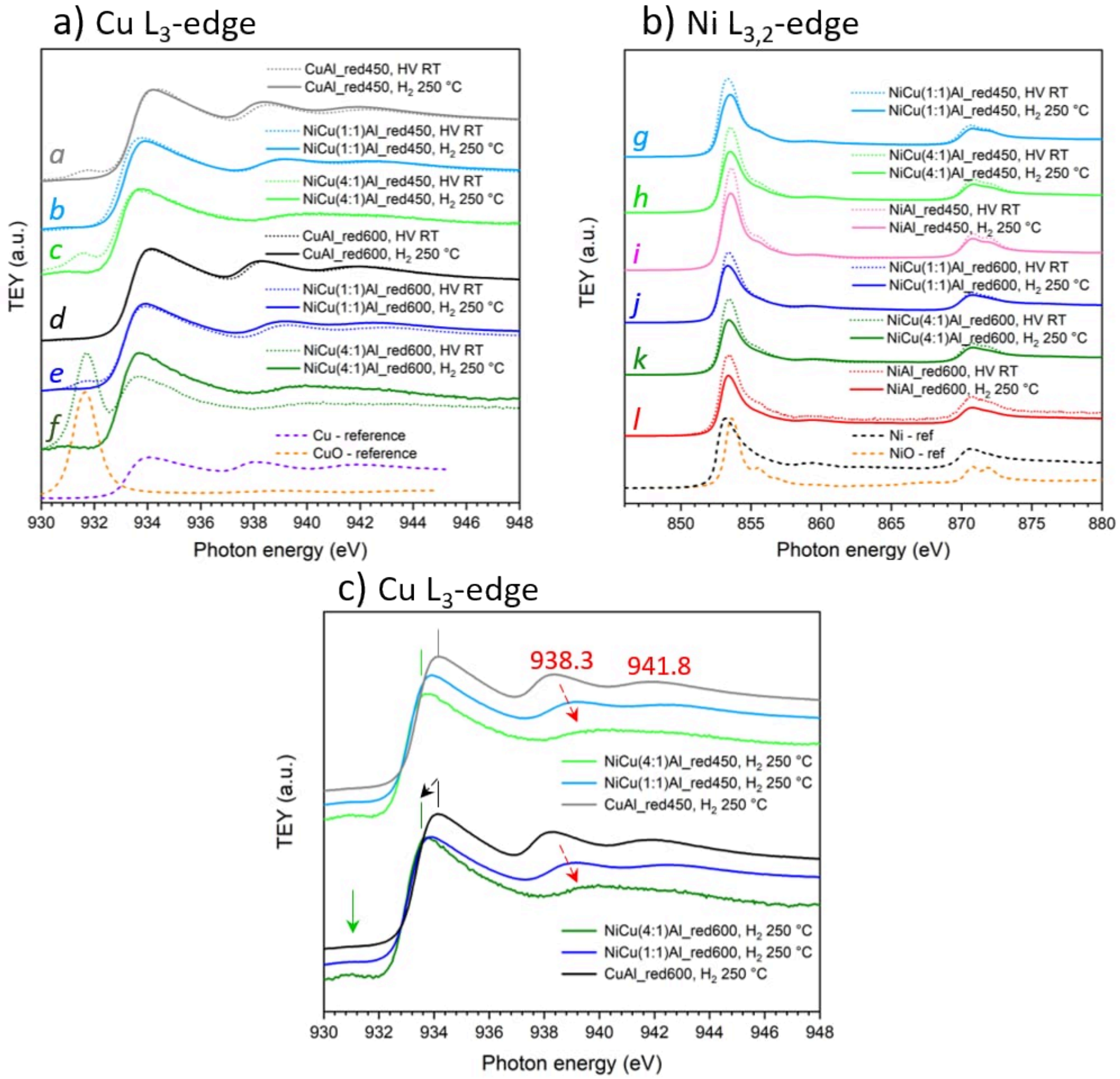

Figure 23: NEXAFS spectra of the reduced samples. a) Cu L_3-edge and b) Ni $L_{3,2}$-edge of the reduced samples (ex situ) at 600 °C and 450 °C. Spectra were acquired at high vacuum and room temperature (HV RT, dotted curves), and under 0.5 mbar of H_2 at 250 °C (solid curves). c) Cu L_3-edge of the samples under H_2, showing the effect of Ni content on the Cu electron structure.

The effect of Ni on the Cu L-edge is visible on the spectra of the re-reduced samples, after both reduction to 450 and 600 °C (Figure 23c). The pre-peak at 931.6 eV, which evidenced CuO, is not present anymore. However, the samples NiCu(4:1)Al (green and light green curves) show a small feature at around 931 eV, before the white line. This novel feature appears at a lower photon energy regarding the CuO peak, as it can also be seen in the Figure 23a (solid curves *c* and *f*). It should be noted that the presence of Cu_2O on the sample cannot be excluded from the NEXAFS measurement [141], [142]. More Ni content in the composition causes a shift in the main peak of Cu L-edge spectra from 934 eV (for CuAl) toward lower photon energies, as shown in Figure 23c (black arrow). Additionally, the features at 938.3 and 941.8 eV lose intensity and are shifted to higher photon energies as the Ni content increases (red arrow). These observations are similar for both sets of samples: reduced at 450 °C and at 600 °C. Comparable behavior has also been reported for bulk Ni-Cu metal alloys prepared by quenching the melt and using XPS and XANES to study the electronic structure [143]. In their study, similar to our results, there was no change in the Ni L-edge, but a shift mainly in the second and third features of the Cu L-edge was reported. This shift is related to charge redistribution at the atomic sites of Cu and Ni in the alloy. Furthermore, the author explained the difference between Ni and Cu features to either a higher resolution of the Cu L-edge (instrument and long core-hole lifetime) or to a unique feature of 3*d* metals with full (or almost filled) *d* bands.

The electronic structure of the reduced samples was also investigated by XPS with the analysis of the core level Ni and Cu $2p_{3/2}$ presented in Figure 24a and b (for the complete 2p levels see SI Figure 67). It is worth noting that the XPS spectra were acquired after the in situ re-reduction under mild conditions described above. Furthermore, a probing depth of around 10 Å was used. Both Cu 2p spectra after reduction at 450 and 600 °C, were characteristic of metallic species (Cu^0). The Cu $2p_{3/2}$ peak at a binding energy of 932.7 eV is typical for metallic Cu [144]; however, our BE position was 1 eV higher (933.7 eV). Similarly, the peak position of Ni $2p_{3/2}$ at 852.6 eV is related to the metallic Ni [145], and our experimental BE was found at 853.7. This ~ 1 eV shift could be caused by different variations in the electronic structure due to the support, or by a different manner for performing energy calibration: some use the C 1s peak, and others, like in this study, the Fermi edge of the valence band). Interestingly, a chemical shift, or shift in the BE, is observed for the bimetallic samples compared to those of the NiAl and CuAl. The Cu $2p_{3/2}$ position for CuAl was 933.7 eV for both reduced at 450 and 600 °C; while for the bimetallic NiCu(1:1)Al and NiCu(4:1)Al, the peak position is changed to 933.5 eV. This shift may indicate a redistribution of charge in the Cu electronic structure due to the presence of Ni. A similar shift to higher BE has already been reported in the literature [129], [146], but that shift was dependent on the composition. However, in our case, the Cu $2p_{3/2}$ position for both the bimetallic samples NiCu(1:1)Al and NiCu(4:1)Al were at the same BE. This could indicate that the surface might be similar for both samples and that it might not be dependent on the bulk Cu composition.

Regarding the Ni $2p_{3/2}$ (Figure 24b), a peak at 857 eV after reduction at 450 °C indicates the presence of some oxidic species. Its absence after reduction at 600 °C supports higher reduction at higher temperatures (Table 3). Moreover, there are only small changes in BE with varying Ni content. In almost all spectra, the position of Ni $2p_{3/2}$ was 853.7 eV; but it was shifted to 853.6 and 853.4 eV for NiCu(1:1)Al reduced at 450 and 600 °C, respectively. The slight shift to lower values is, in fact, opposite to that reported by Jha et al. [146]. They described a shift to higher BE of the Ni $2p_{3/2}$ peak from Ni supported on Fe_3O_4 alone to NiCu bimetal and assigned this effect to charge redistribution at the Ni and Cu atomic sites, indicating a strong interaction between Ni and Cu. However, they have a mixture of species (metallic and oxide) that are not straightforward to analyze in terms of chemical shift. In our case, almost no change may signify no redistribution of charge. However, theoretical simulation would be needed to clarify this.

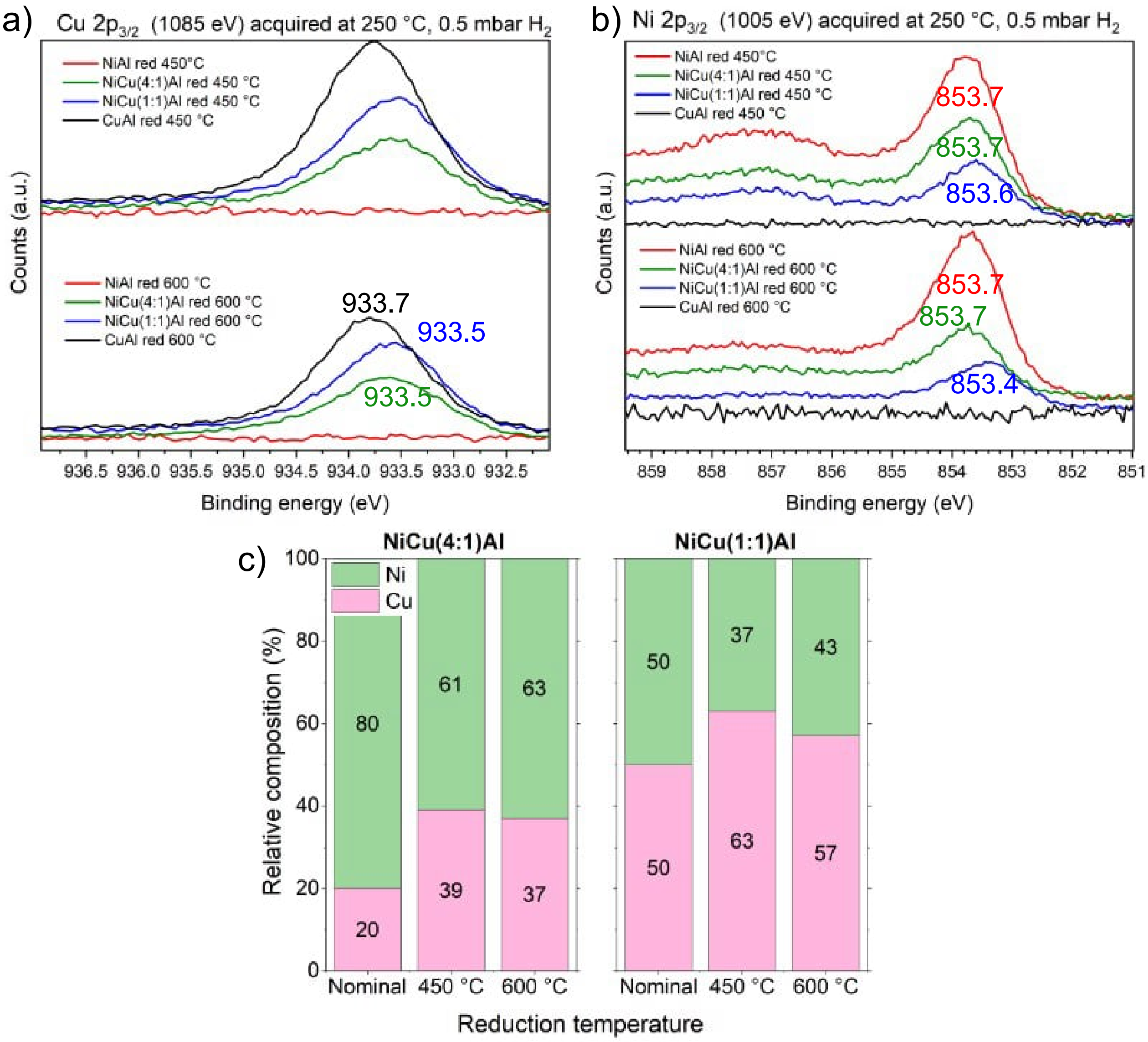

Figure 24: XPS spectra of a) Cu $2p_{3/2}$ and b) Ni $2p_{3/2}$, of the samples NiAl, NiCu(4:1)Al, NiCu(1:1)Al, and CuAl reduced at 450 °C (top) and 600 °C (bottom). Spectra acquired after re-reduction in the analysis chamber using 0.5 mbar H_2 and 250 °C. c) Relative Ni and Cu composition of the surface of the bimetallic samples (NiCu(4:1)Al and NiCu(1:1)Al) reduced at 450 and 600 °C.

Additionally, the relative quantification from the XPS spectra indicates the abundance of surface elements, in about 10 Å (few atomic layers). Quantification was performed by integration of the overall Cu and Ni 2p spectra (SI Figure 67) and the results are plotted in Figure 24c. The sample NiCu(4:1)Al, which should be theoretically 20% Cu, has 39% and 37% Cu at the surface after reduction at 450 and 600 °C, respectively. Furthermore, in the sample NiCu(1:1)Al (in which should be 50% Cu), 63% and 57% Cu content were observed for the reduction processes at 450 and 600 °C, respectively. These values indicate a systematic surface enrichment of Cu, which is a good agreement with other characterization techniques. This slight decrease in surface Cu composition when increasing temperature could indicate a possible rearrangement of the Ni-Cu metals in the nanoparticles. Moreover, there is probably no further segregation of Cu during the reduction from 450 to 600 °C.

3.7 CO adsorption

3.7.1 Microcalorimetry

The surface properties of the activated materials were studied by CO adsorption using microcalorimetry and diffuse reflectance infrared Fourier transform spectroscopy (DRIFTS). The whole amount of accessible metal sites (Cu and/or Ni) of the activated samples (after calcination 290 °C and reduction 450 °C) were calculated using microcalorimetry. Figure 25 shows the differential heat of CO adsorption on NiAl_ox290_red450, NiCu(4:1)Al_ox290_red450, NiCu(1:1)Al_ox290_red450, and CuAl_ox290_red450, as a function of the adsorbed CO molecules. All samples showed distinct heat profiles. At low coverage, the differential heat of the CuAl sample was 85 kJ·mol^{-1}, indicating the presence of Cu^0 sites on Al_2O_3. The reference differential heat for Cu^0 is 80 kJ·mol^{-1} [147]; and the slight difference can be caused by a different interaction of Cu with the alumina support due to different synthesis processes. The NiAl sample shows differential heats between 100-120 kJ·mol^{-1} that can be assigned to CO adsorption on Ni^0 sites [148], [149].

The heat profile for the bimetallic samples shows interesting dynamic behavior. At low coverage, the differential heat is approximately 80 kJ·mol^{-1}, and it increases to 100-110 kJ·mol^{-1} at higher CO coverage, reaching a plateau-like state. This indicates that CO interacts with Cu^0 species first because they are more accessible at the surface, compared to Ni^0 species. The differential heat of the NiAl sample is slightly higher (115 kJ·mol^{-1}) than the bimetallic samples at higher CO coverage (ca. 95 kJ·mol^{-1} for NiCu(1:1)Al and 110 kJ·mol^{-1} for NiCu(4:1)Al). These differences may be attributed to the presence of Cu interacting with Ni which reflects mixed heat. Therefore, the observed heat is an intermediate value that could correspond to the relative average between the heats of Cu^0 (85 kJ·mol^{-1}) and Ni^0 (115 kJ·mol^{-1}). Furthermore, at higher CO coverage, the plateau of the NiCu(4:1)Al sample is wider than that of the NiCu(1:1)Al sample. This indicates quantitively the amount of Ni in the material. In summary, based on the microcalorimetry analysis of heat of adsorption, it is evident that the Cu species are located on the surface of the bimetallic nanoparticles.

The metal surface areas were estimated assuming a stoichiometry CO:metal of 1:1. This parameter indicates the number of metal sites that might be (in theory) available for catalytic reactions. This metal surface area ($m^2_{metal}\cdot g^{-1}_{cat}$) varies in the order:
NiCu(4:1)Al (26.3) > NiAl (15.6) > NiCu(1:1)Al (5.1) > CuAl (2.6). Since the sample with the highest metal area was the NiCu(4:1)Al, we assumed that the presence of Cu not just promotes the reducibility of Ni (as described before), but also the total amount of metal surface sites available for catalysis.

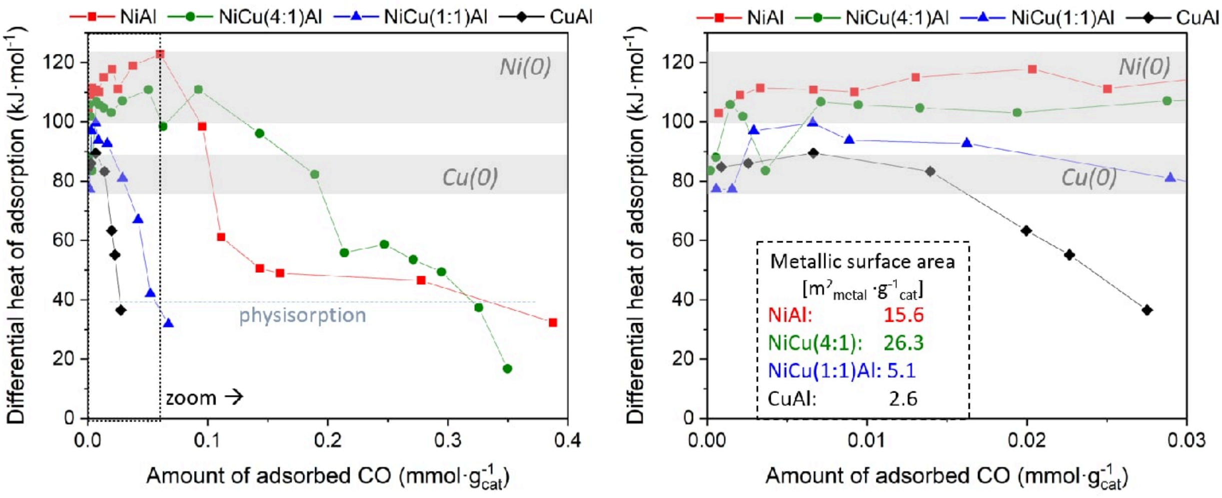

Figure 25: CO adsorption studied by microcalorimetry at 30 °C. Differential heats of adsorption as a function of the amount of adsorbed CO of NiAl_ox290_red450, NiCu(4:1)Al_ox290_red450, NiCu(1:1)Al_ox290_red450, and CuAl_ox290_red450.

Note: The grey bars mark the heat ranges of CO adsorption on different Ni and Cu sites. Inset shows the metal surface area obtained from the experiment.

3.7.2 Diffuse reflectance infrared Fourier transform spectroscopy (DRIFTS)

To further gather a structural description of the surface of the bimetallic sample, DRIFTS experiments were performed at the same temperature (30 °C). The materials NiCu, CuAl, and NiCu(4:1)Al were characterized after in situ activation. CO adsorption results in the formation of metal carbonyl complexes. Depending on the observed band in the spectra, it is possible to differentiate the sites of CO adsorption. These sites could be adsorbed linear (terminal to a single metal) or bridged to more than one metal site. In general, CO adsorption bands between 2075 and 2010 cm^{-1} can be assigned to linear CO on Ni^0 or Cu^0; mostly relating to (111) and (100) planes. Bands above 2100 cm^{-1} may indicate the CO adsorption on cationic species Cu^{2+}-CO and Ni^{2+}-CO. Bands below 2000 cm^{-1} are related to bridged adsorption sites [150]–[152]. Additionally, the band position may depend on the presence of the support [153] or another element like in the alloys [154].

Figure 26 shows the residual bands of DRIFT spectra for reduced NiAl (a) and NiCu(4:1)Al (b). The residual bands indicate that the spectrum before CO dosing was subtracted from the following spectra to observe the difference. The experiment involved dosing CO up to 9.4 mbar, followed by desorption to observe the stable species remaining on the surface of the catalysts. The focus was on the adsorption region between 2300-1600 cm^{-1}, where the stretching vibrations of intermediate CO adsorbed (CO$_{ads}$) species occur [155].

According to the DRIFT spectra observed in Figure 26a, when CO is adsorbed on the NiAl sample (Ni/Al$_2$O$_3$) at 0.05 mbar, two bands can be seen. One at 2016 cm^{-1} corresponds to linear coordinated CO$_{ads}$ on atop Ni^0, and the band at 1905 cm^{-1} appears due to CO$_{ads}$ on a bridge Ni^0 position. When increasing CO coverage to 4.3 mbar, the band of linear and bridge CO$_{ads}$ was shifted to higher wavenumbers, reaching 2066 and 1933 cm^{-1}, respectively. Further increase of the CO coverage, at 6.9 mbar, two new bands appear at 2188 and 1643 cm^{-1}. Signals above 2100 cm^{-1} represent the CO$_{ads}$ on cationic species such as Ni^{2+} species or non-reduced Ni cations which are present because of the incomplete reduction (just 75% after thermal treatment at 450 °C, Table 3). The band at 1643 cm^{-1} could represent the formation of carbonate species after CO interacts with alumina. We corroborated that by changes in the OH bands (3666 cm^{-1}) at 6.9 mbar (see inset in Figure 26a). It is reported that dosing CO on alumina (5 mbar) can lead to the formation of hydrogen carbonates [156]. The carbonates band (1643 cm^{-1}) disappears by evacuation, and the stable species were three: CO$_{ads}$ on linear and bridged Ni^0, and CO$_{ads}$ on Ni^{2+} cation.

The CO adsorption spectra of the bimetallic sample NiCu(4:1)Al, are shown in Figure 26b. In this case, the absence of bands > 2100 cm^{-1} denotes the absence of cationic Ni^{2+}, Cu^{2+} species. At room temperature, only metallic Ni and Cu species were observed. The results show that at low CO coverages, 0.021 mbar, the band at 1982 cm^{-1} appears and continues increasing until complete saturation of this band at 0.051 mbar. Subsequently, at 0.107 mbar CO, an adsorption band at 1998 cm^{-1} appears and continues broadening to 2016 cm^{-1} at 0.38 mbar. Furthermore, at higher CO coverage, an increase of the band at 2016 cm^{-1} is observed. After evacuation, only one band persisted at 1998 cm^{-1} (yellow star in Figure 26b), which could correspond to linearly adsorbed CO on top of Ni^0 and/or Cu^0 potentially interacting with the support.

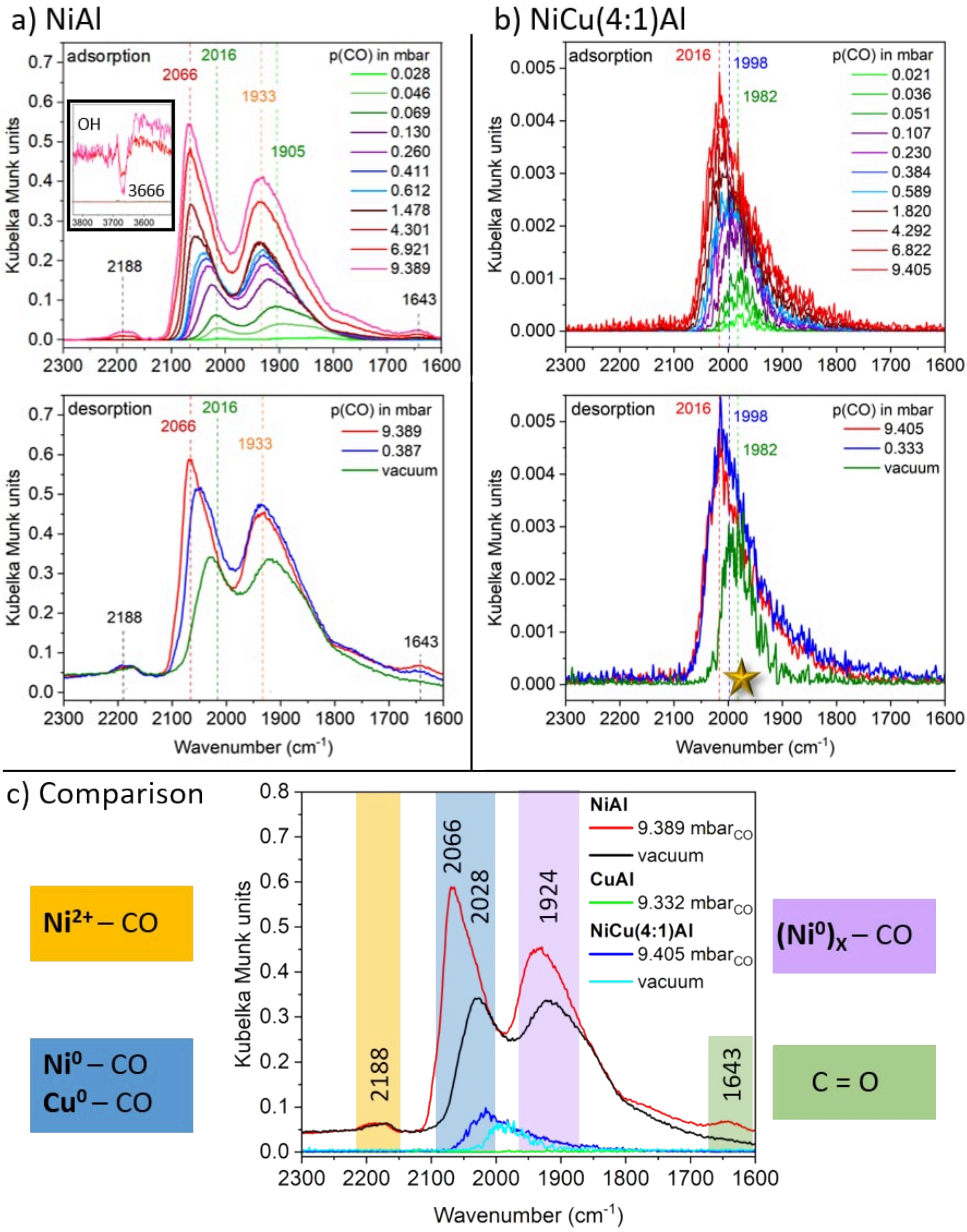

Figure 26: DRIFT spectra of a) NiAl, and b) NiCu(4:1)Al during adsorption (top) and desorption (bottom) of CO at 30 °C. c) Comparison of spectra of NiAl, CuAl and NiCu(4:1)Al after adsorption of CO at 9.4 mbar and subsequent evacuation.

Samples reduced in situ at 450 °C for 3 h with 50 mL·min^{-1} of 5% H_2 in Ar. Spectra recorded before CO dosing were used as background.

The proper structural description of the bimetallic samples requires a comparison with their monometallic references (NiAl and CuAl). Unfortunately, it was not CO adsorption observed for the CuAl sample (green curve in Figure 26c). However, it was found highly interesting the absence of bridged metallic species (1924 cm^{-1}) in the bimetallic sample, compared to the NiAl. This suggests that the presence of Cu in the Ni material inhibits the adsorption of CO on the metallic bridged sites.

From our microcalorimetry results, we observed at low CO coverages, the first adsorption may occur on Cu^0 species, due to heat of adsorption assigned to Cu (80 $kJ\cdot mol^{-1}$); and in a second step at higher CO coverage, the Ni^0 species (100 $kJ\cdot mol^{-1}$). Then, we suggest that the adsorption band (1982 - 1998 cm^{-1}) at low CO coverages may correspond to metallic Cu species; however, this is unusual for Cu systems. Studies of Cu-ZnO-Al catalysts reported a similar band at 1996 cm^{-1}; it was speculated to correspond to CO adsorbed in a bridged Cu-ZnOx interface position [157]. It is worth noting that this band was absent for NiCu alloys prepared from NiCuMgAl LDH compounds [158]. In that case, linear CO on Cu^0 was reported for monometallic and bimetallic samples at 2103 cm^{-1}, and 2096 cm^{-1}, respectively. However, their catalyst pretreatment was different: both calcination and reduction were performed at 800 °C, and Cu-surface enrichment was not observed. The probable cause is the utilization of high temperatures.

The results showed that after the first surface sites are covered, probably metallic Cu interacting with the support, at higher CO coverages (from 0.38 to 9 mbar) the second band is observed at 2016 cm^{-1}. This is due to CO adsorbed linear on Ni^0 species, as it was also observed for the CO adsorption on NiAl (Figure 26a). However, since both linear CO_{ads} species on Cu^0 and Ni^0 share the same wavelength ranges, it is unfortunately not possible to discriminate them clearly. Finally, we concluded that CO interacts with the bimetallic sample NiCu(4:1)Al, forming two distinct complexes. One complex, at low CO coverage, is likely to be linearly coordinated on Cu^0, but in close interaction with the support. The other complex, at high CO coverage, corresponds to linear interaction with metallic Ni^0 and/or Cu^0 species.

3.8 Metal-support interaction

To further understand the nature of the active species formed during reduction and their interaction with the support, a series of EELS experiments were performed. One of the remarkable advantages of using EELS is the high sensitivity and spatial resolution that could give information about the local electronic structure at the bulk and the surface/ interface of the nanoparticles. Figure 27 displays the spectra of the Ni $L_{2,3}$, Cu $L_{2,3}$, Al $L_{2,3}$, and O K edges of the reduced samples. For each sample, two spectra were extracted: the first from the region of the center of a nanoparticle and the second from the outside boundaries (i.e. the region close to the interface with the Al_2O_3 support). In addition to the spectra, the regions from where the spectra were extracted are shown in Figure 27 bottom, together with the corresponding values of the sample thickness in units of the inelastic mean free path (t/λ). The quality of the signal for the analysis of energy loss near edge structures (ELNES) depends on the thickness of the sample. The recommended values for the thickness in units of the inelastic mean free path length are between $0.0 \leq t/\lambda \leq 1.5$ [10].

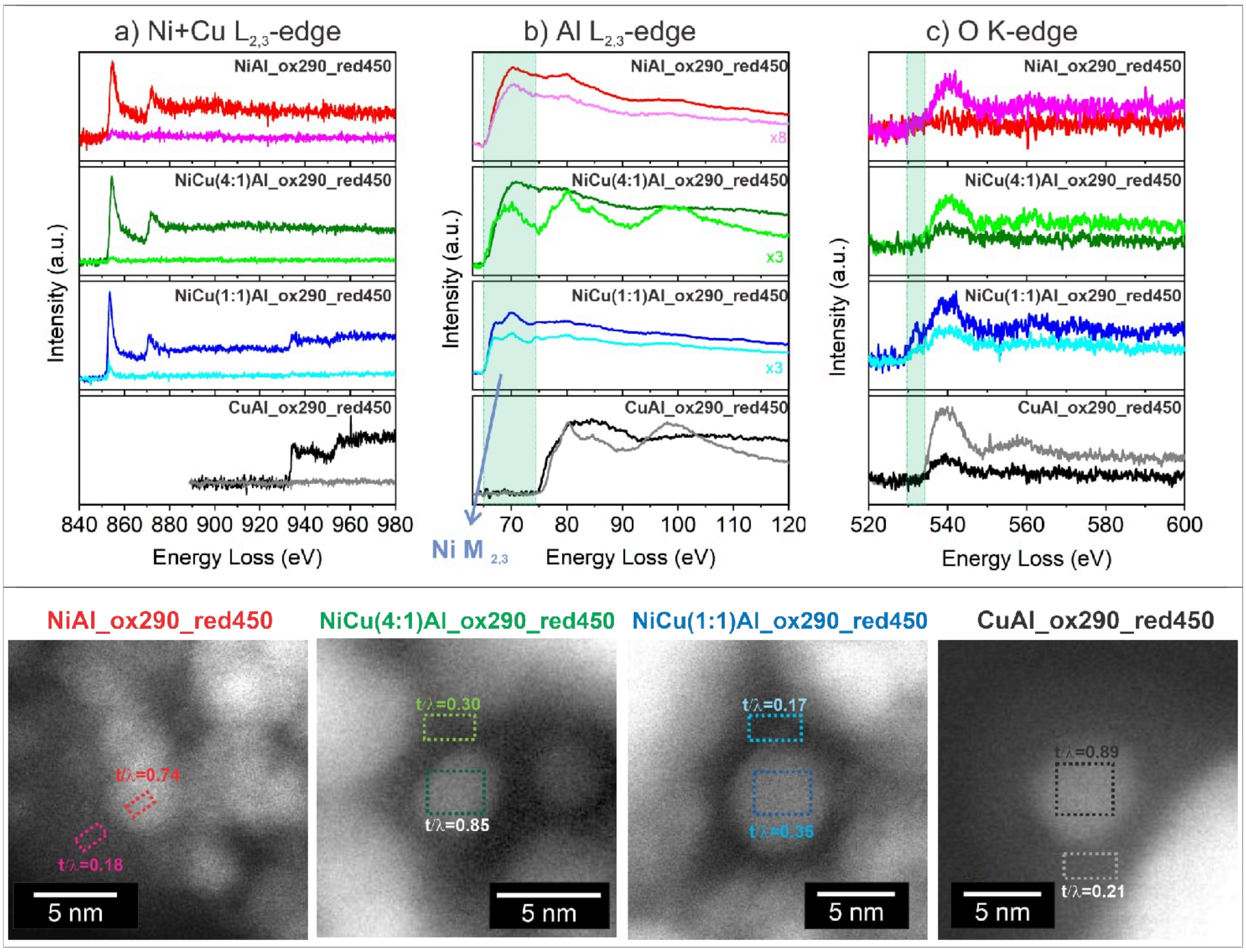

Figure 27: EEL spectra: a) Ni and Cu $L_{2,3}$ edge; b) Al $L_{2,3}$ edge, c) O K-edge, of the reduced samples: NiAl_ox290_red450, NiCu(4:1)Al_ox290_red450, NiCu(1:1)Al_ox290_red450, and CuAl_ox290_red450.

The EEL spectra were extracted from two different regions of each sample, as shown at the bottom: center of a nanoparticle (dark colors: red, green, blue, and black) and support (light colors: pink, light green, light blue, and gray).

Identification of different Ni species is performed by comparing features such as the L_3/L_2 intensity ratio, the energy splitting, and the overall shape (SI Figure 66) [124], [125], [159]. However, the low signal-to-noise ratio of the Ni $L_{2,3}$ edge spectra impedes a proper analysis of the Ni species, and therefore a mere estimation of the present species is given here-after. For the NiAl_ox290_red450 sample, the Ni $L_{2,3}$ edge signal indicates the presence of metallic Ni; for both, NiCu(4:1)Al_ox290_red450 and NiCu(1:1)Al_ox290_red450 samples, a combination of NiO and metallic Ni is observed, probably with a higher contribution of metallic Ni species. The Cu $L_{2,3}$ edge shows a slightly oxidized Cu for the NiCu(1:1)Al_ox290_red450 sample; the white lines do not follow the shape of CuO (Figure 66) and are too low in intensity to be pure Cu_2O but too high to be pure metallic Cu [159]. For CuAl_ox290_red450, the spectrum shows a much higher contribution of metallic Cu. Since the NiAl_ox290_red450 sample has shown different findings from EELS and XRD results, it is relevant to point out that the two techniques may lead to different results because the information is gathered on different scales (local on single nanoparticles vs. averaged over many particles).

The metal-support interaction can be studied by analyzing and comparing the ELNES recorded on the nanoparticles and outside the particles. In the case of CuAl_ox290_red450, the Cu $L_{2,3}$-edges are absent outside the particles. However, for Ni-containing samples, a small contribution of the Ni $L_{2,3}$-edge (mainly the L_3 peak is visible) was observed from between the nanoparticles. Furthermore, the Ni $M_{2,3}$-edge is present at an energy loss value of 68 eV, just in front of the Al $L_{2,3}$ edge (onset at 73 eV) as illustrated in Figure 27b. This makes analysis of the Al $L_{2,3}$-edge fine structure difficult. However, as can be seen from the spectra acquired outside the CuAl_ox290_red450 and NiCu(1:1)Al_ox290_red450 particles, the fine structure of the Al $L_{2,3}$-edge corresponds to the one of γ-Al_2O_3 [160]. It is worth noting that the Ni $M_{2,3}$ + Al $L_{2,3}$ edge of the Ni-containing nanoparticles and their surrounding regions show the same onset at 65 eV. These similarities could be interpreted as an interaction between Ni and the support. The effect of inelastic scattering delocalization and thus contributions of the nanoparticle's atoms when measuring outside the particle could be ruled out. According to Egerton [161], for energy losses of ca. 70 eV the delocalization effects extend ca. 0.7 nm, which might give rise to some contributions in the acquired Ni $M_{2,3}$-edge. However, for energy losses of ca. 850 eV (Ni $L_{2,3}$-edge), the delocalization effect is in the subatomic regime. As both edges can be acquired several nm outside the particles, it is assumed that they originate from the same scatterer, thus ruling out delocalization effects.

For the NiAl_ox290_red450 sample, it can be concluded that the analyzed particle was indeed in a reduced state because of the absence of the oxygen signal (Figure 27c, red spectrum). In contrast to this, outside the particle, an O K-edge signal was detected (pink spectrum), corresponding to the oxygen from the Al_2O_3 support. For the sample NiCu(1:1)Al_ox290_red450, the Ni $M_{2,3}$ edge is characteristic of oxidized species, as reported in the literature [162]. The pre-peak at 532 eV of the O K-edge (blue spectrum) is a characteristic feature of the oxygen bonding in transition metals [163].

Regarding the CuAl_ox290_red450 sample, the Al $L_{2,3}$ and O K edges acquired in the surrounding of the particle (gray spectra) show the characteristic fine structure of the support Al_2O_3 [164]. However, for spectra acquired from the nanoparticle, a different shape is observed. In the Al $L_{2,3}$ edge region, this could be due to the presence of the Cu $M_{2,3}$ edge (74 eV), while the oxygen signal could originate from the support where the particle is located or overlap with oxygen species of possible Cu_2O species. The previous correlation between the signals observed from the particle and the surroundings shows clear evidence of the metal-support interaction for the Ni-containing samples. High stability and metal-support interaction have also been reported for Ni-Mg-Al LDH-derived materials [165].

3.9 Conclusions

A series of bimetallic and monometallic $NiCu/Al_2O_3$ (NiCuAl) materials with different Ni:Cu molar ratios of 1:0, 4:1, 1:1, and 0:1 were successfully synthesized using a layered double hydroxide (LDH) approach and their topotactic transformation to produce highly dispersed nanoparticles was studied. The properties of the LDH precursors (NiAl, NiCu(4:1)Al, NiCu(1:1)Al and CuAl) and their derived materials (calcined and active) were investigated in detail. It was shown that the calcination temperature influences the reduction profiles: when Ni-containing samples were calcined under mild conditions, the reduction profile was shifted to lower temperatures. Lower reduction temperatures were also enough to reduce the Ni^{2+}. This effect is presumably due to the absence of Ni-spinel species when mild conditions are used. Using different reduction temperatures, it was possible to tune the particle size distribution from 3 nm (300 °C), 3.5 nm (450 °C), to 13 nm (900 °C) in the NiCu(4:1)Al sample.

Cu changes the structural and electronic properties of the final Ni-based catalyst. The addition of Cu in small amounts improves the reducibility of Ni oxide species. The activated Ni-Cu bimetallic catalysts formed mainly a solid solution or an alloy, which was evidenced by different characterization techniques. However, slight Cu surface segregation did occur, as observed by the deviation of the Vegard law in the XRD results, combined with several characterization techniques (microcalorimetry, STEM, and XPS). DRIFTS experiments showed CO adsorption on linear and bridged Ni sites for NiAl sample, but the bridged sites were hindered by Cu in the bimetallic sample. The LDH precursor showed platelet-like morphology in different orientations revealed by TEM tilt series. For activated samples (reduced at $T < 450$ °C) the platelets are nicely decorated with small (approx. 3.5 nm) nanoalloys which probably grow in the [111] orientation with respect to the platelets. Furthermore, a detailed local electronic structure investigation (by EELS, including M-edges, which is barely reported in the literature) unravels the metal-support interaction present for the Ni-containing catalyst. In the bimetallic samples, Cu was found to be atomically dispersed in the NiCu(4:1)Al sample due to the absence of the Cu L-edge signal in EELS, but its presence in EDX spectroscopy.

4 Catalytic properties of LDH-derived materials on chemical energy conversion

This chapter discusses the catalytic evaluation of the series of LDH-derived materials on energy conversion reactions: ammonia decomposition and CO_2 hydrogenation. Both are relevant reactions for dehydrogenation and hydrogenation, respectively. The catalysis of the bimetallic NiCu catalyst with two different ratios, 4:1 and 1:1, is compared to the monometallic materials. The results are related to the properties of the samples discussed in the previous chapter and supplemented with the characterization of the spent catalysts to outline possible reaction mechanisms. Furthermore, the CO_2 hydrogenation experiments are also complemented with temperature-programmed desorption of CO_2.

4.1 Catalytic evaluation on hydrogenation of carbon dioxide

Four activated catalysts of varying compositions were tested in CO_2 hydrogenation. The aim was to produce CO through the RWGS reaction. CO is a vital aspect of syngas and can be used to produce light alcohols such as methanol. All materials were pretreated under the same conditions: calcination at 290 °C for 3 h, followed by reduction at 450 °C under 5% H_2 for 3 h. Activated materials are called as NiAl, NiCu(4:1)Al, NiCu(1:1)Al and CuAl. The activity was measured by heating and cooling steps at 500, 550 and 600 °C. The CO_2 conversion, selectivities and productivities of CO and CH_4 are presented in Figure 28. The solid lines in Figure 28a represent the equilibrium conversions assuming RWGS reaction (brown) and RWGS combined with Sabatier methanation reactions (light green). The conversions obtained from all Ni-containing samples were in between both equilibrium lines. Since activities are close to the equilibrium conditions, we focus the analysis to assess the material stability by comparing activity during the heating and cooling steps at 500 °C.

The NiAl catalyst was proved to be highly stable. After being cooled at 500 °C, their initial CO_2 conversion was regained to almost 30%. This material produced less CO due to competitive CH_4 formation. Ni-based catalysts are known for their methanation activity [79]; standalone NiAl catalyst favors the formation of CH_4 (methanation) at lower reaction temperatures, while CO selectivity is favored with increased reaction temperature (endothermic reaction).

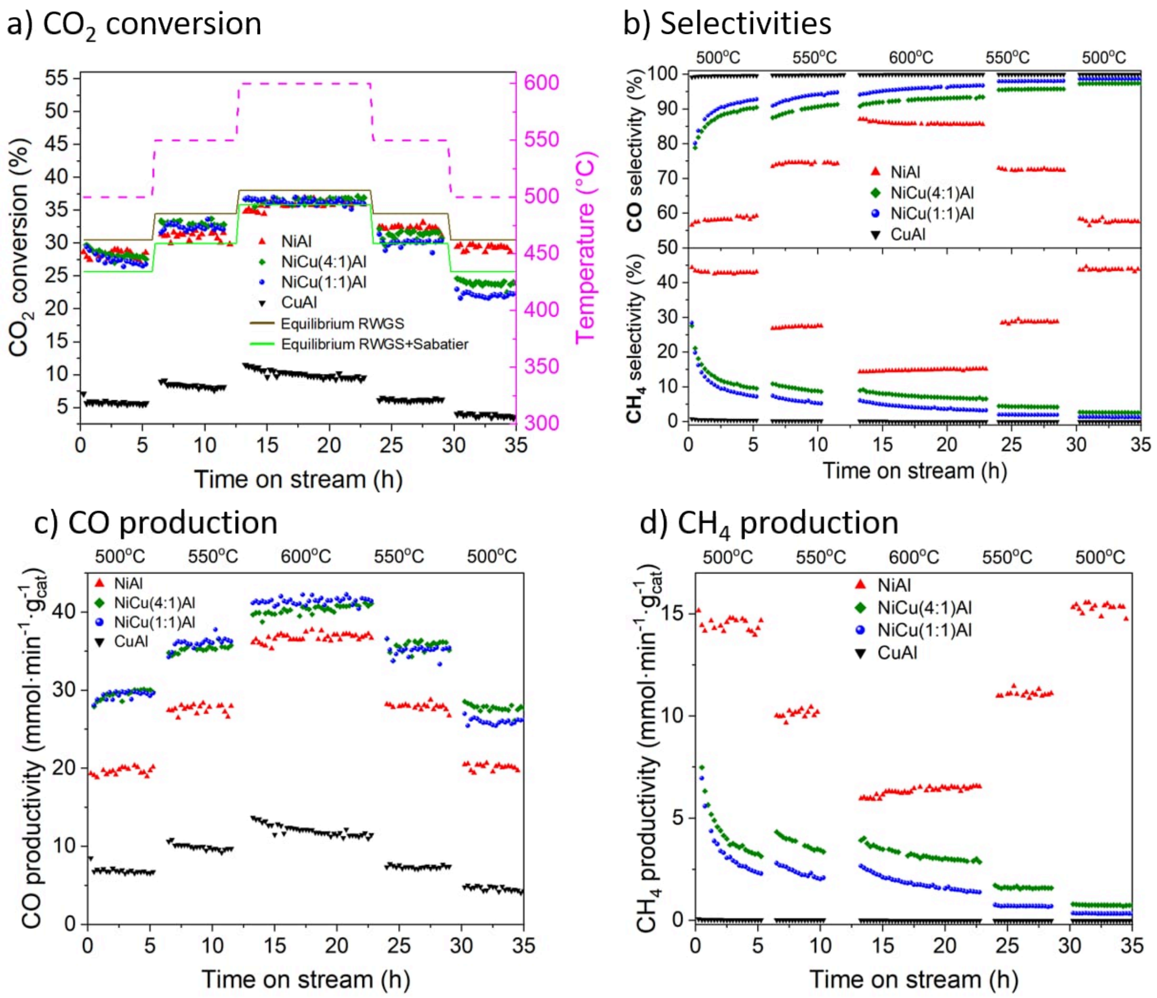

Figure 28: a) CO_2 conversion, b) selectivities, and productivities of c) CO, and d) CH_4 of NiAl, NiCu(4:1)Al, NiCu(1:1)Al, and CuAl; (Gas flow: 100 $mL\cdot min^{-1}$ of CO_2:H_2:He with a 1:1:0.5 ratio; mass of catalysts: 15 mg in 85 mg SiO_2 as diluent; WHSV: 400,000 $mL\cdot g^{-1}\cdot h^{-1}$).

CO_2 consumption is shown in SI Figure 68.

In contrast, the CuAl catalyst exhibited full CO production (100% selectivity, Figure 28b), but its CO_2 conversion was significantly low under the reaction conditions applied. The deactivation of the CuAl catalyst was observed with the conversion decay during the time of stream (TOS) at 600 °C (from 11.8 to 9.2%). Furthermore, deactivation was evident when comparing the performance at the same reaction temperatures during the heating and cooling steps. At 500 °C, a drop from 6 to 3.6% was observed. This deactivation of the CuAl catalyst may be due to the coalescence and sintering of Cu nanoparticles at high reaction temperatures.

The combination of Ni and Cu improves the CO productivity (Figure 28c); both NiCu bimetallic samples (NiCu(4:1)Al and NiCu(1:1)Al) showed higher CO productivity compared to the CuAl and NiAl samples. This is also observed for the material with Ni/Cu ratio of 3 prepared by impregnation [76]. Although both NiCu bimetallic catalysts formed significant amounts of CH_4 (approx. 10% CH_4 selectivity) at 500 °C in the heating period, during the cooling phase, the catalysts did not regain their CH_4 selectivity at 500 °C in contrast to the Ni catalyst. This can be attributed to the possible structural change of the catalyst at high reaction temperatures, leading to the promotion of Ni by Cu. Both NiCu(4:1)Al and NiCu(1:1)Al catalysts exhibited very high CO production, (selectivity above 95%) at the end of time on stream. Overall NiCu(4:1)Al catalyst was more stable for CO production than NiCu(1:1)Al during CO_2 hydrogenation conditions.

Furthermore, bimetallic samples exhibit a shift in selectivity during TOS. The CO selectivity increases by almost 3% at 600 °C, while methanation decreases in a similar amount. This indicates changes during the reaction: the catalysts are restructuring. From the analysis after activation of the NiCu bimetallic catalysts at 450 °C, we observed a slight enrichment of Cu on the surface (previous chapter). It is likely, as it will be described below, that the nanoparticles may be rearranged atomically, with a greater amount of Cu on the surface, leading to decreased methane selectivity and increased CO selectivity.

4.1.1 CO_2 - TPD

TPD of adsorbed CO_2 is a valuable method for understanding the CO_2-catalyst surface interactions. It probes the basicity of the reduced materials. This basicity is characterized by active centers of different strengths that can adsorb CO_2 in different amounts. Figure 29 shows the CO_2-TPD profiles for all four materials (NiAl, NiCu(4:1)Al, NiCu(1:1)Al, and CuAl) after in situ reduction. In the part b, the TPD curves were normalized by the total surface area estimated from BET after calcination process (Table 2). This normalization supposes that the *active centers* rely on the available surface area (in fact, “active centers” is a complex term that involves many different parameters). The desorption peaks are distributed from 100 to 450 °C. The TPD profile has three overlapping peaks showing weak (60 - 200 °C), medium (200 - 320 °C), and strong (320 - 450 °C) basicity, which is consistent with other studies on LDH-derived materials [78]. The presence of medium and strong basic sites could be related to bidentate and monodentate adsorbed carbonates, respectively; while the weak basic sites could correspond to Bronsted basic centers such as hydroxyl groups (where hydrogen carbonate is formed). CO_2 activation is favored on both weak and medium basic sites [166], [167].

Although we do not report quantitatively a number of basic sites, we can describe relative differences among the samples since curves (in Figure 29a) were normalized according to the material's mass used in each experiment. Samples CuAl and NiAl showed the highest and second-highest CO_2 adsorption capacity, respectively. NiAl had a relative total basicity (area under the curve) that was 75% of CuAl. Interestingly, the combination of Ni and Cu resulted in a decrease in total CO_2 adsorption capacity. This capacity for NiCu(4:1)Al and NiCu(1:1)Al were estimated to be only 2% and 0.7% of the CuAl, respectively. Furthermore, the strength of the basic sites also changed depending on the metal composition. The CO_2 species adsorbed on the CuAl sample are spread out in weak, medium, and strong. In particular, this material possesses the strongest sites, compared to the Ni-containing samples. On the other hand, the NiAl sample is characterized by a broader contribution of weak sites combined with medium basic species.

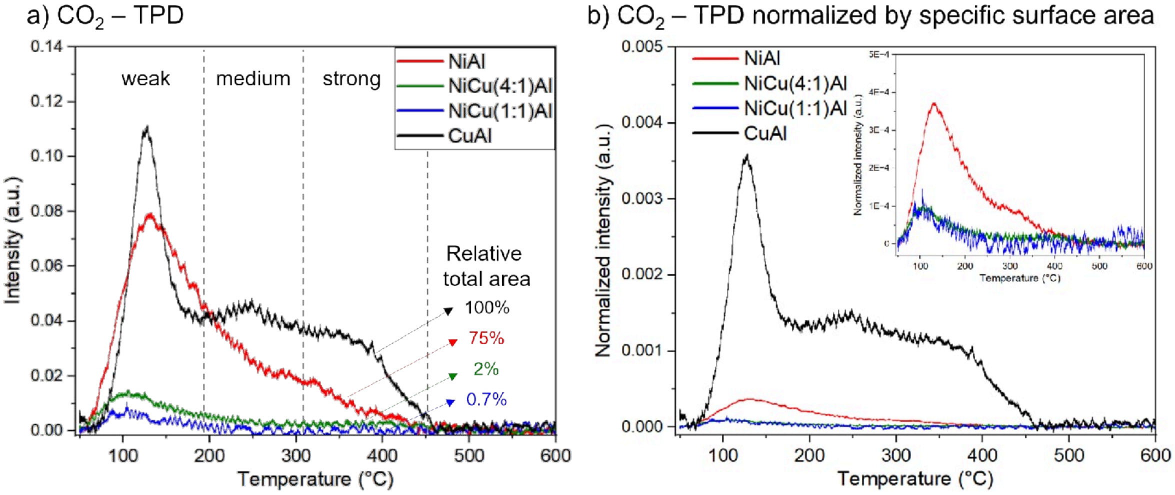

Figure 29: CO_2-TPD profiles of NiAl, NiCu(1:1)Al, NiCu(4:1)Al, and CuAl samples after in situ reduction at 450 °C for 3 h with 5% H_2. Catalyst mass (in mixed metal oxides): 10 mg, heating rate: 10 °C·min^{-1}, desorption range from 50 to 600 °C.

The basicity of both bimetallic samples revealed a lower total basicity, in comparison with the monometallic ones. Moreover, these sites are characterized just by weak basic sites. Assuming that the active species are dependent on the surface area, after normalization of the TPD curves, both bimetallic samples followed the same profile (inset Figure 29b). This indicates that both bimetallic samples exhibit similar surface sites for CO_2 adsorption. Considering the catalytic results (specifically the CO production), we can suggest that these weak basic sites in the bimetallic samples cause CO_2 conversion to CO. However, the real nature of these weak basic sites is uncertain, as the monometallic samples had more of these sites but produced less CO.

The reaction mechanism for CO_2 hydrogenation is still controversial. The formation of CO via RWGS reaction can occur via two main routes [66], [67]. In the first one (direct dissociation), CO-O dissociates directly on a metal site, which causes oxidation of the site after the CO molecule is desorbed. Later, the metal is re-reduced by hydrogen from the feed. The other possible mechanism is the associative route or hydrogen-mediated. In this case, CO_2 adsorption depends highly on the metal-support interface. It is adsorbed and assisted by hydrogen to form formate (HCOO*) species. Further hydrogenation of formate produces CO and H_2O. Finally, once the CO is formed (as adsorbed species) it can be directly hydrogenated, dissociated, or desorbed. There is evidence of both mechanisms occurring for nickel [67] and copper [73], [168].

In light of the physicochemical properties of the reduced materials, some correlations with their catalytic properties can be drawn. Monometallic Cu sample (Cu/Al_2O_3) exhibited a low surface area BET of 31 $m^2 \cdot g^{-1}$ (from N_2 adsorption-desorption experiments) and low accessible metallic surface area (2.6 $m^2{}_{Cu} \cdot g^{-1}$ from microcalorimetry). Despite the highest CO_2 adsorption capacity observed for this material (from CO_2-TPD), the catalytic conversion was the lowest one among the investigated samples. However, complete selectivity to CO was evidenced. This implies that not necessarily high CO_2 adsorption corresponds to high conversion, but the presence of the appropriate active centers (or combination of active centers) is important to convert CO_2 into CO. The hydrogenation of CO_2 on metallic Cu suggests the formation of hydroxycarboxyl (COOH*) which is kinetically more favorable than formate species [169]. The hydroxycarboxyl species are then converted to HCO* (formyl) species, which are unstable and may dissociate to CO [170].

As described above, NiAl sample produced both CH_4 and CO. There is spectroscopic evidence of both mechanisms (direct route and formate-mediated) occurring. According to Vogt *et al.*, the dominant pathway depends on the Ni particle size. For clusters and atomically dispersed nickel, the formate route is the dominant one. With larger Ni particles (6 nm±1.9), direct dissociation became the dominant [67]. From our experiments, the Ni-containing activated samples had similar nanoparticle sizes of approximately 3.7 nm; therefore, a combination of different mechanisms is possible.

The metal-support interface could play a major role in the formation of (bidentate) carbonates which are hydrogenated to formate species. By TPD experiment, we can estimate the presence of these carbonates because of their medium-strength basicity. Our results show that the presence of medium basic sites for NiAl sample (which also exhibited weak basic sites) was completely inhibited with the addition of Cu. The blockage of these sites probably caused the suppression of methanation and the improvement of CO production.

On the other hand, from DRIFTS results we observed that CO absorbs on bridged and linear (atop) metal Ni positions of the reduced NiAl sample. Interestingly, the addition of Cu in the NiCu(4:1)Al sample inhibits the CO adsorption on the bridged positions. Possibly the bridged sites are responsible for methane formation that was suppressed in the bimetallic catalyst.

It is worth noting that the surface area of the metallic species accessible at the surface (estimated from microcalorimetry) did not correlate with the catalytic results. This area decreases in the order NiCu(4:1)Al ($26.3\ \mathrm{m^2}_{\mathrm{Cu+Ni}}\cdot\mathrm{g^{-1}}$) > NiAl ($15.6\ \mathrm{m^2}_{\mathrm{Cu+Ni}}\cdot\mathrm{g^{-1}}$) > NiCu(1:1)Al ($5.1\ \mathrm{m^2}_{\mathrm{Cu+Ni}}\cdot\mathrm{g^{-1}}$) > Cu ($2.6\ \mathrm{m^2}_{\mathrm{Cu}}\cdot\mathrm{g^{-1}}$). This mismatch could prove the complexity of the definition of an *active site*.

4.1.2 Spent catalysts characterization

The key factor in deducing and understanding the properties of the catalysts during the reaction is by the analysis of the spent samples, when in situ or operando experiments are not feasible, and their comparison with the activated samples before the reaction. For the properties of the reduced samples see section 3.5. The spent samples were removed from the reactor under air-contact because completely inert transfer was not feasible. They were stored in a glovebox under inert atmosphere and briefly in contact with air prior further characterization. TEM grids were prepared inside the glovebox, but mounted under air atmosphere in a double tilt-holder. Electron micrographs and their elemental mapping of the four spent catalysts after the CO_2 hydrogenation reaction with their corresponding particle size distribution are shown in Figure 30. The spent NiAl and spent NiCu(4:1)Al samples reveal a unimodal distribution of particle sizes below 15 nm (insets Figure 30a-b). On the contrary, when the catalyst has a Cu-rich content (spent NiCu(1:1)Al and spent CuAl), considerable segregation of Cu is observed (Figure 30c-b): Cu particles reach sizes of 100 nm and 500 nm, respectively. A closer look at the elemental mapping of the sample spent NiCu(4:1)Al reveals the segregation of Cu species to the surface of the nanoparticles, as it is visible in the color-mixed map (Figure 30b) and the line intensity profile in SI Figure 69b. The lower surface energy of Cu, compared to Ni, usually leads to Cu segregation from the bulk of nanoparticles to the surface [41], [129].

a) spent NiAl

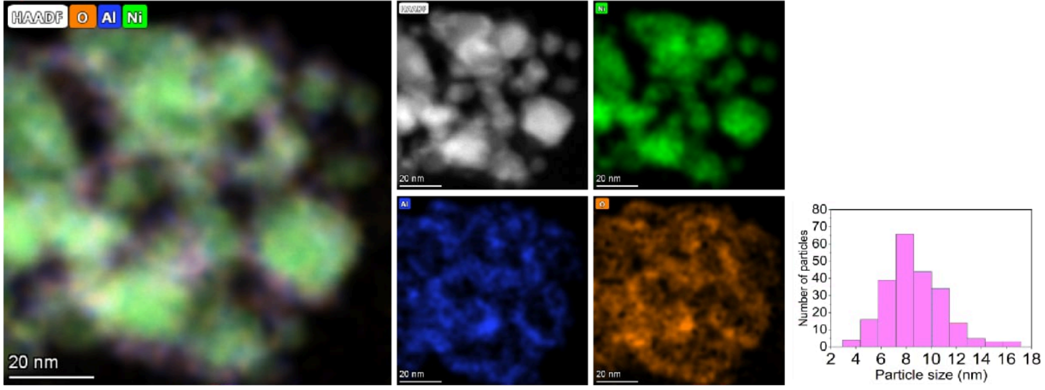

b) spent NiCu(4:1)Al

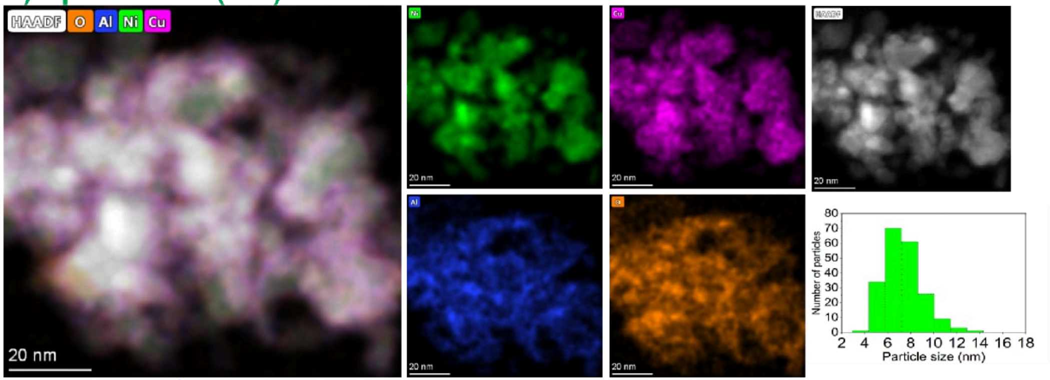

c) spent NiCu(1:1)Al

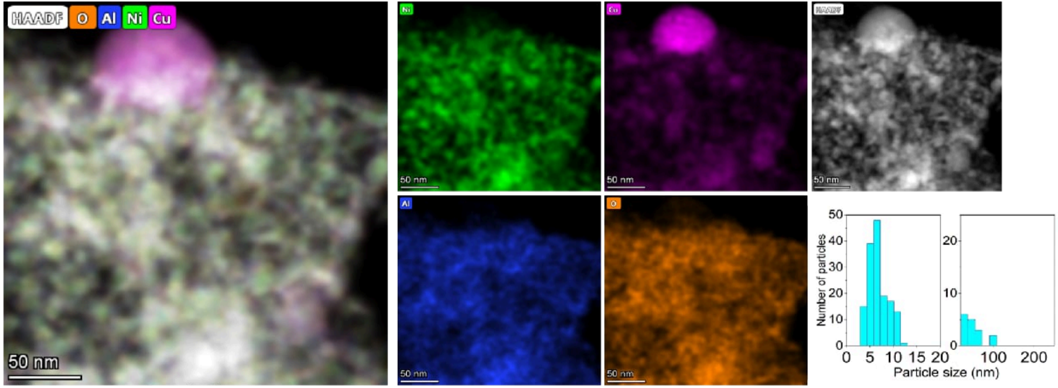

d) spent CuAl

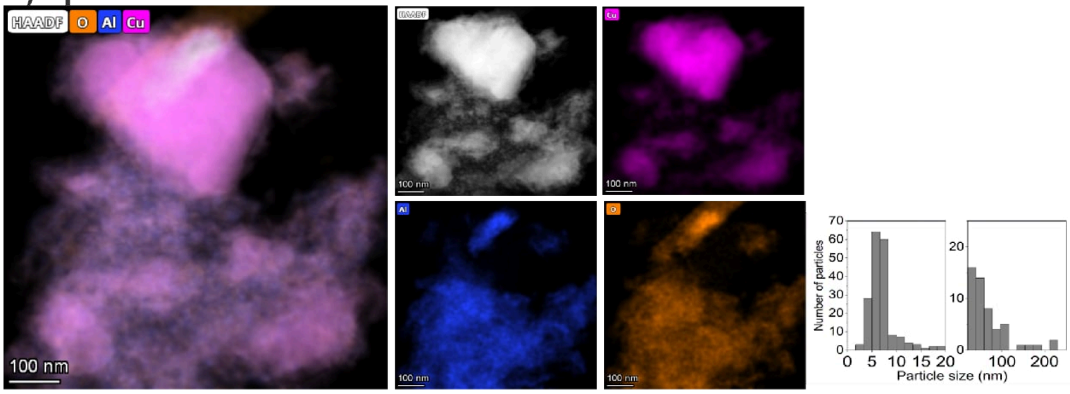

Figure 30: STEM-EDX images and particle size distributions of a) spent NiAl; b) spent NiCu(4:1)Al; c) spent NiCu(1:1)Al; and d) spent CuAl samples. (Black/white: HAADF; green: nickel; magenta: copper; blue: aluminum; and orange: oxygen)

The low catalytic stability of the CuAl and NiCu(1:1)Al samples could be attributed to the sintering of Cu species. In contrast, NiAl and NiCu(4:1)Al catalysts showed greater stability probably due to 'strong' metal-support interaction (SMSI), which prevents sintering [171]. Evidence of a possible SMSI is observed in the HRTEM images of the spent catalysts shown in Figure 31 (the uncolored version is shown in SI Figure 70). Two catalysts, NiAl and NiCu(4:1)Al, had better stability during testing and formed a protective overlayer around the nanoparticles. The overlayer was absent on the reduced materials (see previous chapter, Figure 21); therefore, it was possibly formed at high reaction temperatures, by the interaction of the Ni surface sites with Al and O from the support. In addition, a more in-depth investigation of STEM-EDX could reveal Al on the particles' surface, which might be connected to aluminate formation (line scans in SI Figure 69a, b and c).

While the aluminate-spinel species ($NiAl_2O_4$) may not be highly active towards CO_2 activation, its formation reinforces the metal-support interaction within the catalyst [172] and may stabilize the nanoparticles, preventing their sintering. This agrees with the catalytic results, where NiAl and NiCu(4:1)Al samples showed superior stability compared to NiCu(1:1)Al and CuAl. The mentioned overlayer is partially present in the spent NiCu(1:1)Al, where a 0.234 nm lattice distance is observed on half of the nanoparticle's surface (Figure 31c). The lattice distance might correspond to a contracted $NiAl_2O_4$ (311) = 0.242 nm, or to an expanded Al_2O_3 (222) = 0.231 nm [173]. Moreover, the Cu-segregated particles from the spent NiCu(1:1)Al sample present a high crystalline phase, as is visible in the HRTEM image. The correspondent fast Fourier transform (FFT) with reflections of 0.184 and 0.127 nm, correspond to the (021) and (-222) lattice planes of CuO species. It is uncertain whether these CuO species were formed in situ during the reaction or during the sample transfer (short contact with air). Furthermore, the spent CuAl material (Figure 31d) showed also small Cu nanoparticles with FFT reflections of 0.210 and 0.127 nm, which can be referred to Cu(111) (0.209 nm) and Cu(220) (0.128 nm), respectively. The considerable sintering of the Cu particles might be the reason for the deactivation observed by the CO yields over time on stream.

Among the tested samples, the catalysts NiCu(4:1)Al showed the best balance between CO selectivity, CO_2 conversion, and stability. Although no significant sintering was evidenced, migration of Cu species to the nanoparticle surface was observed. Complementing this, previous studies showed that a combination of Ni Cu with a ratio of 3-to-1, obtained from incipient wetness impregnation of the alumina support, was stable and active for RWGS [76]. Even though Ni-Cu alloying was claimed to be the reason for the stability.

XPS of the bimetallic samples was conducted to confirm the formation of aluminate after catalysis. The spent NiAl and CuAl were not analyzed because of the lack of samples. Figure 32 shows Ni $2p_{3/2}$ and Cu $2p_{3/2}$ spectra of the spent NiCu(4:1)Al and NiCu(1:1)Al. For both samples, the nickel contributions are similar. The peaks observed at 856 and

862 eV correspond to Ni^{2+} species and its satellite, respectively. The presence of the satellite is caused by the charge transfer effect from O 2p to Ni 3d in Ni^{2+} species [174]. Furthermore, a small contribution at 853 eV indicates the presence of Ni^0 species; part of the sample is in a metallic state. The Ni^{2+} contribution may correspond to spinel species [76], [172].

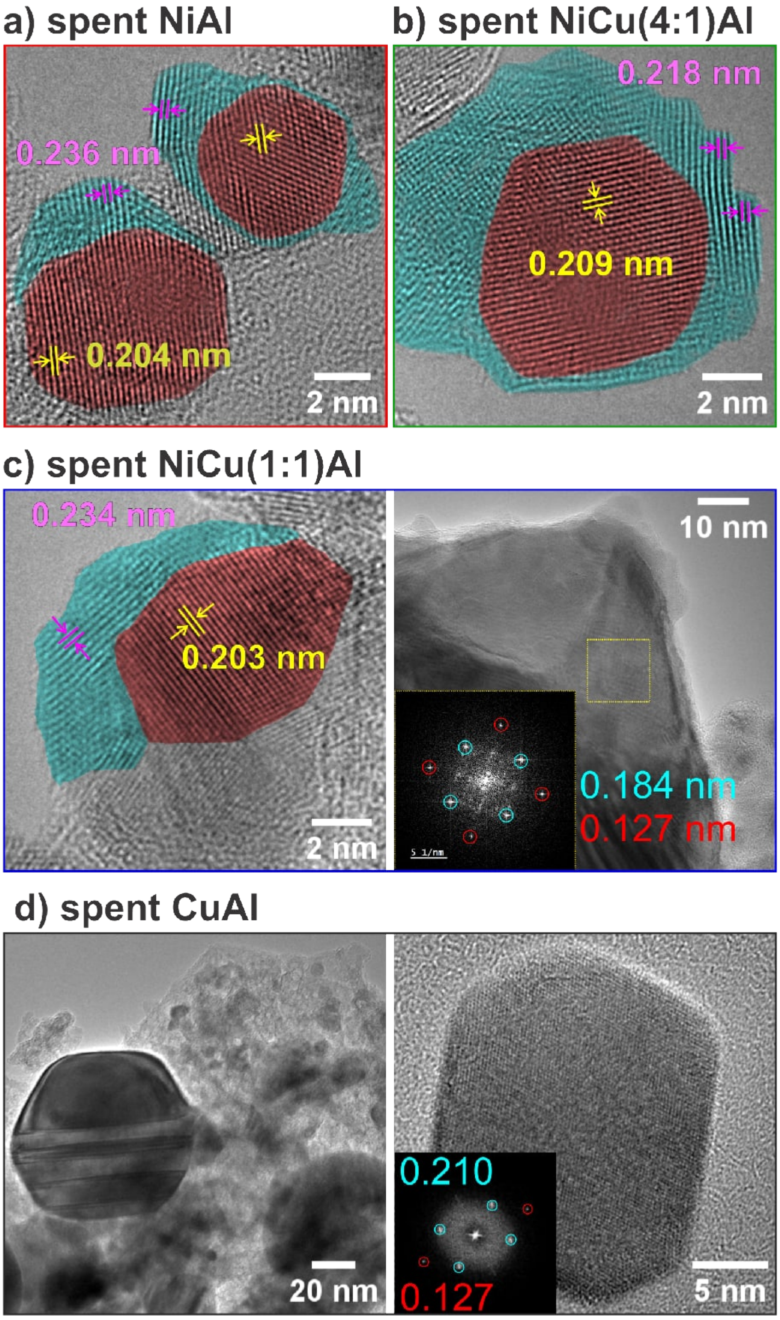

Figure 31: HRTEM images of spent samples after RWGS reaction. Red regions correspond to the metallic nanoparticle. Blue regions correspond to the overlayer (higher d-spacing).

Uncolored images in SI Figure 70.

Regarding the Cu $2p_{3/2}$ spectra, both bimetallic samples presented three main peaks at 932.5, 934.3, and 942 eV, corresponding to Cu^0, Cu^{2+}, and a satellite peak [175]. Cu^{2+} and its satellite are likely CuO species on the surface, formed during the reaction (as deactivation step), or during the transfer under air. The Cu^0 signal represents the remaining metallic copper from the bulk of the nanoparticle. This metallic Cu signal could be overlapped by Cu^{1+} species, which may also be present. Larger differences are observed for NiCu(4:1)Al and NiCu(1:1)Al samples. The sample NiCu(1:1)Al has a higher amount of Cu^0, or (Cu^{1+}) compared to NiCu(4:1)Al. This is explained because of the more accessible Cu metal formed after segregation during the reaction. The metal species in the nanoparticle's center (or bulk) were confirmed through HRTEM (visible in FFT, Figure 31) and EEL spectra, as described below.

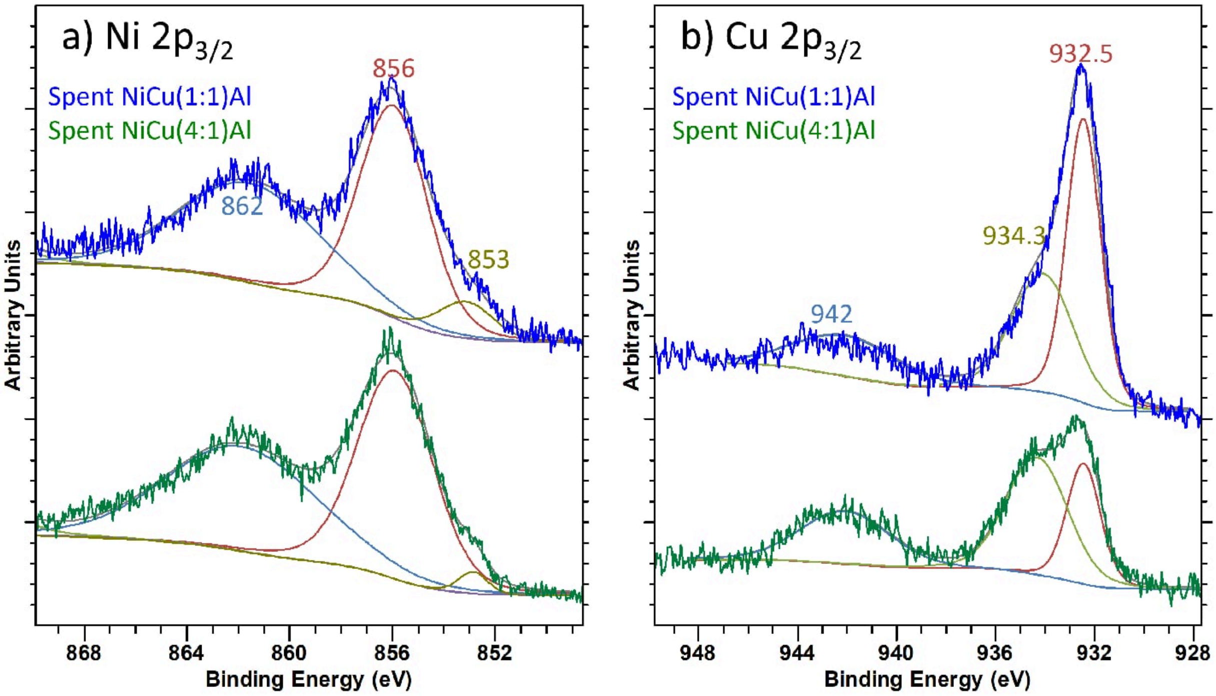

Figure 32: XPS spectra of spent catalysts NiCu(4:1)Al and NiCu(1:1)Al. a) Ni $2p_{3/2}$, and b) Cu $2p_{3/2}$.

The nature of the surface species that are formed during the reaction can be further studied by a series of EELS experiments. EEL spectra were acquired from the center of the particle and the surface. Figure 33 shows the HAADF-STEM images of the spent catalysts and the regions from where the EEL spectra were taken. The corresponding Ni $L_{2,3}$, Al $L_{2,3}$, and O K spectra are reported in Figure 34. As sample thickness is an important property for EELS analysis, the corresponding values of the inelastic mean free path (t/λ) are reported in the images. The recommended thickness values are between $0.0 \leq t/\lambda \leq 1.5$ to assess good energy loss near edge structures (ELNES) [10]. The comparison is presented in terms of surface and bulk species.

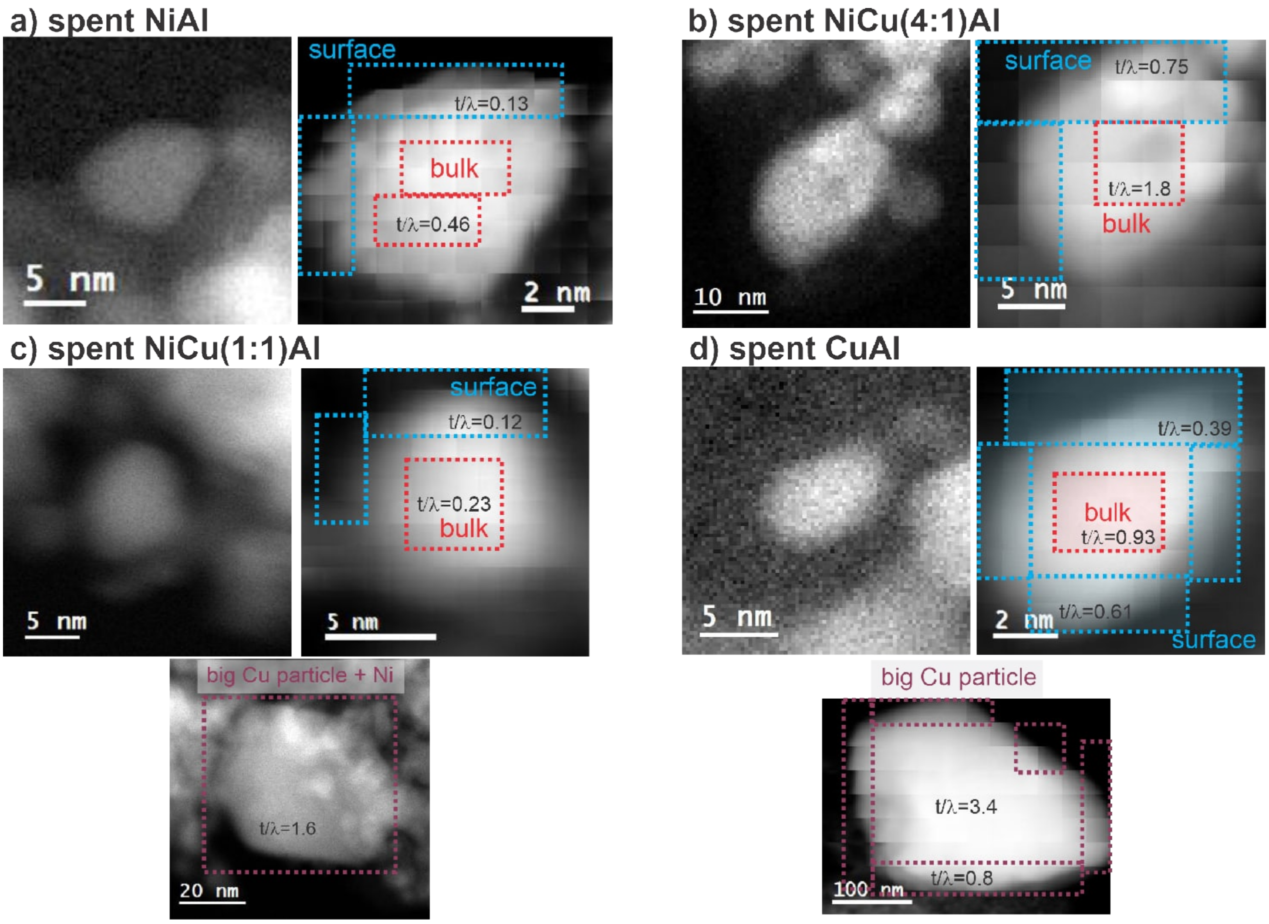

Figure 33: STEM-HAADF images and regions where the EEL spectra were extracted from all spent samples after CO_2 hydrogenation reaction.

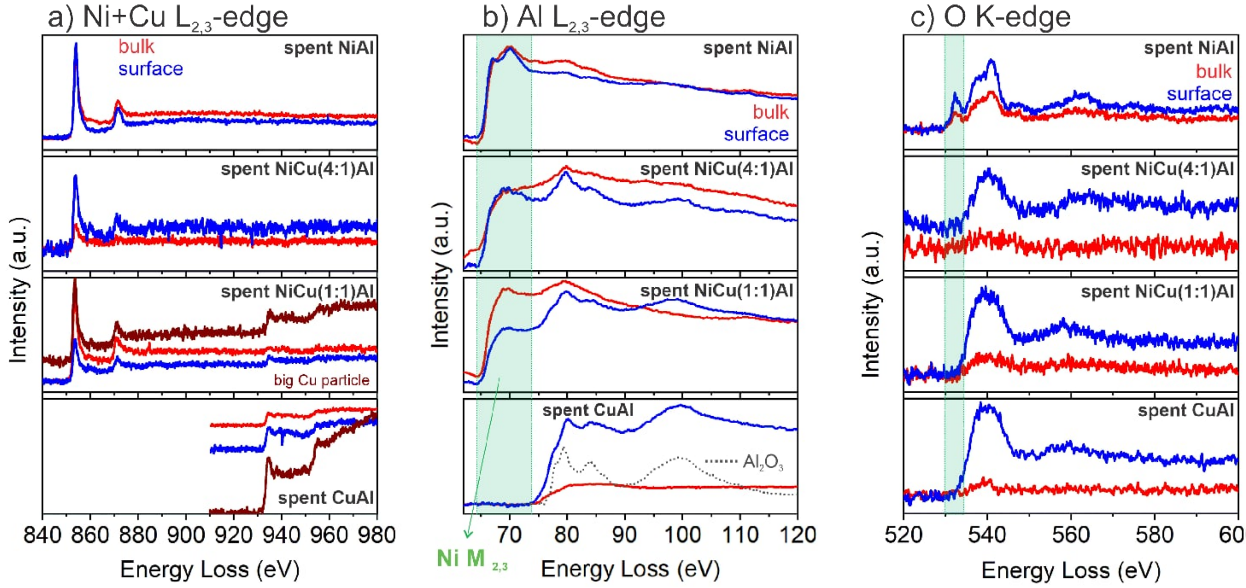

Figure 34: EEL spectra of spent samples after RWGS: a) Ni and Cu $L_{2,3}$ edge; b) Al $L_{2,3}$ edge, c) O K-edge.

Al $L_{2,3}$-edge from Al_2O_3 reference was retrieved from [125], [160].

When the species on the surface are compared with the bulk species, a higher oxygen contribution (O K-edge spectra) is found on the surface compared to the bulk in the four samples (Figure 34c). This happens because of the contact with air during the transport after the reaction, which was not possible to avoid due to the construction of the set up. Although it was minimized by storing the sample in the glovebox prior to characterization. The surface was expected to be passivated with oxygen from the air. We cannot distinguish how much the air transfer has influenced the properties of the material. However, as will be described, the center of the nanoparticles remained metallic. The oxygen prepeak visible for the spent NiAl sample is characteristic of the nickel oxide species [163]. The presence of oxide species is in agreement with the features of the Ni $L_{2,3}$-edge spectra, where the surface spectrum fits close to the NiO, while the bulk spectrum fits to the metallic Ni, references taken from Potapov (SI Figure 66) [124], [125]. Unfortunately, these small features were not clearly distinguishable for the spent NiCu(4:1) and the spent NiCu(1:1), due to the low signal-to-noise ratio in the Ni $L_{2,3}$ edge spectra.

For the spent NiCu(4:1)Al, sample, no Cu $L_{2,3}$-edge signal was observed due to the low Cu content and/or its atomic dispersion. However, we have evidenced that Cu migrated to the nanoparticles' surface [129], evidenced by EDX line profiles across nanoparticles (Figure 69b). Similarly, some regions of the spent NiCu(1:1)Al reveals a Cu enrichment on the surface by comparing the surface and bulk Ni and Cu $L_{2,3}$-edge spectra (Figure 34a, NiCu(1:1)Al). However, elemental line profiles of the same spent sample show the presence of Cu in the center of other nanoparticles (Figure 30c); which indicates the heterogeneity of this spent material. Furthermore, from the Cu $L_{2,3}$-edge fine structure, we observed that the spent Cu and NiCu(1:1)Al samples have a metallic core and slight oxidation at the surface (Figure 34a). This surface oxidation, as described above, is due to unavoidable contact with air after catalytic experiments. For all Ni-containing samples, the region of Al $L_{2,3}$-edge shows the contribution of Ni $M_{2,3}$-edge at lower energy losses, onset at 64.6 eV, while only the sample of spent Cu exhibits an onset at 74 eV, which could be a combination of the edges of Cu $M_{2,3}$ and Al $L_{2,3}$. It is worth noting that the contribution of the alumina support has similar shape features to the Al_2O_3 reference from the literature [125], [160].

In conclusion, we have shown the different morphologies of spent catalysts after the RWGS reaction as a function of their composition and probably related to their metal-support interaction. In the bimetallic material NiCu(4:1)Al, SMSI prevents the catalyst from sintering by the in situ formation of a protective layer around the nanoparticles that was observed in the spent materials. It is presumed that the protective layer is formed by the interaction of Ni with alumina, possibly forming spinel structures. When a higher Cu content is used (NiCu(1:1)Al), the protective layer is unable to prevent sintering and large Cu agglomerates are formed.

4.2 Catalytic evaluation on ammonia decomposition

The nickel metal catalyst is known to be one of the most active primary components for ammonia decomposition catalysts [90], [91]. We then do not attempt to present or discover one best material, but rather to understand the Ni-Cu interaction by correlating the material properties with their catalytic activity. The ammonia conversion and the H_2 production rate of four samples are shown in Figure 35. Similar to the CO_2 hydrogenation, the experiment was performed with a heating-up and cooling-down cycle. As expected, the NiAl sample showed the highest ammonia conversion: 95% at 600 °C. When Cu was added, NiCu(4:1)Al sample, the conversion decreased drastically to 56%. With a further increase of Cu in the material (sample NiCu(1:1)Al), the ammonia conversion dropped to approx. 41%. Figure 35a shows a slight deactivation of NiAl and NiCu(4:1)Al catalysts, noticeable when comparing their conversions at 550 °C. The deactivation caused a small hysteresis in the H_2 production of NiAl during heating and cooling (red line in Figure 35b), not seen in NiCu(4:1)Al.

On the other hand, a slight activation is evident for NiCu(1:1)Al. At a certain temperature (500 or 550 °C), the H_2 production is greater during the cooling than during the heating step. The increase in activity may be linked to a redistribution of the elements during the process. As it was described in the previous chapter, after reduction at 450 °C the surface of the material was enriched with Cu species. Cu is not suitable for NH_3 decomposition reaction. Re-distribution of Cu and Ni species may occur during the heating step, resulting in an increased Ni at the surface. The availability of more Ni species on the surface leads to increased conversion during the cooling phase.

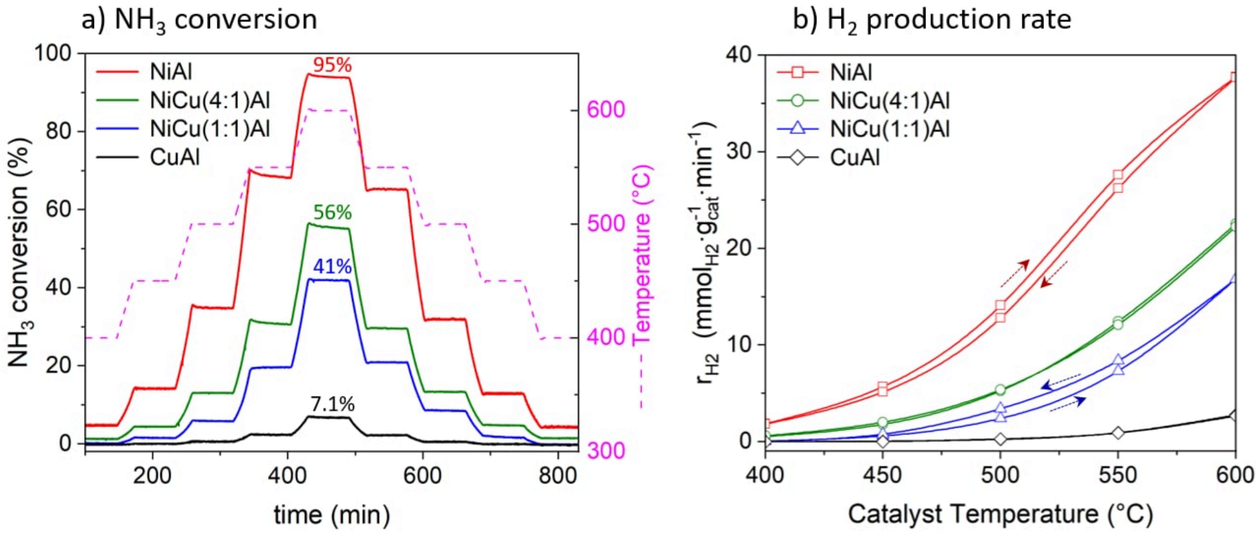

Figure 35: a) Ammonia conversion of NiAl, NiCu(4:1)Al, NiCu(1:1)Al, and CuAl materials as a function of reaction time; b) rate of H_2 production for different temperatures. (Gas flow: 30 mL·min^{-1} of NH_3; catalyst: 50 mg in 100 mg SiC as diluent; WHSV: 36000 mL·g^{-1}·h^{-1})

Finally, the conversion observed from the CuAl sample was less than 7.1% for all temperatures. However, since a similar conversion (6%) was observed during a blank experiment (due to the thermocouple), we assumed Cu does not convert any NH_3. We verified that, in this case, the active species are merely from Ni. When Cu is added, it is mostly at the nanoparticles' surface and the conversion decreases significantly. The spent catalysts were recovered after reaction experiments in contact with air and stored in the glovebox for characterization.

X-ray diffractograms of the spent samples are shown in Figure 36a. Sharp reflections, marked with an asterisk, correspond to SiC that was used as catalysts diluent during the catalytic testing. Although the SiC (355-400 µm) was sieved from the spent material (200-300 µm), some SiC reflections were observed. The main XRD reflections fit with metallic species Ni and Cu. The spent bimetallic samples (NiCu(4:1)Al and NiCu(1:1)A) present a contribution at 2θ values of 41.8°, 48.6°, and 71.4°. These signals could correspond to Ni_4N, which is higher for NiCu(4:1)Al sample. The contribution of Ni_4N, as determined by Rietveld refinement (SI Figure 71) was 15% in the spent NiCu(4:1)Al sample and 11% in the spent NiCu(1:1)Al sample.

The lattice parameters of all spent samples are presented in Figure 36b, in combination with the reduced material discussed in the previous chapter (section 3.5). The results reveal that the lattice parameter of most samples is well in agreement with the expected value assuming Vegard's law for bimetallic alloys. However, the spent NiAl lattice parameter is slightly higher than the expected one. This could be due to a lattice expansion produced by nitrogen in the nickel lattice. The spent NiCu(1:1)Al shows a lattice parameter of 3.5868(2) Å, which is too high for a $Ni_{0.5}Cu_{0.5}$ and may actually correspond to a Cu-rich alloy ($Ni_{0.3}Cu_{0.7}$, see dotted lines in Figure 36b to guide the eye). This could mean that the Cu concentration is higher in the Ni-Cu solid solution because the Ni might form nitrides separately. However, we found some contradictions with the local elemental composition that will be discussed below. Furthermore, if we consider the presence of nickel nitride in both bimetallic samples, they should have less Ni content in the Ni-Cu solid solution. Therefore, it would be a Cu-rich alloy. This could be valid for NiCu(1:1)Al, but not for the NiCu(4:1)Al because the lattice parameter fits with the expected value for the alloy. However, the reflections of the Ni_4N for the sample spent NiCu(4:1)Al, do not match perfectly with the reference: they are slightly shifted. It could be possible that the nickel nitride observed in the NiCu(4:1)Al sample has Al or Cu incorporated into the lattice, forming "doped Ni nitride", whose lattice parameter correlates well with the Vergard's behavior of Ni Cu alloy.

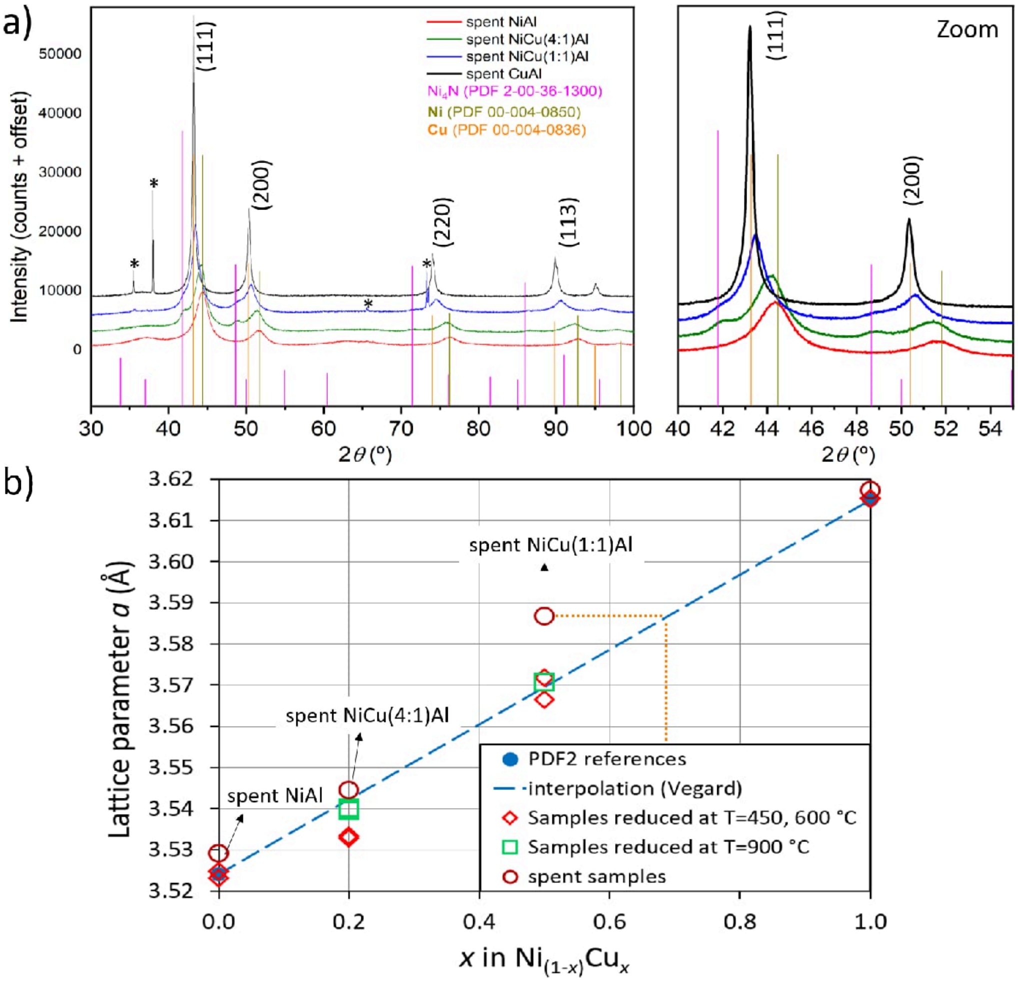

Figure 36: (a) X-ray diffractograms and (b) lattice parameter of spent materials after ammonia decomposition reaction. Asterisks correspond to reflections of SiC used during the catalytic test.

Microanalysis of the spent CuAl and NiCu(1:1)Al materials reveal Cu sintering. The size of Cu particles in the spent NiCu(1:1)Al and CuAl samples reaches up to 100 nm and 200 nm, respectively. Meanwhile, the nickel and copper metal present in the NiCu(4:1)Al sample are apparently alloyed. Figure 37 shows the elemental mapping and EDX spectra from different regions of the four spent samples after NH_3 decomposition (see individual spectrum images for all elements in SI Figure 72). It is clearly visible that the spent CuAl and NiCu(1:1)Al samples have sintered because of the Cu-rich regions. Whereas the spent NiAl and spent NiCu(4:1)Al samples have a more homogeneous distribution of all elements. Nitrogen signal was detected in the EDX spectra from all regions of the spent NiAl and NiCu(4:1)Al samples (see zoom in the N-Kα of Figure 37a and b). In the spent samples of NiCu(1:1)Al and CuAl, the nitrogen Kα peak is smaller (or zero) for the Cu-rich regions (area#2 and area#4 from Figure 37c and d). Interestingly, the presence of nitrogen was also observed in the Ni-free sample (area#1, Figure 37d).

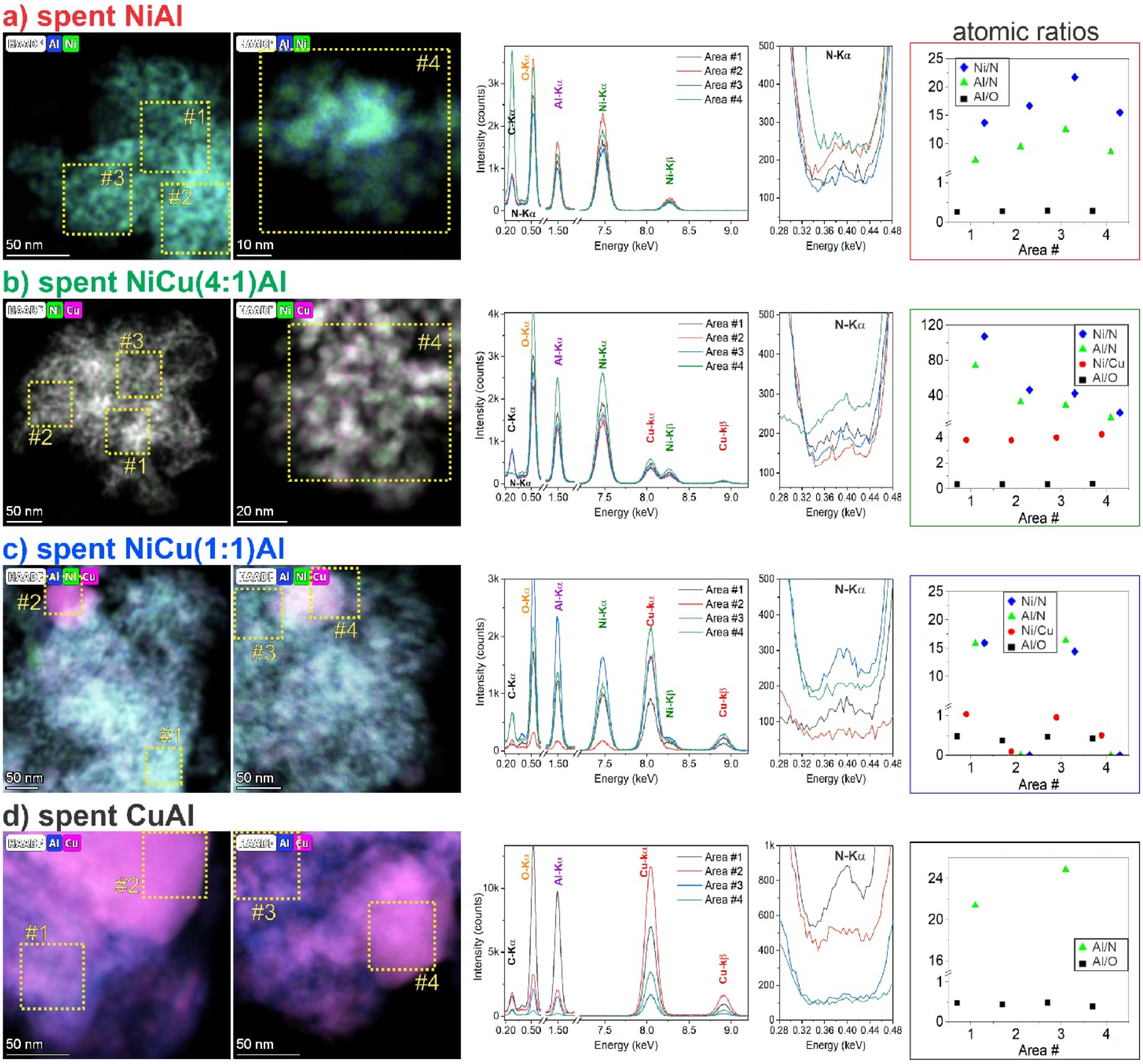

Figure 37: STEM-EDX images and EDX spectra from different regions of all spent catalysts after ammonia decomposition reaction. The right side show different atomic ratios (Ni/N, Al/Ni, NiCu, and Al/O) for all the investigated areas.

For a more detailed quantification study, the atomic ratios of Ni/N, Al/N, Ni/Cu, and Al/O were extracted from all the areas and included at the rightmost of Figure 37. For the spent CuAl samples, the Al/N ratio in areas #2 and #4 (where Cu has not been segregated) may imply the coexistence of Al and N. For Cu-rich regions, nitrogen was zero. It is difficult to correlate with the Al/O ratio because the material may also be oxidized after contact with air after the reaction. Furthermore, the presence of oxygen in the possible Al-N system cannot be ruled out. For the spent NiAl and NiCu(4:1)Al samples, the similar trend of the Ni/N and Al/N ratios suggests that Ni is also involved in Al nitrides. It is possible that some Al form part of the Ni_4N system observed in XRD. That might be the reason for the slight XRD mismatch. This could also applied to areas #1 and #3 of the spent NiCu(1:1)Al sample (in the absence of segregated Cu). We observed a higher Cu content in some regions (areas #2 and #4) while maintaining the Ni/Cu ratio close to 1 in others (areas #1 and #3). This was the nominal ratio from synthesis. On the other hand, as expected, the Ni/Cu ratio of spent NiCu(4:1)Al was close to 4 for all analyzed areas.

Furthermore, STEM-EELS experiments of the bimetallic samples were conducted and the analysis of the N K-edge could shed light on the nature of the nitrogen species. Figure 38 and Figure 39 show the nitrogen, oxygen K-edges and nickel and copper $L_{2,3}$-edges from different regions of the spent NiCu(1:1)Al and NiCu(4:1)Al samples, respectively.

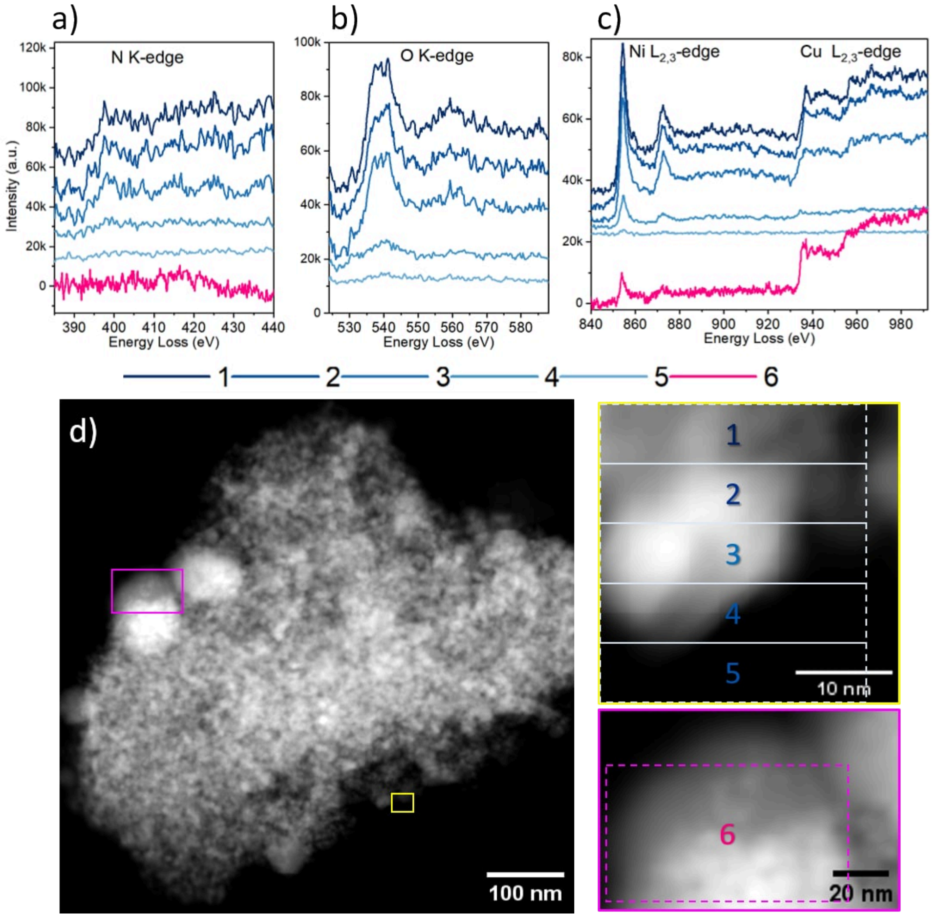

Figure 38: STEM EELS of the spent NiCu(1:1)Al sample after ammonia decomposition. a), b) and c) correspond to the N K-edge, O K-edge, and Ni + Cu $L_{2,3}$-edge, respectively. d) STEM TEM image indicating the region of EELS analysis.

The results of the spent NiCu(1:1)Al sample corroborate that the nitrogen is not present in the Cu-rich areas (pink spectra in Figure 38a and c). There, the Cu signal shows characteristics of metallic Cu species [125], [159]. In contrast, the regions of bimetallic nanoparticles (spectra 1-5 in Figure 38 and Figure 39) show a peak at the N K-edge. In both cases, the presence of nitrogen is higher in the center of the nanoparticle and decreases at the surfaces. Unfortunately, the low N K-edge signal is noisy and hinders the distinction of nitrogen species. However, we observe some similarities with the shape of the N K-edge reference from AlN [125], [176]. Therefore, it might be related to Al nitride species, as observed from XRD, there might be nickel nitride species also involved.

The presence of Ni and Cu in the analyzed region of spent NiCu(1:1)Al sample is evident from the Ni and Cu $L_{2,3}$-edges. The Cu features of the $L_{2,3}$-edge could indicate that there is surface oxidation of copper (and probably also nickel). Particularly, the center of the particle (spectra 2 and 3 Figure 38c) shows similarities to metallic Cu species. Even though the extracted region includes surface regions. With the spent NiCu(4:1)Al sample, the low signal in Cu $L_{2,3}$-edge suggests that copper is atomically dispersed. The Ni $L_{2,3}$-edge has an interesting feature at 857 eV (Figure 38d) which may be characteristic of Ni-nitride species [177]. This agrees with our XRD results. Moreover, N K-edge spectra changes suggest that nitrogen is mainly located in the center of the nanoparticle.

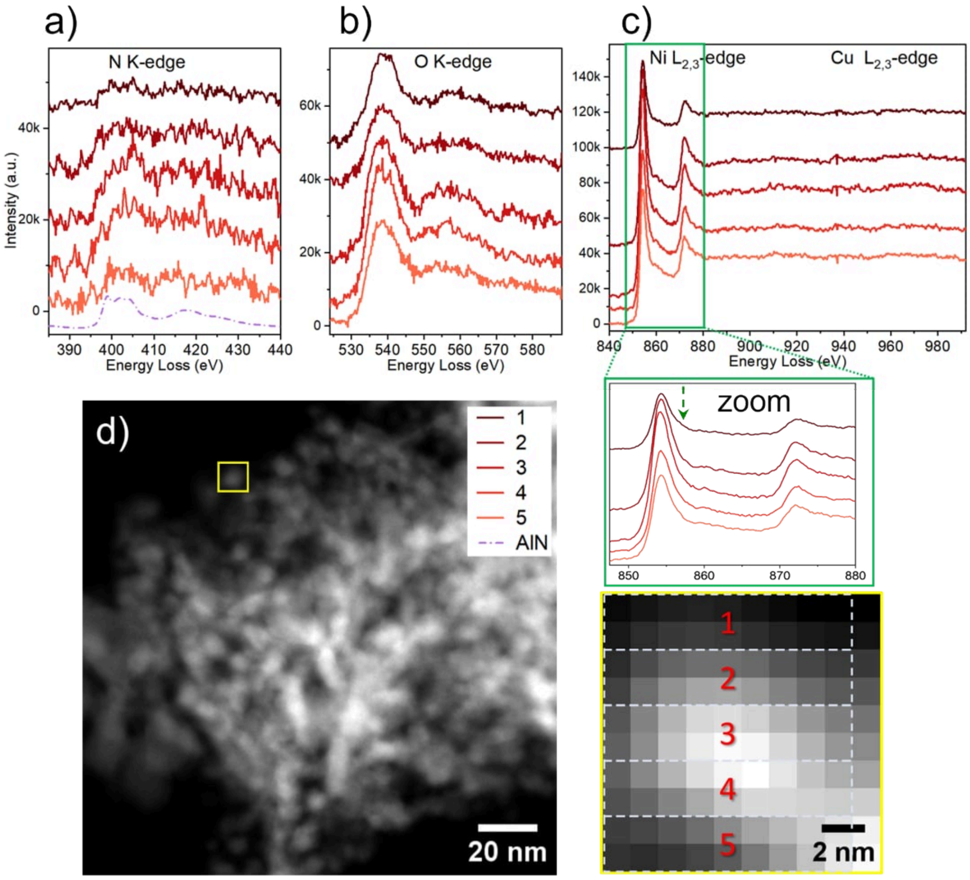

Figure 39: STEM EELS of the spent NiCu(4:1)Al sample after ammonia decomposition. a), b) and c) correspond to the N K-edge, O K-edge, and Ni + Cu $L_{2,3}$-edge, respectively. d) STEM TEM image indicating the region of EELS analysis.

The ammonia conversion is dependent on nickel content in the catalysts. The analysis of the spent samples revealed the presence of nitrogen. This nitrogen could be found in the center of nanoparticles, maybe forming interstitials compound with Ni (and Cu) lattice. The activity of the CuAl sample was the lowest one and Cu does not form nitrides after the ammonia decomposition reaction; however, the aluminum might form. Al and N are coexisting in some regions of the spent CuAl sample.

4.3 Conclusions

The catalytic evaluation of the series of NiCuAl LDH-derived catalysts on relevant energy conversion reactions was investigated. The effect of using NiCu bimetallic catalysts compared to their monometallic samples depends on the catalytic reaction. For CO_2 hydrogenation, the bimetallic combination works as a synergy for RWGS or CO formation. However, that combination was detrimental to ammonia decomposition conversion.

In detail, for the CO_2 hydrogenation reaction, it was found that Ni promotes mainly methanation and the presence of Cu in the system increases the selectivity to CO (suppressing CH_4 formation), resulting in higher CO yield for the bimetallic catalysts. It is possible that the CO formation occurs on Cu, while Ni leads to methane. In our formulation, the Ni component of the bimetallic catalyst adds stability, probably as a spinel overlayer formed during the reaction. The catalyst NiCu(4:1)Al showed the best combination for producing highly stable CO yield over time of stream (TOS), and probably at the end of the experiment, the surface was enriched with Cu species. When Cu content was increased to the same molar content as Ni, segregation of Cu occurred.

On the other hand, the best material for ammonia decomposition reaction was the NiAl sample. When Cu was added to the catalysts, the activity drastically decreased because of the decrease in the access to Ni sites of the catalysts. In the spent catalysts, Cu nitrides were not evidenced, but Ni-nitrides, possibly with Al. Nitrogen species were found at the center of the nanoparticles. Interestingly, also the less active material, CuAl, showed nitrogen-rich regions, which may be Al-N species.

Regarding the NiCu(4:1)Al sample, Ni and Cu are apparently alloyed after NH_3 decomposition, and no Cu surface enrichment was observed, as was the case after CO_2 hydrogenation reaction. The observed differences are most likely due to the distinct chemical potentials in the gas phase. For CO_2 hydrogenation, it promotes the segregation of Cu to the surface; while for ammonia decomposition, the Ni-Cu bimetallic system might remain like an alloy.

5 In situ and operando investigation of NiCu(4:1)Al LDH

This chapter focuses on the analysis of the NiCu(4:1)Al sample under in situ and quasi-in situ XRD calcination and reduction. The integral results are correlated with the local scale changes observed in TEM. The bimetallic sample was also tested on hydrogenation of carbon dioxide under operando TEM, showing remarkable activity in the RWGS reaction. A comparison of the microreactor (OTEM cell) and fixed-bed reactor is briefly discussed.

5.1 Calcination

To understand how the LDH structure changes during calcination, a quasi in situ XRD experiment was performed using the NiCu(4:1)Al LDH sample. Figure 40 shows the evolution of the LDH structure during the calcination process. The diffractogram of the pristine LDH was acquired in static air to avoid possible dehydration of the layer. The interplanar spacing, d_{003}, was 7.57 Å, which corresponds to 22.71 Å of the c parameter ($c = 3{\cdot}d_{003}$). Heating to 185 °C caused the layer to shrink due to water removal from the interlayer space. This process destroys the order between the brucite-like layers, and it is observed as a shift to higher angles and a decrease of the (003) and (006) reflections. (Evidence of water removal during LDH thermal decomposition was observed in the TGA curves described in section 3.2, Figure 13b). The change in the (006) reflection is more pronounced, and its intensity vanished at 250 °C. The (003) reflection decreased even more and disappeared within 4 h during a temperature plateau at 250 °C. The disappearance of the LDH characteristic reflections means that its structure collapses and a mixture of NiO and CuO appears. These reflections increase significantly. LDH structure collapses because of the decomposition of carbonates and dehydroxylation of layers (shown by CO_2 and H_2O signals in TGA, section 3.2, Figure 13b). Finally, thermal treatment at 600 °C led to the crystallization of NiO and CuO, observed by sharper NiO and CuO reflections. The presence of NiO and CuO phases has been identified, but they are difficult to discriminate due to the strong overlap between 2θ values of 30 and 50°. The difference in the sharpness of XRD reflections depending on temperature was also observed during ex situ calcination at 290 and 600 °C (SI Figure 64a). Sharper reflections when higher temperature was used.

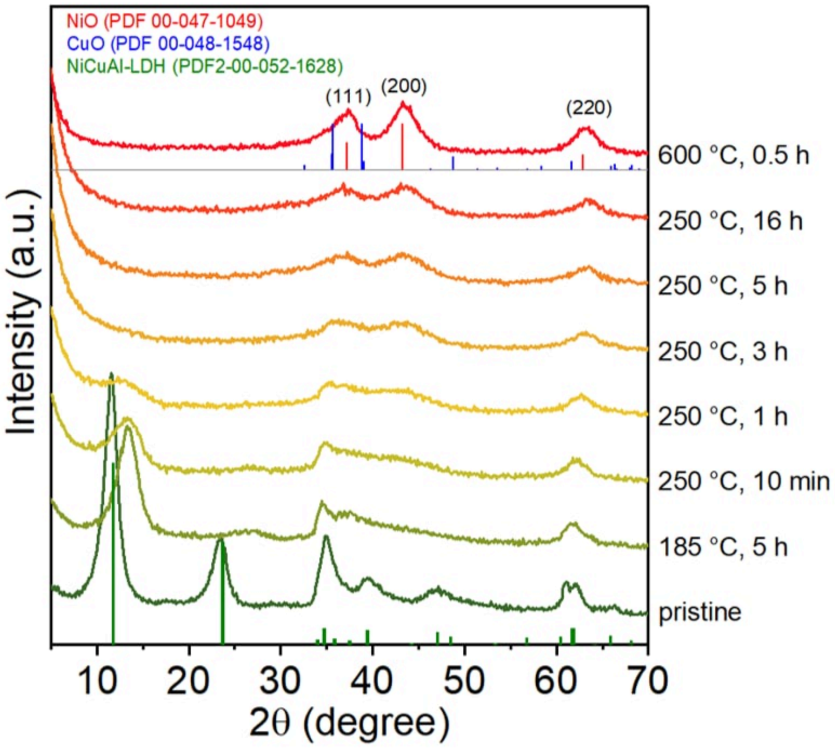

Figure 40: X-ray diffractograms of NiCu(4:1)Al LDH during quasi in situ calcination (Flow: 100 mL·min^{-1} of 20% O_2 in He; heating rate: 6 °C·min^{-1}; all diffractograms taken at 25 °C).

For in situ TEM calcination, a total flow of 20 µL·min^{-1} of 20% O_2 in He was set through the nanoreactor cell and stabilized overnight. The layer distance d_{003} of the pristine LDH is 0.758 nm (measured ex situ from the same LDH sample, section 3.1). Figure 41 displays the LDH micrographs during calcination and how temperature affects the d-spacing of the marked area. For the sample at 50 °C, d_{003} is 0.67 nm, implying that some water from the interlayer space has already been removed. This phenomenon is likely because of the continuous flow used and the stabilization time (~ 10 h). After heating to 180 °C, the layered structure is still visible (HRTEM image) but has shrunk to 0.48 nm. Compared to the in situ XRD results, this corresponds to a peak shift to higher angles: a layer contraction of the d_{003} interplanar spacing from 0.75 nm, at RT, to 0.62 nm, at 185 °C. If we average the d_{003} and d_{006} positions [178], the layer distance shrinks to 0.43 nm (from XRD). Both methods, XRD and TEM, are here in good correlation. After heating for 5 h at 250 °C and up to 290 °C, the layered structure is no longer visible. However, platelet morphology is preserved thanks to the LDH's memory effect property. These platelets were also observed after calcining LDH at 600 °C (SI Figure 64c). They are composed of a mixture of metal oxides: NiO and CuO observed in XRD, and Al_2O_3, which might be amorphous.

During the in situ TEM experiment, the online mass spectrometer (MS) data shows the release of CO_2 as a result of the carbonates decomposition, and a slight release of water (see SI: Figure 73).

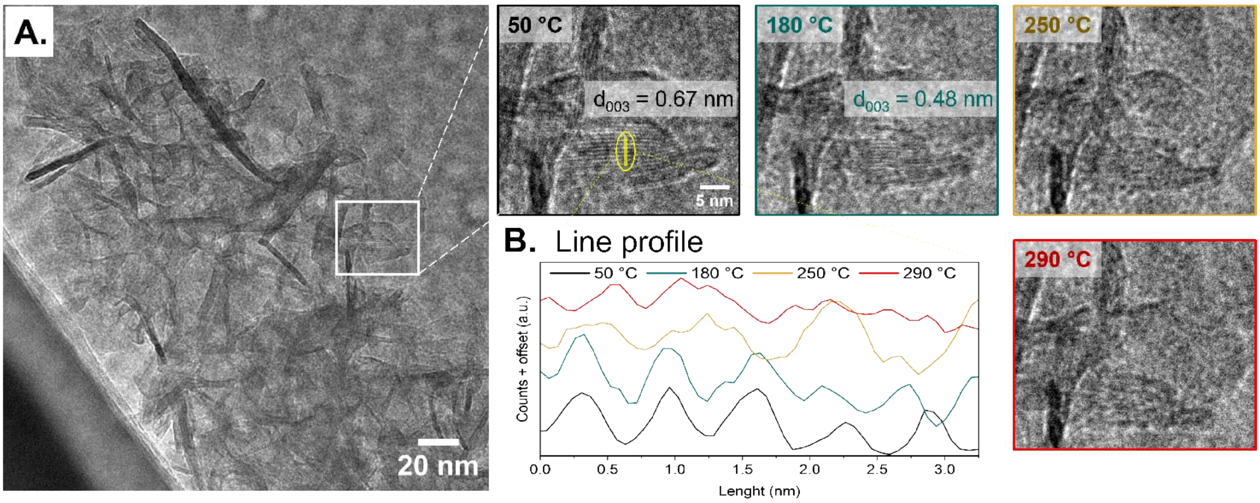

Figure 41: TEM images of the LDH during calcination treatment, and the line profile showing the evolution of the d-spacing while heating (Beam dose: 606 $e^{-}\cdot Å^{-2}\cdot s^{-1}$, flow: 24 µL·min^{-1} of 20% O_2 in He; cell pressure: 0.85 bar).

5.2 Reduction

The temperature profile of reduction (TPR) of the NiCu(4:1)Al sample, previously calcined at 290 °C, is shown in Figure 42. The TPR curve shows that Ni and Cu oxide species are reduced separately. The initial peak represents the reduction of CuO species between 122 and 175 °C; this probably occurs in a two-step process from CuO to Cu2O and finally to Cu. NiO reduction occurs between 180 to 500 °C. In our in situ characterization, the reduction was performed using 5% of H_2 with a total flow of 20 mL·min^{-1} for in situ XRD experiments; and 10% of H_2 with 20 µL·min^{-1} total flow for TEM experiments.

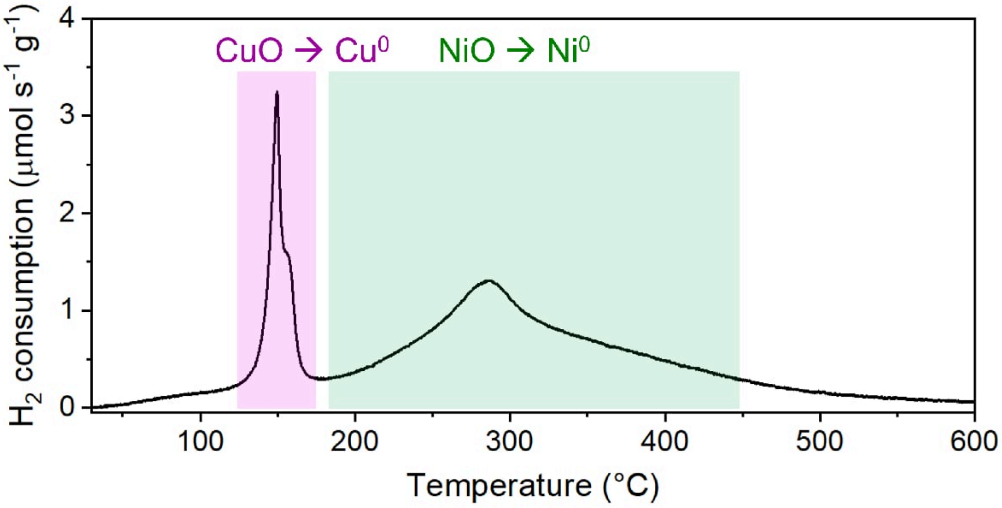

Figure 42: Temperature-programmed reduction profile of NiCu(4:1)Al_ox.290C sample. (Catalyst mass: 80 mg, flow: 100 mL·min^{-1} of 5% H_2 in Ar, heating rate 2 °C·min^{-1})

Two series of X-ray diffractograms were acquired during the reduction process: short scans at high temperatures (HT) and long scans at 50 °C (see section 2.2.3). Figure 43a shows these X-ray diffractograms during the reduction process. Rietveld refinement was used to analyzed both sets of X-ray diffractograms. One oxide contribution (NiO) and one metallic contribution (Ni) were assumed to avoid overinterpretation. Based on this analysis, the phase fraction as a function of temperature is shown in Figure 43b, together with the lattice parameter of the contributions of oxides (c) and metals (d). The X-ray diffractograms at HT and 50 °C match because their phase fraction curves are similar (Figure 43b). The phase fraction of oxides and metallic species is ranged between 200 °C and extends to around 700 °C. In this region, the oxides vanish and the metal species are formed. However, the first event in the TPR profile was observed at temperatures around 122 and 175 °C. This difference can be explained by the atomic dispersion of the Cu species that are not detected in the diffractograms. Moreover, the endpoint might be arbitrary because of the fitting model and the absence of one component.

As observed in Figure 43c, the "NiO" lattice parameter deviates from the literature value (for NiO: 4.18 Å) shortly before 200 °C. This agrees with the reduction of NiO species to Ni^0 observed in the TPR profile with an onset at 180 °C (Figure 42). During reduction, the average NiO lattice parameter *a* decreases until it can be assumed that the "NiO" contribution is zero at 600 °C, because of the large error bars.

On the other hand, the NiCu alloy lattice parameter (Figure 43d) started with 3.60 Å at 200 °C. As the temperature increases, this parameter is getting closer to the literature value of Ni. The lattice parameter *a* for the NiCu(4:1) bimetallic system is 3.542 Å, assuming Vegard behavior (black dot-dashed line). However, the experimental values are instead closer to the Ni value (3.524 Å) at reduction temperatures of 450 to 600 °C approximately (Figure 43d). The lattice parameters obtained after ex situ reduction at 450 and 600 °C (described in section 3.5, Figure 20) also showed the same values, represented by blue squares in Figure 43d. This may indicate Cu surface enrichment, which was also observed from relative surface quantification (from XPS, section 3.6). When the temperature is raised, the lattice parameter *a* increases close to the expected value at 900 °C. This is consistent with the ex situ reduction at 900 °C (section 3.5, Figure 20) and may suggest that the segregated Cu is incorporated into the Ni lattice, forming a solid solution. The previous effect may be linked to the uneven sharpening of the (111) reflection of the metallic contribution. (Figure 43a-right). Finally, at 900 °C there are pure metallic alloy species.

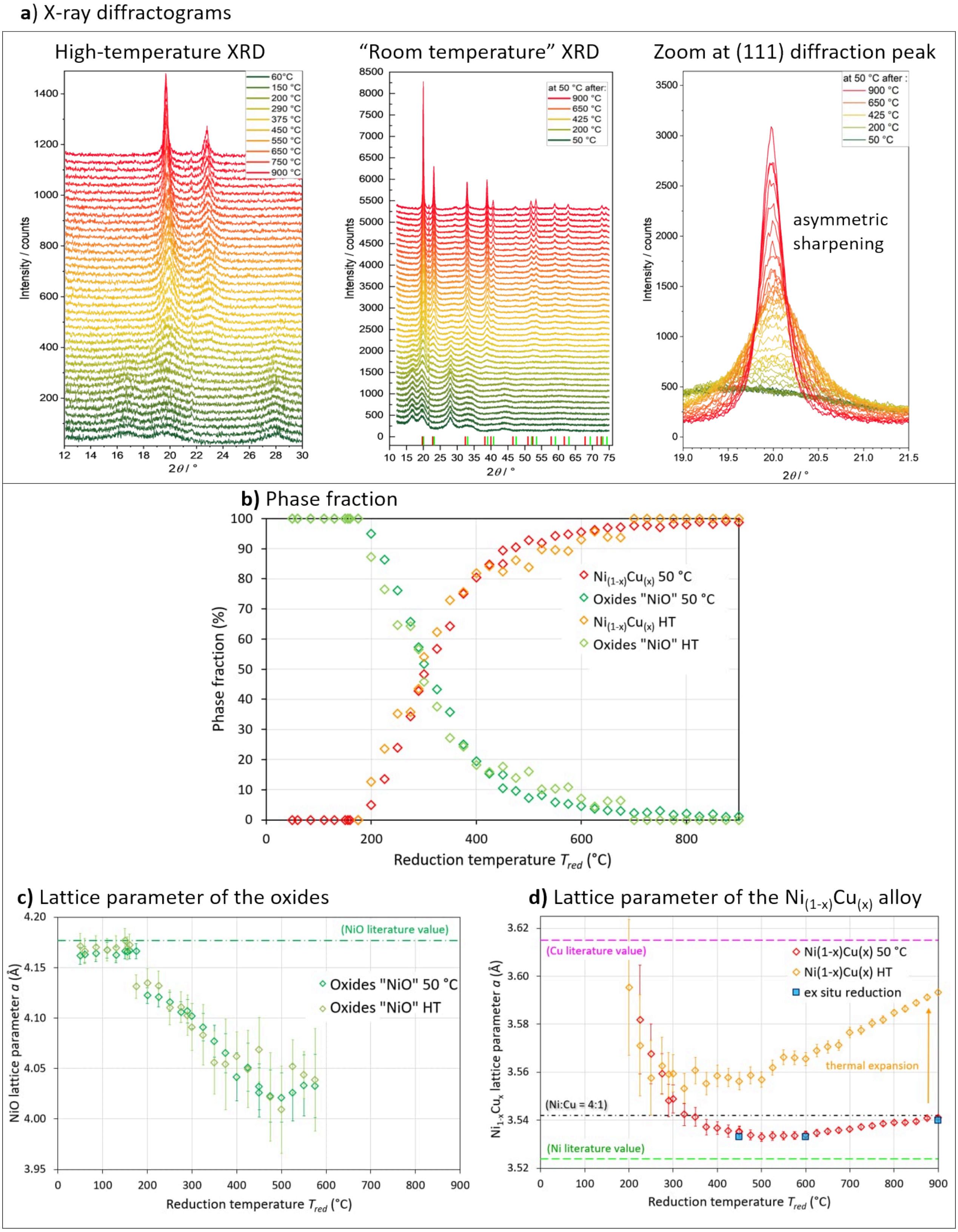

Figure 43: a) X -ray diffractograms at high temperature (HT) and at 50 °C during the reduction process of NiCu(4:1)Al_ox.290C sample. b) Phase fraction as a function of the reduction temperature. c) Lattice parameter of the oxides (modeled with NiO), and d) lattice parameter of the $Ni_{1-x}Cu_x$ alloy. (Conditions: 20 mL·min^{-1} of 5% H_2 in He, heating ramp: 2 °C·min^{-1}, 2 sets of diffractograms taken at HT and 50 °C)

The trend of the lattice parameter *a* of "NiO" is similar for the series at HT and the diffractograms acquired at 50 °C (Figure 43c). However, for the NiCu alloy, the lattice parameter *a* differs at temperatures higher than ~350 °C because of the thermal expansion (Figure 43d). Within the Rietveld refinement, peak broadening due to size contribution was considered (see SI Figure 74). The domain size of the oxides is below 2 nm; while for the metal NiCu alloy, started with 2 nm at 225 °C and is gradually increasing with the reduction temperature up to 11 nm at 900 °C.

Figure 44 shows the TEM micrographs during the reduction process. The complementary MS signals during in situ TEM are shown in SI Figure 73b. The starting material is the LDH sample calcined at 290 °C, which has a 2D material characterized by platelets in different directions (see image at 50 °C). After the reduction process, these platelets are decorated with homogeneously distributed nanoparticles. The nucleation probably starts below 200 °C with metallic Cu species atomically dispersed, as suggested by the TPR profile. However, the nanoparticles were not observed under in situ TEM, until ca. 300 °C.

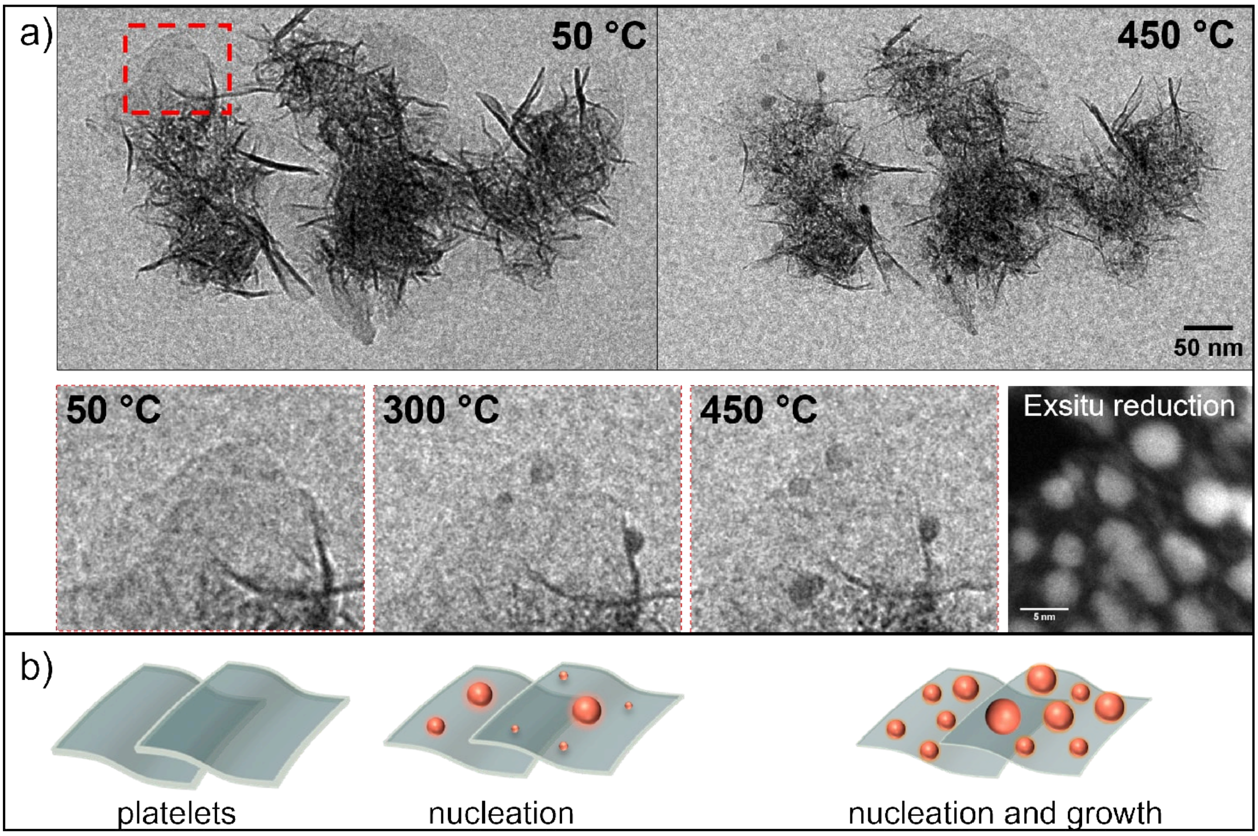

Figure 44: a) TEM micrographs during the reduction process of NiCu(4:1)Al; b) representation of the reduction mechanism through nucleation and growth (Beam dose: 400 $e^{-}\cdot Å^{-2}\cdot s^{-1}$, flow 20 $\mu L\cdot min^{-1}$ of 10% H_2 in He. Pressure: 1 bar. Heating ramp: 2 $°C\cdot min^{-1}$).

These metallic nanoparticles could be formed through different mechanisms. The most common are nucleation and growth, and shrinking core. Studies of NiO reduction have shown that Ni nuclei are formed homogeneously or grow epitaxially on the NiO surfaces, depending on the available interfaces: Ni/Ni and NiO/Ni [127]. In situ TEM of $LaNiO_3$ perovskite-based materials similarly reported that Ni species evolved mainly at grain boundaries during exsolution, which could be called defective sites [179]. In our case, we have no direct evidence about the nature of the nuclei where the nanoparticles start to form. We can speculate that the metal nuclei might start at highly energetic sites such as defects and unsaturated sites which are related to the LDH precursor. Furthermore, the role of Cu in the NiCu bimetallic system might be to accelerate these nucleations via the H_2-spillover from Cu to Ni. This was described in section 3.5: the presence of Cu produces a shift of the Ni reduction peak to lower temperatures. However, it cannot be ruled out whether the nuclei are formed directly over Cu sites (atomically distributed). The similarities between Cu and Ni lattices also hinder the identification of the species even when high-resolution imaging is feasible. Therefore, computational modeling (such as DFT) might be an option for unraveling this and continuing further NiCu investigations.

Figure 45 shows the nanoparticle size as a function of the temperature during the reduction (a) and CO_2 hydrogenation (b). The size of nanoparticles, estimated from in situ TEM, is initially 3.0±0.3 nm at 280 °C and grows as the temperature increases until 5.0±0.9 nm at the end of the reduction at 450 °C. Interestingly, after 360 °C there is apparently a plateau where the nanoparticle sizes change very little. Particle sizes from ex situ reduction at 300 and 450 °C (described in section 3.4, Figure 16) are also included in the figure for comparison. The nanoparticles' sizes obtained after ex situ reduction at 300 and 450 °C are slightly smaller than those obtained from in situ TEM. The difference is higher at higher temperatures. Even though a low dose was used (as explained in section 2.13.3), the electron beam may still cause some heating and therefore slightly larger nanoparticles during in situ TEM experiments. Reactive feed (Figure 45b) caused particle sizes to increase even more, with both spent materials ultimately having similar size values. Details regarding the reaction experiment will be further discussed.

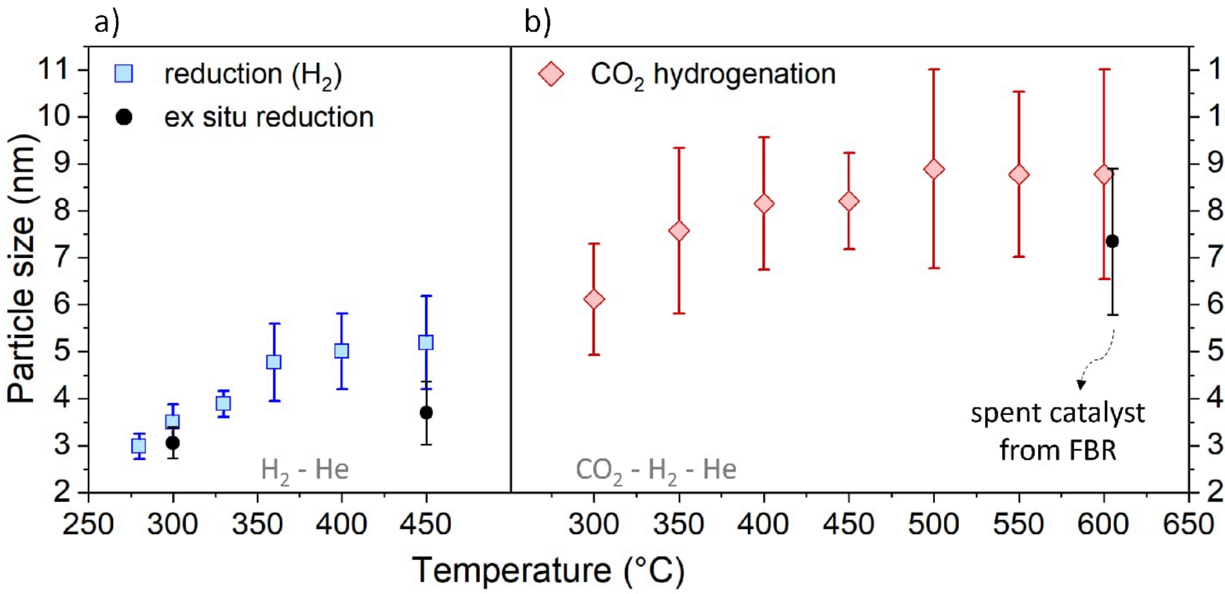

Figure 45: Particle sizes as a function of the temperature during in situ experiment a) reduction using 10% H_2 in He. b) CO_2 hydrogenation using CO_2:H_2:He with ratio 1:1:0.5. (Flow 17 - 20 µL·min^{-1}; pressure: 0.8 - 1 bar; heating ramp: 2 °C·min^{-1})

5.3 Hydrogenation of carbon dioxide reaction

5.3.1 Mass spectrometer signals during the reaction.

Before the reaction in the OTEM cell, the catalyst was in situ reduced with 10% of H_2 and a total flow of 20 µL·min^{-1}. Figure 46 top shows the mass spectrometer signals of in situ TEM experiments #1 and #2. The hydrogen signal decreases while CO and H_2O are formed, as products of the RWGS reaction, when the temperature increases. In a blank experiment, there was neither H_2 consumption nor formation of any product. Hence, the changes in the MS signals are due to the presence of the catalyst in the nanoreactor.

Experiment #1 was performed without microscopy acquisition as a test to evaluate whether the conversion could be detected during the run. The material was promising for further detailed investigations because of the high activity observed in the MS signals, considering the limited amount of sample used (less than 2.5 µg were estimated to be deposited on the chip, see experimental section 2.13.1). Experiment #2 was performed using a different temperature profile and performing image and diffraction experiments. Interestingly, we observed an increase in the H_2O signal at approximately 250 °C (Figure 46 bottom) during both experiments. Since there was no CO signal was observed, the increase in H_2O suggests a further reduction of the material under reactive feed (as was also observed from the structural transformation).

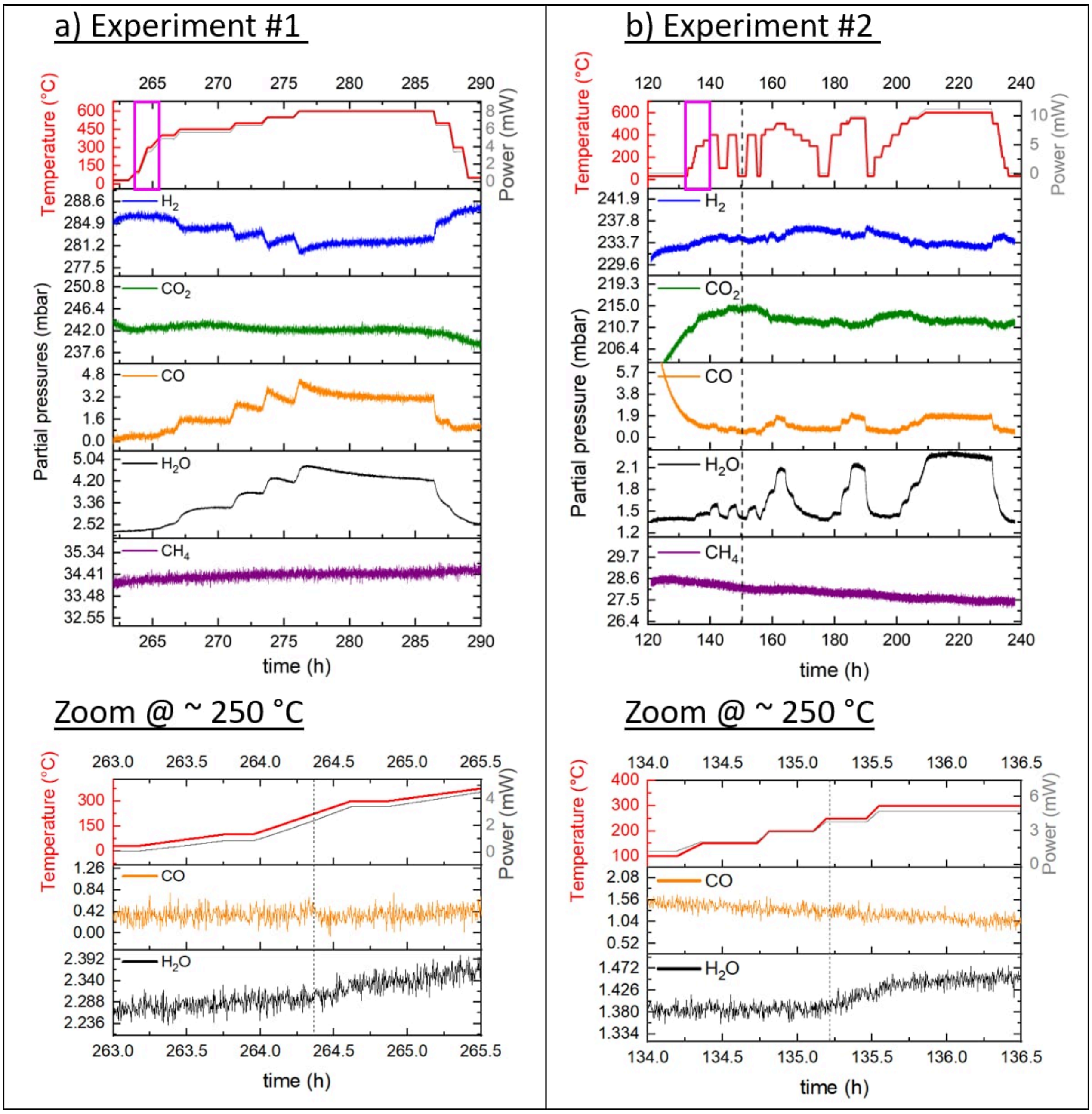

Figure 46: Online temperature and MS data during RWGS reaction in operando TEM a) experiment #1 and b) experiment #2. Bottom: zoom area during heating at ~ 250 °C, where an increase of H_2O signal is visible (Flow: 17 - 20 µL·min^{-1} of CO_2:H_2:He with ratio 1:1:0.5. Pressure: 0.8 bar).

Dashed line represents the lower limit for the background subtraction in experiment #2. Raw MS signals are shown in SI Figure 75.

5.3.2 Structural changes

The structural changes were studied under reactive feed in the nanoreactor and are shown in Figure 47. The continuous rings in the SAED, denote the polycrystalline nature and nanoscale character of the material throughout the entire run. After in situ reduction, the SAED pattern (red line in Figure 47a) reveal both oxidic and metallic species. This means that the material was not completely reduced. This is not surprising because both phase fractions (oxides and metallic) were also observed from in situ XRD at 450 °C (Figure 43b). During the catalytic experiment, under CO_2 and H_2 feed and upon heating, the oxide reflection peaks diminish while the metallic peaks increase. This indicates a further reduction of the material during CO_2 hydrogenation reaction.

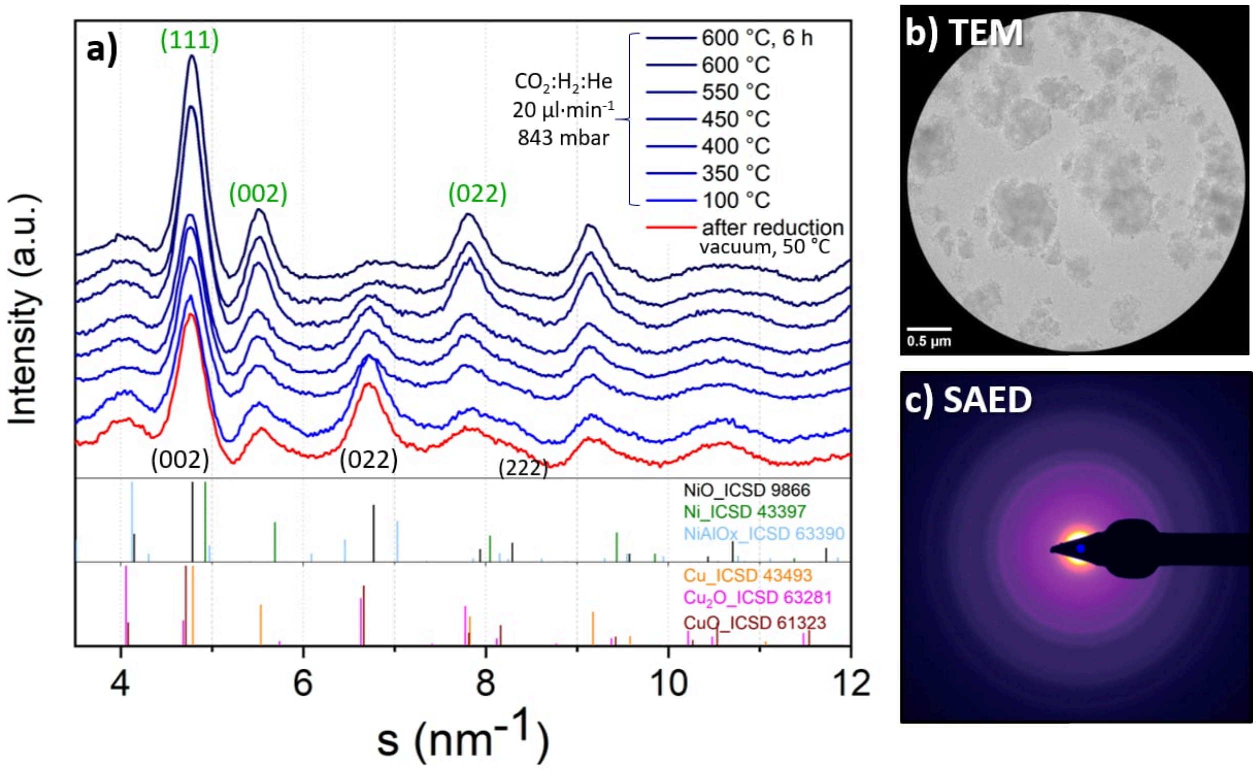

Figure 47: SAED investigation of NiCu(4:1)Al sample during OTEM. a) evolution of the electron diffraction curves after progressively heating under reactive feed (CO_2:H_2:He, ratio 1:1:0.5). b) micrograph showing the analyzed region. c) electron diffraction image showing the polycrystalline nature of the material. Beam dose: 3 $e^{-}\cdot Å^{-2}\cdot s^{-1}$. Green (hkl): metals, black (hkl): oxides.

5.3.3 Morphological changes

Figure 48 shows the morphological changes during the reaction experiment. TEM investigations require a thin region, where we focus to observe the changes. During experiments, the platelets of the material may turn or twist as a result of heating or gas flow. For example, the green arrows in Figure 48 indicate the position that has twisted after the reduction process. After the reduction, some nanoparticles were decorating the platelets (Figure 48b-top). Later, under a reactive feed (CO_2:H_2:He), more nanoparticles were formed with the further reduction of the material. After almost 20 h of reaction, some nanoparticles had sintered to sizes up to ~ 15 nm. However, they were still homogeneously distributed in the layer. The platelet structure could be intimately related to the LDH precursor due to its memory effect property. These findings might elucidate the good stability after a long reaction process which could be attributed to the precursor. Similar results were observed in different regions shown in SI Figure 76 during the reduction and reaction process.

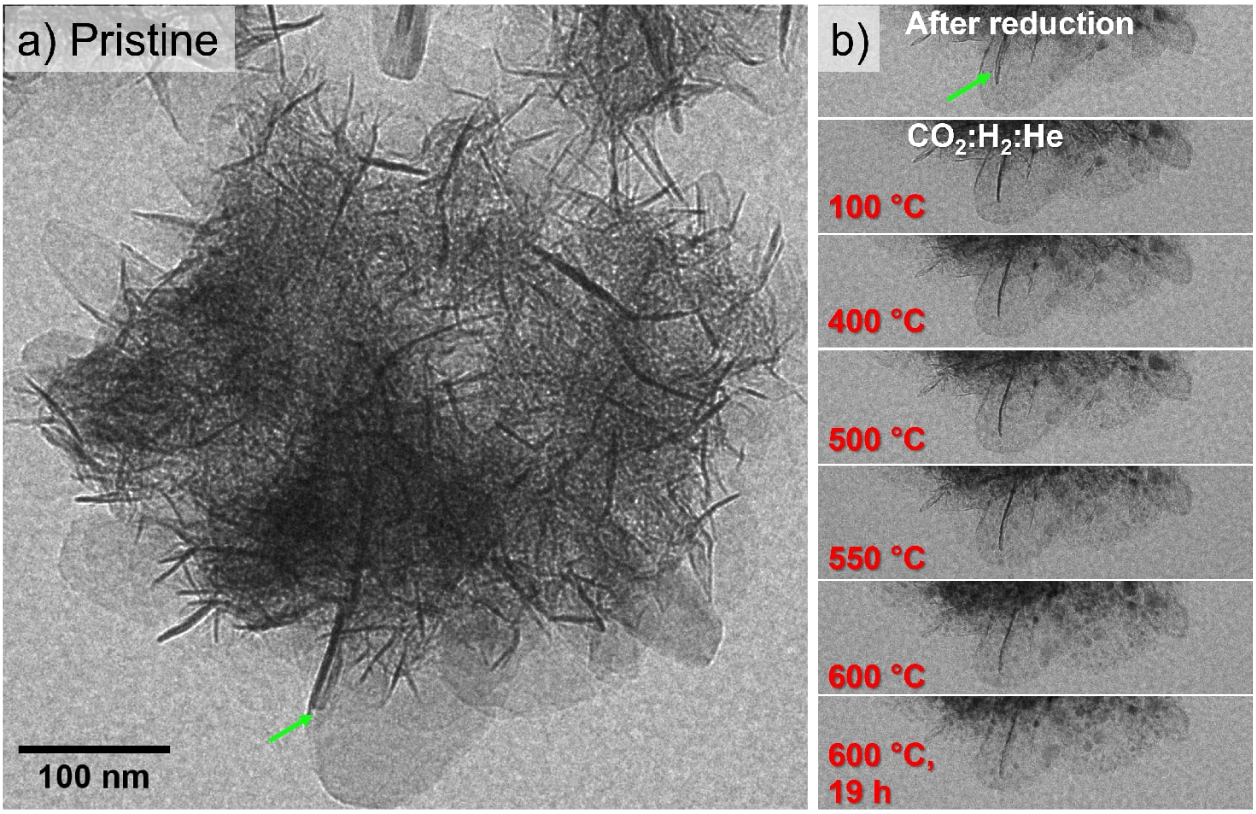

Figure 48: TEM investigation of the LDH-derived sample during OTEM. a) pristine sample: NiCu(4:1)Al_ox290 . b) Zoom area after reduction and after reaction at different temperatures. (Beam dose: 620 $e^{-}\cdot Å^{-2}\cdot s^{-1}$, flow: 20 $\mu L\cdot min^{-1}$ of CO_2:H_2:He with ratio 1:1:0.5. Pressure: 0.8 bar. Heating rate: 2 $°C\cdot min^{-1}$)

Both morphological and structural changes show that the material was further reduced in situ under the reactive feed. This agrees with the MS signals described before, where the H_2O signal increased slightly at 250 °C. The reactive feed mixture allows the reduction of the material at lower temperatures. However, in order to do that, perhaps a few metallic sites or nanoparticles could be the prerequisite. These metallic sites can react with CO_2 to form CO that immediately could be used, together with H_2 already available, for reducing the remaining oxidic species in the material. The absence CO during this reduction (see zoom, Figure 46) may indicate that if CO is formed, it might be consumed very fast.

5.3.4 Apparent activation energies

Figure 49a shows the molar production of H_2O and CO at different temperatures for experiment #1. The molar products' formation was calculated from the relative partial pressures (SI Figure 77). When the temperature increases, the amount of CO and H_2O also increases, and this is consistent with the fixed-bed reactor experiments (shown in SI Figure 78). According to the molar products' production, there is apparently more CO formed at temperatures above 500 °C. However, the differences could be because of the stickiness factor of H_2O, which at higher temperatures may interact more with the tubing walls before reaching the QMS. Thus, the production of CO and H_2O was in a similar range, even when further reduction of the sample under reactive feed was observed.

Figure 49b shows the Arrhenius plots with the apparent activation energies (E_a) estimated from the three MS signals: H_2 consumption, H_2O, and CO formation in the nanoreactor. The production rate values at 400 °C were too noisy (see large error bars) and probably outside the kinetic regime. Therefore, the values at that temperature were not considered for the E_a calculation. The apparent E_a obtained from CO, H_2O, and H_2 signals were 28.9, 33.9, and 34.3 $kJ \cdot mol^{-1}$, respectively. They can be considered similar and agree well despite the further reduction of the material: extra H_2 consumption and H_2O production. To the author's knowledge, few studies in the literature have published apparent activation energies using OTEM. Recently, Tanaka et al., [180], reported comparable activation energies in a pellet-cell reactor, at the same time describing the dynamics of Rh nanoparticles' surface structure during NO reduction. However, in order to achieve that, they needed to modify the cell construction to increase activity.

The Arrhenius plots and E_a could be an option to compare how different our OTEM system is from a real catalytic experiment. The E_a was estimated using the same sample in a fixed bed reactor (FBR), obtaining 42 $kJ \cdot mol^{-1}$ (calculated with 3 data points with conversion below 10% (see SI Figure 78). This rough comparison could indicate that our nanoreactor experiment is *close* to conventional catalytic investigations (29 vs 42 $kJ \cdot mol^{-1}$). However, we have to be cautious as the apparent activation energy measures how sensitive the reaction is to temperature. Thus, this value depends on the reactor construction (geometry), gas flow, heating rate, etc., and it is not a fixed parameter. The geometry and how the gas flow interacts with the catalysts vary a lot. In the OTEM cell, the flow goes over the catalyst layer that is stuck to the SiNx window. In the FBR, the gas flow interacts through the catalytic bed. Mass transport is expected to be significantly different [25].

The important thing to highlight is that our results showed remarkable conversion of the LDH-derived sample under operando TEM conditions, where simultaneous TEM characterization is the main advantage. This is often difficult to achieve. Moreover, despite the differences between the reactor setups (FBR and nanoreactor), we report comparable results from OTEM using a commercial climate holder.

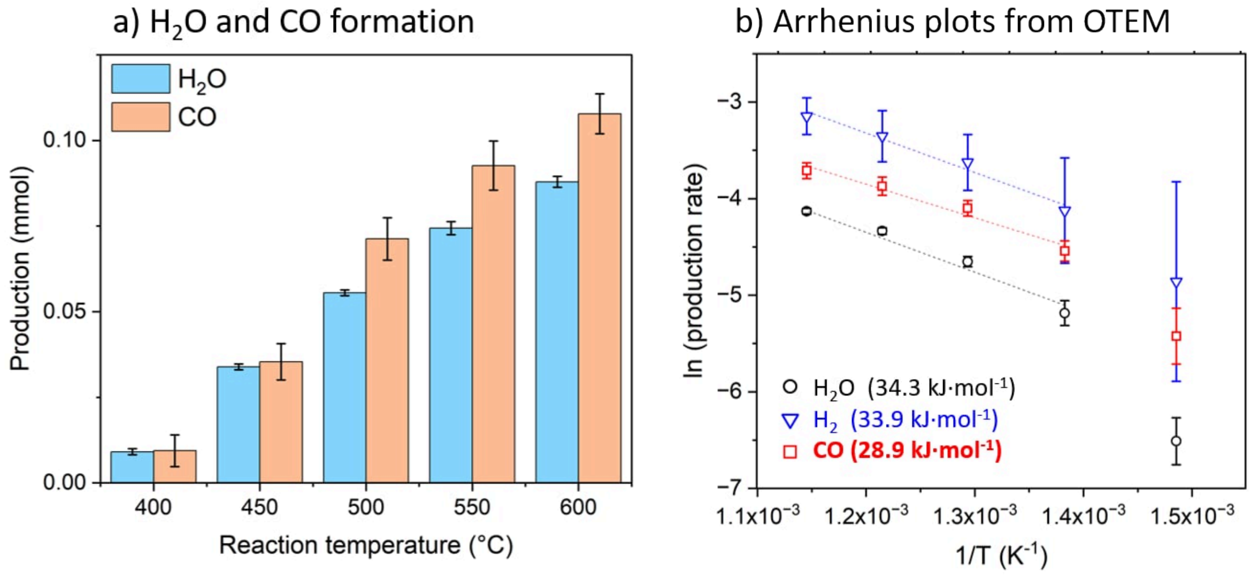

Figure 49: a) Product formation during RWGS reaction at different temperatures. b) Arrhenius plots obtained from OTEM experiments using H_2O, H_2 and CO MS signals (Flow: 20 µL·min^{-1} of CO_2:H_2:He with ratio 1:1:0.5. Pressure: 0.8 bar. Heating rate: 2 °C·min^{-1}).

Finally, we can compare the morphology of the catalysts at the end of the run in the two different setups. Figure 50 shows TEM images of the spent catalysts after RWGS reaction from the FBR (results shown in section 4.1) and from the nanoreactor (OTEM cell). Once again, it is important to be aware of the different geometries. As described above, the mass and heat transport might differ among the setups. In the nanoreactor, a few micrograms of catalysts were stuck to the SiN_x window, and the gas flows above it. In the lab reactor, 15 mg was used, and the gas mixture flows through the catalytic bed.

A clear difference in the morphology is observed, although similar particle sizes were observed (Figure 45b). The spent material after 10 h at 600 °C in the FBR has agglomerates, and the catalyst precursor platelets are no longer visible. On the other hand, from the nanoreactor, the sample showed no agglomeration of the particles, and the platelets were still visible even after almost 20 h at 600 °C. It is worth mentioning that similar morphologies were observed in different regions that were not exposed to the electron beam before (see SI Figure 79). These differences may suggest that the sample in the FBR undergoes more severe experimental conditions than the sample used in the nanoreactor. Probably the morphology we observed in Figure 50a corresponds to the steady-state conditions, whereas the Figure 50b might still be a transient state. The high gas hourly space velocity used in the nanoreactor could be responsible for this behavior. This high flow might remove H_2O vapor faster than in FBR. The presence of water vapor has been reported to be detrimental to the catalyst because it promotes sintering and/or agglomeration [181]. In fact, the incorporation of a water removal membrane in the modeling for methanol synthesis via RWGS reaction resulted in reduced deactivation and longer catalysts lifetime [182].

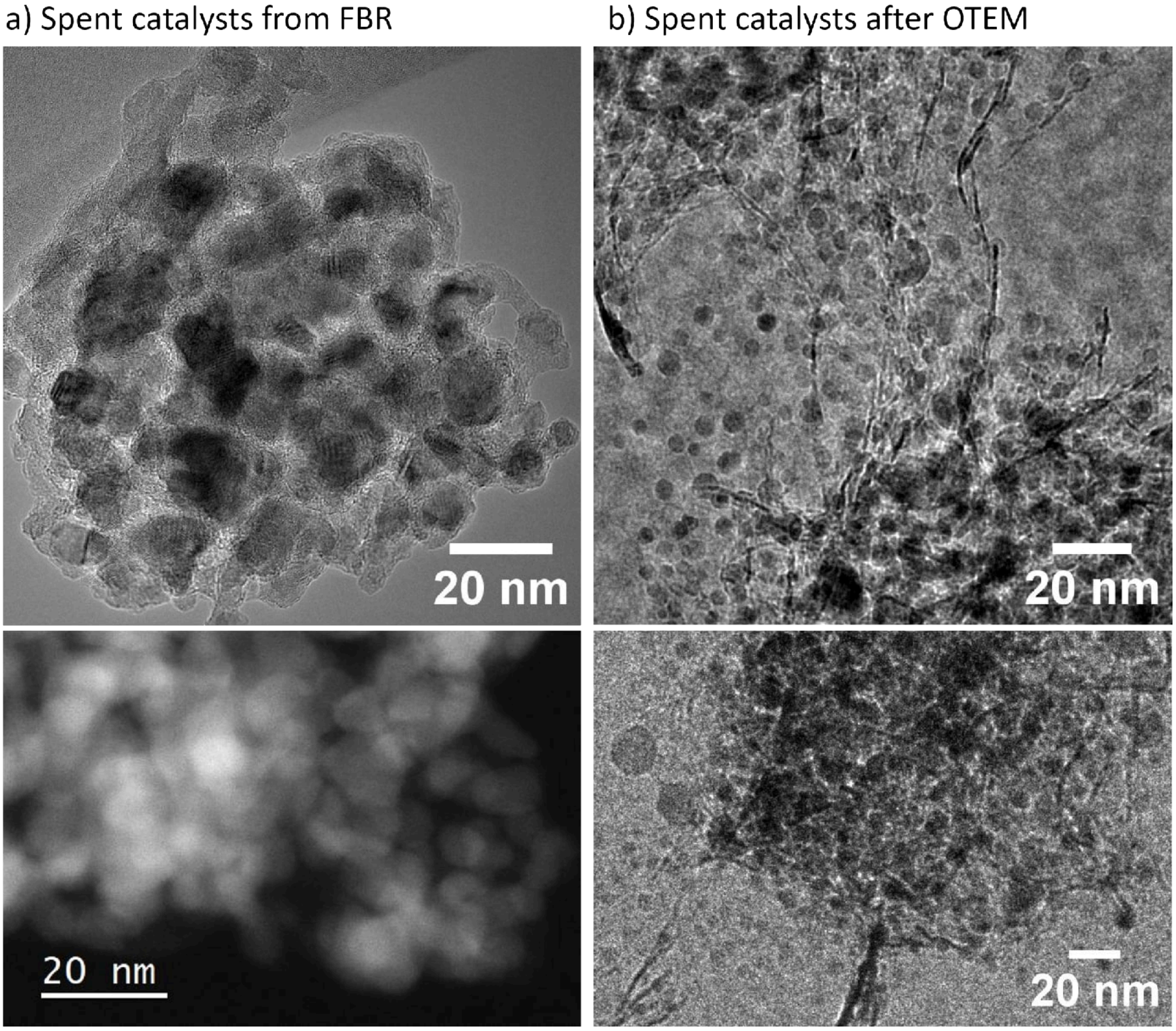

Figure 50: TEM images of spent catalyst after RWGS reaction. a) in a fixed-bed reactor (catalyst: 15 mg; flow: 100 mL·min^{-1} of CO_2:H_2:He with ratio 1:1:0.5; atm pressure; temperature: 600 °C for 10 h); and b) after a nanoreactor OTEM experiment #2 (Beam dose: 1080 e$^-$·Å^{-2}·s^{-1}, catalyst: < 2.5 µg; flow: 20 µL·min^{-1} of CO_2:H_2:He with ratio 1:1:0.5; pressure: 0.8 bar; temperature: 600 °C for 19 h).

5.4 Conclusions

The morphological and structural changes of NiCu(4:1)Al LDH from the calcination step to the catalytic evaluation were investigated using in situ and operando characterization. XRD and TEM results agree regarding the structural changes during calcination; the layers of the LDH precursor shrink, the platelet structure is maintained, and mixed metal oxides are formed after the calcination process.

The reduction process goes as follows: first, the CuO species are reduced but are atomically dispersed on the material (absence of reflections in the XRD). Second, these metallic Cu species may promote the reduction of NiO species via H_2-spillover. Nanoparticles were observed during in situ TEM from 300 °C; however, the sites where the nucleation started were not clear. It can be speculated to be highly defective sites. Once the nanoparticles have formed (nucleated), they grow with temperature, forming a core-shell structure with Cu enriched at the surface and a Ni-rich core. Above 600 °C, the Cu might be incorporated into the Ni-Cu solid solution.

After in situ TEM reduction, performed up to 450 °C, a mixture of oxides and metallic Ni and Cu species was observed. The particle sizes were slightly bigger than the obtained after ex situ reduction. Under CO_2 hydrogenation conditions, the catalyst was further reduced at temperatures above 250 °C.

Our operando TEM investigation showed high activity for the RWGS reaction: similar amounts of CO and H_2O were produced. The catalytic performance was *comparable* with the fixed-bed reactor experiments, but two different morphologies were observed in the spent materials. After OTEM, the LDH memory effect played a role in keeping the platelets with well-dispersed nanoparticles; while after FBR, agglomerates were visible. The results reported might motivate further operando investigations with similar LDH formulations.

6 Electron beam-induced transformation of LDH and derived materials

The electron beam-matter interactions can cause changes that might lead to inaccurate analysis. This is the major obstacle to TEM investigation. In this chapter, we systematically present the influence of beam irradiation on the LDH (and derived) samples that were the focus of the thesis.

6.1 General considerations on beam effects

6.1.1 Introduction

Transmission electron microscopy (TEM) enables the direct observation of particles at atomic or subatomic scale. It can be described as the analysis of the interactions between electrons (80 - 300 kV) and the sample under investigation. This strong electron-matter interaction may produce different signals, as shown in Figure 51. Specific detectors can provide valuable information about the material under investigation, such as its morphology, crystal and electronic structure, and chemical composition. Unfortunately, the high-energy electrons may cause undesired permanent or temporary changes in the sample properties. This important topic has devoted the attention of various books [183] and reviews [184]–[188], and has also been used to simulate in situ transformation samples [189]. However, it is still often overlooked when reporting TEM investigations.

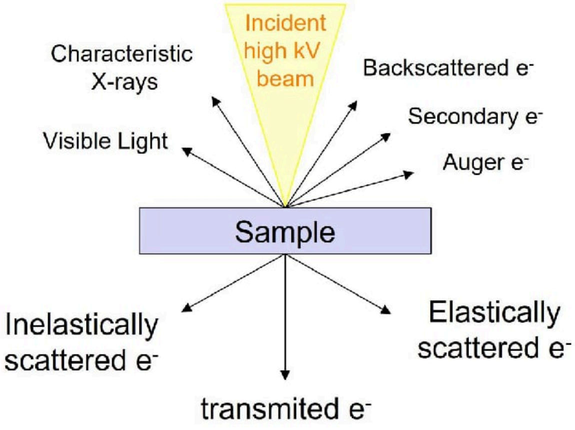

Figure 51: Representation of the common signals generated on the electron-matter interaction.

The high-energy electrons interact elastically with the nuclei of the sample or inelastically with the sample electrons. Both may cause damage to the sample. Elastic interaction could cause atomic displacement and sputtering, whereas the inelastic interaction transfer higher amount of energy and may induces specimen heating, knock-on, structural damage, radiolysis, and mass loss [185], [188]. The extent and mechanism of these changes are highly related to the nature of the sample under analysis and their (if any) specific pretreatment. Weakly bonded atoms, or atoms with small bonding energy (such as hydroxides), may be displaced first under the electron beam [187]. Some strategies for investigating electron beam damage during the TEM analysis are the quantitative study of mass loss and the evolution of the chemical bonding by EELS during electron irradiation. Since electron diffraction requires a low electron dose during acquisition, and it is highly sensitive to structural changes, it would be safe to monitor changes in electron diffraction patterns upon irradiation [184].

In this chapter, we study the effect of irradiation on NiCuAl LDH and derived materials, which is crucial for the TEM investigation discussed. Specifically, we studied the influence of electron beam irradiation on the structure as a function of the (1) LDH composition for four different compositions; and (2) LDH pretreatment, i.e., calcination and reduction of NiCu(4:1)Al LDH.

6.1.2 Experimental

Transmission electron microscopy (TEM) analysis was performed systematically in order to understand how the synthesized material can be changed with the beam exposure. To track how the beam changes the structure of the material, a series of selected area electron diffraction (SAED) patterns were recorded on a FEI Talos F200X electron microscope. It was operated using an acceleration voltage of 200 kV, a condenser aperture of 70 µm, and a selected area aperture of 10 µm for the acquisition of the electron diffraction patterns. The settings led to an average beam current of ca. 480 pA on the sample, but the acquisition time and image size may vary. The workflow used during the experiment is summarized in Figure 52. First, a region of interest was chosen where the SAED was acquired using a magnification of 22.5 kx. Subsequently, a magnification of 190 kx was set, and the sample was irradiated using a dose rate of approximately 51 $e{\cdot}Å^{-2}{\cdot}s^{-1}$ during *t* seconds; then, the next SAED was recorded (using the same magnification of 22.5 kx). This process (blue boxes in Figure 52) may be repeated several times. Finally, the microscope settings were changed to scanning mode for the final electron beam irradiation at a higher dose (approximately 670 $e{\cdot}Å^{-2}{\cdot}s^{-1}$), and the last SAED was acquired. All SAED patterns were integrated azimuthally using the PASAD script [190] in Digital Micrograph. The reduced sample was transferred under air-free conditions using a specialized Gatan single tilt 648 holder. The X-ray diffractograms of the samples (LDH and derived materials) were shown elsewhere in the thesis and in this chapter are included for reference.

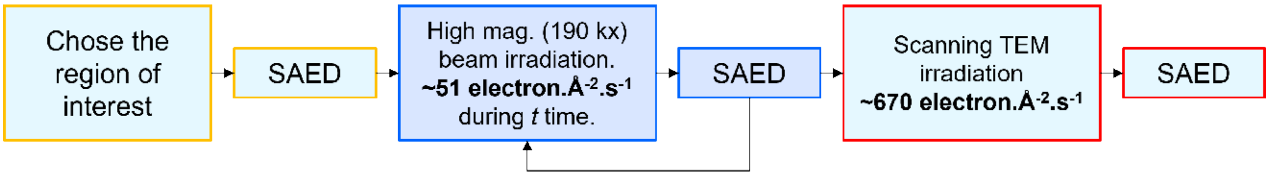

Figure 52: Workflow used for the electron beam irradiation studies.

6.2 Effect of vacuum on LDH

The sample's SAED patterns were compared pre and post vacuum exposure to rule out any vacuum-caused changes. Figure 53 shows this vacuum effect for the sample NiCu(1:1)Al investigated in two different positions. The black diffraction curves correspond to the SAED patterns acquired after insertion into the microscope (3 min pumping time on the stage). The red curves correspond to the patterns after 16 h in a vacuum of approximately $1x10^{-7}$ mbar. For comparison, X-ray diffractograms of LDH and the LDH after in situ calcination (185 °C, 5 h) were also included. As observed, there is almost no change between the SAED patterns before (t=0 h) and after (t=16 h) for both positions. The characteristic (003) reflection of the LDH was not observed in the SAED pattern because it may be hidden under the beam stopper. The low intensity of the (006) reflection from SAED, compared to the one from XRD may be due to vacuum conditions. Under vacuum, water is removed from the interlayer domain. The (006) reflection was slightly shifted to higher values after 16 h; this could correspond to the shift because of the dehydration of the layers during the calcination process. Since the beam effect experiments for each sample last less than 16 h, effects due to vacuum conditions are completely excluded.

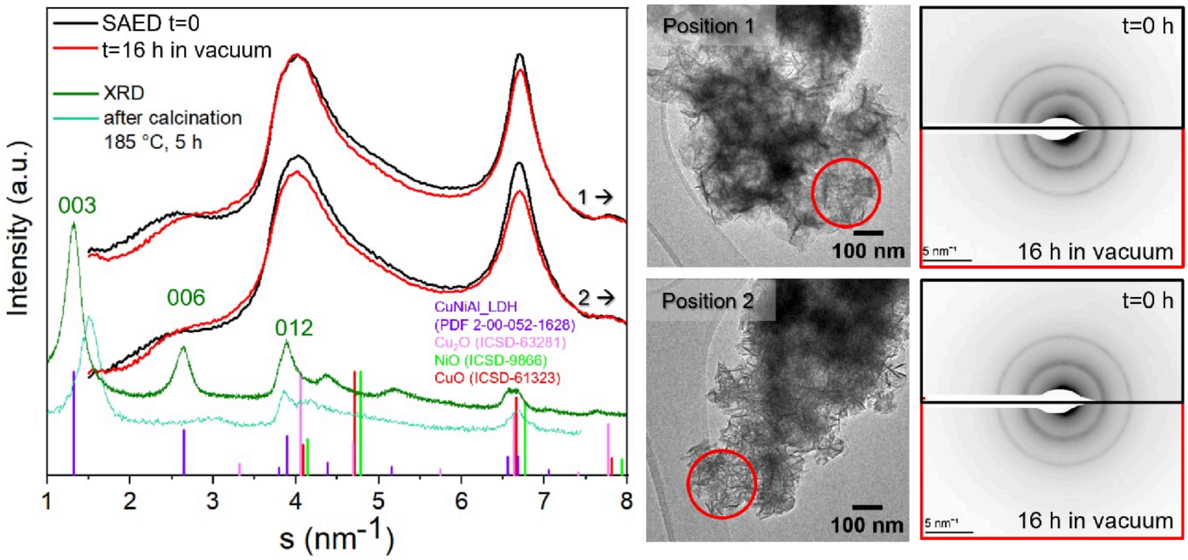

Figure 53: a) Electron diffractograms extracted from SAED patterns of the sample NiCu(1:1)Al before and after 16 h in the microscope; X-ray diffractograms are plotted for reference. b) TEM image of the analyzed area and their respective SAED patterns.

6.3 Effect of electron beam irradiation

The influence of the electron beam on the properties of the LDH and its derived materials was investigated systematically and qualitatively in two parts. In the first part, we report the changes in the structure for four LDH samples: NiAl, NiCu(4:1)Al, NiCu(1:1)Al, and CuAl. In the second part, the influence of pretreatment is compared for the NiCu(4:1)Al sample, investigated after calcination at 290 °C and after reduction at 300 °C. For all samples, the diffractogram at zero seconds represents the pristine structure of the investigated material (LDH, calcined, or reduced samples), assuming the electron dose is too low that it does not cause significant changes at that point.

6.3.1 LDH with different composition

The beam irradiation results for the LDH samples are shown from Figure 54 to Figure 57. In all figures, part A corresponds to the diffraction curves extracted from SAED patterns after sequential electron beam irradiation of the area shown in part C, which displays three images of the irradiation in TEM mode and the last STEM-HAADF image after the electron irradiation in STEM mode. Part B shows the first and last SAED patterns with the inset of the selected area analyzed. Moreover, X-ray diffractograms were added to part A as a reference for the bulk structure.

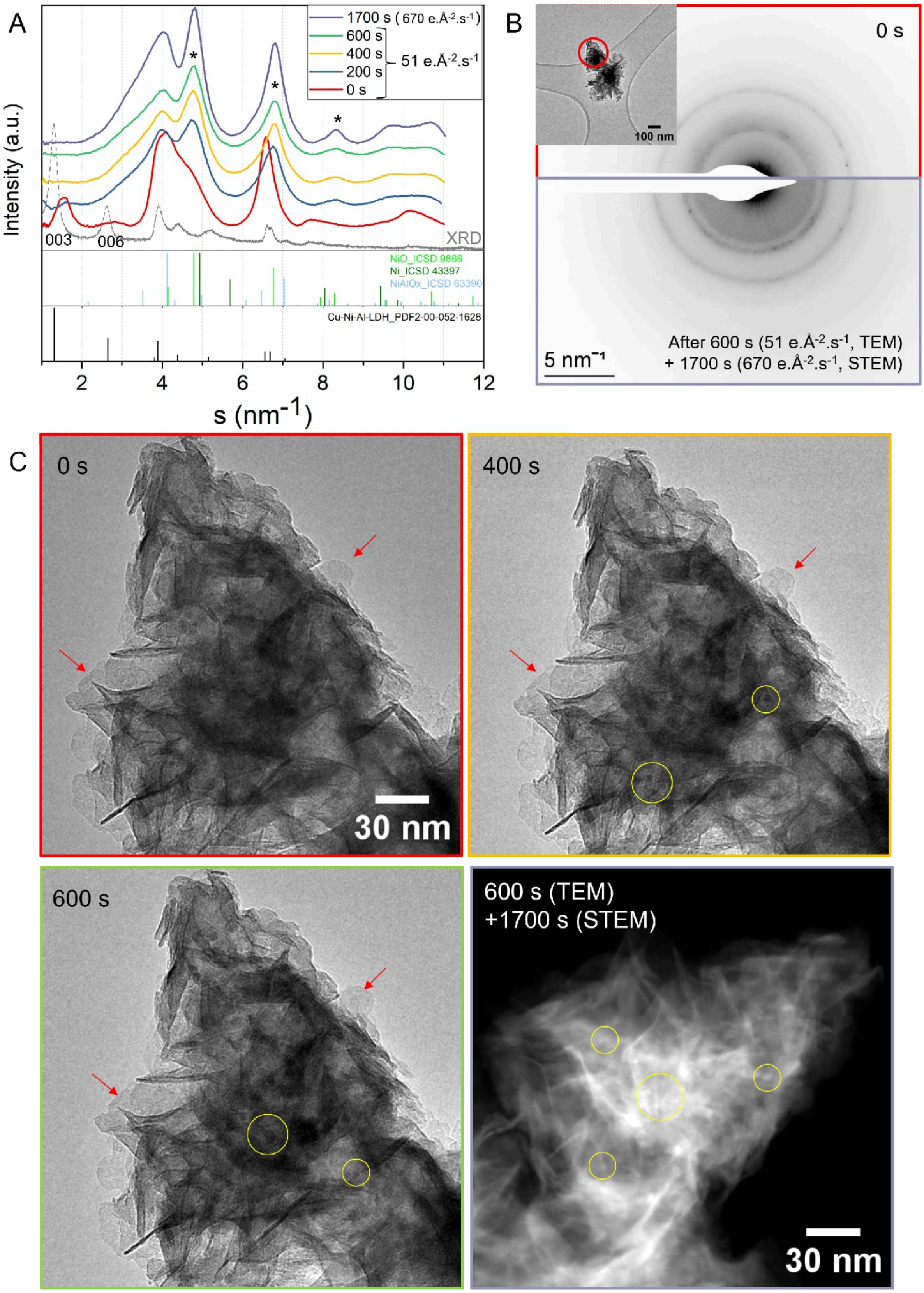

Figure 54: Electron beam studies of NiAl LDH sample. A) electron diffractograms with consecutive irradiation; B) SAED before and after beam irradiation and inset: the overview of the analyzed region. C) higher resolution TEM images.

Figure 54 shows the beam irradiation results of the NiAl LDH sample. From part A, it can be noted that the first electron diffractogram at 0 s shows the reflections 003 and 006 from the LDH, but with less intensity and shifted to higher values. This indicates the dehydration of the layers because of the vacuum under the microscope. After a cumulative dose of 10200 $e{\cdot}Å^{-2}$ (200 s at a dose of 51 $e{\cdot}Å^{-2}{\cdot}s^{-1}$), the diffractograms showed new reflections (asterisks marked in the figure), which might correspond to nickel oxides. Those new reflections are becoming sharper with increasing beam irradiation. The absence of metallic Ni reflections shows that the material was not reduced under the electron beam. As highlighted in Figure 54C, platelets at the edges of the LDH did not undergo significant changes during the experiment (red arrows). However, at the center of the irradiated area, a dark round-shaped contrast appeared (yellow circles). This might indicate that some nanoparticles were formed. These nanoparticles of less than 5 nm were also visible in the last step, where a higher dose was used for STEM imaging.

Similar results were observed for NiCu(4:1)Al (Figure 55) and NiCu(1:1)Al and (Figure 56) samples but apparently without the formation of nanoparticles. Platelets of the LDH did not show significant changes in morphology. However, the LDH structure quickly changed when exposed to the initial irradiation and showed oxide species, which may be a combination of nickel and copper. The reflections of the oxides became sharper as the electron dose increased, which indicates a higher long-range order or crystallinity. Furthermore, the analyzed area may also twist during the experiment as a consequence of the electron beam. This was more evident for sample NiCu(4:1)Al, as is marked with yellow circles in Figure 55C. What is interesting here is the absence of metallic species in all Ni-containing LDH samples.

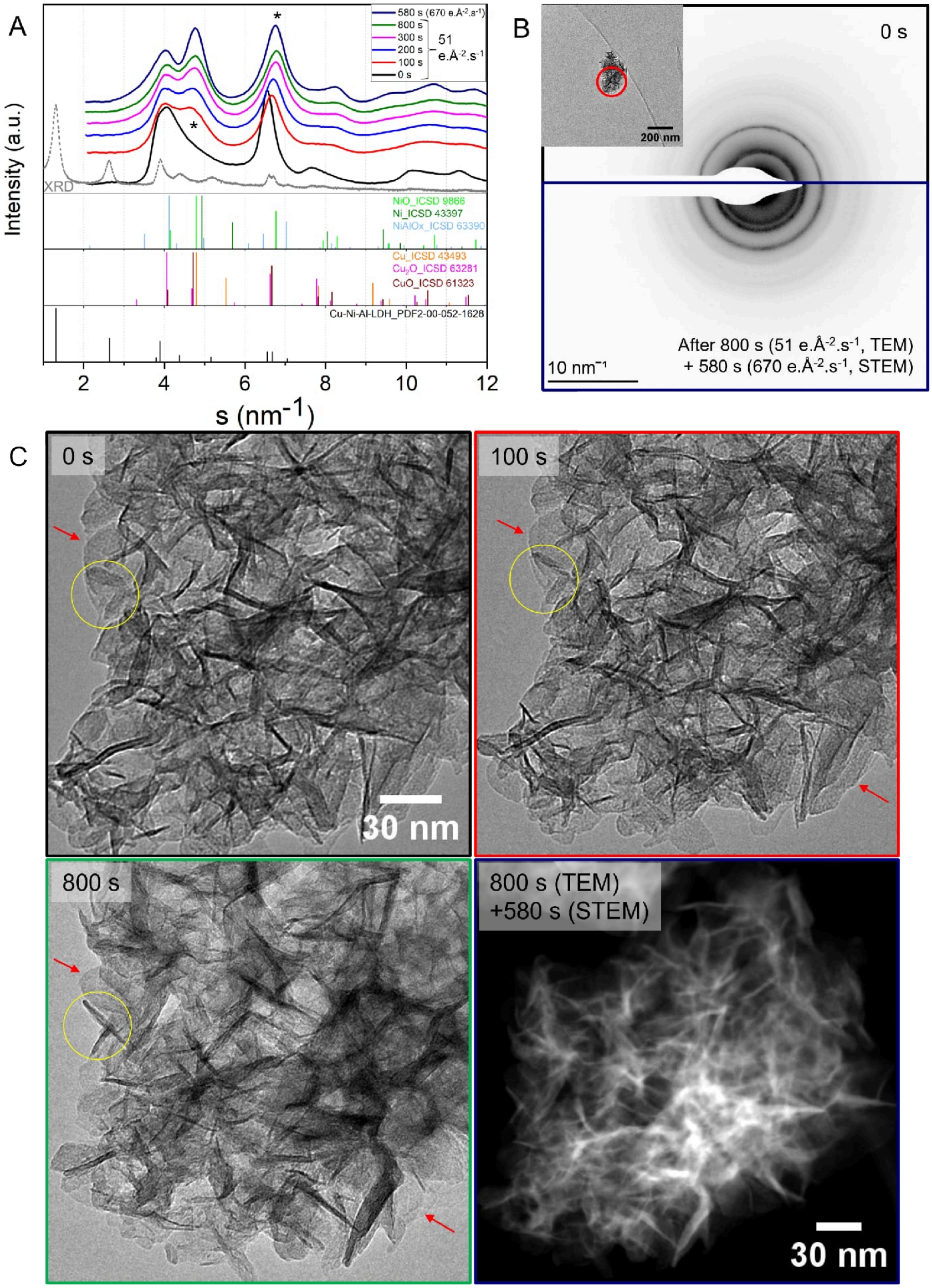

Figure 55: Electron beam studies of NiCu(4:1)Al LDH sample. A) electron diffractograms with consecutive irradiation; B) SAED before and after beam irradiation and inset: the overview of the analyzed region. C) higher resolution TEM images.

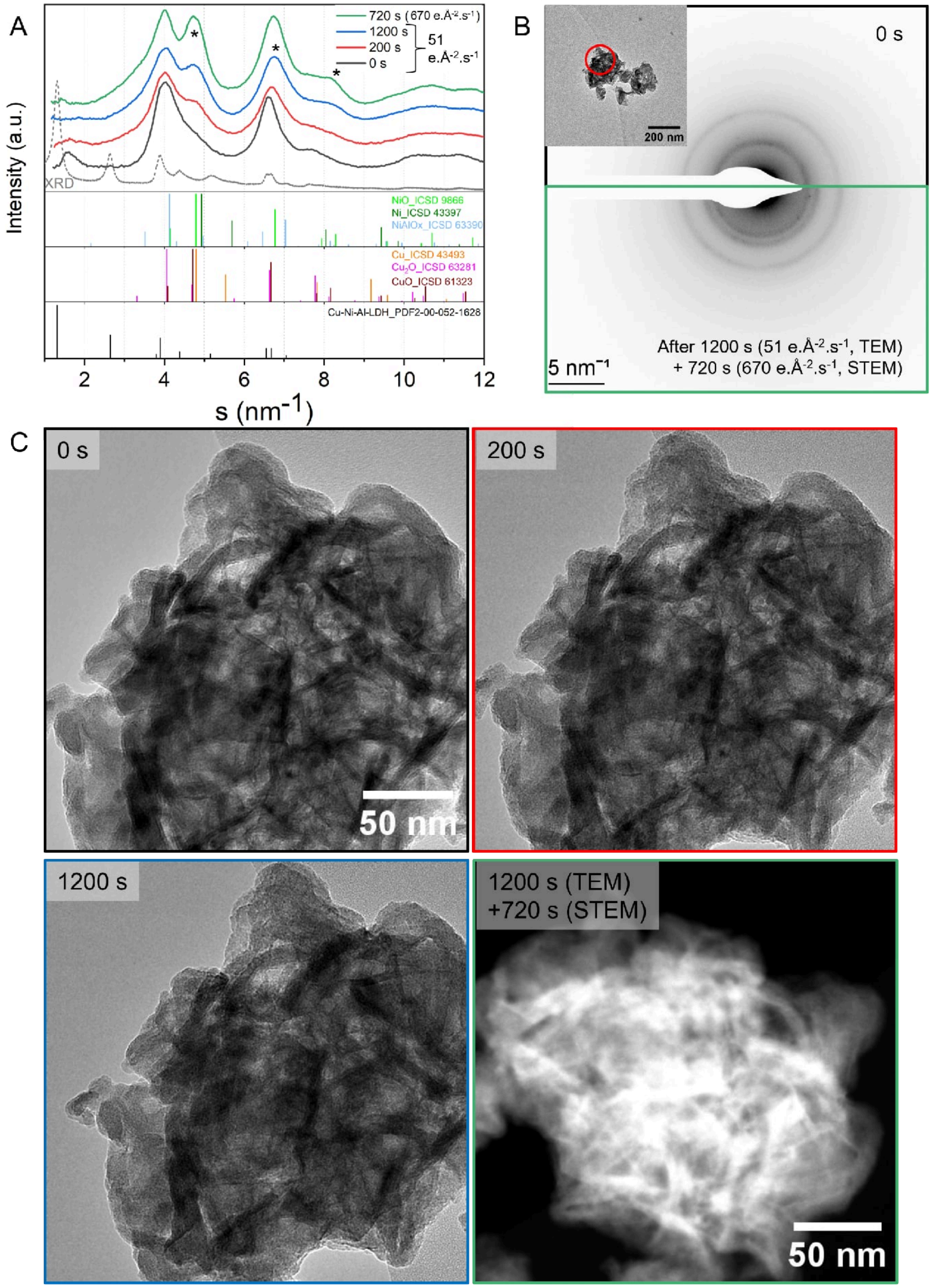

Figure 56: Electron beam studies of NiCu(1:1)Al LDH sample. A) electron diffractograms with consecutive irradiation; B) SAED before and after beam irradiation and inset: the overview of the analyzed region. C) higher resolution TEM images.

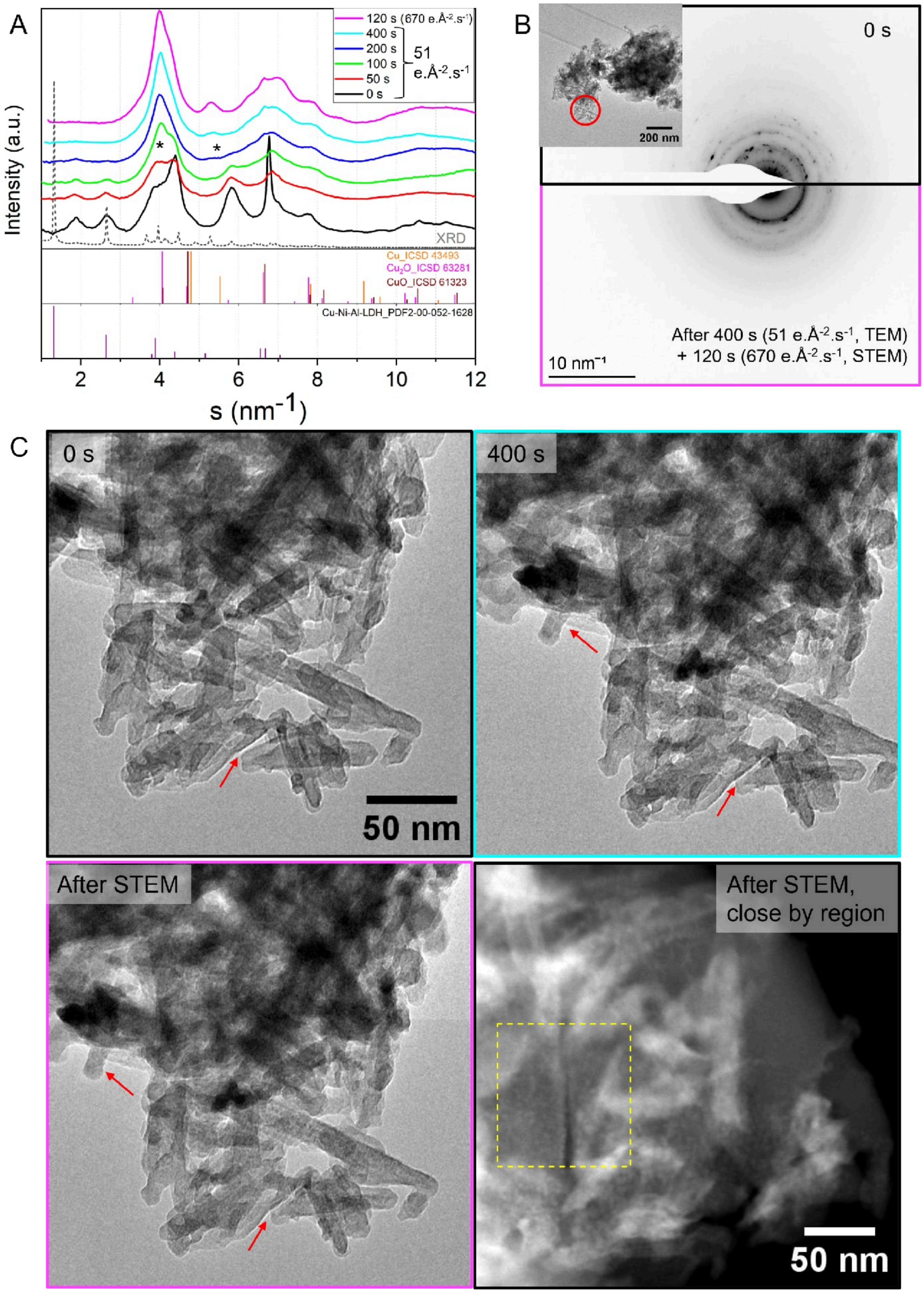

Figure 57: Electron beam studies of CuAl LDH sample. A) electron diffractograms with consecutive irradiation; B) SAED before and after beam irradiation and inset: the overview of the analyzed region. C) higher resolution TEM images.

Finally, Figure 57 shows the electron beam studies for the CuAl sample. The SAED pattern of the sample before electron irradiation showed characteristics of crystalline material (sharp spots), together with the polycrystalline (rings). Upon electron beam exposure, after just 50 s at a dose rate of 51 e·Å^{-2}·s^{-1} (cumulative dose of 2550 e·Å^{-2}·s^{-1}), the sharp reflection at 6.8 nm^{-1} was lost and the signal at 5.8 nm^{-1} decreased, possibly because of the destruction of the LDH structure. Furthermore, a new reflection at ca. 4.1 nm^{-1} appears (asterisk in Figure 57A), which might represent CuO or Cu_2O species. After 200 s, a new reflection arose at ca. 5.40 nm^{-1}, probably corresponding to metallic Cu. Seemingly, after irradiation in STEM mode, this Cu peak is slightly shifted to lower values, probably because of an expansion in the lattice due to the incorporation of oxygen or aluminum. However, further investigation, such as EELS, would be needed to corroborate this. The presence of metallic Cu reflections could be related to the small nanoparticles observed in the STEM-HAADF image at the end of the experiment. Similar to the NiCu(4:1)Al sample, the platelets of the CuAl sample appear to tilt or twist during the investigation, indicated by the red arrows in Figure 57C. No significant changes in morphology were observed at the magnification used for the TEM images. However, as mentioned above, after the last irradiation, a cumulative electron dose of 100800 e·Å^{-2} small nanoparticles were observed, indicated in the yellow square in Figure 57C.

Overall, these results indicate that LDHs are both sensitive to the microscope's vacuum and electron beam. Vacuum removes the water from the interlayer domain. Under the electron beam, these structures change unceasingly. After long TEM experiments, the Ni-containing LDH samples might rearrange to mixed metal oxides, or in cases of low cumulative electron dose, perhaps a combination of the remaining LDH and oxides. Metallic species were formed under the electron beam just for the CuAl sample; owing to the property of Cu to be easily reduced.

6.3.2 LDH after pretreatment

Figure 58 shows the electron beam irradiation studies of the NiCu(4:1)Al_ox290 sample, which is the NiCu(4:1)Al LDH after calcination at 290 °C for 3 h. In the same way as in the previous figures, in part A the evolution of the electron diffractograms is observed, in part B the SAED patterns and the inset of the TEM image show the analyzed area, and in part C the higher resolution TEM images are shown. For this sample, two irradiation experiments were performed. The first was 'short' irradiation, using conditions similar to those of the experiments presented in the previous section; and 'long' irradiation, where the electron beam was irradiated for a prolonged time in STEM mode to investigate whether metallic species were formed. During the 'short' irradiation experiment, the (Ni and Cu) oxide reflections in the diffractograms (Figure 58A) became sharper as the electron dose increased; no new reflections were observed and there were no changes in the morphology, as can be seen in Figure 58C. This indicates an increase in the long-range order or crystallinity of the (already present) oxide species that maintain their platelet structure.

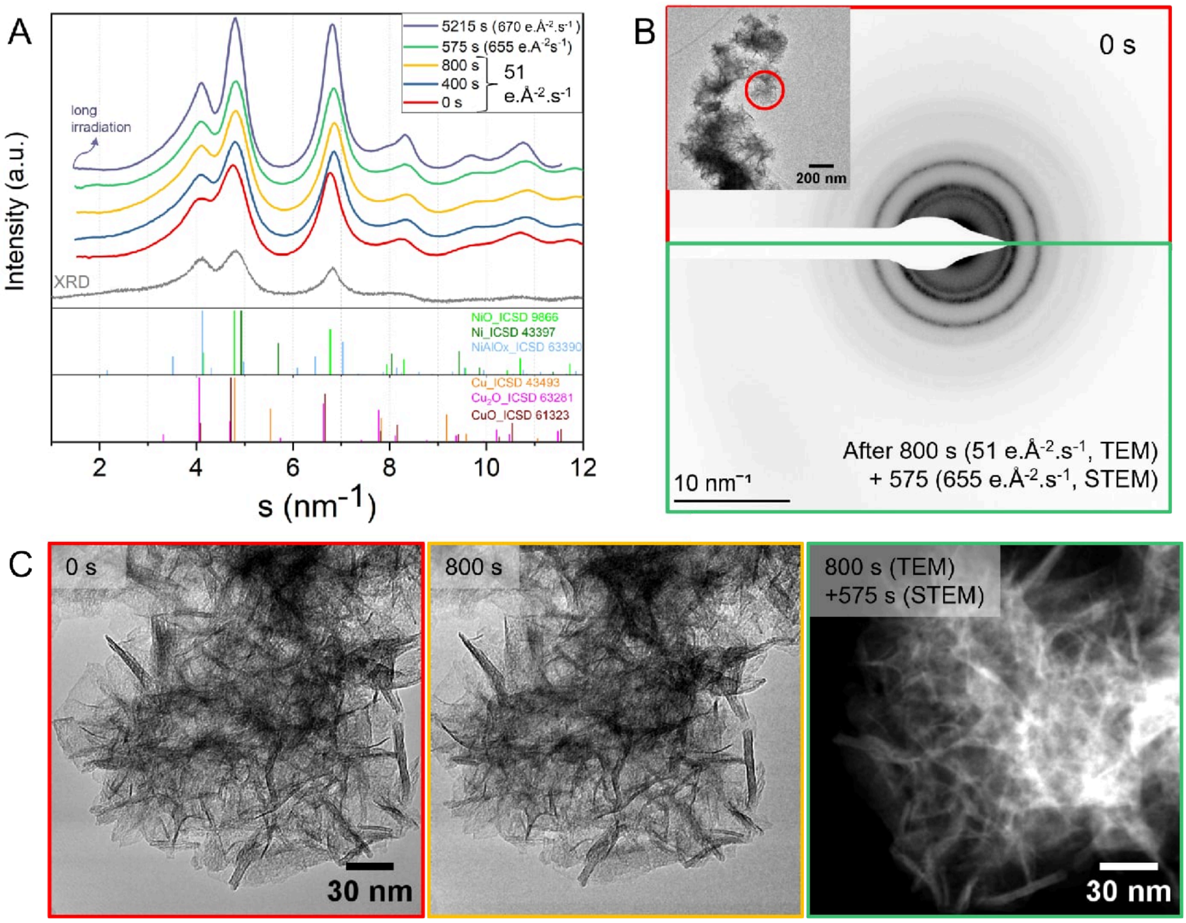

Figure 58: Electron beam studies of NiCu(4:1)Al_ox290 sample. A) electron diffractograms with consecutive irradiation. B) SAED before and after beam irradiation and inset: the overview of the analyzed region. C) higher resolution TEM images.

Figure 59 shows the SAED patterns and images of the NiCu(4:1)Al_ox290 sample during long electron beam irradiation. The electron diffractogram was included in Figure 58A (see the 'long irradiation' curve). Interestingly, after the experiment, more than 5200 s at 670 e·Å^{-2}·s^{-1} (cumulative dose of 3.5x10^{6} e·Å^{-2}), no evidence of metallic species was observed. The metal oxide reflections became sharper, as described above, because of the increase of the long-range order. However, significant changes in morphology were observed. STEM-HAADF images (Figure 59C) show the formation of some voids or probably porous structures that were large enough to be distinguished when the cumulative dose reached 1.7x10^{6} e·Å^{-2}. This may represent the destruction of the platelet morphology due to electron beam irradiation. Higher resolution TEM images (Figure 59B) clearly display the voids, which randomly appear along the layer; a schematic representation is shown in the inset. This process probably started with the formation of isolated vacancies at atomic scale because of the rearrangement (and slight crystallization) of the amorphous oxide layer. With longer irradiation time, the vacancies may grow and generate what looks like the layer's destruction.

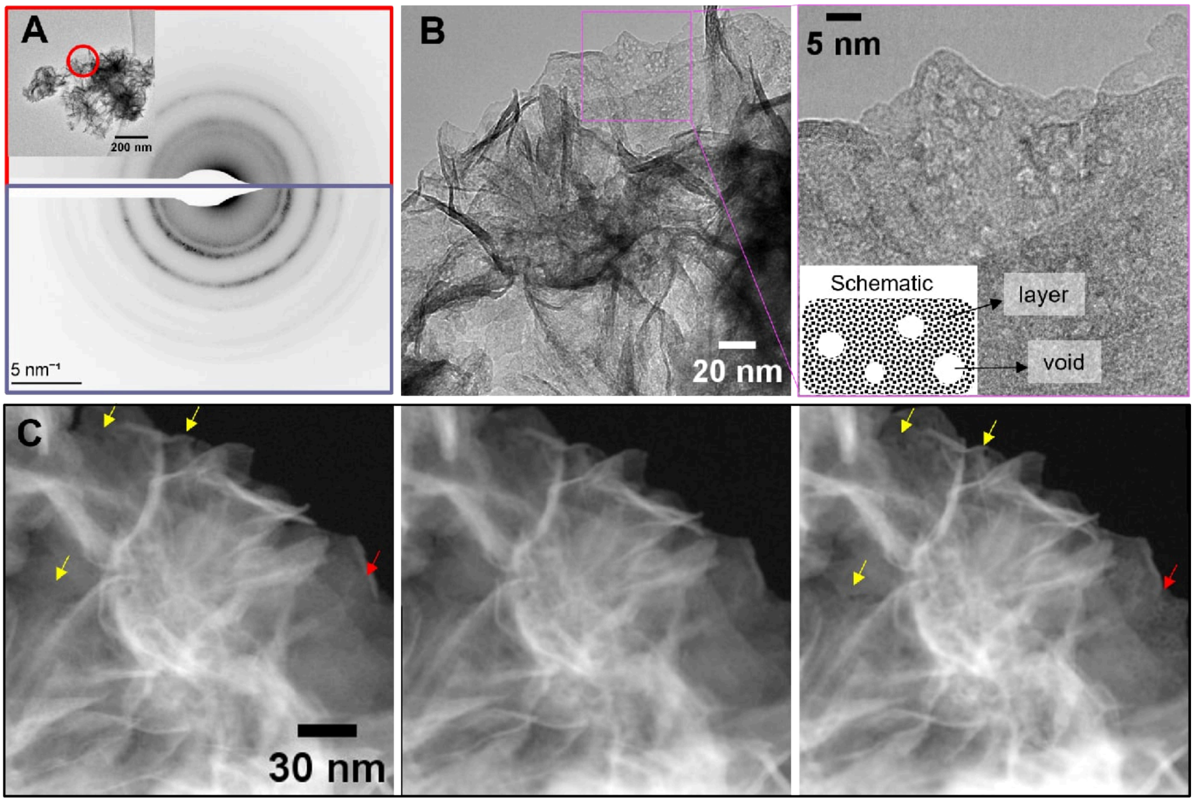

Figure 59: Prolongated electron beam studies of NiCu(4:1)Al_ox290 sample. A) SAED before and after beam irradiation and inset: the overview of the analyzed region. B) higher resolution TEM images showing the damage of the platelets. C) STEM images during beam irradiation.

Figure 60 shows the electron beam studies of the sample NiCu(4:1)Al_ox290 after the reduction process at 450 °C. For this experiment, the sample was transferred inertly from the glove box to the electron microscope. The electron diffractogram of the zero irradiation (red curve) fits the reflections of the X-ray diffractogram. After 200 s of electron beam irradiation (51 $e \cdot \text{Å}^{-2} \cdot s^{-1}$) no drastic changes were observed. Rather, the metallic reflections (4.9, 5.6, and 8 nm^{-1}) decreased during the experiment. Moreover, the presence of aluminates can be suspected because of reflections emerging at ca. 4 and 7 nm^{-1}. This implies the transformation of metal into spinel structures.

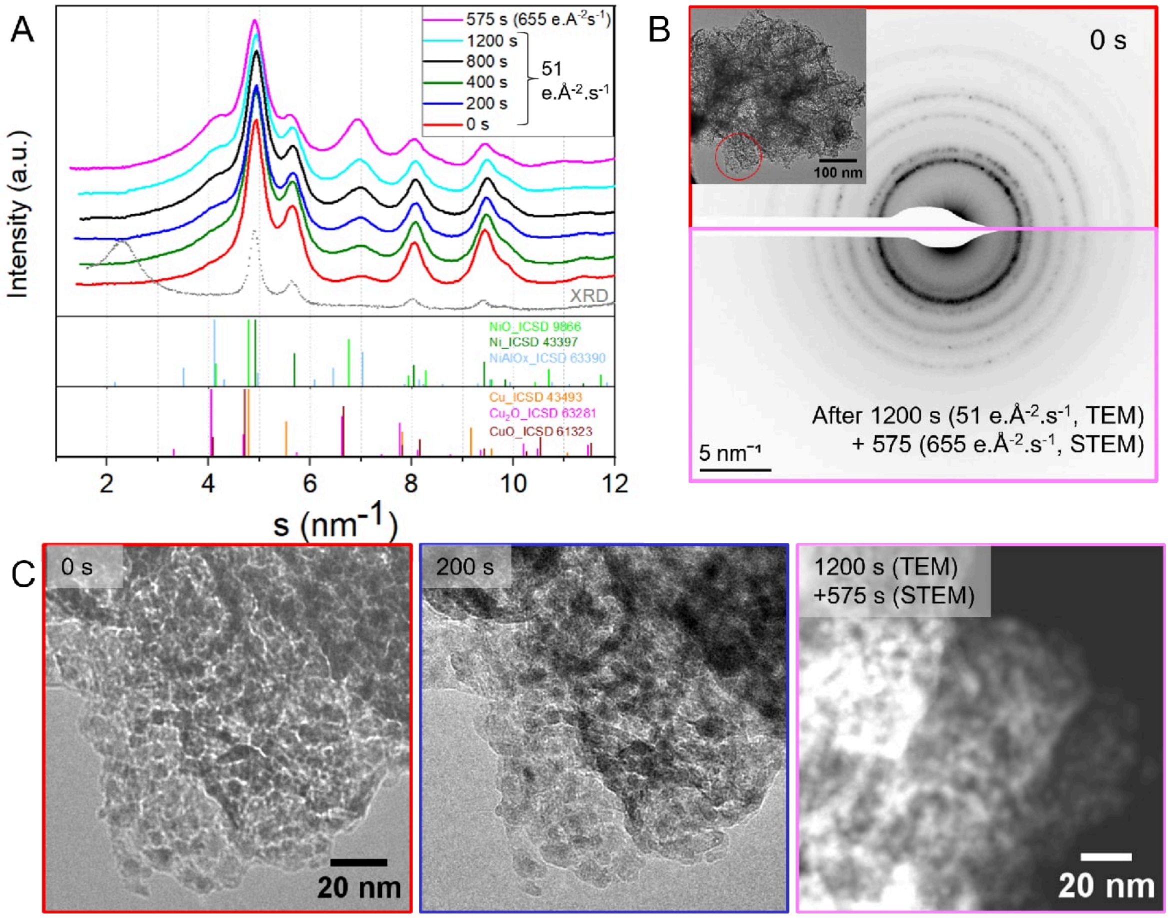

Figure 60: Electron beam studies of NiCu(4:1)Al_ox290_red450 sample. A) electron diffractograms with consecutive irradiation; B) SAED before and after beam irradiation and inset: the overview of the analyzed region. C) higher resolution TEM images.

6.4 Conclusions

The structural changes of the LDH and derived materials were qualitatively tracked to analyze the effect of consecutive electron beam irradiation. The structure was measured by SAED patterns. Results show that the LDHs' structure is sensitive to vacuum and electron-beam, but kept their platelet morphology. Due to the vacuum conditions, the water molecules located in the interlayer domain (weakly bonded atoms) are removed first. The former was evidenced by a shift of the (003) and/or (006) reflections to higher values. Those are characteristic reflections of LDH structures.

The structure of the LDH might change upon beam irradiation, even when no clear morphological changes are visible. These changes were evaluated by tracking the SAED signal in comparison with the zero irradiation curve in each sample. The most likely outcome due to electron-beam irradiation is the removal of the weakly bounded water; followed by the expulsion of the hydroxy (OH-) groups of the LDH, as reported for hydroxyapatite [187]. The hydrogen may be removed through the vacuum, and the oxygen may be combined with the metals to form metal oxides. Those oxides can increase their long-range order or crystallinity with increasing electron dose. The CuAl sample was the most beam-sensitive, and metallic species were observed after the irradiation experiment. Interestingly, there was no formation of metallic species under the electron beam for the NiCu(4:1)Al sample previously calcined, even after prolonged irradiation. We produced long-range order oxidic species. When metallic species were already present in the reduced sample (NiCu(4:1)Al_ox290_red450), it is likely that the electron beam caused a transformation of these species to spinel structures.

For investigating LDH materials in the TEM it is important to perform systematic experiments in order to minimize the electron beam irradiation. When the LDH samples are treated at higher temperatures, it is *safer* to perform longer TEM characterization.

7 Summary and final conclusions

The climate change and recent global energy crisis motivate the search for environmentally friendly CO_2 utilization and alternatives for hydrogen storage and transport. Transition metal catalysts, such as Ni-Cu, are a promising option for energy conversion. Recently, layer double hydroxides (LDH) are being considered as promising catalyst precursors due to the synergistic effects of their components. The aim of the present work was to gain a fundamental understanding of the Ni-Cu interaction of materials derived from LDH precursors. For that, a series of NiCuAl LDH samples were synthesized and different activation procedures were investigated. Their reactivity was tested for the hydrogenation of CO_2 and dehydrogenation of NH_3 reactions; the latter being a promising way for hydrogen transport. Chemical electron microscopy was employed, combined with complementary techniques, to investigate the NiCu bimetallic structures from the as-synthesized LDH, to the activated and spent catalysts after reactivity. In order to gain fundamental understanding of the structure-function relationships, the focus was on investigating the properties of the catalysts with respect to combinations of nickel and copper components in different ratios.

Initially, NiAl, NiCu(4:1)Al, NiCu(1:1)Al, and CuAl LDH materials were synthesized by the co-precipitation method with a homogeneous distribution of the elements and carbonate ions in the interlayer domain. The measured Ni/Cu molar ratio was close to the nominal value, indicating a successful synthesis. The 3D morphology of the NiCu(4:1)Al LDH sample (observed by TEM tilt series) revealed flower-type nanoplatelet structures oriented in different directions. For the LDH samples with a higher Cu content (NiCu(1:1)Al and CuAl) the flower-type morphology became flat nanoplatelets of different dimensions. Moreover, these Cu-containing samples formed high-temperature carbonates observed by TG that were not present in the sample with a lower Cu content. CuAl LDH had the highest long-range order crystallinity (sharp XRD reflections).

To produce highly dispersed nanoparticles supported on alumina, different activation pretreatments were studied. The effect of calcination temperature on the reducibility of nickel and copper (the reducible species) showed that when the material is calcined under mild conditions (290 °C), lower temperatures are needed to achieve the reduction. On the contrary, when high calcination temperatures are used, it may lead to the formation of highly thermostable Ni spinel structures, which require high reduction temperatures. We successfully avoided spinel formation by calcination at 290 °C. The long-range order increased with temperature during calcination and reduction experiments. The reduction of NiCu(4:1)Al (previously calcined at 290 °C) to 300 °C showed a preferential growth of nanoparticles facing the [111] direction with respect to the sheet. At higher temperatures, the nanoparticles are probably reoriented while their particle sizes are increased with the temperature. A reduction temperature of 450 °C was chosen to prepare homogeneously dispersed nanoparticles.

The effect of Cu on Ni reducibility was clearly evidenced. Cu incorporation promoted the reduction of Ni at lower temperatures, probably through the H_2 spillover in the sample NiCu(4:1)Al. The further addition of Cu did not cause any additional changes to the Ni reduction peak. A small amount of Cu (Ni/Cu ratio of 4) is enough to produce this effect. Here, we used a molar ratio of 4:1; however, future studies should aim to optimize the amount of Cu. After reduction at 450 °C, the NiCu bimetallic nanoparticles showed Cu enrichment on the surface, explained by the miscibility gap of the Ni Cu solid solution, barely reported for supported bimetallic nanoparticles. Above 600 °C, the Cu that was on the surface is incorporated into the lattice of the alloy or solid solution. The activated samples (calcined at 290 °C and reduced at 450 °C) showed a platelet-like morphology decorated with nanoparticles. The local electronic structure (by EELS) suggested a metal-support interaction for the Ni-containing samples, but weak for the CuAl sample.

The catalytic performance of the series of NiCuAl was evaluated in CO_2 hydrogenation and ammonia decomposition reactions, as model reactions for hydrogenation and dehydrogenation. The characterization of the spent catalysts after both reactions has highlighted that when Cu is used in the same molar content as Ni (NiCu(1:1)Al), notable Cu segregation occurred, forming particles larger than 100 nm with metallic core and oxidized surfaces due to the air-contact during transport. In low amounts, i.e. sample NiCu(4:1)Al, the effect of Cu addition differs depending on the reaction studied.

For the CO_2 hydrogenation reaction, Ni promotes methanation, and the addition of Cu suppressed CH_4 formation by enhancing CO selectivity. In this bimetallic formulation, the Ni component adds stability, probably because of an overlayer formed during the reaction. On the other hand, the highest activity for ammonia decomposition was obtained with NiAl material (91% at 600 °C) and was significantly suppressed with the addition of Cu (41%). Furthermore, the presence of nitrogen species coexisting with Ni was detected in the center (bulk) of the nanoparticles. Although the CuAl sample was not active for ammonia decomposition (<7%), some nitrogen species were observed in the spent catalyst, which could be related to AlN formation; Cu nitrides were not observed. Interestingly, the spent NiCu(4:1)Al sample showed more Cu on its surface after CO_2 hydrogenation, but not after ammonia decomposition. After ammonia decomposition, the NiCu bimetallic system might remain as an alloy. This could be associated with the different chemical potentials that affect the same material differently.

The sample, NiCu(4:1)Al was further studied under operando TEM for the reverse water gas shift reaction as a model process of the CO_2 hydrogenation. Before the reaction, the activation process was also studied and correlated with in situ XRD. During calcination, local and integral characterization showed the shrinkage of the layered structure and the formation of oxides. The reduction of CuO species might form metallic Cu dispersed atomically at temperatures below 200 °C. The operation conditions in the OTEM did not allow for direct observation of the Cu species or the nature of the nuclei where the nanoparticles are formed. However, nanoparticles were observed in TEM images from 300 °C and were homogeneously distributed along the platelets. Using the same calcination and reduction conditions as those in the ex situ experiments, the activated catalyst presented a combination of oxides and metallic species. During the CO2 hydrogenation on the operando TEM cell, the oxides were further reduced and there was a remarkable CO and H_2O production despite the low amount of catalyst used (few micrograms). The apparent activation energies of the nanoreactor were comparable with those of the lab-reactor experiments. However, these results need to be interpreted with caution because of the different geometries of the setups.

Since all samples analyzed by TEM are likely to undergo damage due to the high-intensity probe, the last chapter of the thesis was dedicated to studying the beam effects of the LDH and derived materials. Systematic experiments were conducted to describe the structural changes, using electron diffraction patterns, during consecutive beam irradiation. All investigated LDH samples (NiAl, NiCu(4:1)Al, NiCu(1:1)Al, and CuAl LDH) are highly sensitive to beam irradiation. The Ni-containing LDH samples transform into metal oxides under the electron beam. Only the CuAl LDH sample may form metallic copper during electron beam irradiation. For LDH-derived samples, the material NiCu(4:1)Al was studied after its calcination at 290 °C and its reduction at 450 °C. We conclude that the degree of damage of the investigated samples varies in the order LDH < mixed metal oxides (MMO) < reduced samples. When the material is pretreated at higher temperatures, it can withstand higher electron doses before its structure changes. The MMO increases its crystallinity (long-range order) with beam irradiation. Surprisingly, no metallic nickel and copper species are observed after prolonged irradiation, even when voids or holes are created in the layer morphology. However, when the sample is already reduced, the electron may induce further reduction, and probably the formation of Ni-spinel structures. Our results show the importance of considering electron damage during TEM investigations because it might cloud the interpretation of the results. The observed beam effects are not limited to microscopy techniques, but to all characterizations that involve the electron-matter interaction.

Further investigations could attempt to optimize the copper content in Ni-Cu bimetallic nanocatalyst systems derived from LDH and study the influence of other supports. Computational studies could shed light on the nucleation process and probably confirm our assumption that nucleation starts at defect sites; but beyond that, it could hopefully describe whether the nature of defect sites is related to the atomically dispersed copper. Operando TEM characterization is and will continue to be very important for unraveling the catalysts' changes during chemical reactions. It is, however, limited to well-defined catalyst and model reactions for a deep understanding of the catalyst behavior. The combination of knowledge of the ammonia synthesis and decomposition, together with cutting-edge operando characterizations, can allow a comprehensive description of the ammonia decomposition process. This will help the new energy infrastructure because ammonia can be used for hydrogen storage. However, carbon dioxide hydrogenation is much more complex because of the multiple-reaction network.

A Supplementary information

A.1 Supplementary information Chapter 3

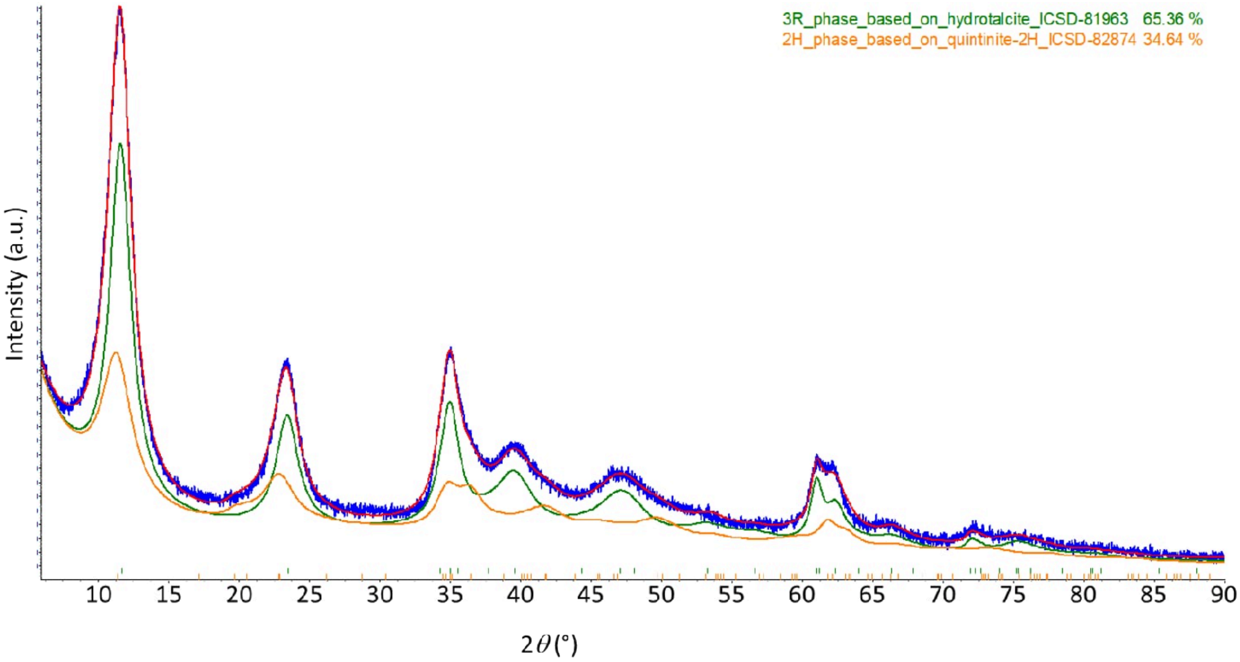

Figure 61: X-ray diffractogram fitting of NiCu(4:1)Al LDH sample. It indicates the presence of two stacking variants of LDH: 3R structure and the 2H structure.

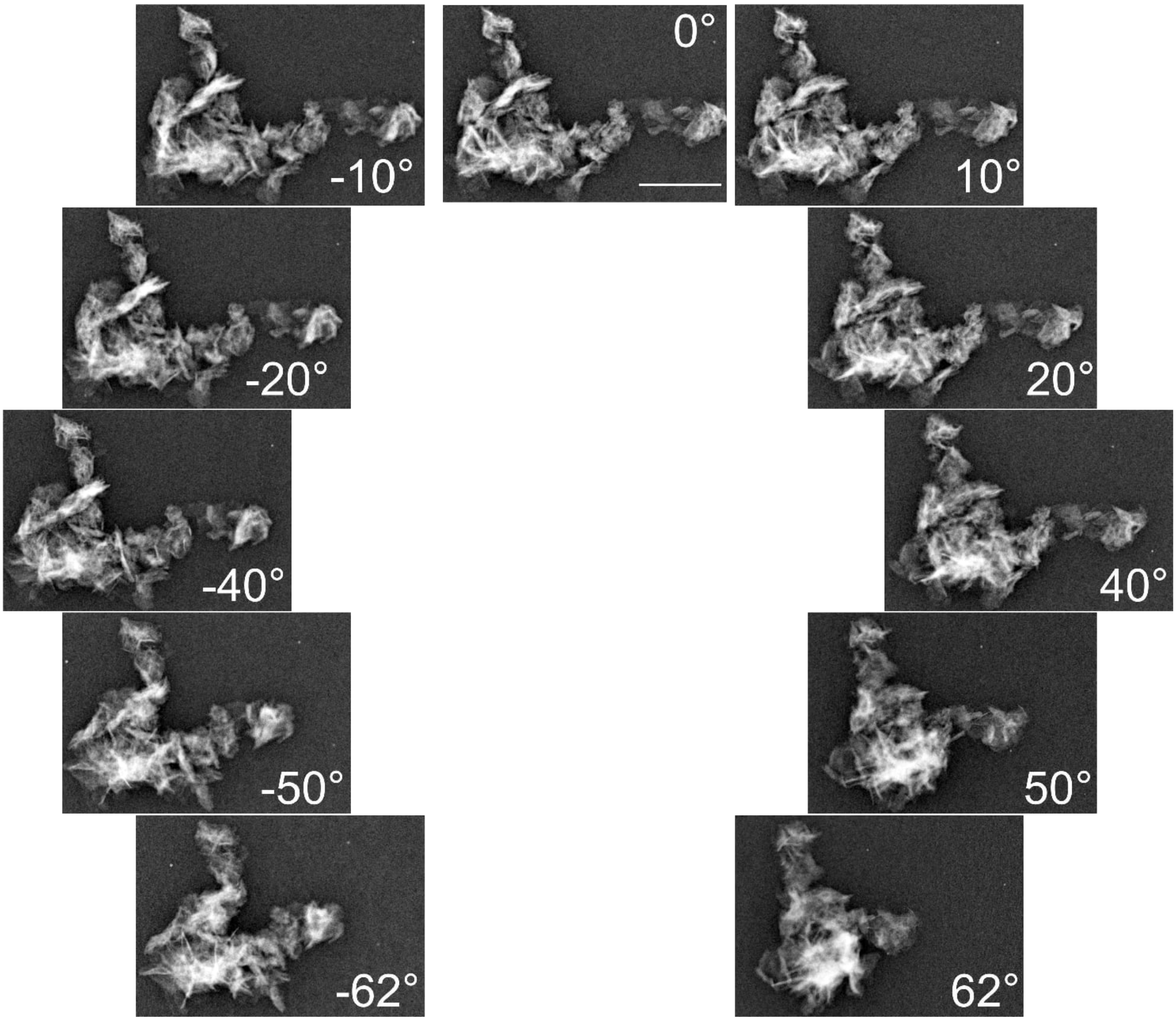

Figure 62: TEM tilt series of NiCu(4:1)Al-MMO: TEM images acquired at different tilt angles. Scale bar: 200 nm.

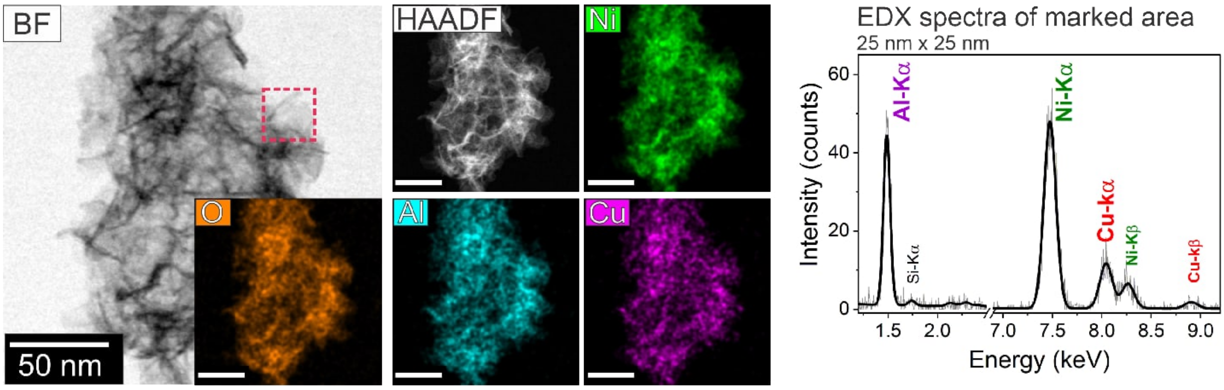

Figure 63: STEM-EDX mapping of NiCu(4:1)Al_ox290. Integrated spectrum from the marked area (25 nm x 25 nm) shows the homogeneous distribution of all elements after calcination.

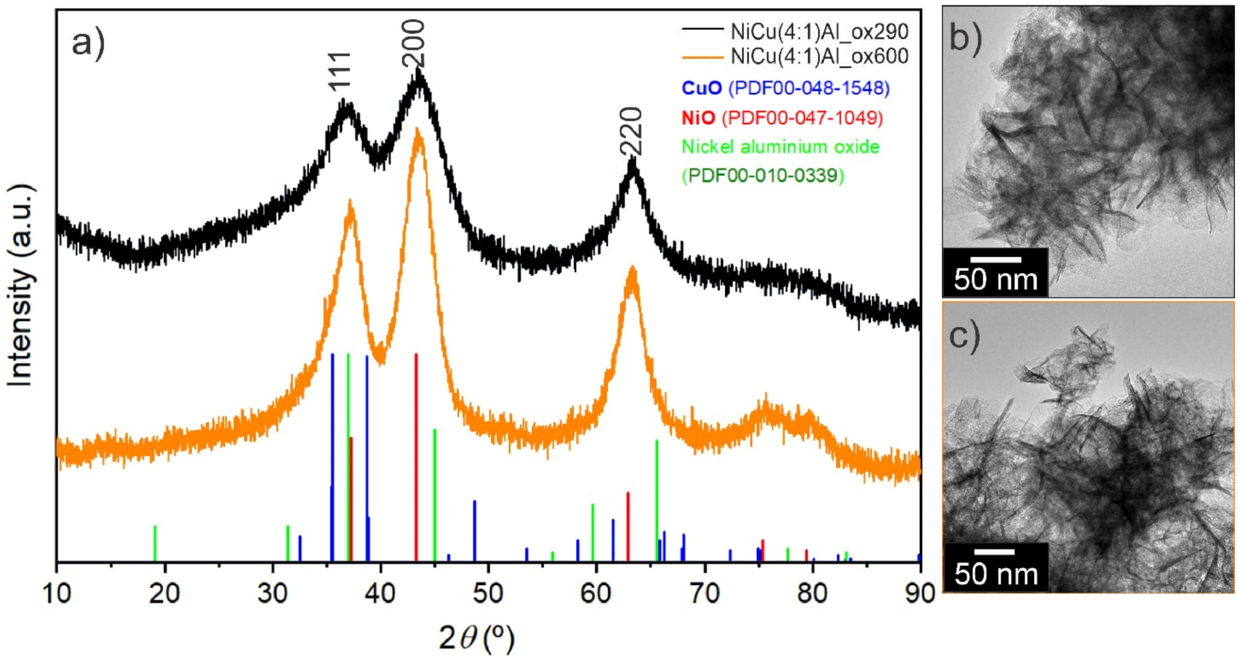

Figure 64: X-ray diffractograms of NiCu(4:1)Al sample calcined at 290 °C for 3 h and 600 °C for 10 min, with the corresponding TEM micrographs in b) and c), respectively.

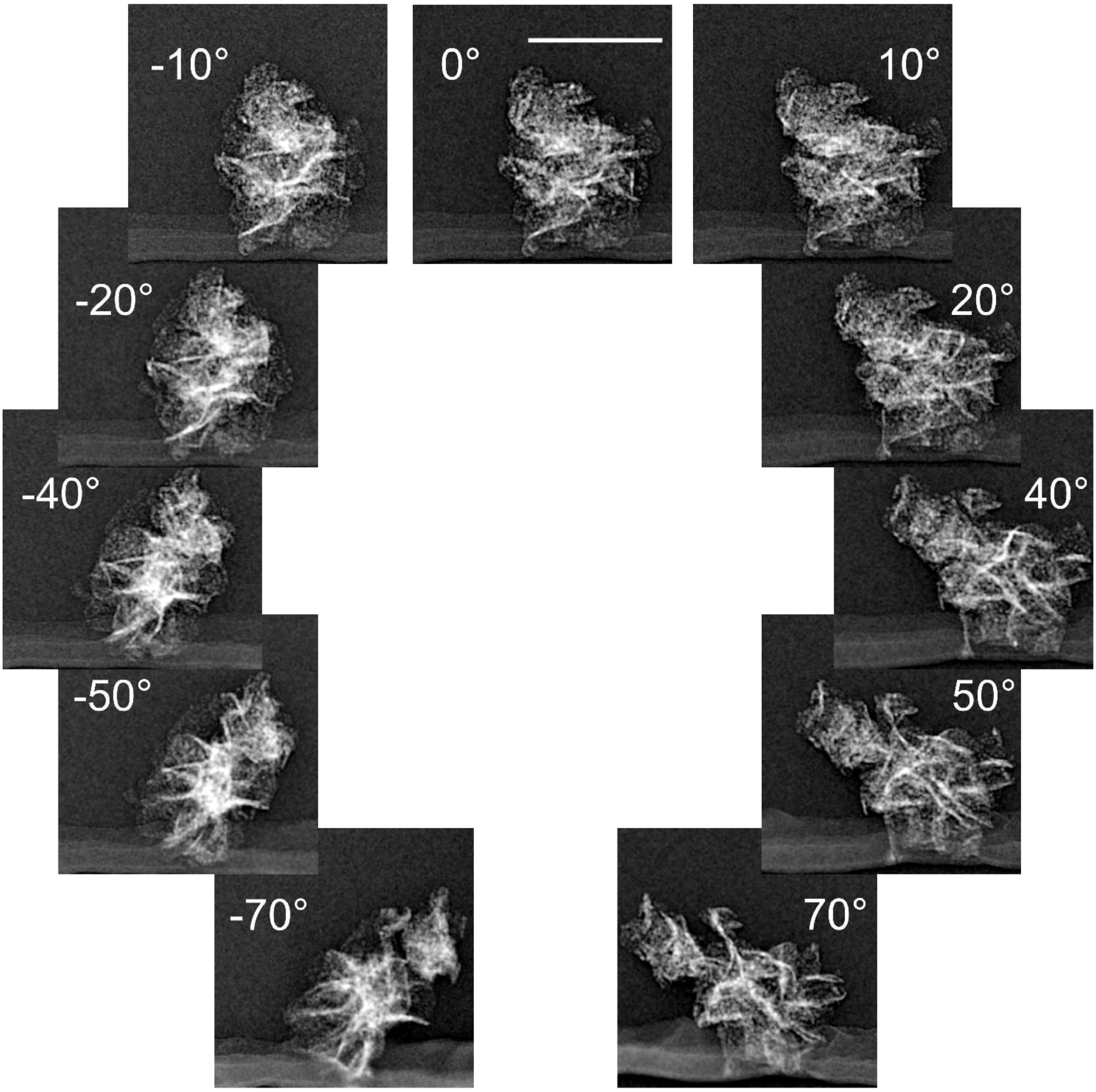

Figure 65: TEM tilt series of NiCu(4:1)Al_ox290_red450. TEM images acquired at different tilt angles. Scale bar: 200 nm

Table 5: Comparison of the expected and observed (refined) lattice parameters a [Å] for the reduced samples for an alloy formation of $Ni_{(1-x)}Cu_x$.

Sample	x in $Ni_{(1-x)}Cu_x$	a [Å] theory	a [Å] observed
Ni, PDF2 00-004-0850	0	3.524	
NiAl_ox290_red450 (sn.34494)	0	3.524	3.523
NiCu(4:1)Al_ox290_red450 (sn.34513)	0.2	3.542	3.533
NiCu(1:1)Al_ox290_red450 (sn.34505)	0.5	3.570	3.572
CuAl_ox290_red450 (sn.34522)	1	3.615	3.616
Cu, PDF2 00-004-0836	1	3.615	

The theoretical a-parameter was estimated by linear interpolation between the Ni and Cu PDF references assuming Vegard behavior; the observed one, from Rietveld refinement of the experimental diffractograms.

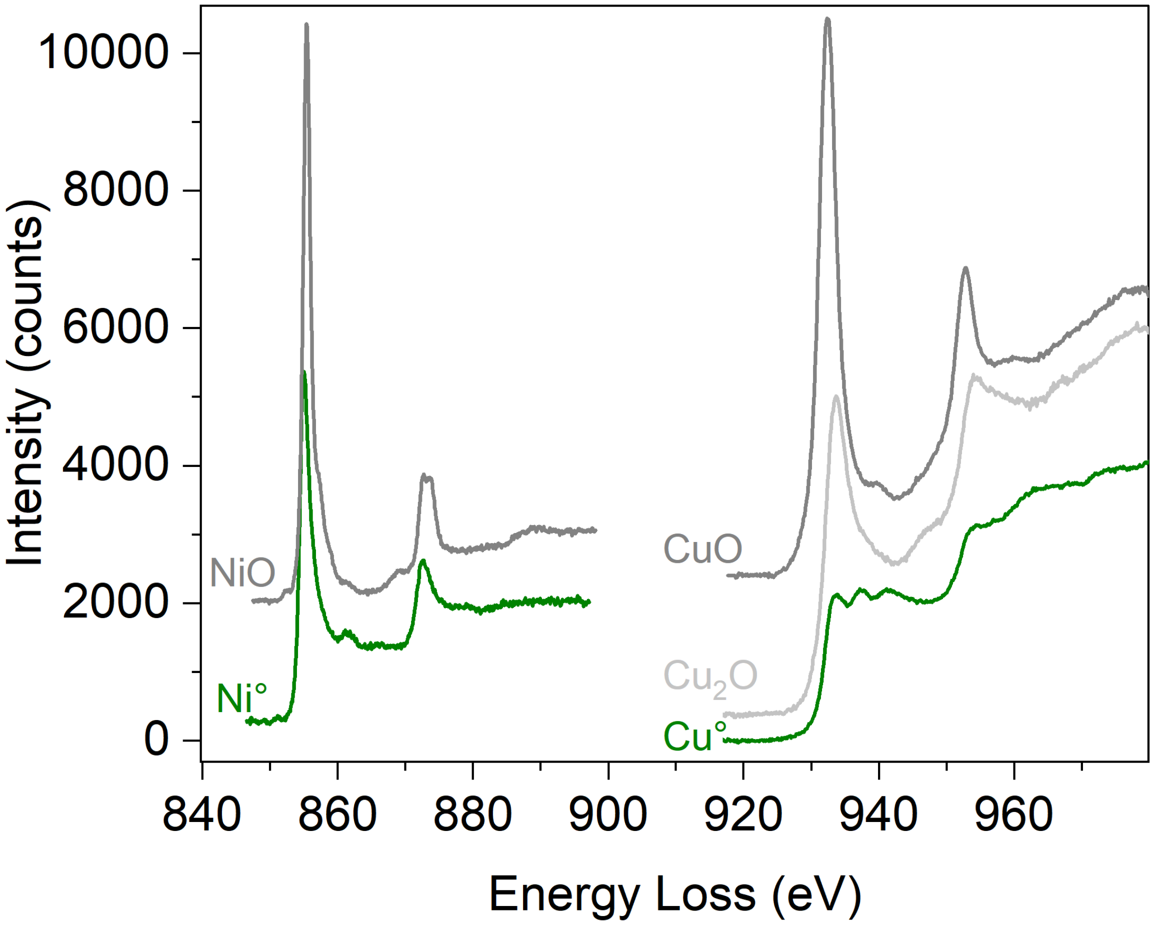

Figure 66: ELNES references for Ni and Cu species.

Adapted from Potapov [124] (Ni) and Ngantcha [159] (Cu).

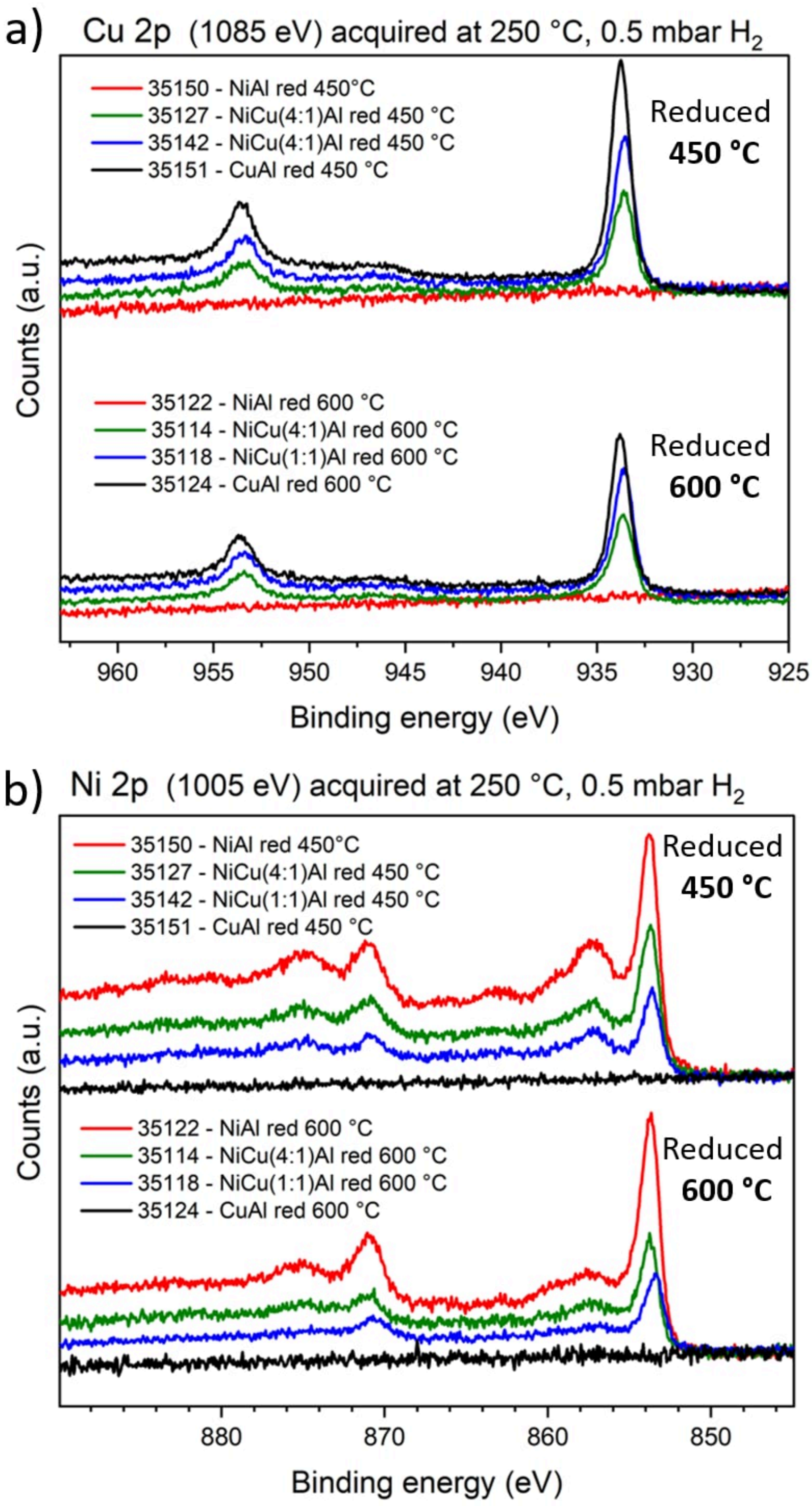

Figure 67: XPS core-level spectra of a) Cu and b) Ni 2p from the four samples (NiAl, NiCu(4:1)Al, NiCu(1:1)Al, and CuAl) reduced at 450 °C (top) and 600 °C (bottom).

1085 eV and 1005 eV were the excitation energy used for Cu 2p and Ni 2p, respectively. Elemental abundance was determined by XPS analysis adjusting the conditions to have the same probing depth for both elements, from around 10 Å.

A.2 Supplementary information Chapter 4

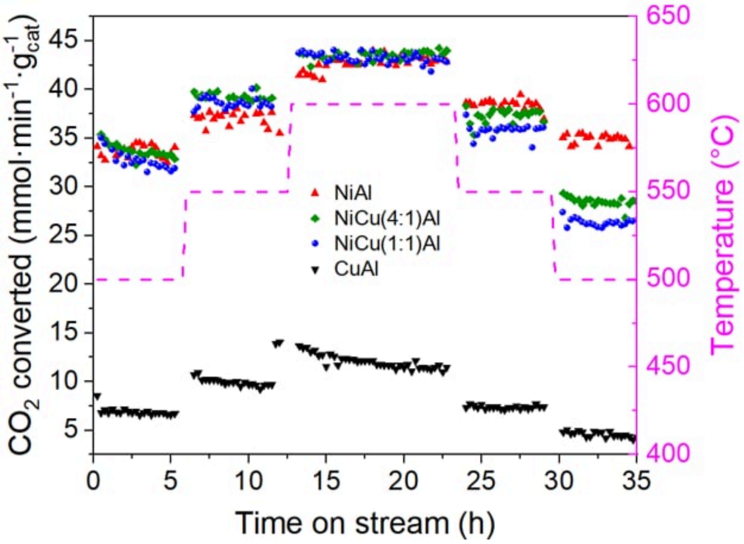

Figure 68: CO$_2$ hydrogenation reaction on LDH-derived materials: CO$_2$ consumption rate. (Gas flow: 100 mL·min^{-1} of CO$_2$:H$_2$:He with a 1:1:0.5 ratio; mass of catalysts: 15 mg in 85 mg SiO$_2$ as diluent; WHSV: 400,000 mL·g^{-1}·h^{-1}).

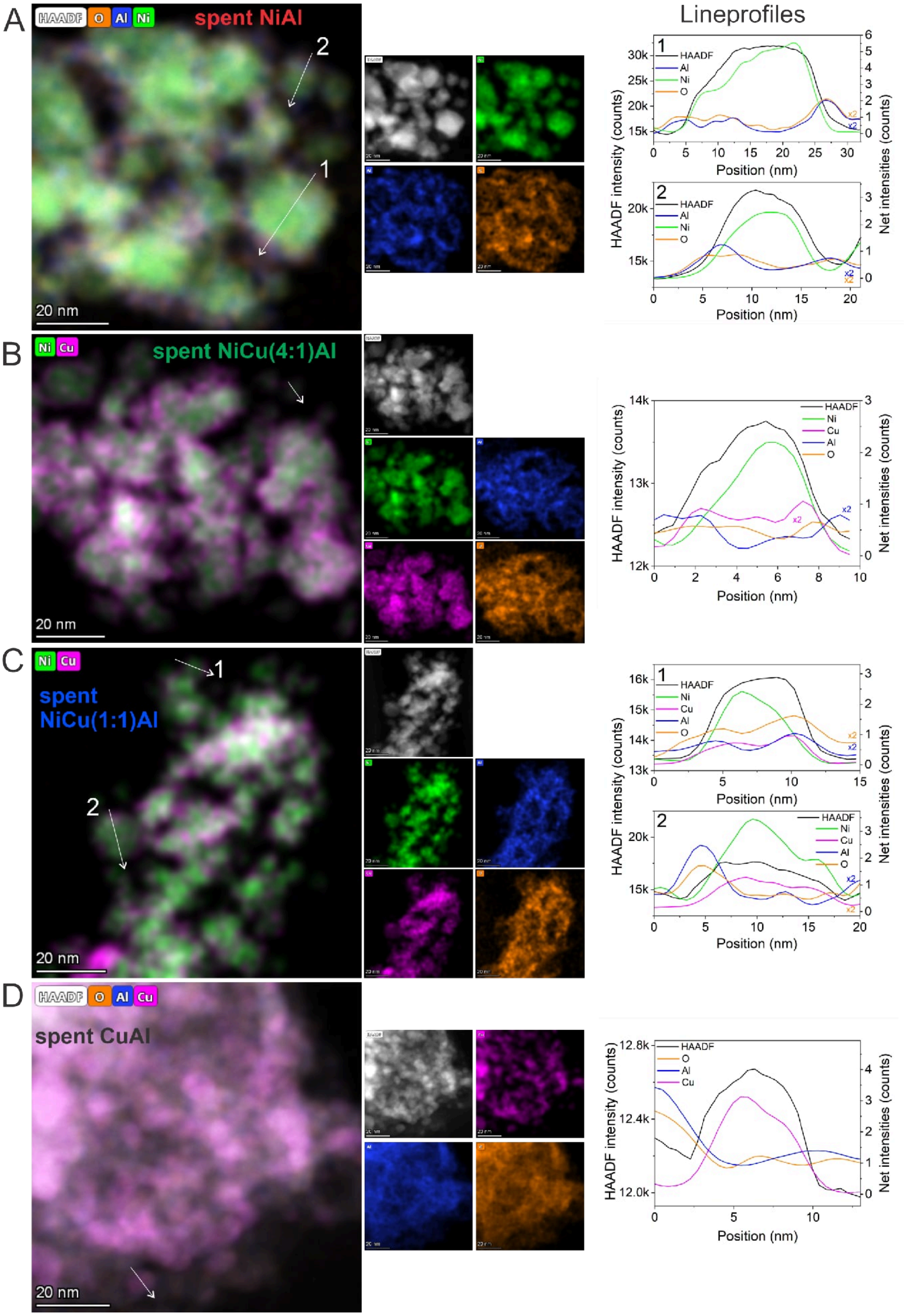

Figure 69: STEM-EDX images of spent catalysts after RWGS reaction and line scans over one particle in each case. a) spent NiAl; b) spent NiCu(4:1)Al; c) spent NiCu(1:1)Al; and d) spent CuAl. (Black/white: HAADF; green: nickel; magenta: copper; blue: aluminum; orange: oxygen)

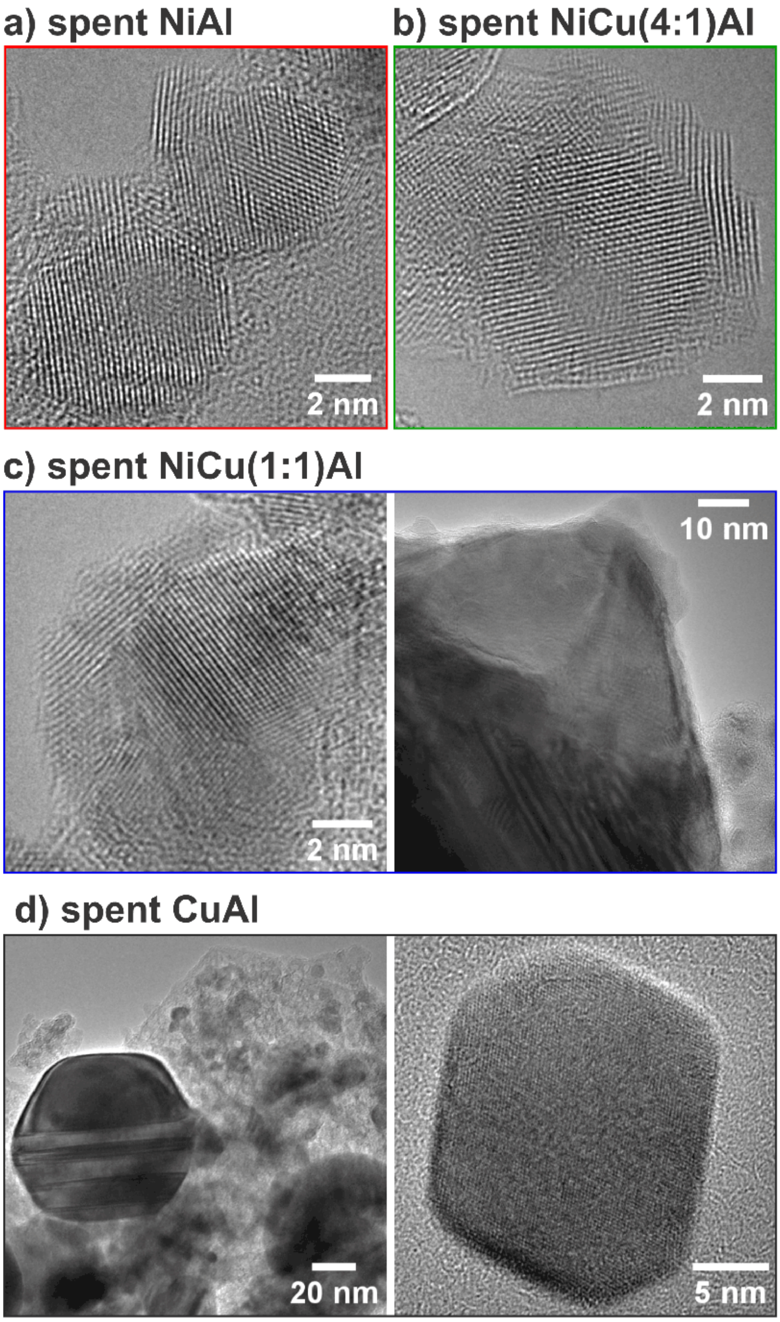

Figure 70: Uncolored HRTEM images of spent samples after CO_2 hydrogenation reaction.

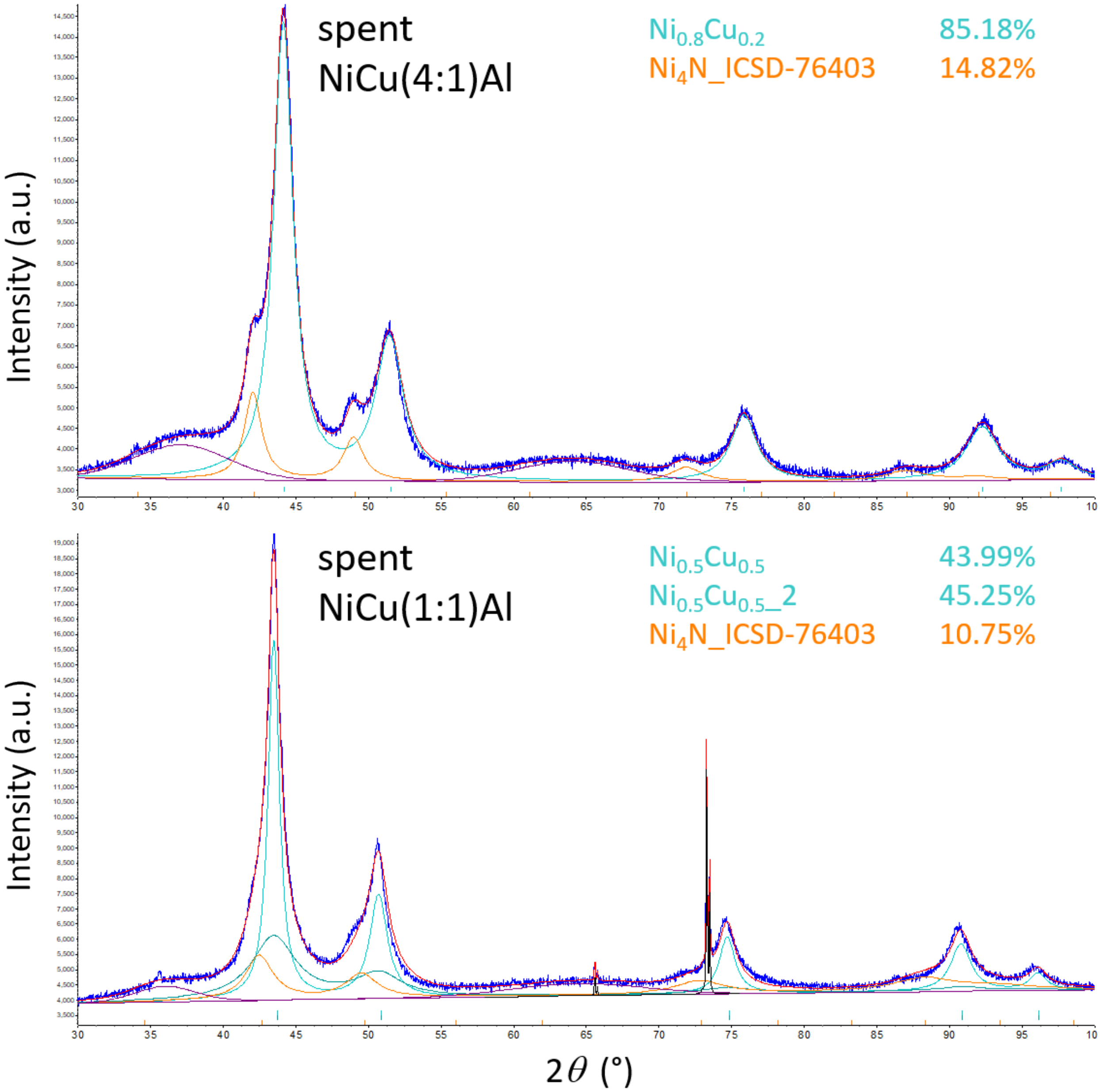

Figure 71: X-ray diffractograms: Rietveld fitting of spent NiCu(4:1)Al and NiCu(1:1)Al after ammonia decomposition.

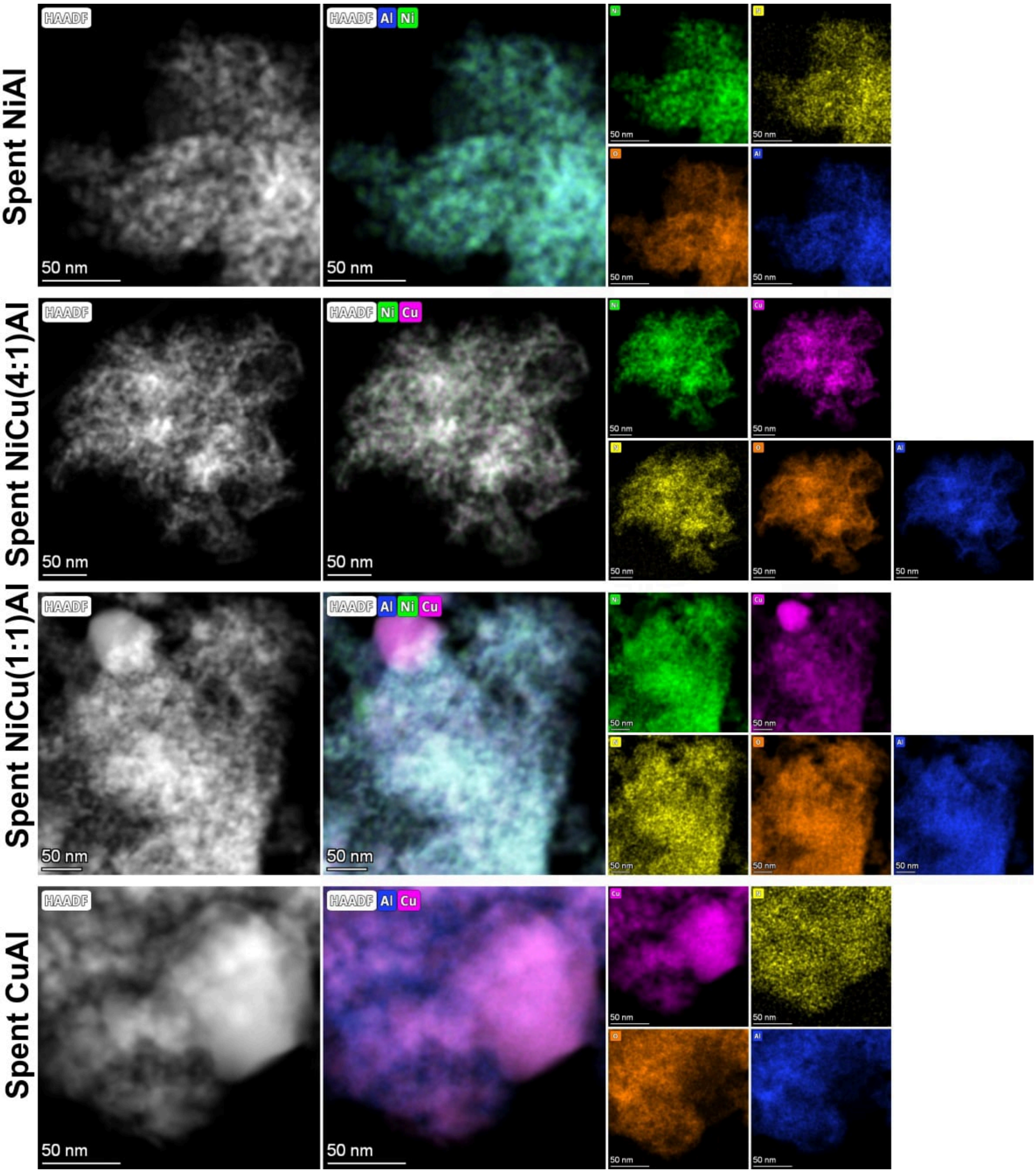

Figure 72: STEM-EDX images of spent catalysts after NH_3 decomposition.

A.3 Supplementary information Chapter 5

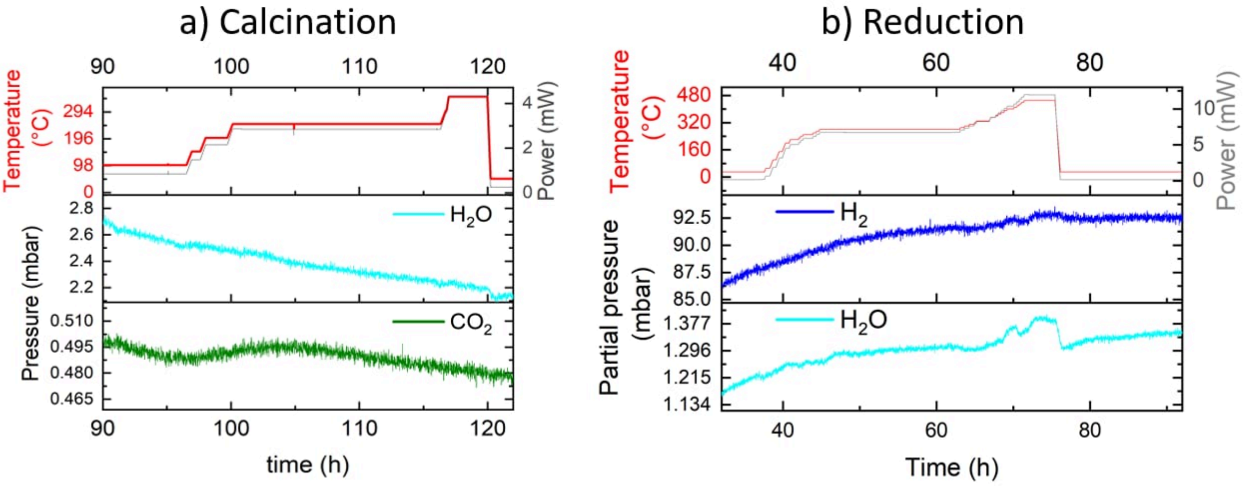

Figure 73: Partial pressure signals during calcination and reduction experiments.

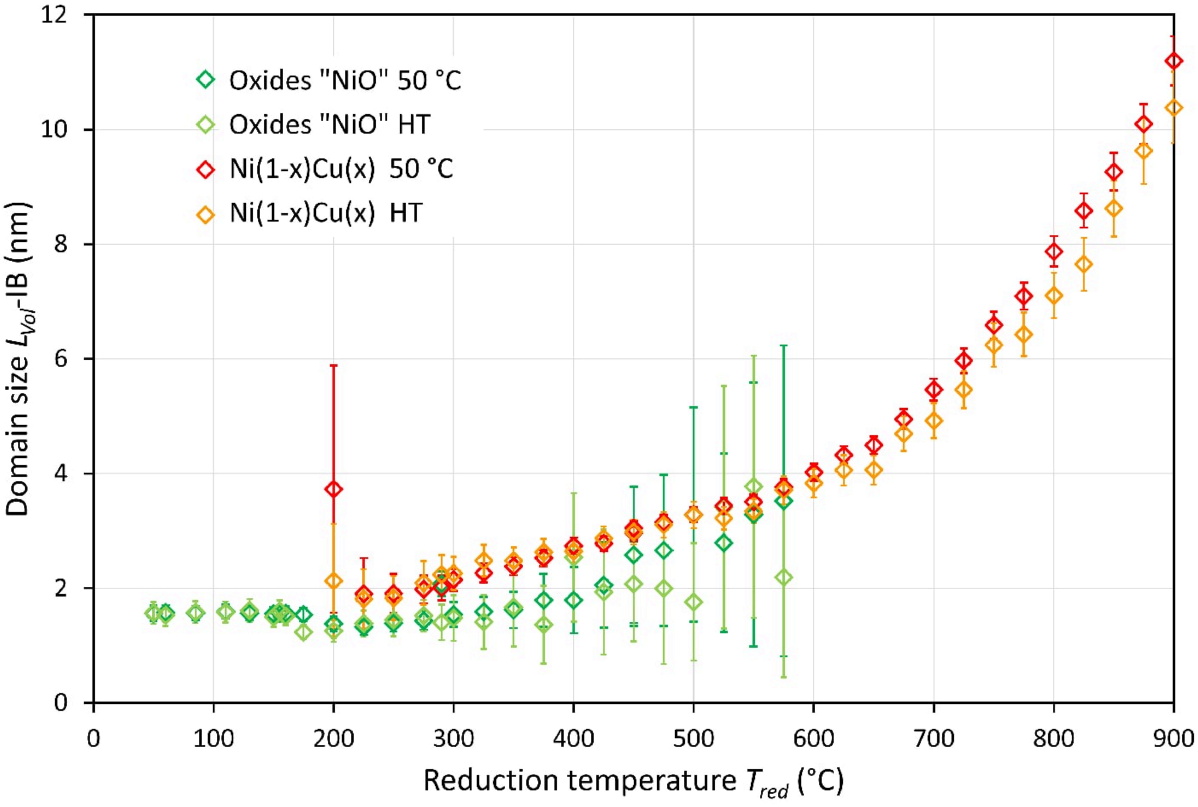

Figure 74: Domain size vs temperature during reduction process under 5% H_2 flow.

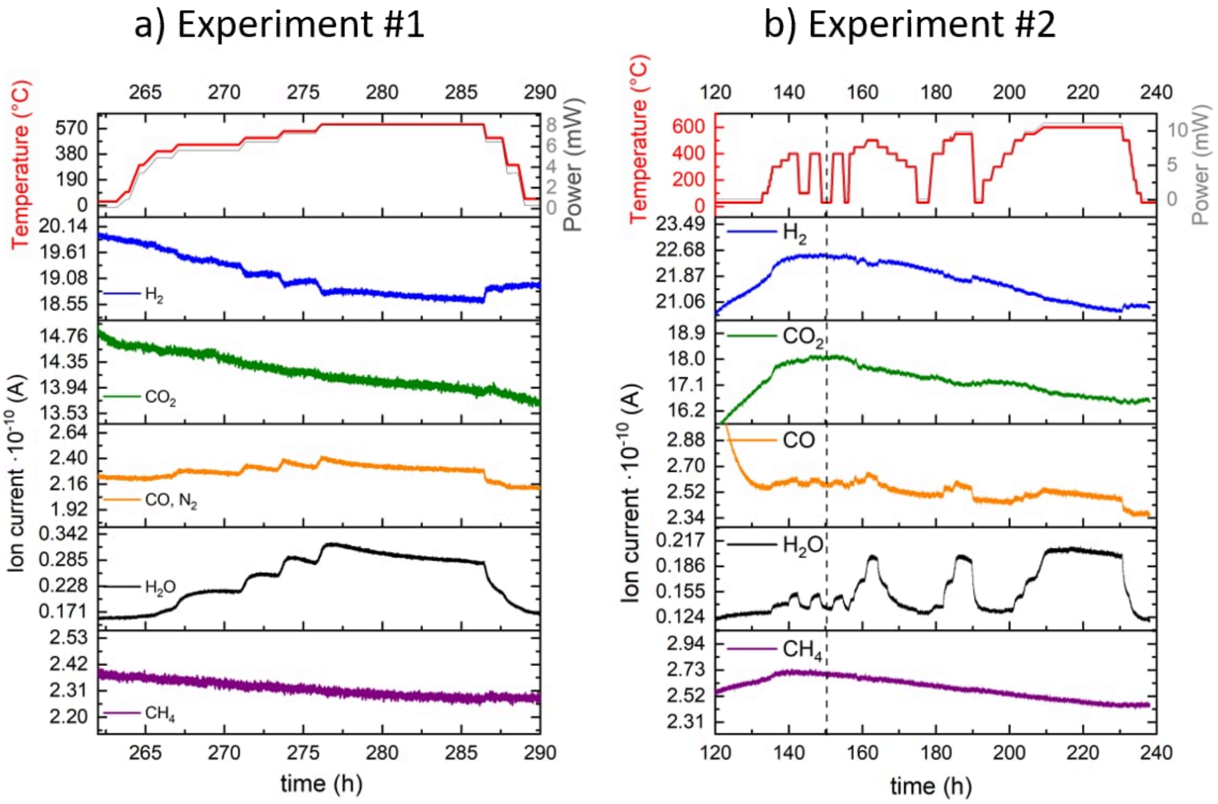

Figure 75: Raw MS signals during OTEM experiments for RWGS reaction. a) experiment #1 and b) experiment #2. For both experiments, the mixture CO_2: H_2: He was used in the ratio 1:1:0.5. The vertical dotted line in b) indicates the starting point of the baseline.

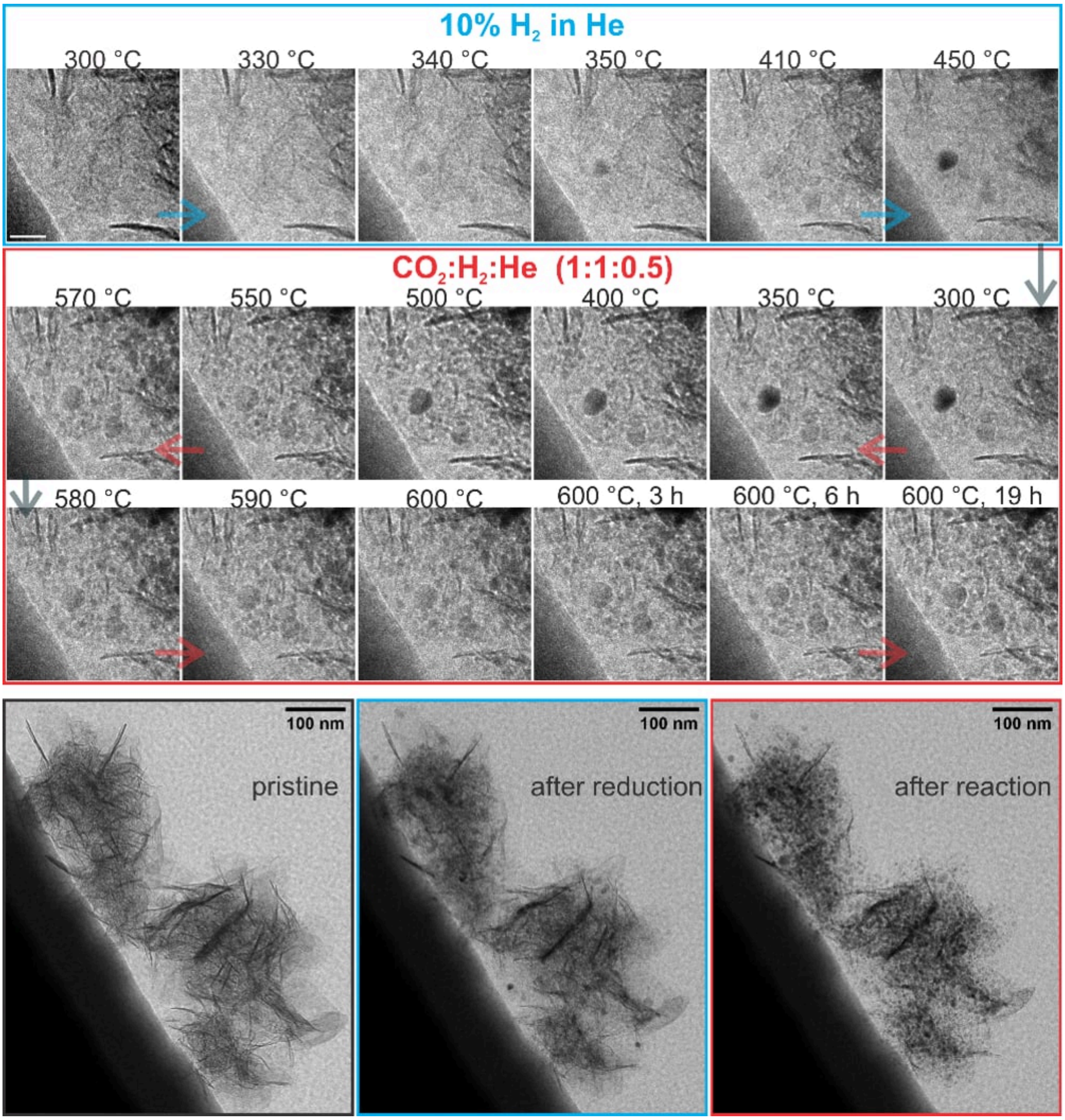

Figure 76: Other position: Morphological transformation of NiCu/Al_2O_3 from LDH precursor during reduction process (blue) and RWGS reaction (red). Beam dose: 940 $e^{-}\cdot$Å$^{-2}\cdot s^{-1}$.

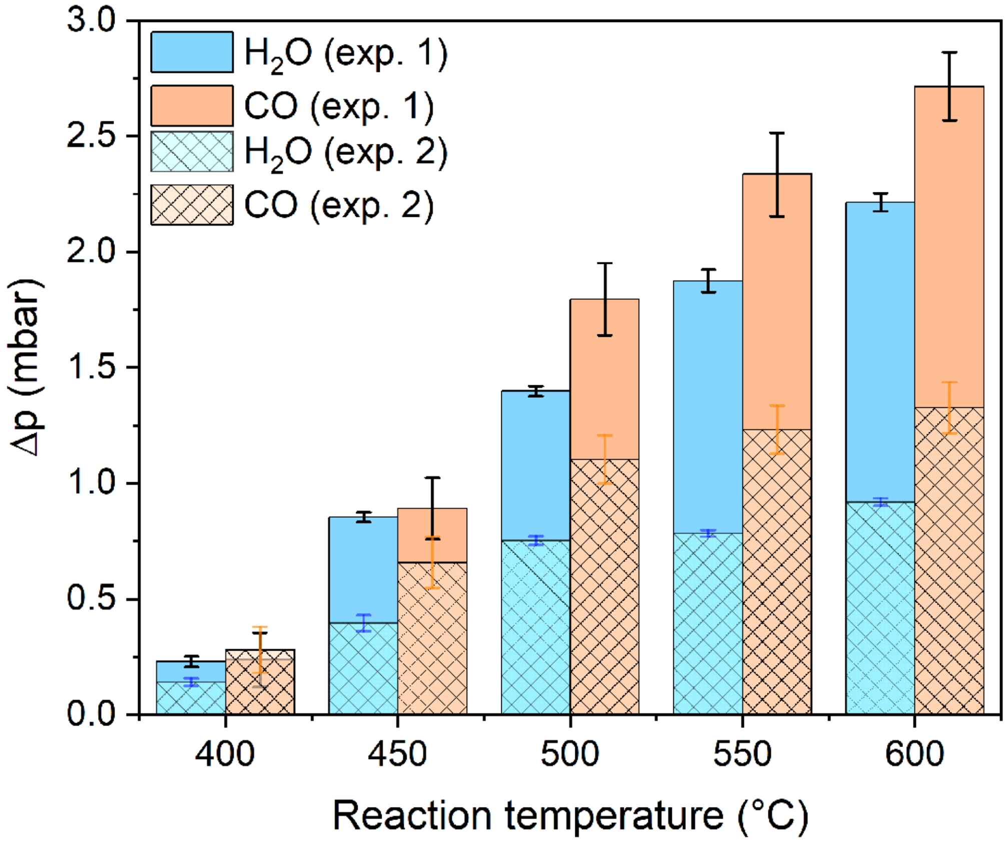

Figure 77: Product formation (CO and H_2O) during experiment #1 and #2 at different temperatures. The differences between Experiments #1 and #2 may be due to uncontrolled variables like the actual amount of sample deposited on the chip (which participates in the reaction), the pressure in the cell, the specific flow, etc.

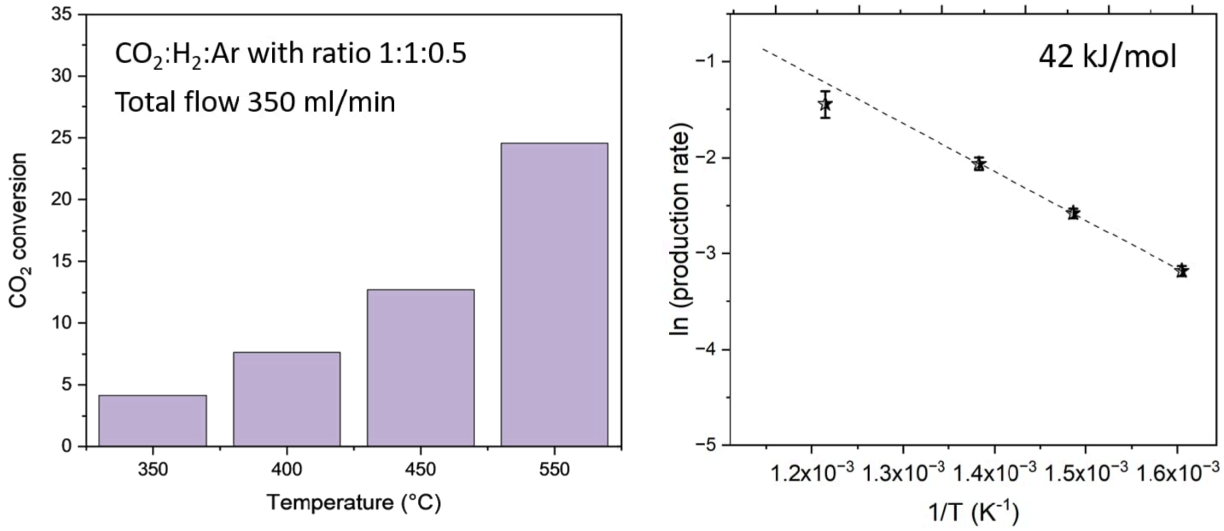

Figure 78: CO_2 conversion and Arrhenius plot of NiCu(4:1)Al sample evaluated in the fixed-bed (Chinchen reactor) reactor.

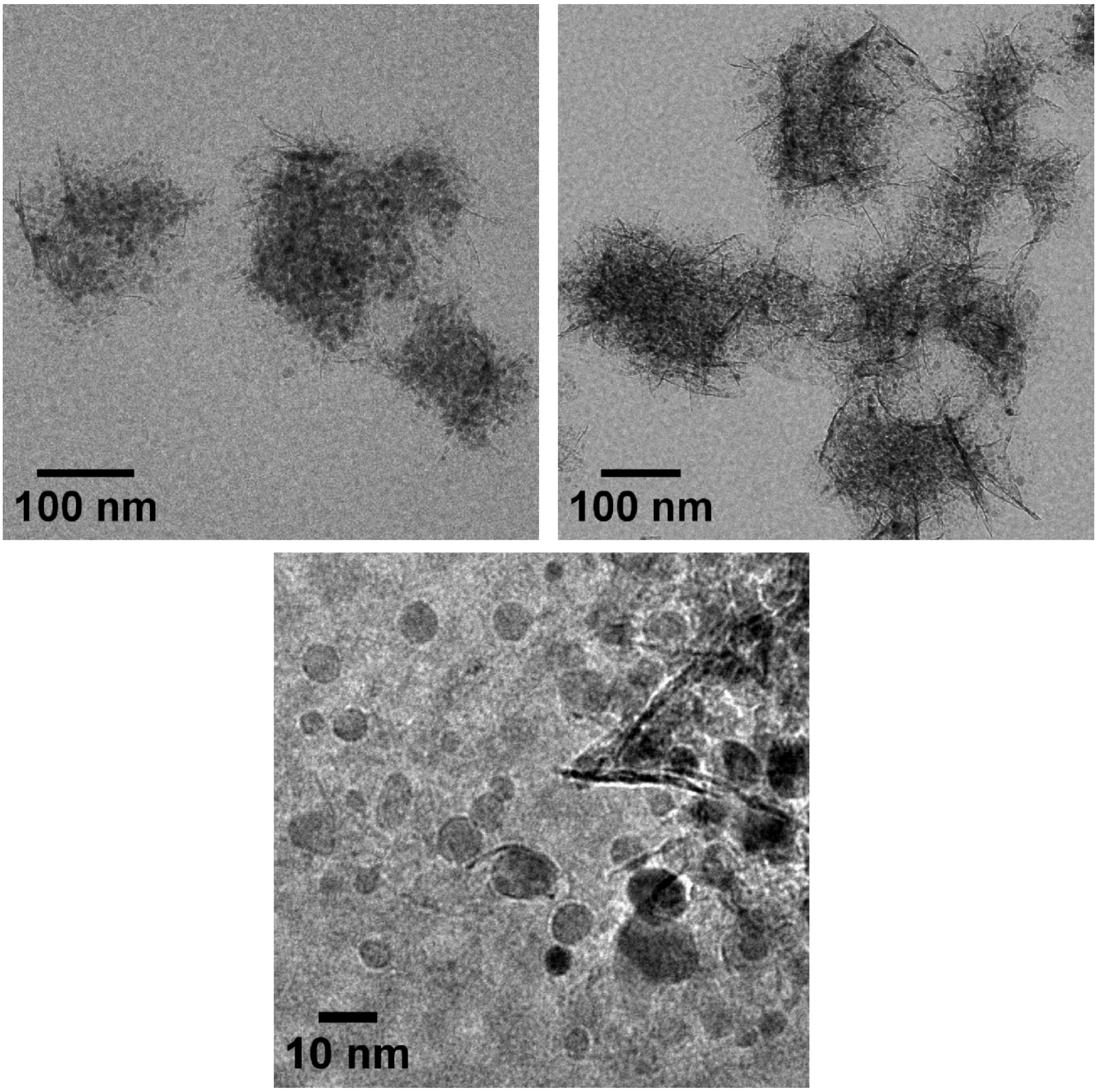

Figure 79: TEM images of different positions after CO2 hydrogenation in the OTEM cell. Catalyst: < 0.5 µg; flow: 20 µL·min^{-1} of CO_2:H_2:He with ratio 1:1:0.5; pressure: 0.8 bar; temperature: 600 °C for 19 h.

B Appendix: Contributions

B.1 Papers contributions

- Walid Hetaba, Robert Imlau, **Liseth Duarte-Correa**, Maximilian Lamoth, Stephan Kujawa, Thomas Lunkenbein.
  ChemiTEM – Transmission Electron Microscopy Optimized for Chemistry and Material Science, Chemistry - Methods, 2021(1), 401-407.

- Esteban Gioria, **Liseth Duarte-Correa**, Najmeh Bashiri, Walid Hetaba, Reinhard Schomäcker, Arne Thomas.
  Rational design of tandem catalysts using a core–shell structure approach, Nanoscale Advances, 2021(3), 3454-3459.

B.2 Oral presentations

- 03/2023 56th German Catalysis Meeting (Jahrestreffen Deutscher Katalytiker)
    - ″Tracking the behavior of NiCuAl LDH-derived catalysts by in situ TEM: Ni-Cu synergy towards chemical energy conversion″
- 08/2022 American Chemical Society (ACS) Fall 2022: Sustainability in a Changing World
    - ″Strong metal-support interaction on Ni-Cu-Al-LDH derived catalyst: The key of stability during RWGS″

B.3 Poster presentations

- 05/2022 The 27th North American Catalysis Society Meeting (NAM27)
    - ″Electron-beam induced structural changes on layered double hydroxides and derived materials″
- 06/2022 55th German Catalysis Meeting (Jahrestreffen Deutscher Katalytiker)
    - ″Structural changes of layered double hydroxides during transmission electron microscopy studies″
- 08/2021 Microscopy Conference 2021 (MC2021, Online)

    - ″Transmission Electron Microscopy of Ni-Cu bimetallic nanomaterial prepared by impregnation and coprecipitation: studying the activation process″
    - ″Transmission Electron Microscopy of bimetallic tandem catalyst for coupling reactions″
- 03/2021 54th German Catalysis Meeting (Jahrestreffen Deutscher Katalytiker, Online)
    - “Morphological changes during activation of NiCu/Al2O3 bimetallic catalysts investigated by electron microscopy″

Acknowledgments

I wish to express my profound gratitude to Professor Dr. Robert Schlögl, for the opportunity to pursue my doctoral studies in the Department of Inorganic Chemistry at the prestigious Fritz-Haber-Institute of the Max-Planck-Society. Your immense knowledge and expertise have encouraged me during my academic research. It has been an honor and pleasure to be part of this marvelous team.

I am deeply thankful to Dr. Walid Hetaba for his guidance, feedback, and continuous support during my PhD journey. I am grateful for the chance to work on this interesting topic and to get training in using the transmission electron microscopes. After 4 years, I have learned a lot, but there's still a long way to go.

I extend my gratitude to the doctoral committee members Prof. Dr. Maria Andrea Mroginski, PD Dr. Thomas Lunkenbein, Prof. Dr. Arne Thomas, Prof. Dr. Thomas W Hansen, and Prof. Dr. Malte Behrens. I appreciate the time you have invested in reviewing this thesis.

I thank the scientists and experts who helped with characterization, analysis, and academic discussions. I thank Dr. Katarzyna Skorupska, Maike Hashagen, Dr. Maximillian Lamoth, Dr. Li He, and Dr. Matus Stredansky for their support with LDH synthesis, calcination-reduction experiments, and scientific discussions. I also thank Jasmin Allan (TGMS); Dr. Frank Girgdies and Dr. Gregor Koch (XRD); Leonie Franke, Jasmin Deichmann, and Dr. Clara Marshal (N_2 sorption); Dr. Nils Pfister (N_2 sorption and IR discussions); Dr. Matus Stredansky (NEXAFS, XPS); Dr. Sabine Wrabetz (Microcalorimetry); Jutta Kröhnert (DRIFTS); Dr. Paulina Summa (CO_2 TPD); and Dr. Baris Alkan (NH_3 decomposition). Moreover, I thank BasCat colleague Piyush Ingale (CO_2 hydrogenation); and colleagues from MPI-CEC: Dr. Justus Werkmeister and Annika Gurowski (ICPMS); Dr. Christian Froese and Dr. Christoph Göbel (equilibrium calculation). Thanks to Dr. Thomas Götsch, Dr. Maxime Boniface, and Dr. Kassioge Dembele for the training and troubleshooting support during operando TEM experiments. Wiebke Frandsen has my gratitude for her advice with sample preparation and nice discussions.

I extend my gratitude to current and former members of the Electron Microscopy group and the Inorganic Chemistry Department for their support. I express my gratitude to Dr. Franz Schmidt and Dr. Christian Rohner for their help with the unexpected issues at the microscopes. I thank Dr. Wulyu Jiang for supporting with illustration figures. I am grateful to Dr. Clara Marshal, Dr. Agata Plucienik, Dr. Luis E. Sandoval, Dr. Maxime Boniface, Dr. Elizabeth Wolf, Dr. Annette Trunschke, and Dr. Holger Ruland (CEC-MPG) for reading part of my thesis and providing feedback. I am thankful to all the PhD fellows

I had the chance to interact with, Giulia, Ezgi, Frederic, Shirin, and Julia. Furthermore, I thank UniSysCat for financial support funded by the Deutsche Forschungsgemeinschaft (DFG, German Research Foundation) under Germany's Excellence Strategy – EXC 2008 – 390540038 – UniSysCat.

I want to give the biggest thanks to my husband for always being patient and supportive. I couldn't have done it without you. Thank you for everything. Nuestro matrimonio es el mejor resultado de mi doctorado. Gracias a toda mi familia. A mis padres y hermanos por todo su apoyo y motivarme a ser perseverante a pesar de las dificultades. A mis abuelos que me acompañan desde el cielo.

References

[1] Y. Pu, B. He, Y. Niu, X. Liu, and B. Zhang, “Chemical Electron Microscopy (CEM) for Heterogeneous Catalysis at Nano: Recent Progress and Challenges,” *Research*, vol. 6, Jan. 2023, doi: 10.34133/research.0043.

[2] B. E. Leland Cratty and W. Walker Russell, “Nickel, Copper and Some of their Alloys as Catalysts for the Hydrogenation of Carbon Dioxide1,” *Mineral. Mag*, vol. 30, p. 293, 1954, [Online]. Available: https://pubs.acs.org/sharingguidelines

[3] J. Wu, G. Gao, J. Li, P. Sun, X. Long, and F. Li, “Efficient and versatile CuNi alloy nanocatalysts for the highly selective hydrogenation of furfural,” *Applied Catalysis B: Environmental*, vol. 203, pp. 227–236, 2017, doi: 10.1016/j.apcatb.2016.10.038.

[4] S. D. Robertson, S. C. Kloet, and W. M. H. Sachtler, “Study of copper-nickel alloy formation on silica supports by the magnetostatic and other methods,” *Journal of Catalysis*, vol. 39, no. 2, pp. 234–248, 1975, doi: 10.1016/0021-9517(75)90328-0.

[5] D. S. Su, B. Zhang, and R. Schlögl, “Electron microscopy of solid catalysts - Transforming from a challenge to a toolbox,” *Chemical Reviews*, vol. 115, no. 8, pp. 2818–2882, 2015, doi: 10.1021/cr500084c.

[6] M. Knoll and E. Ruska, “Das Elektronenmikroskop,” *Zeitschrift für Physik*, vol. 78, pp. 318–339, 1932, doi: 10.1007/BF01342199.

[7] B. Fultz and J. M. Howe, *Transmission electron microscopy and diffractometry of materials*. Heidelberg: Springer Berlin, 2008. doi: 10.1007/978-3-540-73886-2.

[8] D. B. Williams and C. B. Carter, *Transmission electron microscopy: A textbook for materials science*, 2nd ed. Springer New York, NY, 2009. doi: 10.1007/978-0-387-76501-3.

[9] R. F. Egerton, *Electron Energy-Loss Spectroscopy in the Electron Microscope*, 3rd ed. Springer New York, NY, 2011. doi: 10.1007/978-1-4419-9583-4.

[10] T. Malis, S. C. Cheng, and R. F. Egerton, “EELS log-ratio technique for specimen-thickness measurement in the TEM,” *Journal of Electron Microscopy Technique*, vol. 8, no. 2, pp. 193–200, 1988, doi: 10.1002/jemt.1060080206.

[11] T. W. Hansen, J. B. Wagner, P. L. Hansen, S. Dahl, H. Topsøe, and C. J. H. Jacobsen, “Atomic-resolution in situ transmission electron microscopy of a promoter of a heterogeneous catalyst,” *Science*, vol. 294, no. 5546, pp. 1508–1510, Nov. 2001, doi: 10.1126/science.1064399.

[12] P. J. Kooyman, “Development of Operando transmission electron microscopy,” in *Springer series in chemical physics*, vol. 114, Springer, Cham, 2017, pp. 111–129. doi: 10.1007/978-3-319-44439-0.

[13] J. R. Jinschek and S. Helveg, “Image resolution and sensitivity in an environmental transmission electron microscope,” *Micron*, vol. 43, no. 11, pp. 1156–1168, Nov. 2012, doi: 10.1016/j.micron.2012.01.006.

[14] J. F. Creemer *et al.*, “Atomic-scale electron microscopy at ambient pressure,” *Ultramicroscopy*, vol. 108, no. 9, pp. 993–998, 2008, doi: 10.1016/j.ultramic.2008.04.014.

[15] N. De Jonge, W. C. Bigelow, and G. M. Veith, “Atmospheric Pressure Scanning Transmission Electron Microscopy,” *Nano Letters*, vol. 10, no. 3, pp. 1028–1031, 2010, doi: 10.1021/nl904254g.

[16] M. A. Bañares, “Operando methodology: combination of in situ spectroscopy and simultaneous activity measurements under catalytic reaction conditions,” *Catalysis Today*, vol. 100, no. 1–2, pp. 71–77, Feb. 2005, doi: 10.1016/j.cattod.2004.12.017.

[17] J. L. Vincent, J. W. Vance, J. T. Langdon, B. K. Miller, and P. A. Crozier, “Chemical kinetics for operando electron microscopy of catalysts: 3D modeling of gas and temperature distributions during catalytic reactions,” *Ultramicroscopy*, vol. 218, p. 113080, 2020, doi: 10.1016/j.ultramic.2020.113080.

[18] S. B. Vendelbo *et al.*, “Visualization of oscillatory behaviour of Pt nanoparticles catalysing CO oxidation,” *Nature Materials*, vol. 13, no. 9, pp. 884–890, 2014, doi: 10.1038/nmat4033.

[19] T. W. Hansen, J. B. Wagner, and R. E. Dunin-Borkowski, “Aberration corrected and monochromated environmental transmission electron microscopy: challenges and prospects for materials science,” *Materials Science and Technology*, vol. 26, no. 11, pp. 1338–1344, Nov. 2010, doi: 10.1179/026708310X12756557336355.

[20] “Web of Science Core Collection.” [Online]. Available: https://www.webofscience.com/wos/woscc/basic-search

[21] K. Jungjohann and C. B. Carter, “In Situ and Operando,” in *Transmission electron microscopy*, Springer, Cham, 2016, pp. 17–80. doi: 10.1007/978-3-319-26651-0.

[22] “DENSsolutions Climate In Situ TEM Gas & Heating.” [Online]. Available: https://denssolutions.com/products/climate/

[23] B. He, Y. Zhang, X. Liu, and L. Chen, “In-situ Transmission Electron Microscope Techniques for Heterogeneous Catalysis,” *ChemCatChem*, vol. 12, no. 7, pp. 1853–1872, 2020, doi: 10.1002/cctc.201902285.

[24] S. Hwang, X. Chen, G. Zhou, and D. Su, "In Situ Transmission Electron Microscopy on Energy-Related Catalysis," *Advanced Energy Materials*, vol. 10, no. 11, p. 1902105, Mar. 2020, doi: 10.1002/aenm.201902105.

[25] S. W. Chee, T. Lunkenbein, R. Schlogl, and B. Roldan Cuenya, "In situ and operando electron microscopy in heterogeneous catalysis-insights into multi-scale chemical dynamics," *Journal of Physics Condensed Matter*, vol. 33, no. 15, 2021, doi: 10.1088/1361-648X/abddfd.

[26] M. Boniface, M. Plodinec, R. Schlögl, and T. Lunkenbein, "Quo Vadis Micro-Electro-Mechanical Systems for the Study of Heterogeneous Catalysts Inside the Electron Microscope?," *Topics in Catalysis*, vol. 63, no. 15–18, pp. 1623–1643, 2020, doi: 10.1007/s11244-020-01398-6.

[27] M. Plodinec, E. Stotz, L. Sandoval-Diaz, R. Schlögl, and T. Lunkenbein, "Multimodal Operando Electron Microscopy Approach to Study Pt Catalyst During CO Oxidation Reaction," *Microscopy and Microanalysis*, vol. 25, no. S2, pp. 1448–1449, 2019, doi: 10.1017/s1431927619007979.

[28] M. Plodinec, H. C. Nerl, F. Girgsdies, R. Schlögl, and T. Lunkenbein, "Insights into Chemical Dynamics and Their Impact on the Reactivity of Pt Nanoparticles during CO Oxidation by Operando TEM," *ACS Catalysis*, vol. 10, no. 5, pp. 3183–3193, 2020, doi: 10.1021/acscatal.9b03692.

[29] L. Sandoval-Diaz *et al.*, "Visualizing the importance of oxide-metal phase transitions in the production of synthesis gas over Ni catalysts," *Journal of Energy Chemistry*, vol. 50, pp. 178–186, 2020, doi: 10.1016/j.jechem.2020.03.013.

[30] J. Cao *et al.*, "In situ observation of oscillatory redox dynamics of copper," *Nature Communications*, vol. 11, no. 1, pp. 1–11, 2020, doi: 10.1038/s41467-020-17346-7.

[31] X. Huang *et al.*, "Phase Coexistence and Structural Dynamics of Redox Metal Catalysts Revealed by Operando TEM," *Advanced Materials*, vol. 33, no. 31, p. 2101772, Aug. 2021, doi: 10.1002/ADMA.202101772.

[32] M. Plodinec, H. C. Nerl, T. Lunkenbein, and R. Schlögl, "Deactivation Mechanism of Ni Nanoparticles in Dry Reforming of Methane Revealed by Operando TEM," *Microscopy and Microanalysis*, vol. 28, no. S1, pp. 146–148, 2022, doi: 10.1017/s1431927622001489.

[33] A. Beck *et al.*, "The dynamics of overlayer formation on catalyst nanoparticles and strong metal-support interaction," *Nature Communications*, vol. 11, no. 1, pp. 1–8, Jun. 2020, doi: 10.1038/s41467-020-17070-2.

[34] S. Zhang *et al.*, "Dynamical observation and detailed description of catalysts under strong metal-support interaction," *Nano Letters*, vol. 16, no. 7, pp. 4528–4534, Jul. 2016, doi: 10.1021/acs.nanolett.6b01769.

[35] M. Boniface *et al.*, “Dynamics of the Cu-Zn synergy in a Cu/ZnO/Al2O3 catalyst revealed by operando TEM,” *In preparation*, 2023.

[36] B. Hammer and J. K. Nørskov, “Theoretical surface science and catalysis—calculations and concepts,” *Advances in Catalysis*, vol. 45, no. C, pp. 71–129, 2000, doi: 10.1016/S0360-0564(02)45013-4.

[37] J. K. Nørskov, “Chemisorption on metal surfaces,” *Rep. Prog. Phys.*, vol. 53, pp. 1253–1295, 1990, doi: 10.1088/0034-4885/53/10/001.

[38] M. Araki and V. Ponec, “Methanation of carbon monoxide on nickel and nickel-copper alloys,” *Journal of Catalysis*, vol. 44, no. 3, pp. 439–448, 1976, doi: 10.1016/0021-9517(76)90421-8.

[39] V. R. Calderone, N. R. Shiju, D. C. Ferré, and G. Rothenberg, “Bimetallic catalysts for the Fischer-Tropsch reaction,” *Green Chemistry*, vol. 13, no. 8, pp. 1950–1959, 2011, doi: 10.1039/c0gc00919a.

[40] Y. Shen, M. Ge, and A. Chong Lua, “Deactivation of bimetallic nickel-copper alloy catalysts in thermocatalytic decomposition of methane †,” *Cite this: Catal. Sci. Technol*, vol. 8, p. 3853, 2018, doi: 10.1039/c8cy00339d.

[41] M. Kang, M. W. Song, T. W. Kim, and K. L. Kim, “\gamma-Alumina supported Cu-Ni bimetallic catalysts: Characterization and selective hydrogenation of 1,3-butadiene,” *The Canadian Journal of Chemical Engineering*, vol. 80, no. 1, pp. 63–70, Feb. 2002, doi: 10.1002/CJCE.5450800107.

[42] D. Zahn, F. Haarmann, and Y. Grin, “Atomistic simulation study of Cu0.327Ni0.673 alloys: From solid solution to phase segregation,” *Zeitschrift fur Anorganische und Allgemeine Chemie*, vol. 634, no. 14, pp. 2562–2566, 2008, doi: 10.1002/zaac.200800345.

[43] H. Baker *et al.*, *ASM Handbook Volume 3 Alloy Phase Diagrams Prepared under the direction of the ASM International Alloy Phase Diagram and Handbook Committees*. 1992, p. 173.

[44] W. T. Reichle, “Catalytic reactions by thermally activated, synthetic, anionic clay minerals,” *Journal of Catalysis*, vol. 94, no. 2, pp. 547–557, Aug. 1985, doi: 10.1016/0021-9517(85)90219-2.

[45] F. Cavani, F. Trifirò, and A. Vaccari, “Hydrotalcite-type anionic clays: Preparation, properties and applications.,” *Catalysis Today*, vol. 11, no. 2, pp. 173–301, 1991, doi: 10.1016/0920-5861(91)80068-K.

[46] W. Feitknecht and M. Gerber, “Zur Kenntnis der Doppelhydroxyde und basischen Doppelsalze III. Über Magnesium-Aluminiumdoppelhydroxyd,” *Helvetica Chimica Acta*, vol. 25, no. 1, pp. 131–137, Feb. 1942, doi: 10.1002/hlca.19420250115.

[47] R. Allmann, “The crystal structure of pyroaurite,” *Acta Crystallographica Section B*, vol. 24, no. 7, pp. 972–977, Jul. 1968, doi: 10.1107/S0567740868003511.

[48] H. F. W. Taylor, “Segregation and cation-ordering in sjögrenite and pyroaurite,” *Mineralogical Magazine*, vol. 37, no. 287, pp. 338–342, Sep. 1969, doi: 10.1180/minmag.1969.037.287.04.

[49] M. Nocchetti and U. Costantino, “Progress in layered double hydroxides: From synthesis to new applications,” *Progress In Layered Double Hydroxides: From Synthesis To New Applications*, pp. 1–528, Feb. 2022, doi: 10.1142/12378.

[50] R. M. M. Santos, J. Tronto, V. Briois, and C. V. Santilli, “Thermal decomposition and recovery properties of ZnAl-CO3 layered double hydroxide for anionic dye adsorption: Insight into the aggregative nucleation and growth mechanism of the LDH memory effect.,” *Journal of Materials Chemistry A*, pp. 9998–10009, 2017, doi: 10.1039/c7ta00834a.

[51] A. Hameed, M. Batool, Z. Liu, M. A. Nadeem, and R. Jin, “Layered Double Hydroxide-Derived Nanomaterials for Efficient Electrocatalytic Water Splitting: Recent Progress and Future Perspective,” *ACS Energy Letters*, vol. 7, no. 10, pp. 3311–3328, Oct. 2022, doi: 10.1021/acsenergylett.2c01362.

[52] D. P. Sahoo, K. K. Das, S. Mansingh, S. Sultana, and K. Parida, “Recent progress in first row transition metal Layered double hydroxide (LDH) based electrocatalysts towards water splitting: A review with insights on synthesis,” *Coordination Chemistry Reviews*, vol. 469, p. 214666, Oct. 2022, doi: 10.1016/j.ccr.2022.214666.

[53] W. Ye, T. W. Kim, and D. H. Park, “Layered double hydroxide nanomaterials for bifunctional ORR/OER electro-catalyst,” *Journal of the Korean Ceramic Society*, vol. 59, no. 6, pp. 763–774, Nov. 2022, doi: 10.1007/s43207-022-00241-w.

[54] C. Li, M. Wei, D. G. Evans, and X. Duan, “Layered double hydroxide-based nanomaterials as highly efficient catalysts and adsorbents,” *Small*, 2014, doi: 10.1002/smll.201401464.

[55] A. Elhalil *et al.*, “Effects of molar ratio and calcination temperature on the adsorption performance of Zn/Al layered double hydroxide nanoparticles in the removal of pharmaceutical pollutants,” *Journal of Science: Advanced Materials and Devices*, vol. 3, no. 2, pp. 188–195, Jun. 2018, doi: 10.1016/j.jsamd.2018.03.005.

[56] M. Xu and M. Wei, “Layered Double Hydroxide-Based Catalysts: Recent Advances in Preparation, Structure, and Applications,” *Advanced Functional Materials*, vol. 28, no. 47, pp. 1–20, 2018, doi: 10.1002/adfm.201802943.

[57] G. Fan, F. Li, D. G. Evans, and X. Duan, “Catalytic applications of layered double hydroxides: Recent advances and perspectives,” *Chemical Society Reviews*, vol. 43, no. 20, pp. 7040–7066, 2014, doi: 10.1039/c4cs00160e.

[58] D. Tichit, F. Medina, C. Bernard, and R. Dutartre, “Activation under oxidizing and reducing atmospheres of Ni-containing layered double hydroxides,” *Applied Catalysis A: General*, vol. 159, no. 1–2, pp. 241–258, Oct. 1997, doi: 10.1016/S0926-860X(97)00085-9.

[59] A. Romero, M. Jobbágy, M. Laborde, G. Baronetti, and N. Amadeo, "Ni(II)–Mg(II)–Al(III) catalysts for hydrogen production from ethanol steam reforming: Influence of the activation treatments," *Catalysis Today*, vol. 149, no. 3–4, pp. 407–412, Jan. 2010, doi: 10.1016/j.cattod.2009.05.026.

[60] C. Hobbs, "The in-situ structural characterization of layered double hydroxide materials in catalytic and biological applications," PhD thesis, Trinity College Dublin. School of Physics. Discipline of Physics, 2019. [Online]. Available: http://www.tara.tcd.ie/handle/2262/86068

[61] C. Hobbs *et al.*, "Structural transformation of layered double hydroxides: an in situ TEM analysis," *npj 2D Materials and Applications*, vol. 2, no. 1, 2018, doi: 10.1038/s41699-018-0054-6.

[62] C. Hobbs, C. Downing, S. Jaskaniec, and V. Nicolosi, "TEM and EELS characterization of Ni–Fe layered double hydroxide decompositions caused by electron beam irradiation," *npj 2D Materials and Applications*, vol. 5, no. 1, pp. 1–9, 2021, doi: 10.1038/s41699-021-00212-5.

[63] A. Mikhaylov, N. Moiseev, K. Aleshin, and T. Burkhardt, "Global climate change and greenhouse effect," *Entrepreneurship and Sustainability Issues*, vol. 7, no. 4, pp. 2897–2913, 2020, doi: 10.9770/jesi.2020.7.4(21).

[64] G. Centi and S. Perathoner, "Opportunities and prospects in the chemical recycling of carbon dioxide to fuels," *Catalysis Today*, vol. 148, no. 3–4, pp. 191–205, 2009, doi: 10.1016/j.cattod.2009.07.075.

[65] T. Sakakura, J. C. Choi, and H. Yasuda, "Transformation of carbon dioxide," *Chemical Reviews*, vol. 107, no. 6, pp. 2365–2387, 2007, doi: 10.1021/cr068357u.

[66] M. González-Castaño, B. Dorneanu, and H. Arellano-García, "The reverse water gas shift reaction: A process systems engineering perspective," *Reaction Chemistry and Engineering*, vol. 6, no. 6, pp. 954–976, 2021, doi: 10.1039/d0re00478b.

[67] C. Vogt *et al.*, "Unravelling structure sensitivity in CO2 hydrogenation over nickel," *Nature Catalysis 2017 1:2*, vol. 1, no. 2, pp. 127–134, Jan. 2018, doi: 10.1038/s41929-017-0016-y.

[68] Y. A. Daza and J. N. Kuhn, "CO2 conversion by reverse water gas shift catalysis: Comparison of catalysts, mechanisms and their consequences for CO2 conversion to liquid fuels," *RSC Advances*, vol. 6, no. 55, pp. 49675–49691, 2016, doi: 10.1039/c6ra05414e.

[69] C. Wang *et al.*, "Product Selectivity Controlled by Nanoporous Environments in Zeolite Crystals Enveloping Rhodium Nanoparticle Catalysts for CO2 Hydrogenation," *Journal of the American Chemical Society*, vol. 141, no. 21, pp. 8482–8488, 2019, doi: 10.1021/jacs.9b01555.

[70] X. Chen, X. Su, H. Duan, B. Liang, Y. Huang, and T. Zhang, "Catalytic performance of the Pt/TiO2 catalysts in reverse water gas shift reaction: Controlled product selectivity and a mechanism study," *Catalysis Today*, vol. 281, pp. 312–318, 2017, doi: 10.1016/j.cattod.2016.03.020.

[71] G. C. Chinchen, K. C. Waugh, and D. A. Whan, "The activity and state of the copper surface in methanol synthesis catalysts," *Applied Catalysis*, vol. 25, no. 1-2 C, pp. 101–107, 1986, doi: 10.1016/S0166-9834(00)81226-9.

[72] M. J. L. Ginés, A. J. Marchi, and C. R. Apesteguía, "Kinetic study of the reverse water-gas shift reaction over CuO/ZnO/Al2O3 catalysts," *Applied Catalysis A: General*, vol. 154, no. 1–2, pp. 155–171, 1997, doi: 10.1016/S0926-860X(96)00369-9.

[73] C. S. Chen, W. H. Cheng, and S. S. Lin, "Mechanism of CO formation in reverse water-gas shift reaction over Cu/Al2O3 catalyst," *Catalysis Letters*, vol. 68, no. 1–2, pp. 45–48, 2000, doi: 10.1023/a:1019071117449.

[74] Y. Qi, Y.-A. Zhu, and D. Chen, "Mechanism investigation and catalyst screening of high-temperature reverse water gas shift reaction," *Green Chemical Engineering*, vol. 1, no. 2, pp. 131–139, 2020, doi: 10.1016/j.gce.2020.10.001.

[75] F. M. Sun, C. F. Yan, Z. D. Wang, C. Q. Guo, and S. L. Huang, "Ni/Ce-Zr-O catalyst for high CO2 conversion during reverse water gas shift reaction (RWGS)," *International Journal of Hydrogen Energy*, vol. 40, no. 46, pp. 15985–15993, 2015, doi: 10.1016/j.ijhydene.2015.10.004.

[76] E. Gioria, P. Ingale, F. Pohl, R. Naumann d'Alnoncourt, A. Thomas, and F. Rosowski, "Boosting the performance of Ni/Al2O3 for the Reverse Water Gas Shift reaction through formation of CuNi nanoalloys," *Catalysis Science & Technology*, vol. 12, pp. 474–487, 2022, doi: 10.1039/d1cy01585k.

[77] O. Arbeláez *et al.*, "Mono and bimetallic Cu-Ni structured catalysts for the water gas shift reaction," *Applied Catalysis A: General*, vol. 497, pp. 1–9, 2015, doi: 10.1016/j.apcata.2015.02.041.

[78] P. Summa *et al.*, "Investigation of Cu promotion effect on hydrotalcite-based nickel catalyst for CO2 methanation," *Catalysis Today*, vol. 384–386, no. March 2021, pp. 133–145, 2022, doi: 10.1016/j.cattod.2021.05.004.

[79] P. Marocco *et al.*, "CO2 methanation over Ni/Al hydrotalcite-derived catalyst: Experimental characterization and kinetic study," *Fuel*, vol. 225, no. April, pp. 230–242, 2018, doi: 10.1016/j.fuel.2018.03.137.

[80] G. Ertl, "Primary steps in catalytic synthesis of ammonia," *Journal of Vacuum Science & Technology A: Vacuum, Surfaces, and Films*, vol. 1, no. 2, pp. 1247–1253, 1983, doi: 10.1116/1.572299.

[81] G. Ertl, "The Arduous Way to the Haber–Bosch Process," *Zeitschrift für anorganische und allgemeine Chemie*, vol. 638, no. 3–4, pp. 487–489, Mar. 2012, doi: 10.1002/zaac.201190458.

[82] J. B. Hansen, "Kinetics of Ammonia Synthesis and Decomposition on Heterogeneous Catalysts," *Ammonia*, pp. 149–190, 1995, doi: 10.1007/978-3-642-79197-0.

[83] T. V. Choudhary, C. Sivadinarayana, and D. W. Goodman, "Catalytic ammonia decomposition: COx-free hydrogen production for fuel cell applications," *Catalysis Letters*, vol. 72, no. 3–4, pp. 197–201, Apr. 2001, doi: 10.1023/A:1009023825549.

[84] A. Klerke, C. H. Christensen, J. K. Nørskov, and T. Vegge, "Ammonia for hydrogen storage: challenges and opportunities †," *Journal of Materials Chemistry*, vol. 18, pp. 2285–2392, 2008, doi: 10.1039/b720020j.

[85] F. Schüth, R. Palkovits, R. Schlögl, and D. S. Su, "Ammonia as a possible element in an energy infrastructure: catalysts for ammonia decomposition," *Energy & Environmental Science*, vol. 5, no. 4, pp. 6278–6289, Mar. 2012, doi: 10.1039/c2ee02865d.

[86] I. Lucentini, X. Garcia, X. Vendrell, and J. Llorca, "Review of the Decomposition of Ammonia to Generate Hydrogen," *Industrial and Engineering Chemistry Research*, vol. 60, no. 51, pp. 18560–18611, Dec. 2021, doi: 10.1021/acs.iecr.1c00843.

[87] W. U. Khan, H. S. Alasiri, S. A. Ali, and M. M. Hossain, "Recent Advances in Bimetallic Catalysts for Hydrogen Production from Ammonia," *The Chemical Record*, vol. 22, no. 7, p. e202200030, Jul. 2022, doi: 10.1002/tcr.202200030.

[88] S. Ristig *et al.*, "Ammonia Decomposition in the Process Chain for a Renewable Hydrogen Supply," *Chemie-Ingenieur-Technik*, vol. 94, no. 10, pp. 1413–1425, Oct. 2022, doi: 10.1002/cite.202200003.

[89] A. Boisen, S. Dahl, J. K. Nørskov, and C. H. Christensen, "Why the optimal ammonia synthesis catalyst is not the optimal ammonia decomposition catalyst," *Journal of Catalysis*, vol. 230, no. 2, pp. 309–312, Mar. 2005, doi: 10.1016/j.jcat.2004.12.013.

[90] T. A. Le, Q. Cuong Do, Y. Kim, T.-W. Kim, and H.-J. Chae, "A review on the recent developments of ruthenium and nickel catalysts for CO x-free H2 generation by ammonia decomposition," *Korean J. Chem. Eng*, vol. 38, no. 6, pp. 1087–1103, 2021, doi: 10.1007/s11814-021-0767-7.

[91] SAM Gas Projects Pvt. Ltd., "Ammonia Cracker." [Online]. Available: https://www.psa-nitrogen.com/ammonia-cracker.html

[92] M. I. Temkin, "Kinetics of heterogeneous catalysis," *J Phys Chem (USSR)*, vol. 14, pp. 1153–1158, 1940.

[93] C. T. Campbell, "Micro-and macro-kinetics: their relationship in heterogeneous catalysis," *Topics in Catalysis I*, pp. 353–366, 1994.

[94] R. W. McCabe, “Kinetics of ammonia decomposition on nickel,” *Journal of Catalysis*, vol. 79, no. 2, pp. 445–450, Feb. 1983, doi: 10.1016/0021-9517(83)90337-8.

[95] J. C. Ganley, F. S. Thomas, E. G. Seebauer, and R. I. Masel, “A priori catalytic activity correlations: the difficult case of hydrogen production from ammonia,” *Catalysis Letters*, vol. 96, pp. 117–122, 2004, doi: 10.1023/B:CATL.0000030108.50691.d4.

[96] J. Zhang, H. Xu, and W. Li, “Kinetic study of NH3 decomposition over Ni nanoparticles: The role of la promoter, structure sensitivity and compensation effect,” *Applied Catalysis A: General*, vol. 296, no. 2, pp. 257–267, 2005, doi: 10.1016/j.apcata.2005.08.046.

[97] X. Duan *et al.*, “Structure sensitivity of ammonia decomposition over Ni catalysts: A computational and experimental study,” *Fuel Processing Technology*, vol. 108, pp. 112–117, 2013, doi: 10.1016/j.fuproc.2012.05.030.

[98] J. K. Dixon, “The kinetics of the decomposition of ammonia on copper,” *Journal of the American Chemical Society*, vol. 53, no. 5, pp. 1763–1773, May 1931, doi: 10.1021/ja01356a018.

[99] L. Deng, H. Lin, X. Liu, J. Xu, Z. Zhou, and M. Xu, “Nickel nanoparticles derived from the direct thermal reduction of Ni-containing Ca–Al layered double hydroxides for hydrogen generation via ammonia decomposition,” *International Journal of Hydrogen Energy*, vol. 46, no. 77, pp. 38351–38362, 2021, doi: 10.1016/j.ijhydene.2021.09.071.

[100] Q. Su *et al.*, “Layered double hydroxides derived Nix(MgyAlzOn) catalysts: Enhanced ammonia decomposition by hydrogen spillover effect,” *Applied Catalysis B: Environmental*, vol. 201, pp. 451–460, 2017, doi: 10.1016/j.apcatb.2016.08.051.

[101] J. Zhao, L. Deng, W. Zheng, S. Xu, Q. Yu, and X. Qiu, “Nickel-induced structure transformation in hydrocalumite for enhanced ammonia decomposition,” *International Journal of Hydrogen Energy*, vol. 45, no. 22, pp. 12244–12255, Apr. 2020, doi: 10.1016/j.ijhydene.2020.02.201.

[102] K. Sato, N. Abe, T. Kawagoe, S. Miyahara, K. Honda, and K. Nagaoka, “Supported Ni catalysts prepared from hydrotalcite-like compounds for the production of hydrogen by ammonia decomposition,” *International Journal of Hydrogen Energy*, vol. 42, no. 10, pp. 6610–6617, 2017, doi: 10.1016/j.ijhydene.2016.11.150.

[103] C. Li *et al.*, “Binary Cu-Co catalysts derived from hydrotalcites with excellent activity and recyclability towards NH3BH3 dehydrogenation,” *Journal of Materials Chemistry A*, vol. 1, no. 17, 2013, doi: 10.1039/c3ta10424a.

[104] J. Schumann, “Cu, Zn-based catalysts for methanol synthesis,” PhD thesis, Technischen Universität Berlin, 2015. [Online]. Available: https://pure.mpg.de/rest/items/item_2110555/component/file_2144572/content

[105] A. Knop-Gericke *et al.*, “Chapter 4 X-Ray Photoelectron Spectroscopy for Investigation of Heterogeneous Catalytic Processes,” in *Advances in catalysis*, vol. 52, Academic Press, 2009, pp. 213–272. doi: 10.1016/S0360-0564(08)00004-7.

[106] M. Plodinec *et al.*, “Versatile Homebuilt Gas Feed and Analysis System for Operando TEM of Catalysts at Work,” *Microscopy and Microanalysis*, vol. 26, no. 2, pp. 220–228, 2020, doi: 10.1017/S143192762000015X.

[107] R. Trujillano, M. J. Holgado, F. Pigazo, and V. Rives, “Preparation, physicochemical characterisation and magnetic properties of Cu-Al layered double hydroxides with (CO3)2- and anionic surfactants with different alkyl chains in the interlayer,” *Physica B: Condensed Matter*, 2006, doi: 10.1016/j.physb.2005.11.154.

[108] U. Costantino, F. Marmottini, M. Nocchetti, and R. Vivani, “New synthetic routes to hydrotalcite-like compounds - Characterisation and properties of the obtained materials,” *European Journal of Inorganic Chemistry*, no. 10, pp. 1439–1446, 1998, doi: 10.1002/(sici)1099-0682(199810)1998:10<1439::aid-ejic1439>3.0.co;2-1.

[109] M. Behrens, “Meso- and nano-structuring of industrial Cu/ZnO/(Al2O3) catalysts,” *Journal of Catalysis*, vol. 267, no. 1, pp. 24–29, 2009, doi: 10.1016/j.jcat.2009.07.009.

[110] K. S. W. Sing, “Reporting physisorption data for gas/solid systems with special reference to the determination of surface area and porosity (Recommendations 1984),” *Pure and Applied Chemistry*, vol. 57, no. 4, pp. 603–619, 1985, doi: 10.1351/pac198557040603.

[111] Z. Abdelsadek *et al.*, “Examination of the Deactivation Cycle of NiAl- and NiMgAl-Hydrotalcite Derived Catalysts in the Dry Reforming of Methane,” *Catalysis Letters*, vol. 151, no. 9, pp. 2696–2715, 2021, doi: 10.1007/s10562-020-03513-4.

[112] M. Thommes, “Physical adsorption characterization of nanoporous materials,” *Chemie-Ingenieur-Technik*, vol. 82, no. 7, pp. 1059–1073, 2010, doi: 10.1002/cite.201000064.

[113] C. Forano, T. Hibino, F. Leroux, and C. Taviot-Guého, “Chapter 13.1 Layered Double Hydroxides,” in *Developments in clay science*, vol. 1, Elsevier, 2006, pp. 1021–1095. doi: 10.1016/S1572-4352(05)01039-1.

[114] J. Schumann, A. Tarasov, N. Thomas, R. Schlögl, and M. Behrens, “Cu,Zn-based catalysts for methanol synthesis: On the effect of calcination conditions and the part of residual carbonates,” *Applied Catalysis A: General*, vol. 516, pp. 117–126, 2016, doi: 10.1016/j.apcata.2016.01.037.

[115] T. Stanimirova, I. Vergilov, G. Kirov, and N. Petrova, “Thermal decomposition products of hydrotalcite-like compounds: low-temperature metaphases,” *Journal of Materials Science*, vol. 34, pp. 4153–4161, 1999, doi: 10.1023/A:1004673913033.

[116] P. J. Smith *et al.*, “A new class of Cu/ZnO catalysts derived from zincian georgeite precursors prepared by co-precipitation,” *Chemical Science*, vol. 8, no. 3, pp. 2436–2447, Feb. 2017, doi: 10.1039/C6SC04130B.

[117] B. Bems, M. Schur, A. Dassenoy, H. Junkes, D. Herein, and R. Schlögl, "Relations between synthesis and microstructural properties of copper/zinc hydroxycarbonates," *Chemistry - A European Journal*, vol. 9, no. 9, pp. 2039–2052, 2003, doi: 10.1002/chem.200204122.

[118] L. Chmielarz *et al.*, "An influence of thermal treatment conditions of hydrotalcite-like materials on their catalytic activity in the process of N2O decomposition," *Journal of Thermal Analysis and Calorimetry*, vol. 105, no. 1, pp. 161–170, Jul. 2011, doi: 10.1007/s10973-011-1284-4.

[119] S. Kühl, A. Tarasov, S. Zander, I. Kasatkin, and M. Behrens, "Cu-based catalyst resulting from a Cu,Zn,Al hydrotalcite-like compound: A microstructural, thermoanalytical, and in situ XAS study," *Chemistry - A European Journal*, 2014, doi: 10.1002/chem.201302599.

[120] A. Tarasov, S. Kühl, J. Schumann, and M. Behrens, "Thermokinetic study of the reduction process of a CuO/ZnAl2O4 catalyst," *High Temperatures - High Pressures*, vol. 42, no. 4, pp. 377–386, 2013.

[121] M. Behrens, I. Kasatkin, S. Kühl, and G. Weinberg, "Phase-pure Cu,Zn,Al hydrotalcite-like materials as precursors for copper rich Cu/ZnO/Al2O3 catalysts," *Chemistry of Materials*, vol. 22, no. 2, pp. 386–397, 2010, doi: 10.1021/cm9029165.

[122] A. Tarasov, J. Schumann, F. Girgsdies, N. Thomas, and M. Behrens, "Thermokinetic investigation of binary Cu/Zn hydroxycarbonates as precursors for Cu/ZnO catalysts," *Thermochimica Acta*, vol. 591, pp. 1–9, 2014, doi: 10.1016/j.tca.2014.04.025.

[123] A. J. Akande, R. O. Idem, and A. K. Dalai, "Synthesis, characterization and performance evaluation of Ni/Al2O3 catalysts for reforming of crude ethanol for hydrogen production," *Applied Catalysis A: General*, vol. 287, no. 2, pp. 159–175, 2005, doi: 10.1016/j.apcata.2005.03.046.

[124] P. L. Potapov, S. E. Kulkova, D. Schryvers, and J. Verbeeck, "Structural and chemical effects on EELS L3,2 ionization edges in Ni-based intermetallic compounds," *Physical Review B - Condensed Matter and Materials Physics*, vol. 64, no. 18, p. 184110, 2001, doi: 10.1103/physrevb.64.184110.

[125] P. Ewels, T. Sikora, V. Serin, C. P. Ewels, and L. Lajaunie, "A Complete Overhaul of the Electron Energy-Loss Spectroscopy and X-Ray Absorption Spectroscopy Database: Eelsdb.eu," *Microscopy and Microanalysis*, vol. 22, no. 3, pp. 717–724, 2016, doi: 10.1017/S1431927616000179.

[126] J. Gao, C. Jia, M. Zhang, F. Gu, G. Xu, and F. Su, "Effect of nickel nanoparticle size in Ni/\alpha-Al2O3 on CO methanation reaction for the production of synthetic natural gas," *Catalysis Science and Technology*, vol. 3, no. 8, pp. 2009–2015, 2013, doi: 10.1039/c3cy00139c.

[127] Q. Jeangros *et al.*, “Reduction of nickel oxide particles by hydrogen studied in an environmental TEM,” *Journal of Materials Science*, vol. 48, no. 7, pp. 2893–2907, 2013, doi: 10.1007/s10853-012-7001-2.

[128] X. Meng, Y. Yang, L. Chen, M. Xu, X. Zhang, and M. Wei, “A Control over Hydrogenation Selectivity of Furfural via Tuning Exposed Facet of Ni Catalysts,” *ACS Catalysis*, vol. 9, no. 5, pp. 4226–4235, May 2019, doi: 10.1021/acscatal.9b00238.

[129] A. R. Naghash, T. H. Etsell, and S. Xu, “XRD and XPS study of Cu-Ni interactions on reduced copper-nickel-aluminum oxide solid solution catalysts,” *Chemistry of Materials*, vol. 18, no. 10, pp. 2480–2488, 2006, doi: 10.1021/cm051910o.

[130] A. Crucq, L. Degols, G. Lienard, and A. Frennet, “Hydrogen spillover from Ni to CuNi alloys,” *Studies in Surface Science and Catalysis*, vol. 17, no. C, pp. 137–147, 1983, doi: 10.1016/S0167-2991(08)64668-6.

[131] Y. Yao and D. W. Goodman, “Direct evidence of hydrogen spillover from Ni to Cu on Ni-Cu bimetallic catalysts,” *Journal of Molecular Catalysis A: Chemical*, vol. 383–384, pp. 239–242, 2014, doi: 10.1016/j.molcata.2013.12.013.

[132] L. D. Rogatis, T. Montini, B. Lorenzut, and P. Fornasiero, “NixCuy/Al2O3 based catalysts for hydrogen production,” *Energy and Environmental Science*, vol. 1, no. 4, pp. 501–509, 2008, doi: 10.1039/b805426f.

[133] A. R. Naghash, Z. Xu, and T. H. Etsell, “Coprecipitation of nickel-copper-aluminum takovite as catalyst precursors for simultaneous production of carbon nanofibers and hydrogen,” *Chemistry of Materials*, vol. 17, no. 4, pp. 815–821, 2005, doi: 10.1021/cm048476v.

[134] D. J. Chakrabarti, D. E. Laughlin, S. W. Chen, and Y. A. Chang, “Phase diagrams of binary nickel alloys,” *by Nash, P., ASM International, Materials Park, OH*, p. 85, 1991.

[135] Rü. Duran, P. Stender, S. M. Eich, and G. Schmitz, “Atom Probe Study of the Miscibility Gap in CuNi Thin Films and Microstructure Development,” *Microscopy and Microanalysis*, vol. 28, no. 4, pp. 1359–1369, 2022, doi: 10.1017/S1431927621012988.

[136] Y. Iguchi, G. L. Katona, C. Cserháti, G. A. Langer, and Z. Erdélyi, “On the miscibility gap of Cu-Ni system,” *Acta Materialia*, vol. 148, pp. 49–54, 2018, doi: 10.1016/j.actamat.2018.01.038.

[137] A. Shirinyan, M. Wautelet, and Y. Belogorodsky, “Solubility diagram of the Cu-Ni nanosystem,” *Journal of Physics Condensed Matter*, vol. 18, no. 8, pp. 2537–2551, 2006, doi: 10.1088/0953-8984/18/8/016.

[138] A. S. Shirinyan, “Two-phase equilibrium states in individual Cu-Ni nanoparticles: Size, depletion and hysteresis effects,” *Beilstein Journal of Nanotechnology*, vol. 6, no. 1, pp. 1811–1820, 2015, doi: 10.3762/bjnano.6.185.

[139] A. B. Gurevich, B. E. Bent, A. V. Teplyakov, and J. G. Chen, "A NEXAFS investigation of the formation and decomposition of CuO and Cu2O thin films on Cu(100)," *Surface Science*, vol. 442, no. 1, pp. L971–L976, Nov. 1999, doi: 10.1016/S0039-6028(99)00913-9.

[140] L. Wang *et al.*, "Deciphering the Exceptional Performance of NiFe Hydroxide for the Oxygen Evolution Reaction in an Anion Exchange Membrane Electrolyzer," *ACS Applied Energy Materials*, vol. 5, no. 2, pp. 2221–2230, Feb. 2022, doi: 10.1021/acsaem.1c03761.

[141] M. Abbate *et al.*, "Probing depth of soft x-ray absorption spectroscopy measured in total-electron-yield mode," *Surface and Interface Analysis*, vol. 18, no. 1, pp. 65–69, Jan. 1992, doi: 10.1002/sia.740180111.

[142] M. Grioni *et al.*, "Studies of copper valence states with Cu L 3 x-ray-absorption spectroscopy," *PHYSICAL REVIEW B*, vol. 39, pp. 15–1989.

[143] H. H. Hsieh *et al.*, "Electronic structure of Ni-Cu alloys: The d-electron charge distribution," *Physical Review B.*, vol. 57, no. 24, pp. 15204–15210, 1998, doi: 10.1103/PhysRevB.57.15204.

[144] A. C. Miller and G. W. Simmons, "Copper by XPS," *Surface Science Spectra*, vol. 2, no. 1, pp. 55–60, Jan. 1993, doi: 10.1116/1.1247725.

[145] A. C. Miller and G. W. Simmons, "Nickel by XPS," *Surface Science Spectra*, vol. 1, no. 3, pp. 312–317, Sep. 1992, doi: 10.1116/1.1247658.

[146] A. Jha *et al.*, "Hydrogen production by the water-gas shift reaction using CuNi/Fe2O3 catalyst," *Catalysis Science & Technology*, vol. 5, no. 5, pp. 2752–2760, Apr. 2015, doi: 10.1039/C5CY00173K.

[147] R. Naumann d'Alnoncourt *et al.*, "The influence of ZnO on the differential heat of adsorption of CO on Cu catalysts: a microcalorimetric study," *Journal of Catalysis*, vol. 220, no. 1, pp. 249–253, Nov. 2003, doi: 10.1016/S0021-9517(03)00288-4.

[148] A. Tanksale, J. N. Beltramini, J. A. Dumesic, and G. Q. Lu, "Effect of Pt and Pd promoter on Ni supported catalysts—A TPR/TPO/TPD and microcalorimetry study," *Journal of Catalysis*, vol. 258, no. 2, pp. 366–377, Sep. 2008, doi: 10.1016/j.jcat.2008.06.024.

[149] J. T. Stuckless, N. Al-Sarraf, C. Wartnaby, and D. A. King, "Calorimetric heats of adsorption for CO on nickel single crystal surfaces," *Journal of Chemical Physics*, vol. 99, no. 3, pp. 2202–2212, 1993, doi: 10.1063/1.465282.

[150] J. Pritchard, T. Catterick, and R. K. Gupta, "Infrared spectroscopy of chemisorbed carbon monoxide on copper," *Surface Science*, vol. 53, no. 1, pp. 1–20, Dec. 1975, doi: 10.1016/0039-6028(75)90113-2.

[151] I. A. Fisher and A. T. Bell, "In Situ Infrared Study of Methanol Synthesis from H2/CO over Cu/SiO2 and Cu/ZrO2/SiO2," *Journal of Catalysis*, vol. 178, no. 1, pp. 153–173, Aug. 1998, doi: 10.1006/jcat.1998.2134.

[152] G. Poncelet, M. A. Centeno, and R. Molina, "Characterization of reduced \alpha-alumina-supported nickel catalysts by spectroscopic and chemisorption measurements," *Applied Catalysis A: General*, vol. 288, no. 1–2, 2005, doi: 10.1016/j.apcata.2005.04.052.

[153] A. W. Smith and J. M. Quets, "Adsorption of carbon monoxide on copper: Infrared absorption spectra and thermodesorption," *Journal of Catalysis*, vol. 4, no. 2, pp. 163–171, Apr. 1965, doi: 10.1016/0021-9517(65)90007-2.

[154] T. Elgayyar, R. Atwi, A. Tuel, and F. C. Meunier, "Contributions and limitations of IR spectroscopy of CO adsorption to the characterization of bimetallic and nanoalloy catalysts," *Catalysis Today*, vol. 373, pp. 59–68, Aug. 2021, doi: 10.1016/j.cattod.2021.01.009.

[155] J. C. Campuzano and R. G. Greenler, "The adsorption sites of CO on Ni(111) as determined by infrared reflection-absorption spectroscopy," *Surface Science*, vol. 83, no. 1, pp. 301–312, Apr. 1979, doi: 10.1016/0039-6028(79)90495-3.

[156] K. Föttinger, R. Schlögl, and G. Rupprechter, "The mechanism of carbonate formation on Pd–Al2O3 catalysts," *Chemical Communications*, no. 3, pp. 320–322, Jan. 2008, doi: 10.1039/B713161E.

[157] J. Schumann, J. Kröhnert, E. Frei, R. Schlögl, and A. Trunschke, "IR-Spectroscopic Study on the Interface of Cu-Based Methanol Synthesis Catalysts: Evidence for the Formation of a ZnO Overlayer," *Topics in Catalysis*, vol. 60, no. 19–20, pp. 1735–1743, 2017, doi: 10.1007/s11244-017-0850-9.

[158] D. Li, M. Lu, K. Aragaki, M. Koike, Y. Nakagaka, and K. Tomishige, "Characterization and catalytic performance of hydrotalcite-derived Ni-Cu alloy nanoparticles catalysts for steam reforming of 1-methylnaphthalene," *"Applied Catalysis B, Environmental,"* vol. 192, pp. 171–181, 2016, doi: 10.1016/j.apcatb.2016.03.052.

[159] J. P. Ngantcha, M. Gerland, Y. Kihn, and A. Rivière, "Correlation between microstructure and mechanical spectroscopy of a Cu-Cu2O alloy between 290 K and 873 K," *European Physical Journal Applied Physics*, vol. 29, pp. 83–89, 2005, doi: 10.1051/epjap:2004200.

[160] D. Bouchet and C. Colliex, "Experimental study of ELNES at grain boundaries in alumina: Intergranular radiation damage effects on Al-L23 and O-K edges," *Ultramicroscopy*, vol. 96, no. 2, pp. 139–152, 2003, doi: 10.1016/S0304-3991(02)00437-0.

[161] R. F. Egerton, "Scattering delocalization and radiation damage in STEM-EELS," *Ultramicroscopy*, vol. 180, pp. 115–124, Sep. 2017, doi: 10.1016/j.ultramic.2017.02.007.

[162] P. Mukherjee *et al.*, “Surface Structural and Chemical Evolution of Layered LiNi0.8Co0.15Al0.05O2 (NCA) under High Voltage and Elevated Temperature Conditions,” *Chemistry of Materials*, vol. 30, no. 23, pp. 8431–8445, 2018, doi: 10.1021/acs.chemmater.7b05305.

[163] W. Hetaba, P. Blaha, F. Tran, and P. Schattschneider, “Calculating energy loss spectra of NiO: Advantages of the modified Becke-Johnson potential,” *Physical Review B*, vol. 85, no. 20, pp. 1–6, 2012, doi: 10.1103/PhysRevB.85.205108.

[164] V. Edlmayr, T. P. Harzer, R. Hoffmann, D. Kiener, C. Scheu, and C. Mitterer, “ Effects of thermal annealing on the microstructure of sputtered Al 2 O 3 coatings ,” *Journal of Vacuum Science & Technology A: Vacuum, Surfaces, and Films*, vol. 29, no. 4, p. 041506, 2011, doi: 10.1116/1.3584803.

[165] H. Düdder *et al.*, “The role of carbonaceous deposits in the activity and stability of Ni-based catalysts applied in the dry reforming of methane,” *Catalysis Science and Technology*, vol. 4, no. 9, pp. 3317–3328, 2014, doi: 10.1039/c4cy00409d.

[166] Q. Pan, J. Peng, T. Sun, S. Wang, and S. Wang, “Insight into the reaction route of CO2 methanation: Promotion effect of medium basic sites,” *Catalysis Communications*, vol. 45, pp. 74–78, Feb. 2014, doi: 10.1016/j.catcom.2013.10.034.

[167] X. Guo *et al.*, “Highly Active Ni-Based Catalyst Derived from Double Hydroxides Precursor for Low Temperature CO2 Methanation,” *Industrial and Engineering Chemistry Research*, vol. 57, no. 28, pp. 9102–9111, Jul. 2018, doi: 10.1021/acs.iecr.8b01619.

[168] L. C. Grabow and M. Mavrikakis, “Mechanism of methanol synthesis on Cu through CO2 and CO hydrogenation,” *ACS Catalysis*, vol. 1, no. 4, pp. 365–384, Mar. 2011, doi: 10.1021/cs200055d.

[169] Y. F. Zhao, Y. Yang, C. Mims, C. H. F. Peden, J. Li, and D. Mei, “Insight into methanol synthesis from CO2 hydrogenation on Cu(111): Complex reaction network and the effects of H2O,” *Journal of Catalysis*, vol. 281, no. 2, pp. 199–211, Jul. 2011, doi: 10.1016/j.jcat.2011.04.012.

[170] Y. Yang, J. Evans, J. A. Rodriguez, M. G. White, and P. Liu, “Fundamental studies of methanol synthesis from CO2 hydrogenation on Cu(111), Cu clusters, and Cu/ZnO(000),” *Physical Chemistry Chemical Physics*, vol. 12, no. 33, pp. 9909–9917, Aug. 2010, doi: 10.1039/C001484B.

[171] K. Mette *et al.*, “High-Temperature Stable Ni Nanoparticles for the Dry Reforming of Methane,” *ACS Catalysis*, vol. 6, no. 10, pp. 7238–7248, 2016, doi: 10.1021/acscatal.6b01683.

[172] L. Karam, J. Reboul, N. El Hassan, J. Nelayah, and P. Massiani, "Nanostructured nickel aluminate as a key intermediate for the production of highly dispersed and stable nickel nanoparticles supported within mesoporous alumina for dry reforming of methane," *Molecules*, vol. 24, no. 22, 2019, doi: 10.3390/molecules24224107.

[173] M. Li, S. Fang, and Y. H. Hu, "Self-stabilization of Ni/Al2O3 Catalyst with a NiAl2O4 Isolation Layer in Dry Reforming of Methane," *Catalysis Letters*, vol. 152, no. 9, pp. 2852–2859, Sep. 2022, doi: 10.1007/s10562-021-03867-3.

[174] A. P. Grosvenor, M. C. Biesinger, R. S. C. Smart, and N. S. McIntyre, "New interpretations of XPS spectra of nickel metal and oxides," *Surface Science*, vol. 600, no. 9, pp. 1771–1779, May 2006, doi: 10.1016/j.susc.2006.01.041.

[175] P. Jiang *et al.*, "Experimental and theoretical investigation of the electronic structure of Cu2O and CuO thin films on Cu(110) using x-ray photoelectron and absorption spectroscopy," *Journal of Chemical Physics*, vol. 138, no. 2, p. 24704, Jan. 2013, doi: 10.1063/1.4773583.

[176] V. Serin, R. Brydson, S. Matar, and F. Boucher, "EELS investigation of the electron conduction-band states in wurtzite AlN and oxygen-doped AlN(O)," *Physical Review B*, vol. 58, no. 8, pp. 5106–5115, 1998, doi: 10.1103/PhysRevB.58.5106.

[177] M. E. Kreider *et al.*, "Precious Metal-Free Nickel Nitride Catalyst for the Oxygen Reduction Reaction," *ACS Applied Materials and Interfaces*, vol. 11, no. 30, pp. 26863–26871, 2019, doi: 10.1021/acsami.9b07116.

[178] V. Rives, "Characterisation of layered double hydroxides and their decomposition products," *Materials Chemistry and Physics*, vol. 75, no. 1–3, pp. 19–25, Apr. 2002, doi: 10.1016/S0254-0584(02)00024-X.

[179] P. Cao *et al.*, "Atomic-Scale Insights into Nickel Exsolution on LaNiO3 Catalysts via In Situ Electron Microscopy," *Journal of Physical Chemistry C*, vol. 126, no. 1, pp. 786–796, 2022, doi: 10.1021/acs.jpcc.1c09257.

[180] H. Tanaka *et al.*, "Dynamics of Rh nanoparticle surface structure during NO reduction revealed by operando transmission electron microscopy," *Applied Catalysis A: General*, vol. 626, p. 118334, 2021, doi: 10.1016/j.apcata.2021.118334.

[181] A. T. Delariva, T. W. Hansen, S. R. Challa, and A. K. Datye, "In situ Transmission Electron Microscopy of catalyst sintering," *Journal of Catalysis*, vol. 308, pp. 291–305, Dec. 2013, doi: 10.1016/j.jcat.2013.08.018.

[182] F. Samimi, D. Karimipourfard, and M. R. Rahimpour, "Green methanol synthesis process from carbon dioxide via reverse water gas shift reaction in a membrane reactor," *Chemical Engineering Research and Design*, vol. 140, pp. 44–67, Dec. 2018, doi: 10.1016/j.cherd.2018.10.001.

[183] L. W. Hobbs, "Radiation Effects in Analysis of Inorganic Specimens by TEM," in *Introduction to analytical electron microscopy*, Springer, Boston, MA, 1979, pp. 437–480. doi: 10.1007/978-1-4757-5581-7.

[184] Q. Chen *et al.*, "Imaging Beam-Sensitive Materials by Electron Microscopy," *Advanced Materials*, vol. 32, no. 16, 2020, doi: 10.1002/adma.201907619.

[185] R. F. Egerton, P. Li, and M. Malac, "Radiation damage in the TEM and SEM," *Micron*, vol. 35, no. 6, pp. 399–409, Aug. 2004, doi: 10.1016/j.micron.2004.02.003.

[186] L. W. Hobbs, "Electron-beam sensitivity in inorganic specimens," *Ultramicroscopy*, vol. 23, no. 3–4, pp. 339–344, Jan. 1987, doi: 10.1016/0304-3991(87)90244-0.

[187] J. Reyes-Gasga and R. García-García, "Analysis of the electron-beam radiation damage of TEM samples in the acceleration energy range from 0.1 to 2 MeV using the standard theory for fast electrons," *Radiation Physics and Chemistry*, vol. 64, no. 5–6, pp. 359–367, Aug. 2002, doi: 10.1016/S0969-806X(01)00578-3.

[188] R. F. Egerton, F. Wang, and P. A. Crozier, "Beam-Induced Damage to Thin Specimens in an Intense Electron Probe," *Microscopy and Microanalysis*, vol. 12, no. 1, pp. 65–71, Feb. 2006, doi: 10.1017/S1431927606060065.

[189] D. Wang, D. S. Su, and R. Schlögl, "Electron Beam Induced Transformation of MoO3 to MoO2 and a New Phase MoO," *Zeitschrift für anorganische und allgemeine Chemie*, vol. 630, no. 7, pp. 1007–1014, Jul. 2004, doi: 10.1002/zaac.200400052.

[190] C. Gammer, C. Mangler, C. Rentenberger, and H. P. Karnthaler, "Quantitative local profile analysis of nanomaterials by electron diffraction," *Scripta Materialia*, vol. 63, no. 3, pp. 312–315, Aug. 2010, doi: 10.1016/j.scriptamat.2010.04.019.